Kristoffer Høyem Aronsen

An Experimental Investigation of In-line and Combined In-line and Cross-flow Vortex Induced Vibrations

Thesis for the degree doctor philosophiae

Trondheim, December 2007

Norwegian University of
Science and Technology
Faculty for Engineering Science and Technology
Department of Marine Technology

Abstract

This thesis presents results from an experimental investigation of hydrodynamic forces on a cylinder under prescribed harmonic motions in uniform flow. The purpose of the experiments has been to find hydrodynamic coefficients for pure in-line (IL) oscillations and investigate the interaction between IL and cross-flow (CF) vortex induced vibrations (VIV). Hydrodynamic forces are hence measured in both directions.

The experiments are performed in a towing tank of 40m, using a rigid cylinder of aspect ratio 20. The cylinder is installed in a yoke structure which in turn is suspended to an overhanging tow carriage. Model oscillations are achieved by oscillating the yoke on the carriage, while the flow velocity is obtained by moving the carriage at constant speed in still water. All experiments are performed at Reynolds number $2.4 \cdot 10^4$.
Three main types of experiments are carried out:

1. IL oscillations where the frequencies and amplitudes are varied to obtain a detailed map of the forces acting on a cylinder in the pure IL VIV regime.

2. Two degree-of-freedom motions resembling the oscillation patterns observed in a flexible beam experiment.

3. Two degree-of-freedom motion tests where the shape and direction of the orbital paths are systematically varied.

From the detailed knowledge of the excitation forces in the pure IL VIV regime, obtained in the first set of experiments, a novel approach for determining the effect of structural damping is introduced. This approach makes it possible to distinguish between the effect of structural damping and the effect of mass ratio on the response of a body subjected to VIV. A response model for predicting IL VIV is presented based on this method. The results also reveal that IL oscillations will give rise to CF forces that contribute to an earlier start-up of CF VIV, compared to conditions where the IL motion is restrained.

The results of the second set of experiments indicate that hydrodynamic coefficients from forced oscillation experiments and the assumption that strip theory is valid, can be used to predict two degree-of-freedom response of a flexible beam. In the third set of experiments it is revealed that changing the shape and direction of the orbital path significantly changes the forces acting on the cylinder. Hydrodynamic forces at multiples of the oscillation frequency, known as higher order harmonic forces, are also measured.

Acknowledgments

I wish to thank my supervisor Professor Carl Martin Larsen for guiding me through this study. Valuable ideas, suggestions, comments and fruitful discussions are gratefully acknowledged. His patience and encouragement, especially during the long lasting process of finalizing the thesis, have been highly appreciated.

I wish to thank Professor Michael Triantafyllou and his group at MIT for their hospitality during my stay in Boston, for spending the time to help solving my problems with the data processing and for pointing out important results in my data set.

I also wish to express my thanks to NTNU laboratory staff, Torgeir Wahl, Knut Arne Hegstad and Ole Erik Vinje for helping with the experiments. A special thank to Dr. Svein Ersdal for working late hours and weekends in order to get the experimental setup working. The experiments could not have been conducted without his help. I also wish to thank Dr. Kjetil Skaugseth for good teamwork during the PIV experiments.

I am grateful to Dr. Kim Mørk (DNV) and Halvor Lie (Marintek) for shearing their experience and knowledge both in the process of planning the experiments and during the course of the work.

Last, but not the least I owe thanks to my family, friends and colleagues for their contributions and encouragement during these years.

Contents

Nomenclature

General

- Symbols are generally defined where they appear in the text for the first time.

- All units given are based on the SI system

- Over-dots signify differentiation with respect to time

- Over-line signify mean value or generalized value

Abbreviations

2D	Two dimensional
3D	Three dimensional
CF	Cross-flow
CFD	Computational fluid dynamics
DOF	Degree of freedom
DNV	Det Norske Veritas
DRE	Data reduction equation
IL	In-line
max	Maximum value
min	Minimum value
MIT	Massachusetts Institute of Technology
NTNU	Norwegian University of Science and Technology
PIV	Particle image velocimetry
rms	Root mean square
RP	Recommended practice
SB	Starboard
SD	Standard deviation
VIV	Vortex induced vibrations

Roman symbols

A	Amplitude, Fourier transformed of acceleration signal
$(A/D)_{IL/CF}$	Amplitude ratio in IL or CF direction
a_0	Acceleration amplitude, Fourier coefficient
a_n	Fourier coefficient
B	Bias error
B_t	Breadth of towing tank
b_0	Fourier coefficient
b_n	Fourier coefficient
$C_{a,IL/CF}$	Added mass coefficient in IL or CF direction
C_D	Drag coefficient
$C_{e,IL/CF}$	Dynamic excitation coefficient in IL or CF direction
$C_{rms,IL/CF}$	RMS force coefficient in IL or CF direction
$C_{t,IL/CF}$	Total hydrodynamic force coefficient in IL or CF direction
C_{t,S_t}	Total hydrodynamic force coefficient at the Strouhal frequency
c	Linear damping coefficient
$\hat{c}$	Nondimensional damping, $\frac{c}{\rho D U_0}$
D	Cylinder diameter
D_t	Water depth of towing tank
E	Young's modulus
e	Error
F	Force
F_0	Force amplitude
F_{hydro}	Hydrodynamic force
$F_{hydro,0}$	Hydrodynamic force amplitude
$F_{IL,mean}$	Mean value of measured IL force
F_n	Froude number
f	Frequency
f_0	Eigenfrequency in still water
$f_{osc,IL/CF}$	Oscillation frequency in IL or CF direction
f_s	Vortex shedding frequency
$\hat{f}_{IL/CF}$	Nondimensional frequency in IL or CF direction, $\frac{f_{osc}D}{U_0}$
g	Acceleration of gravity, m/s^2
$H_{xy}(\omega)$	Transfer function
h	Water depth
I	Area moment of inertia
KC	Keulegan-Carpenter number for oscillatory flow, $\frac{U_m}{fD}$
K_s	Stability parameter, $\frac{4\pi m \zeta}{\rho D^2}$
k	Characteristic size of roughness, calibration factor

L	Cylinder length
L_t	Length of towing tank
M	Mass of test cylinder
m	mass
$\bar{m}$	Mass ratio
n	Integer number
P	Power transfer, Precision error
$\bar{P}$	Average power transfer
p	Pressure
Re	Reynolds number, $\frac{DU_0}{\nu}$
S_G	Response parameter
S_t	Strouhal number, $\frac{f_s D}{U_0}$
S_{xx}	Auto spectrum
S_{xy}	Cross spectrum
T	Time, effective tension
T_{osc}	Oscillation period
t	Time variable. Also used for weight specifying confidence interval.
U	Total error, uncertainty
U_0	Flow velocity
U	Fluid velocity vector
V	Fourier transformed of velocity signal
V_r	Reduced velocity, $\frac{U_0}{f_0 D}$
X	Fourier transformed of displacement signal
x, x_0	Cylinder displacement, displacement amplitude
$\dot{x}$, $\dot{x}_0$	Cylinder velocity, velocity amplitude
$\ddot{x}$, $\ddot{x}_0$	Cylinder acceleration, acceleration amplitude

Greek symbols

α Phase angle describing orbital shape, cross talk angle

δ Boundary layer thickness, logarithmic decrement

κ Influence coefficient

ζ Damping ratio

μ Viscosity

ν Kinematic viscosity

π 3.141592..

ρ Density of water

ρ_{xy} Correlation coefficient

Φ Mode shape

ϕ Phase angle between force and displacement, velocity potential

ω Circular frequency, $2\pi f$

ω_{osc} Circular oscillation frequency, $2\pi/T_{osc}$

Mathematical operators

∇ Differential operator, $[\mathbf{i}\partial/\partial x, \mathbf{j}\partial/\partial y, \mathbf{k}\partial/\partial z]^T$

Chapter 1

Introduction

1.1 Background and motivation

In recent years new deep water oil and gas fields have been developed in areas with very irregular seabed conditions, and this trend is expected to continue in the coming years. Installation of pipelines in such areas is likely to result in a large number of free spans. Ocean currents will here lead to separated flow and vortex shedding. These vortices will again induce forces on the pipe that may result in horizontal and vertical oscillations. This phenomenon is known as vortex induced vibrations (VIV), and the horizontal and vertical oscillations are denoted in-line (IL) and cross-flow (CF) respectively. These oscillations will give time varying stresses in the pipe, and hence lead to accumulation of fatigue damage.

Vortex induced vibration of slender marine structures has been the subject of extensive research for several decades. The focus of the research has to a large degree been on offshore risers. Risers can in this respect be regarded as infinitely long structures where the boundary conditions are of minor importance. Free spanning pipelines are, on the other hand, characterized by:

- Relatively short spans, i.e. the boundary conditions become important for the dynamics of the span.

- Large variety of span configurations.

- Proximity to seabed. This might influence the inflow conditions and can also cause nonlinear response due to seabed interaction for large oscillations.

- Damping at span shoulders due to pipe soil interaction.

- Dynamic interaction with adjacent spans, known as multi-span.

The response in IL direction has often been neglected in earlier VIV studies mainly because CF response amplitudes are larger. However, studies have shown that for free spanning pipelines fatigue damage due to IL response may become significant and even more critical than CF. There are two reasons for this:

- IL response is initiated at lower current velocity than CF, and will hence take place more often. This is easily realized by taking statistics of current velocity into consideration.

- IL response will take place at two times the frequency of CF, which means that number of stress cycles due to IL will become two times the number of CF cycles.

Models exist for estimation of response and thus fatigue damage accumulation due to VIV. These are parametric response models, models based on empirical force coefficients and direct solution of the hydroelastic problem by computational fluid dynamics (CFD). The first method is by far the most used for free spanning pipelines while the second method is mainly used for riser analysis. CFD based methods are still too demanding with respect to computing time and is therefore a research method and not a tool for engineers.

A large number of parameters are important for the response caused by VIV. Experiments performed by different experimental methods and by different research groups are often hard to compare because several of these parameters are related and are different from one set of experiments to the next. Models for prediction of VIV response, based on empirical force coefficients have hence inherent uncertainties. Three effects are in particular important in this context:

- Data for hydrodynamic coefficients are found from tests with oscillating rigid cylinders and applied on flexible beams according to a strip theory approach. This means that forces at a specific position on a beam are assumed to depend on the local oscillation condition. Hence, no "hydrodynamic communication" along the beam is accounted for. The validity of this approach has never been studied in detail.

- CF and IL response have often been considered separately, and the interaction between the two response modes has hence been neglected. A flexible beam may have IL response without any CF, but for most cases of practical interest IL will be present as soon as CF response occurs. Observation of VIV for flexible beams clearly indicate that there is a strong interaction between the two types.

- The amplitudes of IL response are well known for free oscillations of a rigid cylinder with insignificant damping. This type of experiments will, however, only give data for fixed combinations of amplitude and frequency. However, real structures may have significant damping. In order to predict the response for such cases one have to know the hydrodynamic coefficients for arbitrary combinations of amplitude and frequency. This type of data has so far not been available.

Failure of a submarine pipeline is considered unacceptable from an environmental perspective and repair of deep water pipelines is also extremely expensive. Hence, the acceptable probability of failure is low (typically 10^{-4}). Due to the uncertainty in the models for prediction of fatigue damage, high safety factor are applied on the estimated result in order to achieve the desired safety level. If the calculation indicate that the fatigue damage over the design life of the pipeline is too high, the following measures can be taken:

- Rerouting of the pipeline to avoid areas of uneven seabed. This is often not an option either because the particular area can not be avoided or because the actual length of the span is found in the as-laid survey

- Seabed intervention

- Rock dumping
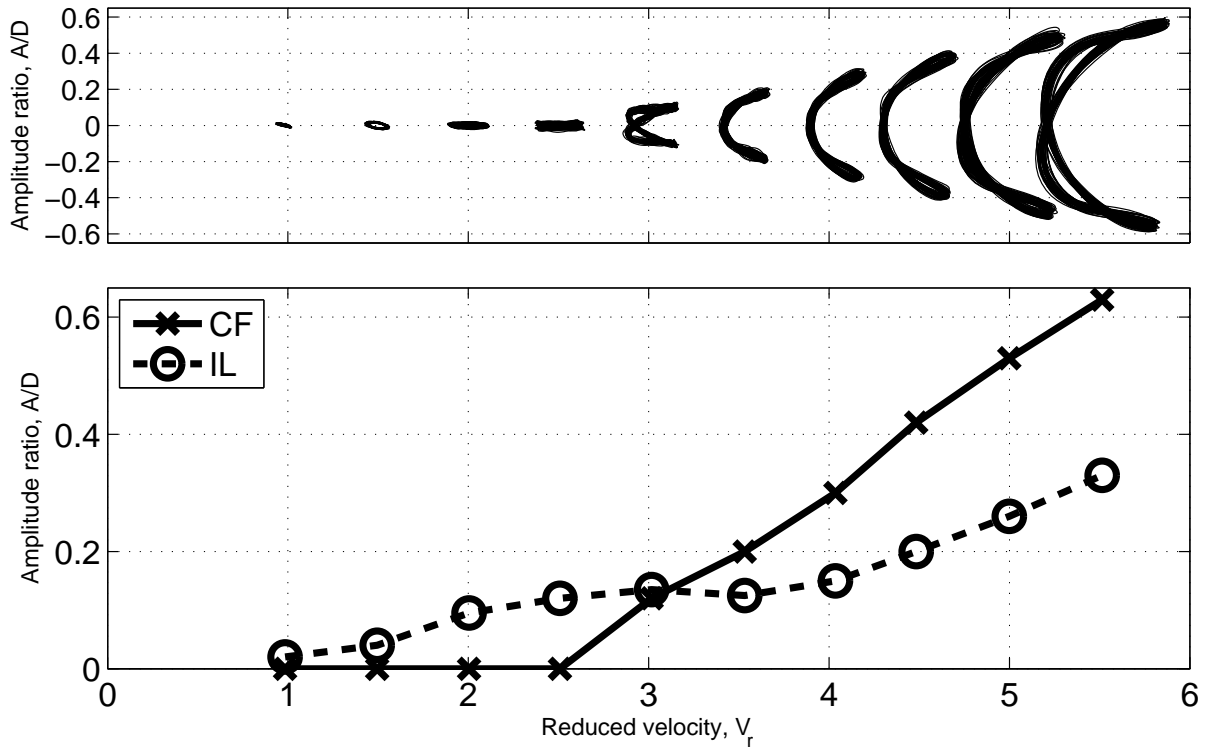
Figure 1.1: Results from a flexible beam experiment performed for the Ormen Lange pipeline project. The lower figure shows maximum response amplitude in IL and CF direction, while the upper figure shows the corresponding response trajectory at mid-span. The increasing V_r is generated by increasing the flow velocity. For definition of V_r see chapter 2

The motivation for the present work is that we still do not have a full understanding of VIV for slender marine structures. Various empirical models for prediction of VIV do not give the same results, and various experimental methods may lead to diversing conclusions. The effect of IL vibrations has not been included in empirical force coefficient models due to lack of data. Hence, we do not know much about the actual forces acting on a slender marine structure subjected to VIV, as the response in most cases is a combination of IL and CF motion.

1.2 Approach of the present work

The work presented in this thesis is based on further investigations of findings from the large experimental program carried out for the Ormen Lange pipeline project. These experiments were carried out by towing a flexible beam representing a scaled model of a free span for the actual pipeline. This type of experiment allows response both in IL and CF direction. An example of one of the test series is shown i Figure 1.1. Some of the main findings from the project were:

- The gradual increase of CF response for increased current speed was slower than seen for pure CF tests with rigid cylinders, i.e. the maximum oscillation amplitude was

approximately the same, but it occurred at a higher reduced velocity.

- For cases where the dominating IL mode had higher order than the dominating CF mode, the maximum amplitude was significantly lower than found from pure CF tests. Large CF amplitudes were seen only for cases where the 2nd IL eigenfrequency was sufficiently far from the 1st IL eigenfrequency, i.e. relatively short spans where lateral stiffness was controlled by bending and less influenced by axial tension.

- The start up of CF response was seen for a lower reduced velocity than predicted from pure CF experiments.

The reason for the new findings was expected to be the fact that the flexible cylinder was free to oscillate in IL direction. In this thesis the effect of these IL oscillations are investigated. The motivation for investigating this is twofold:

1. Fatigue damage in IL direction.

2. IL motion will influence and change the CF motion, and hence the fatigue damage in CF direction.

The investigation presented in this thesis has been performed by forced oscillation experiments of a short rigid cylinder in constant flow. From this type of experiment the hydrodynamic force acting on the cylinder can be extracted, and this has been used to understand how IL response can influence CF vortex induced vibrations. Experiments designed to investigate three conditions were performed:

1. Pure IL oscillations were performed in order to map the hydrodynamic forces acting on the cylinder for arbitrary combinations of oscillation amplitude and frequencies in the regime where pure IL VIV is seen. From these forces the magnitude of the excitation force can be extracted, which is important for how sensitive these oscillations are to damping. Information on the added mass can also be obtained, which is important for predicting the oscillation frequency. In addition, the mean IL force gives the actual drag coefficient. Forces measured in the CF direction may give some answers to why CF response is seen for lower current velocities for conditions where the cylinder is free to oscillate in IL direction.

2. The second set of tests were performed in order to investigate if strip theory can be used when modeling VIV of flexible beams, i.e. investigate whether the force at one point along a flexible beam can be found from the oscillation state at this point only. Trajectories for a given flow velocity, as shown i Figure 1.1, were found for 9 section along the length of the flexible beam tested in the Ormen Lange Project. Two harmonic functions (IL and CF components), were fitted to the measured trajectories and tested by the forced oscillation method. If strip theory is valid the transfer of energy from the fluid to the cylinder should balance the structural damping and the measured added mass should correspond to the measured oscillation frequency.

3. The third step of the investigation was to perform a systematic variation of shape and direction of orbital paths in order to investigate if there were certain shapes that would extract energy and other shapes that would absorb energy. The aim of this investigation was to see if the hydrodynamic forces would give information on occurrence of orbits possible for freely oscillating cylinders and a clue on how to predict response for two degrees of freedom cases.

1.3 Outline of thesis

The thesis is divided into the following chapters:

Chapter 2 gives a brief overview of the VIV phenomenon and defines some of the most important parameters describing VIV. The experimental methods used to investigate VIV are addressed, and some of the most important contributions are referred. A discussion on how the results from various types of experiments relates to each other is also included. The last part gives an introduction to two methods for modeling VIV of free spanning pipelines.

In *chapter 3* a detailed description of the apparatus used to perform the experiments is given, and controlling parameters for all experiments are described.

Chapter 4 gives an overview of how the post-processing of the measured data is performed. The various hydrodynamic coefficients used to present the results from the experiments are also defined in this chapter.

Chapter 5 presents the uncertainty analysis carried out to determine the reliability of the hydrodynamic coefficients presented. The chapter goes into some details on the theory of uncertainty analysis and it shows how the theory has been applied for the experimental results presented in this thesis.

Chapter 6 presents the results from the pure IL experiments. The main results are contour plots of drag coefficient, added mass coefficient and dynamic excitation coefficient. The results are compared with results from free oscillation experiments found in the literature.

Chapter 7 presents results from the investigation of the validity of strip theory in VIV modeling. Oscillation patterns (trajectories) taken from 9 cross sections along the length of the span of a flexible beam experiment have been tested by forced oscillation experiments in two degree-of-freedom.

Chapter 8 presents the results from a systematic variation of shape and direction of orbital paths. The chapter has been divided into sections describing the main findings from the investigation where some of the experimental results are included in order to describe these findings. Results from all experiments are given in Appendix E.

Chapter 9 presents conclusions from the experimental work by highlighting the contributions from the thesis, and discusses further work on this topic.

Chapter 2

Theory

The intension of the first two sections of this chapter is to give a brief introduction to the phenomena vortex shedding and VIV. The topics are included herein for completeness and more elaborate discussions are given in Ph.D theses by Halse [17], Vikestad [61] and Skaugset [45]. For detailed reading on the topics, reference is made to books by Blevins [5] and Sumer & Fredsøe [52].

The various experimental methods used to investigate VIV are addressed in section 2.3. The aim of the discussion is to highlight what information the various experiments give and what the limitations of the methods are. Earlier experimental work is included in the discussion as examples. For a more complete overview of previous work reference is made to review articles by Sarpkaya [44] and Williamson & Govardhan [62]. In the fourth section of the chapter two methods used to model VIV of free spanning pipelines are reviewed.

2.1 Vortex Shedding

2.1.1 The Navier-Stokes equation

Viscous flow is described by the Navier-Stokes equation:

$$\frac{\partial \mathbf{U}}{\partial t} + (\mathbf{U} \cdot \nabla)\mathbf{U} = -\frac{\mathbf{1}}{\rho}\nabla\mathbf{p} + \frac{\nu}{\rho}\nabla^{\mathbf{2}}\mathbf{U} + \mathbf{g} \tag{2.1}$$

where $\mathbf{U}$ is the fluid velocity vector ($[u\ v\ w]^T$), ∇ is the differential operator, ρ is the density of the fluid, p is the pressure, ν is the kinematic viscosity and g is the acceleration of gravity. Without the viscosity term the Navier-Stokes equation reduces to the well known Bernoulli equation:

$$\rho\frac{\partial \phi}{\partial t} + p + \frac{1}{2}\rho U^2 + \rho g z = constant \tag{2.2}$$

2.1.2 Boundary layer and vortex formation

In an ideal fluid the flow lines around a cylinder in uniform current can be drawn as indicated in Figure 2.1A. For such flow conditions, also referred to as potential flow, the water particles will have the same velocity in the downstream stagnation point as in the upstream. Hence, the water particles are accelerated upstream, reaching a maximum velocity
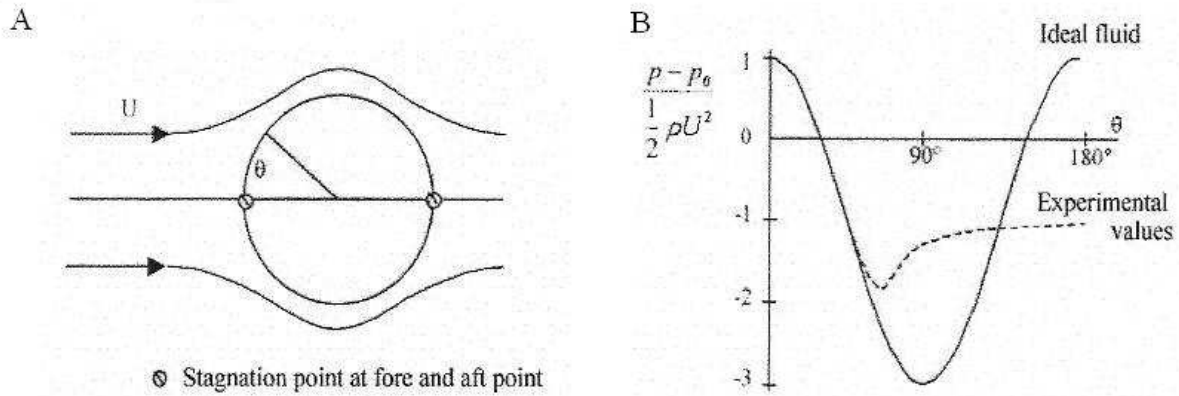
Figure 2.1: Flow and pressure distribution around a circular cylinder. Figure from Pettersen [41].

at $\theta = 90^o$, and decelerated downstream. For this ideal fluid case the Bernoulli equation is valid, see Eqn. (2.2), and we readily see that velocity variation causes a pressure drop upstream and a pressure increase downstream. The pressure distribution over the cylinder for an ideal fluid is shown in Figure 2.1B. The pressure distribution is symmetric, leading to zero drag, which is known as d'Alembert's paradox. In a viscous flow the particles close to the cylinder will loose energy due to friction. The particles may then not have enough kinetic energy to meet the increased pressure field downstream. The pressure distribution from an experiment, see Figure 2.1B, shows that the pressure distribution is asymmetric for a viscous flow. This leads to a drag force on the cylinder.

The boundary layer is the layer in which the flow velocity is increased from zero at the body surface to the free stream velocity at some distance away from the surface, see Figure 2.2. The fluid field can then be divided into two parts:

1. Near the body surface where the velocity gradient normal to the body surface is large, and the shear stress can not be neglected.

2. Outside the boundary layer where the viscosity can be neglected and the flow can be determined by potential theory, i.e. the Bernoulli equation is valid (Eqn. (2.2)).

Several ways of defining the thickness, δ, of the boundary layer have been proposed. One is to define the thickness as the distance between the surface and where the flow velocity is 99% of the free flow velocity. The boundary layer thickness increases with increasing viscosity.

When the kinetic energy of the water particles in the boundary layer is not high enough to overcome the downstream pressure field, the flow will separate from the cylinder as illustrated in Figure 2.2B. The point on the cylinder where this happens is referred to as the separation point. Upstream the separation point is the boundary layer region. Downstream the separation point is the wake region. The continuation of the boundary layer, downstream the separation point, is referred to as the shear layer.
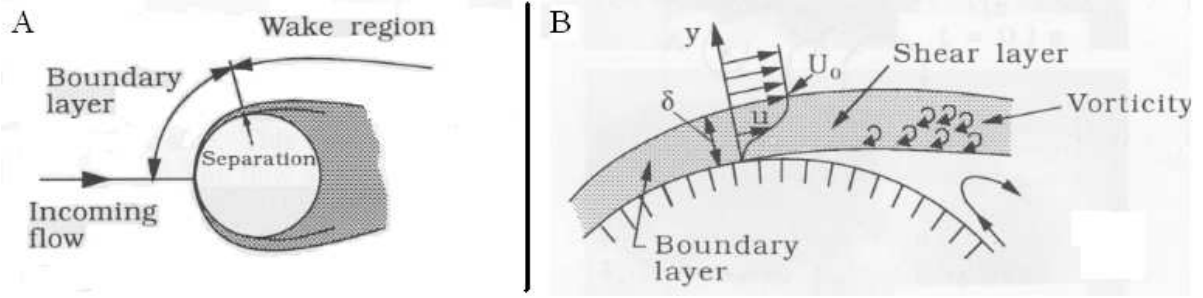
Figure 2.2: Definition sketch. Figure from Sumer and Fredsø [52].
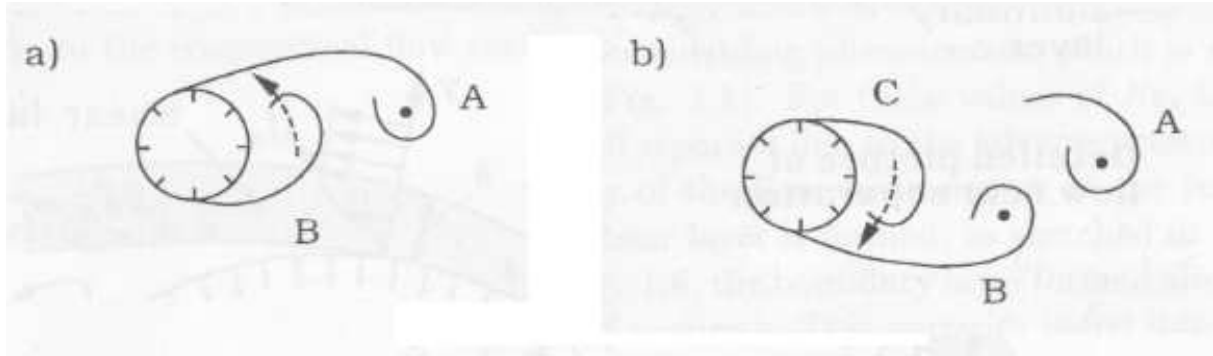
Figure 2.3: Alternating vortex shedding. Figure from Sumer and Fredsøe [52].

Back flow from behind the cylinder meets with the flow from ahead in the separation point and subsequently advances outwards, separating the shear layer from the cylinder. The vortex formed behind cylinder feeds on the the circulation from the separated shear layer. As it grows, it attracts the shear layer from the other side of the wake (see Figure 2.3a). The approaching shear layer with oppositely signed circulation eventually cuts off the supply of vorticity to the growing vortex. The vortex is then shed and moves downstream with the local velocity, see Figure 2.3b, and together with other vortices form the von Kármán vortex street.

2.1.3 Flow regimes

The flow pattern around a stationary cylinder has been investigated by several researcher by the use of various flow visualization techniques. Flow regimes have been classified in several manners, but they are all based on the dimensionless parameter Reynolds number, Re. Re denotes the relation between the inertia force and the viscous force in the boundary layer, and is defined as.

$$Re = \frac{Inertia\ force}{Friction\ force} = \frac{\rho U D}{\mu} = \frac{U D}{\nu} \tag{2.3}$$

A crude division of the flow regimes is given by Blevins [5]:

- $300 < \text{Re} < 1.5 \cdot 10^5$ Subcritical regime

- $1.5 \cdot 10^5 < \text{Re} < 3.5 \cdot 10^5$ Transitional regime

Figure 2.4: Description of flow regimes. Figure from Sumer and Fredsøe [52].

- Re > $3.5 \cdot 10^5$ Supercritical regime

A more detailed classification is given by Sumer & Fredsøe [52], see Figure 2.4.

One should be aware that the division of flow regimes into Reynolds number ranges is not definite. Disturbances may have a profound effect on the flow and change the Re ranges for where the various regimes are seen. Disturbances that may influence the flow can be surface roughness, inflow turbulence and shape imperfections of the cylinder.

2.1.4   Vortex shedding frequency

Strouhal was the first to discover that for varying current velocity U, the vortex shedding frequency, f_s, behind a stationary cylinder is proportional to U/D. The proportionality

constant has later been named the Strouhal number, S_t, and is defined as:

$$S_t = \frac{f_s D}{U} \tag{2.4}$$

The Strouhal number as a function of the Reynolds number for a stationary circular cylinder is shown in Figure 2.5 (a) for the subcritical flow regime. S_t for Re $> 3.5 \cdot 10^5$ is shown in Figure 2.11 (a).

The shedding of vortices generates time varying pressure over the cylinder. Integrated over the cylinder surface this can give rise to time varying forces both in-line (IL) with the flow and transverse (CF) to the flow. The frequency of the oscillating force in CF direction is given by the vortex shedding frequency, while the oscillating frequency in IL direction has a frequency twice the vortex shedding frequency.

2.1.5 Oscillating lift force

The time varying, or oscillating, force in CF direction is referred to as the lift force. The magnitude of the oscillating lift force as a function of Re is shown in Figure 2.5 (b), for the subcritical flow regime (note that the Re axis is in log-scale). The lift coefficient $C_{L'}$ is defined as:

$$C_{L'} = \frac{2L_{rms}}{\rho U^2 D l_c} \tag{2.5}$$

L_{rms} is the root-mean-square value of the force in CF direction, measured over an vanishingly small length l_c. The figure shows a strong increase of the lift force from Re≈1600 to approximately 20.000, where the lift force reaches an almost constant value. Norberg [39] explains the increased lift force by the transition to a turbulent free shear layer. For Re≈1600 vortices are observed in the shear layer of the near wake. These vortices introduce additional shear stress to the near wake and to balance this the formation region shrinks and base suction increases. For increasing Re the transformation to turbulent shear layer move closer to the separation point. At approximately Re=10.000 the transition has reached a position close enough to the separation point so that the actual position of the wake transition has a diminishing relative importance.

Sarpkaya [44] has highlighted the importance of this transition in the shear layer for experiments performed in the subcritical flow regime. He refers to results from Zdravkovich [66] showing that from Re=5.000 to Re=14.000 the eddy formation length decreases from 1.9D to 1.1D. At the same time the distance to the transition from laminar to turbulent free shear layer decreases from 1.0D to 0.4D. The transition in the free shear layer, from laminar to turbulent, is expected to disappear at a Re of approximately 20.000.

2.2 Vortex Induced Vibrations

In the previous section an introduction to the vortex shedding around a fixed cylinder was given, and it was shown that the process give rise to an oscillating force in both IL and CF direction. For a marine structure to be characterized as "fixed", its natural frequency must be much higher than any excitation frequency. For many slender marine

(a) Strouhal number, St   (b) Lift coefficient, $C_{L'}$
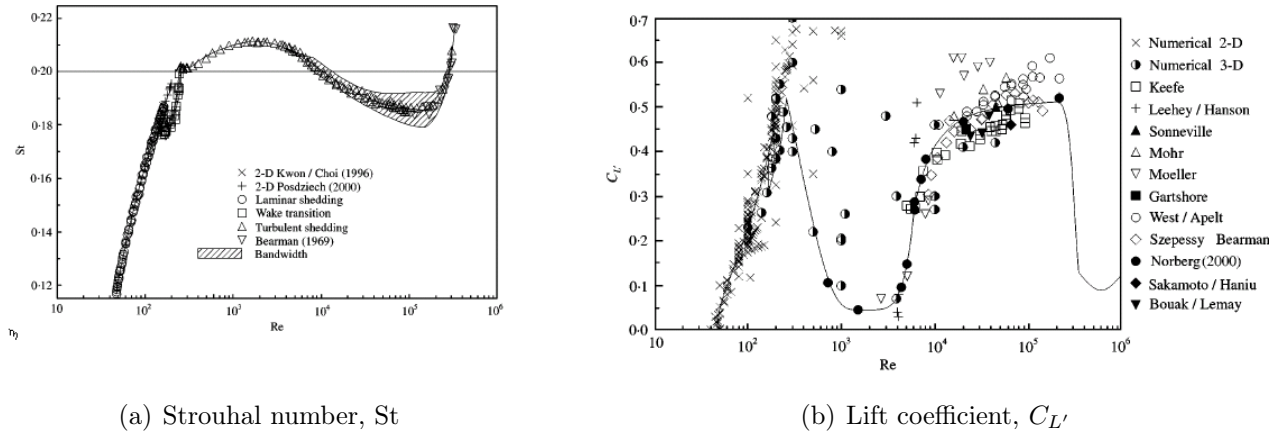
Figure 2.5: Results from fixed cylinder experiments, reported by Norberg [39].

structures, such as a free spanning pipeline, this is often not the case. An interaction between the eigenfrequency of the structure and the shedding frequency causes vortex induced vibrations.

2.2.1 Characteristics of VIV

As stated by Sarpkaya [44] an all inclusive definition of a self-exciting 'Bluff body' does not exist. It can only be described in general terms. In the following the characteristic properties of the phenomenon known as VIV are described.

The origin of the phenomenon is the separated flow, as described in the previous section, where the two shear layers interacts with each other and cause an unsteady wake. When the shedding frequency and the natural frequency of the 'Bluff body' approach a common frequency, the body starts to experience small oscillations (due to dynamic amplification). These small oscillations will help to increase the **correlation** length of the vortices, which is one of the characteristic properties of VIV. For a fixed cylinder the vortex shedding process is correlated only a few diameters along the length of the cylinder. Typically 3-6 diameters for the subcritical flow regime, see Blevins [5]. Hence, the forces acting on the cylinder has different phase over the length of the cylinder and the resulting force is small. When the correlation increases the resulting force on the cylinder increases and the oscillation amplitude will also increase.

When the oscillation amplitude in CF direction reach approximately 0.1D, or 0.02D in IL direction, **increased vortex strength** is seen (Sarpkaya [44]). This will further contribute to increase the oscillation amplitude. If the flow velocity and thus the oscillation amplitude is further increased, the spacing between the shear layers defining the virtual body increases. This apparent increase in D is compensated by the increased flow velocity, thus keeping the shedding frequency nearly constant (see Eqn.(2.4)). This represents a change from the linear increase in shedding frequency for increasing flow velocity, i.e. the shedding frequency is lower than predicted by the Strouhal relation. This represent the

start of the self-excitation region, or more commonly known as the **lock-in** region. The vortex shedding frequency matches the oscillation frequency of the body at a frequency apparently dominated by the still water natural frequency of body. However, the frequency is changed somewhat due to a change in virtual mass (i.e. added mass or hydrodynamic mass) caused by the vortex shedding process. The effect of the change in hydrodynamic mass is influenced by the mass ratio of the body. The oscillation frequency is more influenced by this change for low mass ratio bodies than for heavier bodies.

For increasing flow velocity the oscillation amplitude will increase until some maximum value is reached. This value is typically 1D for purely transverse oscillations at subcritical flow conditions and Re<15.000, 1.2D for Re>15.000, and up to 1.5D (see Jauvtis and Williamson [24]) for a body free to oscillate both in-line with and transverse to the flow. As the oscillation frequency to a large degree is controlled by the natural frequency of the body and the oscillation amplitudes reach a maximum value, VIV is considered a **self-limiting resonance phenomenon**.

2.2.2 Dimensionless parameters

A large number of dimensionless parameters are used to describe the vortex induced vibration phenomenon. Detailed description of the various parameters are given in Halse [17], Vikestad [61] and Skaugset [45]. In the following the parameters used in this thesis are defined.

Flow parameters

The following parameters are used to describe the flow conditions.

Reynolds number, Re: This parameter describes the ratio between the inertia force and the friction force acting on the body. Re is defined by Eqn. (2.3) and the parameter determines the flow regime.

Keulegan-Carpenter number, KC: The parameter describes a harmonic oscillating flow passing a fixed cylinder, and is defined as:

$$KC = \frac{U_m T}{D} = \frac{2\pi A}{D} \tag{2.6}$$

U_m is the maximum flow velocity, T is the period of the oscillating flow and D is the cylinder diameter. A is the flow amplitude and the right hand part of the definition is obtained by using the relation $U_m = \omega A = 2\pi A/T$. The KC number is mainly relevant for slender marine structures in waves.

Turbulence intensity, TI: The parameter describes fluctuations in the incoming flow, and is defined as:

$$TI = \frac{u_{rms}}{U_{mean}} \tag{2.7}$$

u_{rms} is the root-mean-square (rms) of the velocity fluctuations ($u(t) = U(t) - U_{mean}$). The turbulence near the seabed may be quite high, and the parameter is hence important for free spanning pipelines.

Structure parameters

The structure parameters describe cylinder geometry, density and damping. The following parameters have been used.

Aspect ratio: Provides a measure of the geometric shape, cylinder length to diameter:

$$\frac{L}{D} \tag{2.8}$$

Roughness ratio: The parameter describes the cylinder surface:

$$\frac{k}{D} \tag{2.9}$$

k is the characteristic size of the roughness. For increased roughness more kinematic energy will usually be lost in the boundary layer and the flow will behave as if it was at a higher Re.

Mass ratio:, $\bar{m}$: Parameter describing the mass of the cylinder relative to the displaced fluid mass pr. unit length:

$$\bar{m} = \frac{m}{\frac{\pi}{4}\rho D^2} \tag{2.10}$$

Damping ratio, ζ: The damping ratio is defined as

$$\zeta = \frac{c}{2m_n\omega_n} \tag{2.11}$$

ω_n is the n'th natural frequency and m_n is the mass that corresponds to ω_n and the actual restoring coefficient k_n. In this thesis the damping ratio will be used when discussing structural damping.

Interaction parameters

The fluid structure interaction parameters are defined in the following:

Nondimensional amplitude: Used to describe the oscillation amplitude in forced oscillation experiments and response amplitude in free vibration experiments. The subscript indicates the direction of the oscillation.

$$(\frac{A}{D})_{IL/CF} \tag{2.12}$$

Nondimensional frequency: The nondimensional frequency is defined as:

$$\hat{f}_{IL/CF} = \frac{f_{osc,IL/CF}D}{U_0} \tag{2.13}$$

f_{osc} is the actual oscillation frequency. The subscript indicates the direction of the oscillation, IL or CF.

Reduced velocity, V_r: The reduced velocity is defined as the ratio between the path length in flow direction per cycle and the cylinder diameter

$$V_r = \frac{path\ length\ per\ cycle}{Diameter} = \frac{U_0 T}{D} = \frac{U_0}{f_0 D} \tag{2.14}$$

f_0 is the natural frequency in still water. In the literature both the natural frequency in air and the actual oscillation frequency is seen in the definition of the reduced velocity. V_R, V_{rn}, U_r and U_R can also be seen as symbols for the reduced velocity.

Strouhal number, St: The Strouhal number is based on the shedding frequency for a fixed cylinder in constant flow and has been defined in Eqn. (2.4).

Response parameter, S_G: The parameter is used to predict response due to VIV, and is one of several similar parameters which essentially consist of the product of mass ratio and damping ratio. A more thorough discussion on the response parameter is given in section 6.2.4.

2.3   Experimental Methods for Investigation of VIV

This section addresses the various experimental methods that have been used to investigate vortex induced vibrations. An overview of the methods will be given. The information that can be extracted, lab requirements, processing methods and limitations will be addressed, and references to important experiments are given. The section is concluded with a discussion on the relationship between the various methods.

The aim of VIV experiments is to improve the understanding of the phenomenon in order to be able to predict response under various conditions. The response has been found to be a function of a large number of parameters, and VIV experiments are designed to investigate the effect of these parameters.

2.3.1   Free Vibration Experiments

A large number of free vibration or self-excitation VIV experiments have been carried out since the pioneers started in the 1960s. Sarpakaya [44] gives references to the publications on the topic. In the discussion given herein the free vibration experiments have been divided into two groups based on how the eigenfrequency of the system is generated. These are:

- Rigid cylinder tests where the test cylinder is supported by springs in the oscillation direction, and the eigenfrequency is controlled by the spring stiffness and mass of the oscillating parts.

- Flexible beam tests where the eigenfrequencies are controlled by the mass, bending stiffness, axial tension and length of the beam.

In the first group, oscillations can be restrained in either CF or IL direction, or the cylinder may be free to oscillate in both degrees of freedom.

Oscillating rigid cylinder test

The oscillating rigid cylinder tests can again be divided into two groups. These are:

- Spring-mounted cylinder tests

- Pendulum tests

For both types it is assumed that the flow conditions are constant over the length of the cylinder (2D flow). End plates are used to ensure that there are no 3D effects at the two ends of the cylinder. Both types of rigid cylinder experiments have been performed in towing tanks, water flumes and in water tunnels. The instrumentation requirements are force sensors and motion sensors.

Figure 2.6 (a) shows the experimental setup used by Vikestad [61] for free vibration experiments in CF direction. This is an example of a spring mounted setup. The setup is useful for low mass ratio - low damping ratio experiments and it allows force measurements at both ends of the cylinder. The mass, spring stiffness and damping would typically be fixed in this type of experiment while the current speed is varied in order to obtain results for a range of reduced velocities. The results are hence obtained over a range of Reynolds numbers. Results that can be extracted from this type of CF experiment are:

- Response amplitudes, typically reported as A/D vs. V_r. Figure 2.6 (b) shows results from Vikestads experiment.

- Lift force.

- Drag force. Both mean drag force (on which the drag coefficient is based, see Eqn. (4.9)) and oscillating drag force can be found.

- Oscillation frequency, f_{osc}.

- Added mass. This can be found by either using the ratio between the eigenfrequency of the system in air and the oscillation frequency ($C_a = \bar{m}[(f_{air}/f_{osc})^2 - 1]$), or by finding the component of the hydrodynamic force in phase with acceleration (see Eqn. (4.11)).

- Correlation of the hydrodynamic forces from the two sides (see Eqn. (4.17))

- The structural damping in the system can be investigated by calculating the hydrodynamic force in phase with velocity. Averaged over a large number of cycles this force will balance the damping forces in the system.

Note that this set-up can not give the lift coefficient for arbitrary combinations of frequencies and amplitudes, since these two parameters are results from a specific velocity and can not be individually controlled.

Pendulum tests are often beneficial for high mass ratio experiments, as both high mass ratio and low damping can be achieved at the same time. This type of experiment has been performed in order to extract hydrodynamic coefficients from the transient phase. Figure 2.7 (a) shows the experimental setup for an IL pendulum experiment performed by
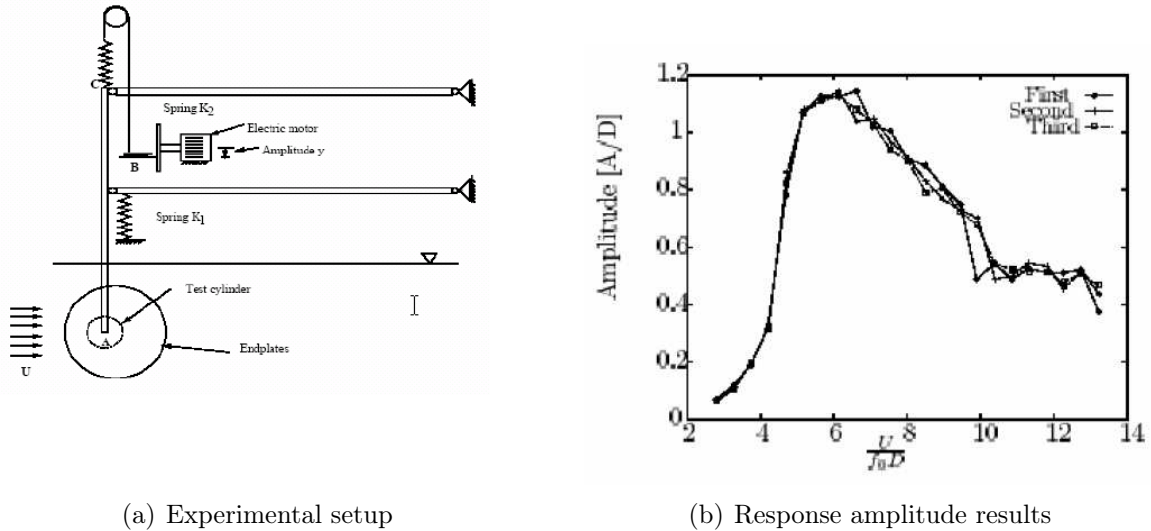
(a) Experimental setup   (b) Response amplitude results

Figure 2.6: Rigid cylinder experiments, spring mounted setup from Vikestad [61]. The motor and upper spring in this apparatus, see Figure (a), can introduce a disturbance at a defined frequency on the cylinder and thereby study damping. If this motor is switched off, one may carry out traditional free oscillation tests.

Johansen [26] and Huse [19]. The experiment was carried out both as excitation tests and decay tests. For the excitation tests the cylinder was initially kept at its neutral position, and at the desired current velocity the cylinder was released. The vortex shedding process will then excite the system and the response amplitude will increase until a steady state amplitude is reached. This transient phase can be used to extract hydrodynamic coefficients in the excitation region. The decay tests were performed by first holding the cylinder at an offset position larger than the expected response amplitude at steady state. For the wanted current velocity the cylinder was released, and the transient phase (until the steady state was reached) could be used to extract hydrodynamic coefficients in the damping region. An example of the response amplitude development for a decay test is shown in Figure 2.7 (b). A high mass ratio is beneficial for this type of experiment as more oscillation periods are required to reach the steady state amplitude. The challenge is, however, to keep the damping force of the apparatus low.

In recent publications by Williamson, [23], [24], [62], [63], results from pendulum experiments with both low mass ratio, and low damping ratio have been reported. The pendulum experiment were performed in a water tunnel and the cylinder, vertical positioned, was free to oscillate both in IL and CF direction. The eigenfrequencies in the two directions were identical. The experiments performed with this setup gave response amplitudes up to 1.5D with corresponding vortex shedding modes not seen for VIV experiments with restricted IL motions.

Flexible beam experiments

The second type of free vibration experiments applies a flexible beam. These experiments are often performed as scaled models of real slender marine structures. The eigenfrequen-

(a) Experimental setup   (b) Response amplitude results, decay test
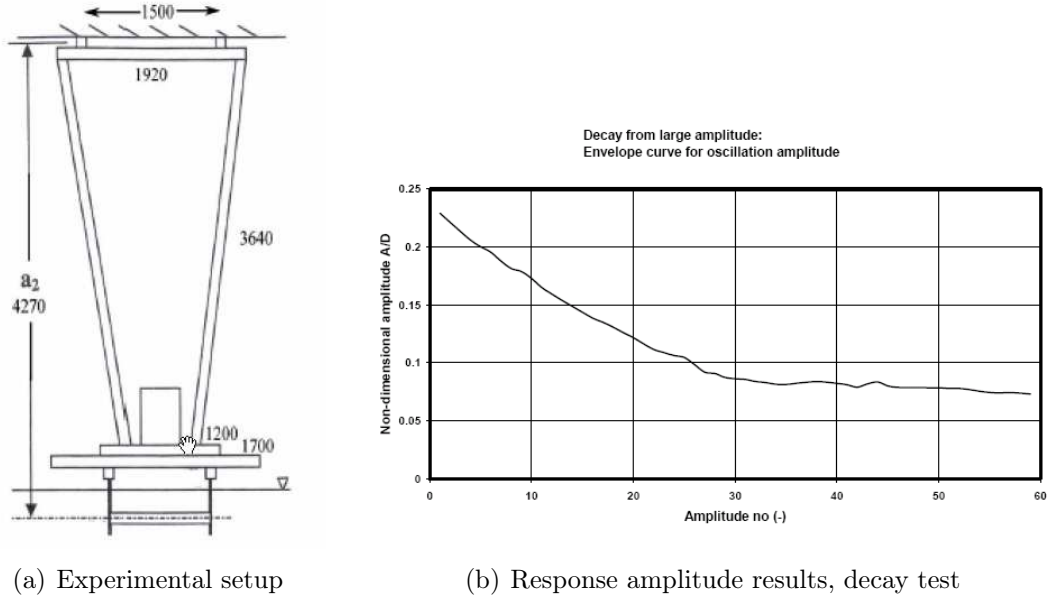
Figure 2.7: Rigid cylinder experiments, pendulum setup from Johansen[26]/Huse[19].

cies of these structures are associated with eigenmodes or modeshapes. Hence, when the structure oscillates the oscillation amplitude varies over the length of the structure. Stationary response for experiments with uniform flow along the beam is reached when there is a balance between excitation from forces in zones with low and moderate oscillation amplitudes, damping in zones with high oscillation amplitudes and structural damping. Maximum response amplitudes for flexible beams are expected to be higher than for rigid cylinder experiments.

A large number of flexible beam experiments have been reported, and for simplicity the various experiments may be divided into three categories:

- Cantilever beams representing scaled models of marine piles.

- Bending stiffness dominated beams, representing scaled models of pipelines.

- Tension dominated beams, representing scaled models of risers.

Cantilever beam experiments may be performed either as a two degree of freedom experiment where the cantilever is free to oscillate in both IL and CF direction, or the physical properties may be such that one of the directions are restrained. Examples of cantilever beam experiments are the IL experiments reported by King [27] and Wootton (results referred in Sarpkaya [53]). Results from these experiments are discussed in chapter 6.4.3. This type of experiments are typically performed such that the first oscillation mode is active, and the tip displacement is reported as a function of reduced velocity (V_r). Both low mass ratio and low damping ratio can easily be achieved. However, as for most free vibration experiments the V_r-range is achieved by varying the current velocity. This give results for varying Reynolds number. In addition to tip displacement measurements, base bending moment has been reported for this type of experiments.

Bending stiffness dominated flexible beam experiments are typically carried out to investigate the response of free spanning pipelines. These tests are performed using flexible beams of aspect ratio (L/D) from 100 to 300. The mass, stiffness and axial tension is chosen to represent a scaled model of an actual span and the beam is towed horizontally through the water to generate current velocity. The eigenfrequency in CF direction would typically be different from the eigenfrequency in IL direction due to sag. Due to the bending stiffness dominated dynamic behavior there is a large spacing between the eigenfrequencies. Hence, the response is expected to be dominated by one eigenmode. The boundary conditions of the beam becomes important for short span lengths and the dynamics of neighbor spans can become important, see Soni and Larsen [49]. This type of flexible beam experiments are mainly performed as towing tank tests. The beam is instrumented by accelerometers or strain gauges so that response can be measured at discrete points along the beam, both in IL and CF direction. By performing a modal analysis, e.g. such as described in Lie and Kaasen [32], response amplitudes, responding modes and response frequencies can be calculated. A comprehensive test program using this type of experiment was performed for the Ormen Lange pipeline project, see Nielsen et al. [37]. Response for one of the shortest spans tested in the program is shown in Figure 1.1.

Tension dominated flexible beam experiments are typically carried out to investigate VIV for risers. What separates these experiments from the experiments performed for free spanning pipelines are:

- Boundary conditions are not important due to the length of the beam.

- A riser has a close to vertical orientation which make the eigenfrequencies in IL and CF direction almost equal.

- The dynamic behavior is tension dominated. Hence, the ratio between the eigenfrequencies is small which makes it more likely that more than one mode will be excited. Response at higher order frequencies (with respect to the vortex shedding frequency) may also appear, see Vandiver et al. [60].

- The flow conditions may vary over the length of the beam in order to investigate the behavior of risers in sheared current profiles.

Results from experiments of this type have been reported by Vandiver et al. [60], Lie and Kaasen [32] and Huse et al. [20].

The instrumentation of the beam used in tension dominated flexible beam experiments and the methods for analyzing the results are similar to those described for the free spanning pipeline experiments. Hence, only response amplitude, active mode and response frequencies can be extracted. However, ongoing research on use of system identification techniques to estimate the forces acting on the beam may give information on hydrodynamic forces, see Barnardo [3].

2.3.2 Forced Oscillation Experiments

In a forced oscillation experiment the test cylinder is given a prescribed motion. The wake behind the cylinder responds to this motion, and the force from the wake acting on the

cylinder can be measured. In order for this method to provide valid data for a cylinder subjected to VIV , the prescribed motions must be identical to the response of free vibrations. Free vibration experiments of short rigid cylinders indicate that the response is harmonic. Hence, forced oscillation experiments have been performed using prescribed harmonic motions. The result from a forced oscillation experiment is knowledge of the hydrodynamic force acting on the cylinder under the tested conditions.

Since the early work by Bishop and Hassan [4] several researchers have used forced oscillation experiments to investigate VIV. The main focus for the majority of these experiments has been on CF oscillations. One exception is, however, Mercier [33] who performed some tests with forced IL oscillations. Jeon and Gharib [25] performed two degree of freedom tests, i.e. combination of IL and CF motions where they combined harmonic oscillations in the two directions.

Results from a pure CF experiment performed by Gopalkrishnan [15] are shown in Figure 2.8. This is one of the most complete works on forced CF oscillation experiments. The test matrix consists of 60 frequencies from $\hat{f} = 0.05$ to $\hat{f} = 0.35$ combined with 6 amplitudes from A/D=0.15 to 1.2. Figure 2.8 (a) shows contours of the excitation coefficient (C_{L_V}). The excitation coefficient is based on the component of the hydrodynamic force in phase with velocity. Hence, the coefficient gives information on the energy transfer between the fluid and the cylinder. A positive coefficient indicates excitation while a negative coefficient indicates damping. The zero contour of the excitation coefficient is shown as a thick black line in Figure 2.8 (a) and this line represent the response amplitude for a freely vibrating cylinder with zero damping. Figure 2.8 (b) shows contours of the added mass coefficient. This coefficient is based on the force in phase with acceleration and is important for determining the oscillation frequency of a freely oscillating cylinder. As the coefficients are related to the motion, they can only be extracted in the directions (CF and/or IL) that are given forced motions.

Chapter 4.4 shows the hydrodynamic coefficients that can be extracted from forced oscillation experiments.

Forced oscillation experiments can be performed both in a towing tank and in a water tunnel. A motion generation system is required, in order to generate the desired oscillations, in addition to force sensors. It is important that the apparatus has a high stiffness so that structural eigenfrequencies in the apparatus do not interact with the oscillation frequencies. Measuring the correct phase between the force and the motion is essential in this type of experiment. Hence, motion sensors, in addition to those used by the control system, are mandatory. A data acquisition system capable of recording data at all channels simultaneously, or with a known delay, is also required.

2.3.3   Combination of Forced and Free Oscillations

Several projects have used a combination of forced and free vibrations. Moe and Wu [35] used an experimental setup where the motions were forced in CF direction and free in IL direction. Vikestad [61] used an electric motor to excite additional frequencies in a free oscillation experiment in order to measure damping, see Figure 2.6 (a). Hover et al.

(a) Excitation coefficient (C_{L_V})

(b) Added mass coefficient, C_a
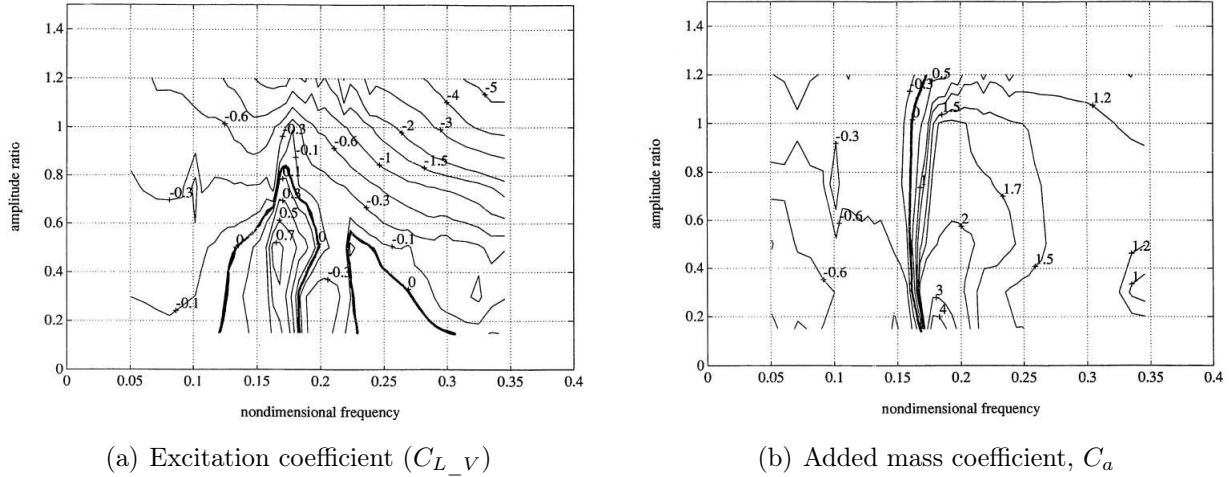
Figure 2.8: Results from forced cylinder experiments by Gopalkrishnan [15].

[18] published results from a "force-feedback control system" apparatus used to simulate free vibration experiments, the Virtual Cable Testing Apparatus. The experiments were repeated by Smogeli et al. [47] after a redesign of the control code allowed for higher Re (19000). Dahl et al. [9] have performed a combined IL and CF free vibration experiment using a force assisted apparatus where structural damping in the system is counteracted by using linear motors.

2.3.4 Comments on the various experimental methods

In the previous section two different experimental methods, free and forced vibrations, have been discussed. Both methods are used to investigate the intrinsic nature of VIV and to extract information that is needed to predict response from VIV. VIV is a fluid structure interaction problem. To simplify, the free vibration experiment can be seen as a method where the wake excites the cylinder, while the forced oscillation experiment can be seen as an experiment where the cylinder excites the wake. Do the two methods give the same results? In the following a short discussion on some of the differences and similarities of the results from various experimental methods are discussed.

Hysteresis

Hysteresis effects, i.e. different response seen for an experiment performed with increasing flow velocity compared to decreasing flow velocity, have been reported in some free vibration experiments. Among others Brika and Laneville [6] and Feng [13] have reported and discussed this phenomenon. However, Triantafyllou et.al. [56] have not reported hysteresis effects for a similar experiment. Sarpkaya [44] suggests two possible reasons: - The Reynolds number is higher in the Triantafyllou experiments, i.e. hysteresis could be a Re effect. - The product of mass ratio and damping ratio is higher in the Triantafyllou experiments, which could indicate that hysteresis is only seen for sufficiently low values of this product. Staubli [51] has shown, by performing pure CF forced oscillation experiments, that hysteresis effects are caused by the nonlinear relation between fluid force and

oscillation amplitude.

Mass ratio and damping ratio

The product of mass ratio and damping ratio is an important parameter for the response seen in free vibration experiment. In forced oscillation experiments, these structural parameters are not relevant. The results from forced oscillation experiments indicate that mass ratio is mainly important for the effect of the added mass, while damping contributes to reduced oscillation amplitude.

Response amplitude

Response amplitude is the main result of a free vibration VIV experiment. There has been discussions whether forced oscillation experiments give the same response amplitude as free vibration experiments. E.g. Vikestands free vibration results show a maximum response of $A_{CF} \approx 1.15D$ (see Figure 2.6 (b)) while Gopalkrishnans forced oscillation experiments predict a maximum response amplitude of $A_{CF} \approx 0.85D$. Experiments performed by Moe and Wu [35] and Hover et al. [18], where basically the same apparatus and the same flow velocities have been used for both free and forced oscillations, show that the response amplitude for the two methods agree reasonably well. Smogeli et al. [47] used the same apparatus as Hover, but performed the experiments at Re=19.000, and reported a maximum response amplitude of $A_{CF} = 1.15D$ for both free and forced oscillations.

Maximum response amplitude seen in flexible beam experiments, is expected to be larger than the maximum response amplitude seen in rigid cylinder tests. For each position along the length of the beam the oscillation amplitude is given by the mode shape and the maximum amplitude. Hence, there are both large and small oscillations present at the same time. For a freely vibrating beam there must be an energy balance between excitation and damping, i.e. the excitation in small and moderate amplitude zones is balanced by damping in the high amplitude zones and by structural damping. To compare modal motion amplitudes with amplitudes from rigid cylinder tests, Blevins [5] has introduced a geometric shape factor:

$$\gamma = \left\{ \frac{\int_0^L \Phi^2(x)dx}{\int_0^L \Phi^4(x)dx} \right\}^{\frac{1}{2}} \tag{2.15}$$

This factor is based on the the hydrodynamic load model used in the wake oscillator model of Iwan [22], and is hence valid for CF oscillations. Reid [42] has proposed similar geometric shape factors for IL oscillations, based on a hydrodynamic model derived from experimental data presented by Moe and Verley [34].

Strouhal number

The Strouhal number is a function of Re, and hence a function of the flow velocity under which the VIV experiments are performed. The results presented in Figure 2.5 (a) show small variations in S_t in the subcritical flow regime. Results from different projects can be brought closer together by plotting the results as a function of the ratio between the vortex shedding frequency (f_s) and the eigenfrequency (f_0) or oscillation frequency (f_{osc}), i.e. $S_t/\hat{f}$ or $St \cdot V_r$. In the critical and supercritical flow regime there is a large change in S_t, compared

to the subcritical regime (see Figure 2.11 (a)). Hence, there is reason to believe that correcting for the actual Strouhal number becomes even more important when experiments performed for high Re are interpreted, or when the results from the subcritical flow regime is used to predict response for critical and supercritical flow conditions. However, more results from high Re experiments are required to confirm this.

Reynolds number

As seen from the discussion so far the Reynolds number is an important parameter in VIV experiments. Even if the effect of S_t has been corrected for, similar experiments performed at different Re have shown results with significant differences. This is especially the case for maximum response amplitude.

Sarpkaya [44] performed forced oscillation experiments for a fixed CF amplitude ratio of 0.5 for 7 Reynolds numbers from 2.500 to 45.000. The results showed a significant variation in the hydrodynamic coefficients for increasing Re. However, for Re>15.000 no significant changes in the coefficients were seen. Sarpkaya explains the results with the transition to turbulence in the free shear layer, as discussed in section 2.1.5. The Re for which this transition disappears is not known for a cylinder subjected to VIV, but experimental results indicate Re of approximately 15.000. VIV experiments performed in the subcritical flow regime for Re higher than this value are expected to be comparable, both free and forced vibration tests. Experiments performed for Re<15.000 can only be regarded as valid for the particular Re for which they are performed.

2.4 Models for Prediction of VIV of Free Spanning Pipelines

In the previous sections VIV, as a physical phenomenon, has been described and various experimental methods used to investigate VIV have been discussed. An important motivation for investigating VIV is to be able to predict the response of a marine structure subjected to loads from vortex shedding. In the following two methods used to estimate response amplitudes for free spanning pipelines are presented. These are:

- Parametric response model method

- Empirical force coefficient method

In the next subsections the two methods will be described, built in assumptions highlighted, limitations will be pointed out and possible improvements to the methods will be discussed.

2.4.1 Parametric response model method

The parametric response models described in DNV-RP-F105 [10], are by far the most used models for predicting response due to VIV for free spanning pipelines. Several curve fit expressions, based on the response parameter S_G, have also been proposed for estimating maximum CF response amplitude. For details reference is made to Sarpkaya [44].

(a) IL response model, DNV-RP-F105 [10]

(b) CF experiment results, figure from Mørk et al. [43]
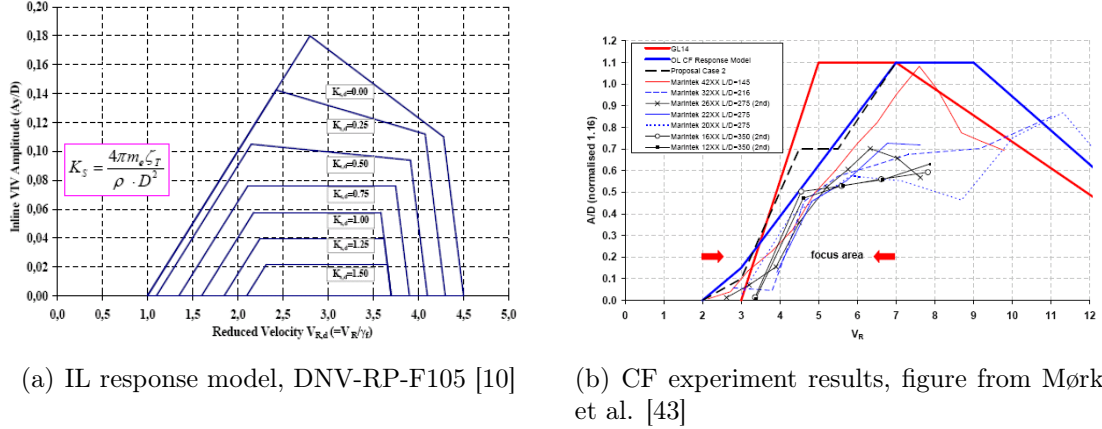
Figure 2.9: Response model

Short description of the DNV-RP-F105

The DNV-RP-F105 is a recommended practice (RP) for predicting fatigue damage due to VIV and direct wave loads of free spanning pipelines. The document provides guidance on how to model wave and current loads. It gives models for VIV response and a force model for prediction of direct wave load response. Guidance on how to perform the structural analysis and how to model pipe-soil interaction is also given.

The models for estimation of response due to VIV are based on several research and development programs, and references to publications from these programs are given in the RP. Response models for both IL and CF VIV are provided; examples are shown in Figure 2.9. As seen from the figure the amplitude ratio (A/D) for both IL and CF directions is presented as a function of the reduced velocity, V_r. The parameters that determine the response amplitude differ for the two directions.

In IL the response amplitude is determined by the stability parameter K_s, which essentially consists of the product of mass ratio and damping ratio, and a reduction factor due to turbulence in the flow. The effect of K_s is illustrated in Figure 2.9 (a). The model predicts reduced response amplitudes for conditions where wave induced flow velocity is present in the total flow velocity. If waves dominate the flow, IL VIV is ignored. The IL response frequency is assumed to be equal to the eigenfrequency of the free span.

The CF response amplitude is given from four parameters. These are:

- Current flow velocity ratio, i.e. the ratio between the flow velocity from current and the sum of the flow velocity from wave and current.

- KC number.

- Ratio between two consecutive eigenfrequencies.

- Stability parameter, K_s.

The condition giving the highest oscillation amplitude is current dominated flow for a bending stiffness dominated span, i.e. high ratio between consecutive eigenfrequencies.

Oscillating flow reduces the response amplitude, while the response of a tension dominated span would change to a higher mode before the highest response amplitude is reached. Structural damping reduces the response amplitude through the parameter K_s, and is included as a reduction factor on the response estimated from the other three parameters. Seabed proximity and trench depth are parameters in the expression determining the V_r for which build up of CF response starts, i.e. onset of CF response. An added mass model is provided for estimation of response frequency in CF direction.

Response models

The parametric response model method is associated with free vibration experiments. The concept is that response amplitudes (A/D) from a large number of free vibration experiments are plotted as a function of reduced velocity (V_r), where results from various experimental methods are normalized by the γ-factor, see Eqn. (2.15). The response model is then chosen as an envelope curve for these results. Examples of results from CF experiments are shown in Figure 2.9 (b).

Considering VIV in uniform current, i.e. no effect of flow turbulence and waves, and neglecting the effect of seabed proximity and trench, the DNV response curves in IL and CF are determined by K_s and frequency ratio respectively. In addition the CF response amplitude is corrected by a factor depending on K_s. Response curves for levels of these parameters may be created by removing the tests where the parameter of interest is outside a chosen range from the data set, e.g. tests of K_s-values below 0.2, and then draw a new envelope curve. The DNV response model for IL VIV, including response curves for several levels of K_s, is shown in Figure 2.9 (a).

Parametric response model means that the envelope curves describing the response are described by mathematical expressions built up by the parameters describing the physical phenomenon.

Assumptions and limitations related to response models

The nature of the method, using envelope curves, is conservative. However, for this to be the case it is obviously important that the relevant experimental results are representative for the actual free-span case. As discussed in previous sections the majority of the reported VIV experiments have been performed within the subcritical flow regime, but at various Reynolds numbers. Both the maximum response amplitude and Strouhal number vary within the subcritical flow regime. These variations must be covered by the data set on which the response curve is based.

It is well known that most free spanning pipelines may experience Reynolds numbers in the critical and supercritical flow regimes. Whether subcritical experiments are representative for these flow conditions is still not fully verified.

In the DNV response model the CF response amplitude is a function the CF eigenfrequency through the parameter V_r. Resent rigid cylinder results, see Dahl et al. [9], indicate that the ratio between the eigenfrequency in IL and CF direction is an important factor for

the response both for IL and CF. Conditions that can influence the eigenfrequency ratio are sag, change in span configuration due to drag and difference in mode number in the two directions. For a response model to give conservative results for all conditions, it is important that the data set on which the model is built covers all frequency ratios.

The methodology described in DNV-RP-F105 assumes that the response frequency in IL direction equals the IL eigenfrequency.

2.4.2   Empirical force coefficient method

Empirical force coefficient methods, such as the method used in the computer program VI-VANA [30]/[65], have traditionally been used for estimating VIV of marine risers. However, a recent update allowing for nonlinear pipe-soil interaction, see Larsen et. al. [29]/[28], has made the program well suited for free spanning pipeline analysis. The fundamental difference from the parametric response model method, described in the previous section, is that here the hydrodynamic forces caused by the vortex shedding process are modeled, and the response is estimated by applying the forces on a finite element model of the free spanning pipeline. A short description of the program will be given, the hydrodynamic model describing VIV will be presented and the assumptions and limitations related to this method will be discussed.

Description of the method

VIVANA is using an iterative procedure for performing dynamic analysis of response dependant loads in frequency domain. The program builds on static results from the finite element program Riflex [14], developed for static and dynamic analysis of slender marine structures. An analysis for estimating the response of a free spanning pipeline subjected to VIV is carried out in the following steps:

- The static configuration of the free spanning pipeline, due to volume forces, bending stiffness, tension, contact with seabed and current, is found by performing a nonlinear finite element analysis in Riflex.

- The results from the static analysis is transferred to VIVANA and eigenfrequencies are calculated.

- A predefined range of $\hat{f}$, defining the excitation region, is used to determine which eigenfrequencies that can be excited under the given current condition.

- Based on an added mass model all possible response frequencies are calculated on the basis of the eigenfrequencies obtained from the static configuration.

- From a model of the hydrodynamic excitation force, response is calculated for each of the possible modes. The dominating response mode is chosen from an energy criterion.

- The forces acting on the pipeline, found in the previous step, are transferred to Riflex and nonlinear pipe-soil interaction can then be included in a second analysis.

(a) Span model

(b) Stress amplitude results
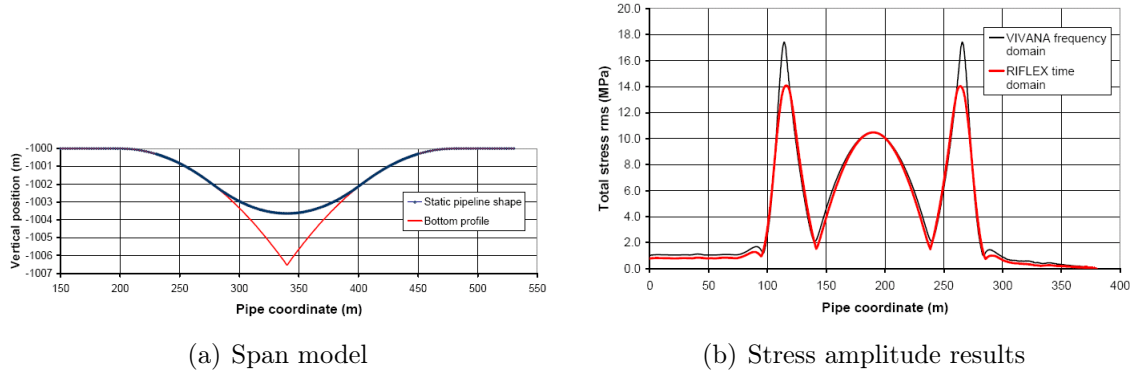
Figure 2.10: Free spanning pipeline analysis performed using Riflex / VIVANA, from Larsen et. al. [28].

(a) Strouhal number model
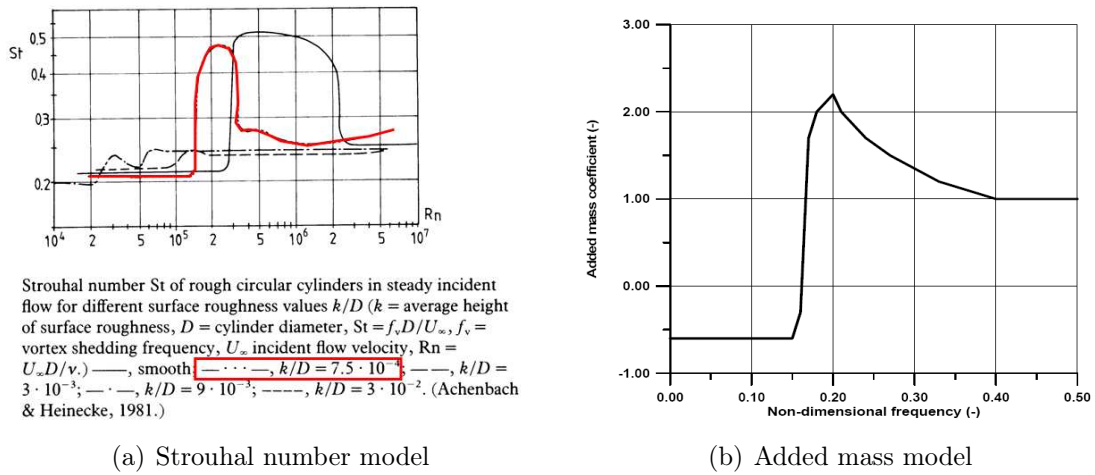
(b) Added mass model

Figure 2.11: VIVANA models for Strouhal number and added mass, figures from Larsen et al. [30].

For this method to be valid the response predicted in the last step can not be significantly different from the response calculated by VIVANA. The benefit of the last step, i.e. performing the time domain analysis, is to get a more accurate result for the local stresses at the span shoulders. An example from Larsen et al. [28] is shown in Figure 2.10.

Empirical force coefficient models

The hydrodynamic models for added mass and excitation coefficient, used in VIVANA, are based on the forced oscillation experiments reported by Gopalkrishnan [15] shown in Figure 2.8.

In order to find the correct response frequency the added mass must be determined. It is seen from Figure 2.8 (b) that the added mass is very weakly dependent on the oscillation amplitude. An amplitude independent model has hence been chosen, see Figure 2.11 (b). The response frequency can therefore be calculated independently of the response ampli-

(a) Energy transfer

(b) Excitation coefficient
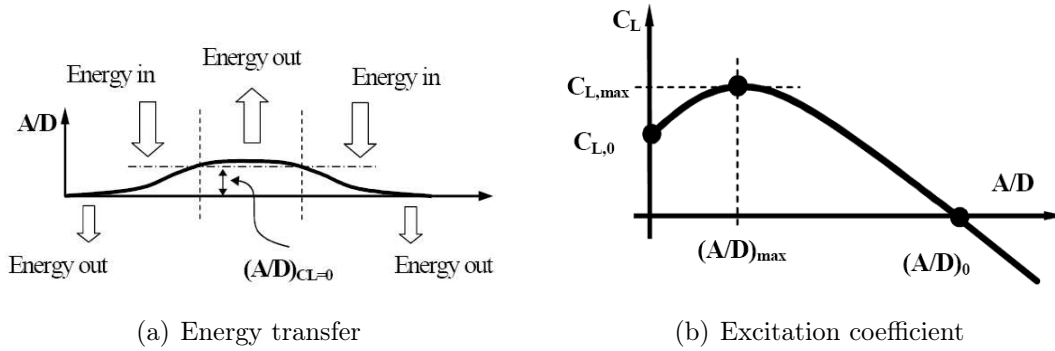
Figure 2.12: Excitation model in VIVANA, figures from Larsen et al. [28].

tude.

As discussed in an earlier section of this chapter the Strouhal frequency (vortex shedding frequency, f_s) depends on the Reynolds number. In VIVANA it is assumed that the ratio between the oscillation frequency and Strouhal frequency is the parameter describing the hydrodynamic forces on the cylinder. By including a model for the Strouhal number, and knowing for which value of S_t the Gopalkrishnan experiments are performed, the force coefficient models is assumed to be valid for a large range of Re. A standard curve for S_t as function of Re is offered in VIVANA. Other relationships might be defined by the user, like the curves shown on Figure 2.11 (a).

The response amplitude for a free spanning pipeline in uniform current, is determined by a balance between excitation in zones of low and moderate oscillation amplitudes and damping in zones of high oscillation amplitudes, as shown schematically in Figure 2.12 (a). The model describing hydrodynamic excitation and damping in VIVANA is based on the lift coefficient that gives the force in phase with velocity presented by Gopalkrishnan, see Figure 2.8 (a). It is seen that the coefficient is a function of both amplitude and frequency. However, as the response frequency is determined independently of the of the response amplitude, a model for the excitation force only depending on response amplitude can be used for a given nondimensional frequency, $\hat{f}$. This excitation force model is a continuous mathematical function fitted to the Gopalkrishnan curves for the $\hat{f}$ of interest, see Figure 2.12 (b). Strip theory is assumed and iterations are performed until consistency between response (amplitude and phase) and response dependent forces is obtained. The damping forces consist of structural damping and hydrodynamic damping for high oscillation amplitudes, while low amplitude oscillations cause excitation.

Assumptions and limitations

The main limitation of the method is that it is valid only for pure CF VIV. It is well known that IL oscillations are important for the fatigue life of a free spanning pipeline. Also, it is questionable whether a model for pure CF oscillations is relevant for the CF response of a free spanning pipeline, as the response would be a combination of IL and CF oscillations. Hydrodynamic models for IL VIV are not available, and to implement models that include the interaction between IL and CF VIV into a frequency domain method such as VIVANA

is not straightforward.

As a complete model for VIV does not exist, several assumptions have been made. Some of the most important ones are summarized below:

- It is assumed that the force coefficients obtained at Re=10.000 are valid for the free spanning pipeline conditions. As previously discussed rigid cylinder experiments performed at Re>15.000 give higher maximum response amplitude and little is known about VIV in the critical and supercritical flow regime.

- Single frequency response is assumed. It is however seen in oscillating beam experiments that several response modes can exist at the same time.

- Strip theory is assumed, i.e. the effect of axial flow along the flexible beam is neglected.

- No realistic correlation model is considered, i.e. forces are assumed to be fully correlated over the length of the flexible beam.

2.4.3 Application for Free Spanning Pipelines

Two methods for estimating response frequency and stress range for free spanning pipelines subjected to VIV have been presented. It is seen that the parametric response method is the more complete in the sense that it provides response models in both IL and CF direction, takes into account effect of seabed proximity, trench depth, flow turbulence and also includes the effect of waves. However, as the response curves are based on envelope curves they would in principle always give conservative results. The model described in DNV-RP-F105 is built on results from experiments performed at a much lower Re than the full scale conditions, the validity of the model can thus be questioned. The empirical force coefficient method described does, in theory, give a less conservative result for a particular span. However, as an IL force coefficient model does not exist, the method is not suitable for free spanning pipelines. A short discussion on how new experimental results can be included in the existing models will be given in the following.

Parametric response model method:

- Given the way the model is developed, using envelope curves, results from new experiment will only change the model if the results exceed the current curves. However, more experimental results will increase the confidence in the existing model. A response model that predicts the response for a given span more accurately than the present model is expected to involve more parameters.

- An added mass model for pure IL VIV does not exist, and can be included in a similar manner as the CF added mass model.

- Experiments at high Re would give valuable results for flow conditions representative for a full scale pipeline.

Empirical force coefficient method:

- Empirical force coefficients for pure IL VIV can be included in a similar manner as the existing model for pure CF VIV. This will make the method much more relevant for free spanning pipelines as the highest fatigue damage is often seen in IL direction.

- CF experiments performed at Re>15.000 give increased response amplitude compared to the experiments on which the existing CF hydrodynamic force model is built. New experiments performed at Re relevant for full scale free spanning pipelines will give improved results.

- It is well known that a free spanning pipeline will respond in a combined IL and CF motion. Modeling the IL-CF interaction requires a better understanding of the fluid structure interaction, a hydrodynamic model and an updated numerical method.

Chapter 3

Description of the Experiment

The purpose of this chapter is to give a detailed description of the apparatus used to perform the experiments and present the key parameters for all individual tests.

3.1   Experimental Setup

The experiment was carried out in the towing tank "Marine Cybernetic Laboratory", ref. [1], at NTNU's facility in Trondheim, Norway. Dimensions of the tank are $(L_t * B_t * D_t)$ 40*6.45*1.5 meter. The tank is equipped with an overhead towing carriage. A computer controlled 5 degrees of freedom motion simulator is located on this main carriage. Figure 3.1 and 3.2 give a schematic overview of the apparatus. Characteristic properties of the experimental setup are given in Table 3.1.

The experimental work this thesis is based upon was performed between October 2004 and September 2005. The equipment was installed in the towing tank several times during this period and in the following there will be referred to three phases, Phase I, II and III. These are three periods of lab time from where data were acquired. Some modifications of the equipment were done between the phases making it necessary to distinguish between them.

3.1.1   Apparatus

A description of the physical apparatus is included to establish confidence with regard to reliability and accuracy of the reported data. Also, a description increases the knowledge of the conditions under which data are acquired, which in turn will be important if the results are to be compared with other data.

The test model used for the Phase II and III experiments was a 10cm diameter painted aluminum cylinder of 2m length. For the Phase I experiment the diameter and length of the model was 15cm and 3m respectively. This gives an L/D-ratio of 20 (see Figure 3.2). The cylinder was installed in a yoke which in turn was attached to the tow carriage. Oscillations were achieved by oscillating the yoke horizontally (IL) and vertically (CF). Microprocessor controlled servo motors controlled the motions, giving the desired oscillation amplitude, frequency and phase difference between the vertical and horizontal directions. The cylinder was air filled with watertight plugs at both ends in order to keep the mass as low as
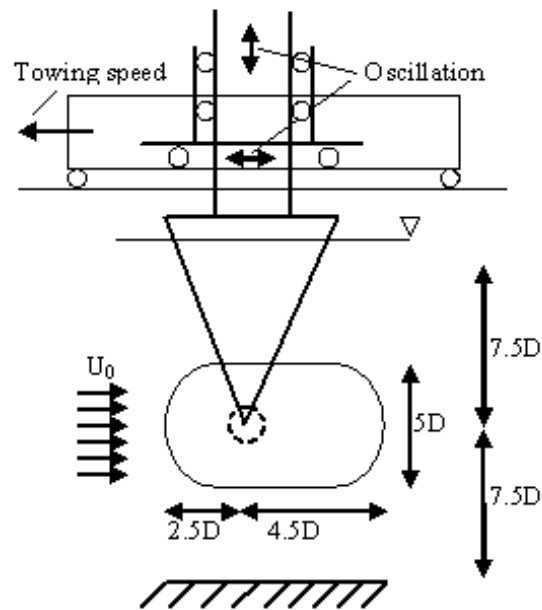
Figure 3.1: Schematic description of apparatus, seen from port side.

possible. End plates were installed to eliminate 3D effects at the cylinder ends. The end plates were designed according to specifications given in Stansby [50], see dimensions in Figure 3.1. Table 3.1 shows the characteristic parameters for the experiment.

3.1.2   Instrumentation

In order to measure all parameters needed to calculate the hydrodynamic coefficients, the apparatus was equipped with force- and motion sensors.
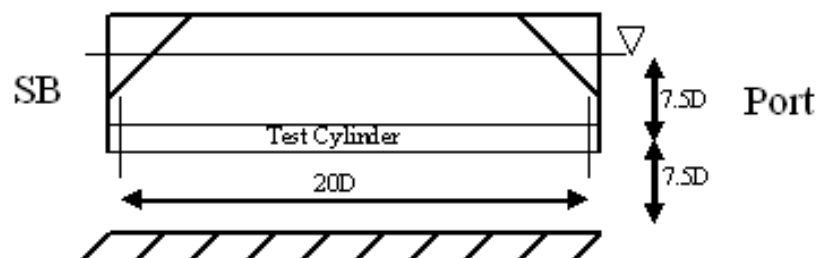
Figure 3.2: Schematic description of apparatus, front view.

Table 3.1: Characteristic properties for the experimental setup.

Characteristic	Symbol	Phase I	Phase II & III
Cylinder diameter [m]	D	0.150	0.100
Cylinder length [m]	L	3.00	2.00
Cylinder mass [kg]	M	15.32	9.68
Towing speed [m/s]	U_0	0.175	0.262
Reynolds number [-]	Re	$2.4 \cdot 10^4$	$2.4 \cdot 10^4$

Force sensors

The force sensors used in these experiments were of the strain gauge type, produced by Hottinger (type PW2GC3). Two sensors were orthogonally mounted together, enabling force measurement in two directions (IL and CF). Forces were measured at both sides of the cylinder. The two sides are in the following referred to as Starboard (SB) and Port side. The force sensors were calibrated in three steps. First each sensor was calibrated to find the calibration coefficient. Then two and two sensors were mounted together and calibrated to see if there were any transfer of forces between the two directions. The third step was performed after the apparatus had been assembled in order to detect possible rotations of the sensors.

Motion sensors

Three different types of motion sensors were used in the experiment. These were accelerometers, string potentiometers and optical encoders.
Accelerometers measuring accelerations in three directions were installed at each side of the cylinder, on top of the force sensor housing on the outside of the end plate. The accelerometers were calibrated against $g = 9.81[\frac{m}{s^2}]$.
The string potentiometers were mounted between the yoke and the tow carriage, one in IL direction and one in CF direction. The potentiometers were factory calibrated, and the calibration was verified by measuring displacements by the use of a ruler.
The optical encoders were mounted on the motors controlling the axes, giving displacements based on the number of rounds of the motors.
As the accelerometers were located closest to the force sensors, these signals were chosen as motion signals in the calculation of hydrodynamic force coefficients. There were, however, some problems with the acceleration signals in CF direction and therefore the string potentiometer signal was chosen in this direction. The measurements taken on the motors were found to contain a phase error and could therefore not be used since the hydrodynamic force coefficients are very sensitive to the phase between the motion and the force.

Data acquisition

The signals from the instrumentation were amplified by a Hottinger MGC+ amplifier and sampled at 100Hz. The computer program Catman was used for the data acquisition. All channels were low-pass filtered at 30 Hz using a Butterworth filter. Table 3.2 gives an overview of the channels.

Table 3.2: Data channels.

Description	phaseI	phaseII	phaseIII	Unit
IL force, Starboard side	1	1	1	[N]
CF force, Starboard side	2	2	2	[N]
IL acceleration, Starboard side	4	4	4	$[m/s^2]$
CF acceleration, Starboard side	5	5	5	$[m/s^2]$
IL force, Port side	6	6	6	[N]
CF force, Port side	7	7	7	[N]
IL acceleration, Port side	8	8	9	$[m/s^2]$
CF acceleration, Port side	10	10	10	$[m/s^2]$
Carriage position, Carriage X-axis	11	11	13	[m]
IL position, Carriage U-axis	12	12	15	[m]
CF position, Carriage Z-axis	na	13	17	[m]
CF position, Carriage W-axis	na	14	18	[m]
IL position, string potentiometer	na	na	12	[mm]
CF position, string potentiometer	na	na	11	[mm]
PIV trigger signal	na	na	19	[V]

All measurements are recorded in Volt. The units shown in table 3.2 are valid when the recorded signals are multiplied with the calibration factors.

3.2 Quality Control

As numerous problems were experienced when setting up and performing the experiments, partly due to the authors limited experience with this type of work, an elaborate system for quality control was implemented.

The measures taken for ensuring data of high quality are summarized in the following:

- The experiments, including calibration of force and motion sensors and pluck tests to determine eigenfrequencies in the setup, were conducted by the author. The daily routines in the lab, e.g. waiting time between each run, were also the same for all experiments. The results should hence be consistent, both over the duration of one experimental phase and between phases.

- Predefined tests were repeated, both several times a day for the duration of a test phase and the same tests were also repeated in later phases. It was thus possible to monitor that the conditions under which the experiments were carried out were not changing.

- Data sheets, also showing graphic presentation of some of the main results, were produced for each individual test. Examples are given in Appendix B.

- A detailed error analysis is carried out, giving a quantitative estimate of the uncertainty in the reported coefficients. The methodology is described in Chapter 5.

- The results are compared with results from other experiments.

Detailed results from the uncertainty analysis and comparison with other experiments are presented for the IL results in chapter 6.4. Similar results are also produced for the interaction experiments of chapter 8. These are, however, not reported as the discussion given on the results from the interaction experiment is more of a qualitative nature.

3.3 Definition of test cases

Four types of experiments were conducted:

- Fixed cylinder tests.

- Pure IL experiments.

- Pure CF experiments.

- Combined IL and CF experiments with varying phase between the two directions, creating orbital paths of different shapes and directions.
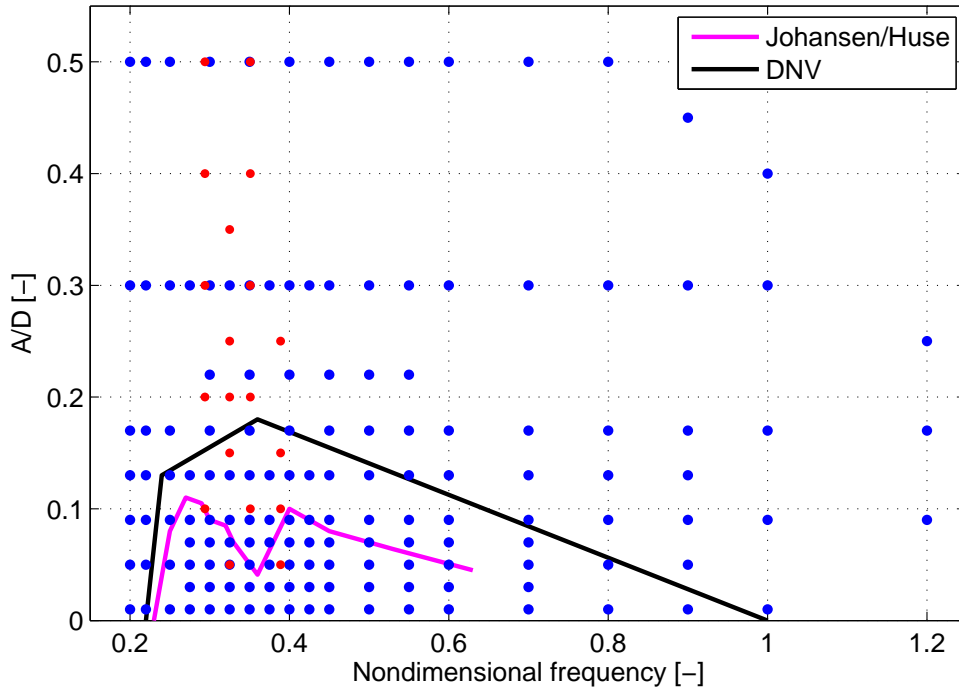
Figure 3.3: Pure in-line test matrix. The cases tested are shown as dots ($\bullet$). Free response curves from DNV [10] and Johansen[26]/Huse[19] are included as solid lines.

The various experiments are explained in some detail in the following:

Fixed cylinder tests. In order to determine the drag coefficient and the Strouhal number, for a selected Reynolds number, the cylinder was towed at constant speed without any oscillations. In total 76 cases were tested; 8 in Phase I, 10 in Phase II and 58 in Phase III. 7 of these cases were tested for Reynolds numbers between $1.0 \cdot 10^4$ and $1.47 \cdot 10^4$, the other tests were performed for a Reynolds number of $2.4 \cdot 10^4$.

Pure IL experiments. A total of 250 pure IL cases were tested, 142 in Phase I, 41 in Phase II and 67 in Phase III. Figure 3.3 shows the combinations of amplitude ratio (A/D) and nondimensional frequency tested. The figure shows 156 cases and the IL results presented in chapter 6 are based on these cases. The other IL cases have been used in the error analysis to investigate the repeatability of the results.

Pure CF experiments were performed for two reasons. Firstly, this type of experiment is very well documented and the results from our experiments can therefore be validated against other experiments. Secondly, pure CF results were required in order to test one of our hypotheses, that combined IL and CF VIV can be estimated based on pure IL and pure CF results. A total of 42 cases were tested, 14 in Phase II and 28 in Phase III. The tested combinations of amplitude ratio and nondimensional frequency are shown in Figure 3.4.

Combined IL and CF experiments A total of 333 combined IL-CF cases were tested, 216 in Phase II and 117 in Phase III. The equation below shows how the orbital paths were
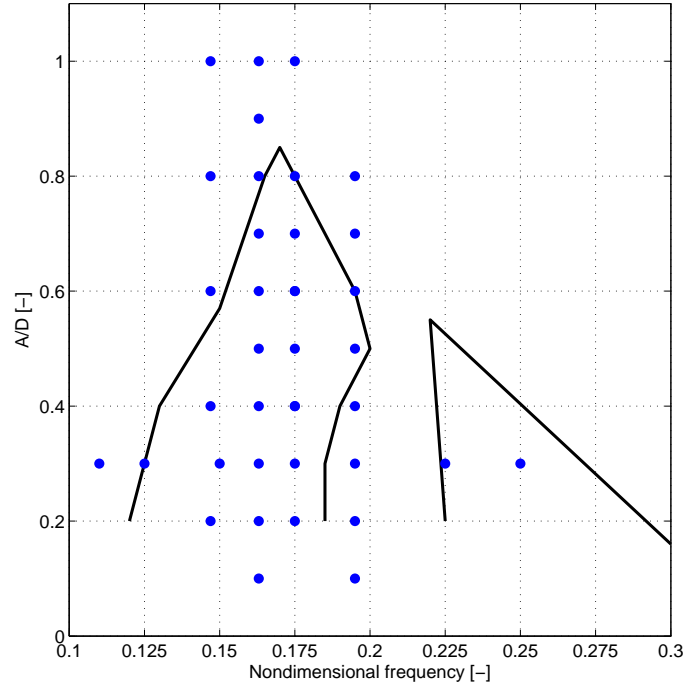
Figure 3.4: Pure cross-flow test matrix. Results from Gopalkrishnan [15] are shown as a solid line.

designed.

$$
\begin{aligned}
IL: \ & x(t) = A_{IL} \sin(2\pi f_{osc,IL} \cdot t + \alpha) \\
CF: \ & z(t) = A_{CF} \cos(2\pi f_{osc,CF} \cdot t)
\end{aligned}
\tag{3.1}
$$

The equation shows that there are 5 parameters describing the orbital path. In order to reduce the number of parameters to be varied, the amplitude ratio A_{IL}/A_{CF} was kept constant at 0.5 and the frequency ratio $f_{osc,IL}/f_{osc,CF}$ was 2. 3 parameters, amplitude, frequency and phase are varied, and Figure 3.5 shows what the orbital paths look like for varying phase, α. In addition to the shape of the orbit, the orbital direction relative to the flow is of importance. In the figure the orbital direction is indicated by arrows.

Figure 3.6 shows tests performed as a systematic variation of the three parameters describing the orbital path. The figure to the right shows the nondimensional frequencies and amplitude ratios, two frequencies were tested in phase II and two in Phase III. The values reported for amplitude and frequency in Figure 3.6 refer to CF direction. The figure to the left shows the phase angles and oscillation amplitudes. 16 phase angles were tested in phase II and and 8 in Phase III.

45 "best fit" cases, 18 in Phase II and 27 in Phase III, were tested. These were tests of orbital paths fitted to trajectories measured from free vibration tests of flexible beams. The experiments are described in more detail in chapter 7. In addition tests were performed for 6 frequencies (0.11, 0.125, 0.15, 0.175, 0.225, 0.25) at amplitude ratio 0.3 for three phase angles (77, 84, 90).
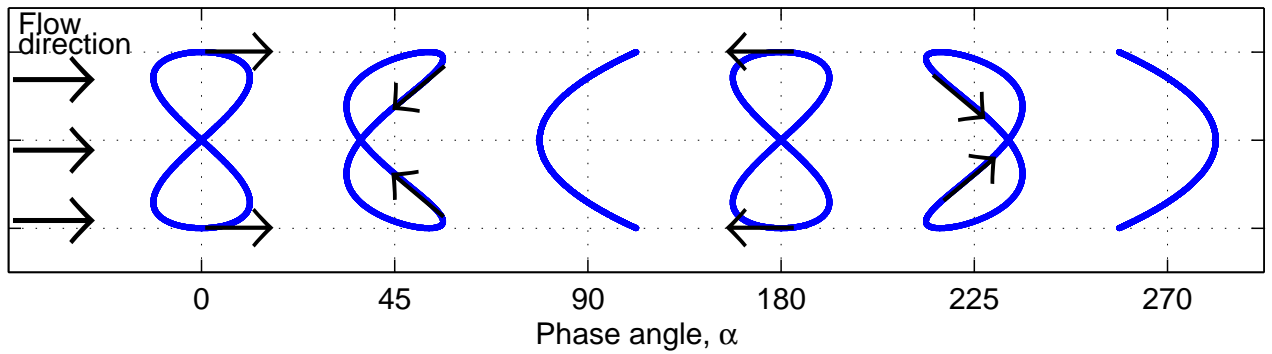
Figure 3.5: Illustration of the orbital path.
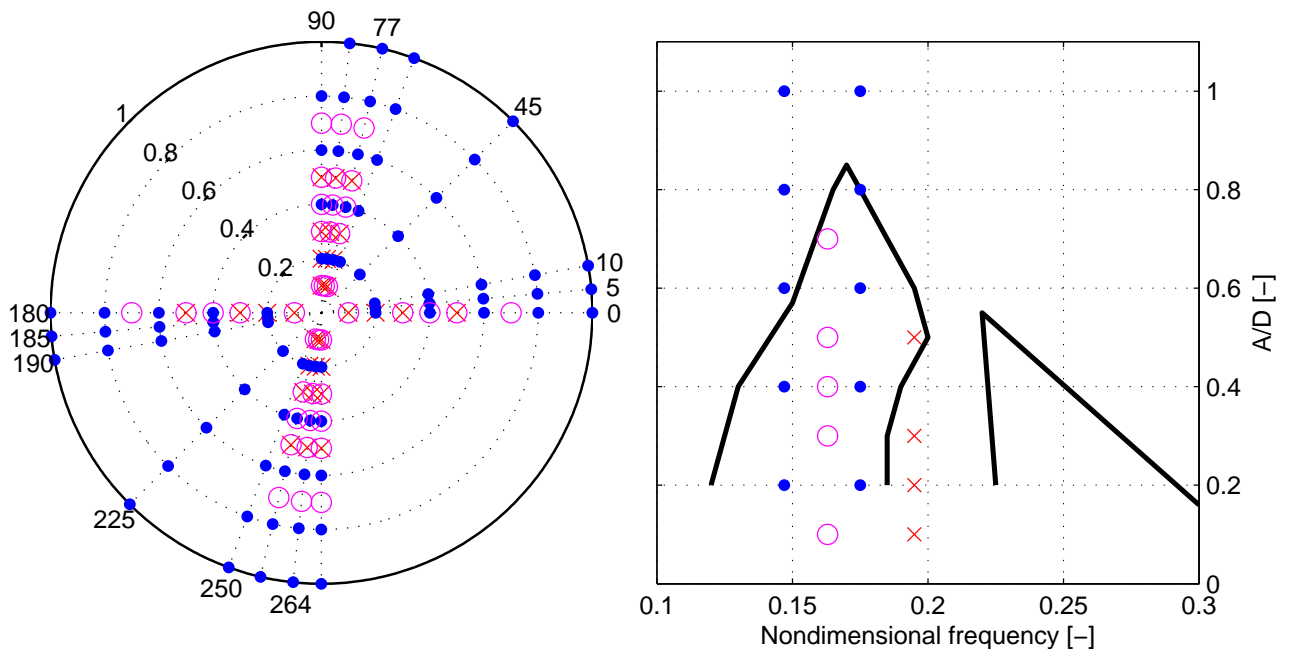
Figure 3.6: Combined IL and CF test matrix. Amplitude and frequency refer to CF direction. Dots (•) represent phase II experiments, circles (○) and crosses (×) represent phase III.

Chapter 4

Data Analysis

The total number of test runs carried out in this project is approximately 700. In order to handle the signal processing of this large quantity of data in a consistent and effective manner a post processor was developed in the computer program MATLAB.

In this chapter a brief overview of the post processor will be given, including a definition of the coordinate system used, the measured signals and the available data sheets. The signal processing will be given a more thorough description, where the main focus will be on how the raw data are filtered and on the methods used to decompose the hydrodynamic force into a component in phase with velocity and a component in phase with acceleration.

4.1 Outline of Post Processor

The post processor is developed in such a manner that it is possible to automatize the calculations, and thereby calculate a large number of cases continuously. It has the following characteristics:

- Reads an input file that describes the cases to be analyzed and gives the input parameters to each case.

- Four types of analyses can be performed; fixed cylinder, oscillations in IL direction, oscillations in CF direction and combined IL and CF motions.

- Presents result sheets for different stages of the analysis; signal processing, final results (coefficients) and results from the uncertainty analysis.

- Results can be presented both as result sheets for each individual case, and as tables of the calculated coefficients for multiple cases.

4.2 Directions

This section defines the coordinate system used in the project, and describes how measured data have been interpreted. The direction, sign of the force and acceleration signal, is dependent on the method used to calibrate the sensor and hence the sign of the calibration coefficient.
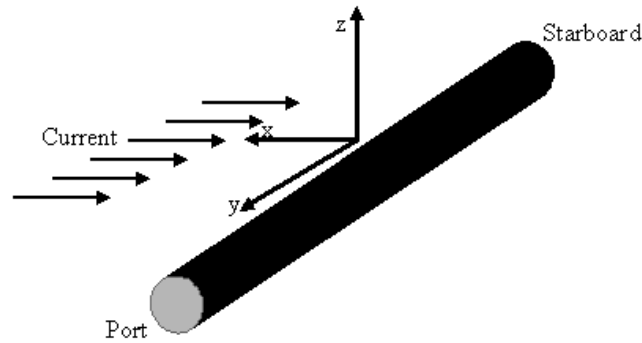
Figure 4.1: Global coordinate system for the experimental setup.

4.2.1   Coordinate system

The coordinate system is shown in Figure 4.1, and the figure shows that the x-axis (IL) is taken as positive in the towing direction and the z-axis (CF) is positive upwards.

4.2.2   Interpretation of measured signals

The stain gauge force sensors and accelerometers, used in the experiments, are calibrated and installed relative to the coordinate system described above. All calibrations are performed statically, and this must be taken into account when the measured signals are interpreted.

Accelerometer

The accelerometers used in this project can be seen as a mass supported by springs in three degrees of freedom. The accelerometers are calibrated by using the acceleration of gravity, g=9.81. By using this method the sign of the calibration coefficient is based on a static force from the mass in the accelerometer on the spring. In the experiment the accelerations measured are due to inertia forces. The sign of the measured acceleration signal must therefore be changed for the measured acceleration to comply with the global coordinate system.

Strain Gauge

The hydrodynamic force is the force from the fluid on the cylinder. The calibration of the force sensors are performed to comply with this. External loads are applied and the calibration coefficients are estimated based on the global coordinate system, see Figure 4.1. The sign of the measured drag force is hence negative, since the current is running in negative x direction.

In the experiments the cylinder is given prescribed displacements. Due to the mass, M, of the cylinder the prescribed oscillations will introduce inertia forces that are taken by the

force sensors. For an acceleration, a, in positive x-direction, this inertia force is seen as a measured force in negative x-direction of magnitude $M \cdot a$. As the coefficients shall be based on the hydrodynamic force, this inertia force must be subtracted from the measured forces.

Position measurements

Two types of position sensors are used, in addition to the accelerometers. These refer to coordinate systems different from the one chosen for this project. The sign of the various axes must therefore be corrected so that the results comply with the chosen coordinate system.

4.3 Signal Processing

In this section the signal processing part of the post processor will be described in some detail. The section consists of a description of how the test runs are performed, the processing of the measured position signals and the processing of the measured force signals.

4.3.1 Execution of the experiment

Each single test was performed as follows:

- Zero setting performed on all channels.

- Data logging started about 10 seconds prior to the start-up of the tow carriage and the oscillations.

- Tow carriage accelerated to the specified tow velocity.

- Period of constant tow velocity, oscillation frequency and amplitude.

- Oscillations stopped and tow carriage slowed down to a complete stop.

- Data logging for an additional 10 seconds.

Figure 4.2 shows a typical raw data time series of forces measured in IL direction. A filtered signal is included to illustrate the force at the oscillation frequency. The first part of the signal, approximately 10 seconds, is used to verify the zero setting. If the mean value of the first 5 seconds is different from zero, this value is subtracted from the time series. The last approximately 5 seconds of the time series is used to verify that there is no sensor drift. If the mean value is significantly different from zero, there is something wrong with the sensor.

4.3.2 Motion signals

In these experiments the motion signals are used as reference signals for the calculation of hydrodynamic force coefficients, and the reported coefficients are hence valid for the given motion, i.e. oscillation amplitude and frequency. The motion was measured by three methods. These methods were accelerometers, string potentiometers and optical encoders.
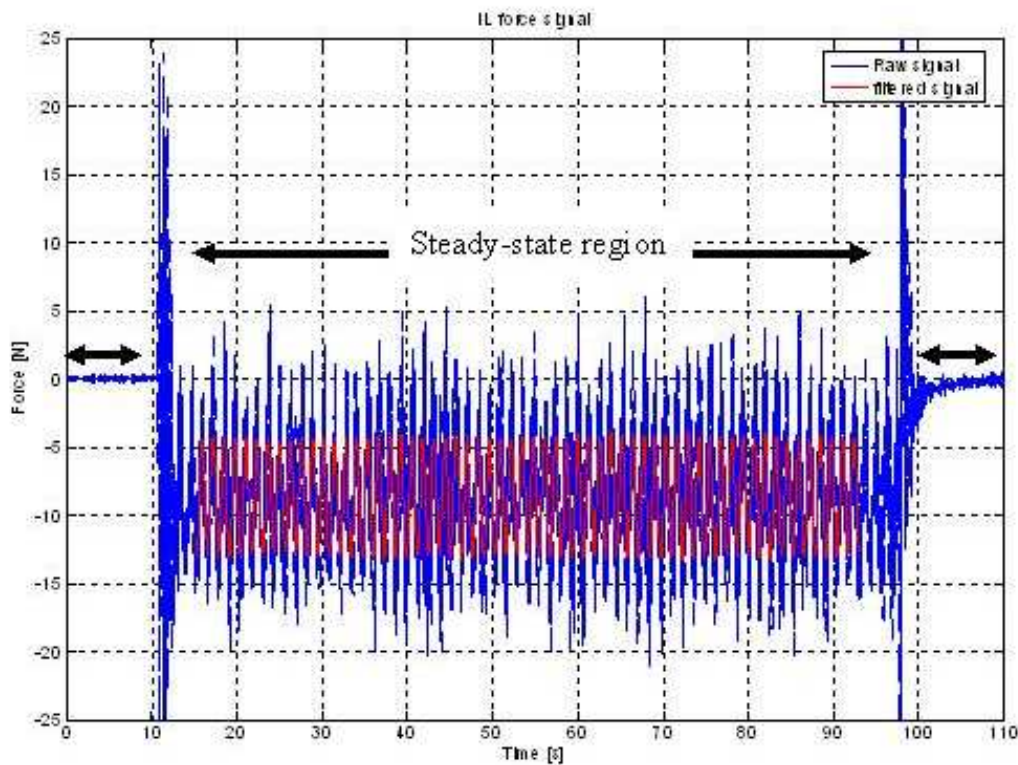
Figure 4.2: Time series of measured IL force, raw signal and filtered signal.

The measured signal from the accelerometers were obviously accelerations, displacements were measured by the two other methods. To obtain time series of acceleration, velocity and displacement the signals are processed in the following manner:

- Subtract offset. The mean value of the first 5 seconds is subtracted from the time series.

- Include calibration factors. For the accelerometer correction for cross-talk is also performed.

- Integration of the acceleration signals by a frequency domain method, see subsection below.

- Differentiation of the displacement signals in time domain.

- Comparing the results from the accelerometers and string potentiometers. Phase difference and amplitude ratio.

- Selecting which motion signal should be used in the hydrodynamic force coefficient calculation.

- Calculating oscillation frequency, oscillation amplitude and phase angle between IL and CF oscillation.

A result sheet is available in the post processor for comparing the motion signals from the three sensors. The most important parameter to consider is the phase difference between individual signals, but also the amplitude ratio is calculated.

When all cases, for a given group of tests, are analyzed, the data is used to investigate the quality of the motion signals, and hence decide which sensor to use for calculation of the hydrodynamic coefficients. In most cases accelerometers are preferred due to high quality and the fact that they were located closest to the force sensors. For cases where problems with the accelerometers are seen, the string potentiometers are used. The measurements from the tow carriage control system contain phase errors, and are consequently not used for calculating force coefficients.

Integration in frequency domain

The well known relations $S_{\dot{x}\dot{x}} = \omega^2 S_{xx}$ and $S_{\ddot{x}\ddot{x}} = \omega^4 S_{xx}$ are used to integrate the measured accelerations to velocity and displacement signals. A MATLAB function, including band pass filtering, has been developed to perform this integration. In short the integration is performed in the following steps:

- The signal a(t) is transformed to frequency domain by the fast fourier transform method, $A = fft(a)$.

- A vector of discrete frequency values, ω, is then constructed. To comply with the vector for the fourier transformed signal, A, the frequency vector is constructed so that the frequency increases from zero to the Nyquist frequency and then increases from the negative value of the Nyquist frequency to zero.

- The band pass filtering is then carried out by setting the A values outside the frequency band to zero

- The integration is performed by $V = A/(\omega * i)$ and $X = A/(\omega * i)^2$.

- Time series of acceleration, velocity and displacement are found by taking the real value of the inverse fourier transform of A, V and X respectively. (x=real(ifft(X))).

Differentiation in time domain

The IL and CF motions do not oscillate around their starting point. The starting point is close to the extreme value, meaning that the mean value of the measured displacement time series is different from zero. The motion matrix, containing acceleration, velocity and displacement is found from measured displacements in the following manner:

- The velocity time series is found by: $\dot{x} = \frac{x_{i+1} - x_{i-1}}{2dt}$

- The acceleration time series is found: $\ddot{x} = \frac{x_{i+1} - 2x_i + x_{i-1}}{dt^2}$

- Both the acceleration- and velocity time series are then low-pass filtered with a cut-off frequency of 2.2Hz.

- The acceleration signal is used to find an integer number of zero up-crossing periods within the steady-state part of the signal. The mean value of the displacement signal is found for the same period. This mean value is then subtracted from the displacement signal.

4.3.3 Force signals

The force signals are processed in the following manner, prior to calculating the hydrodynamic coefficients:

- Subtracting offset. The mean value of the first 5 seconds were subtracted from the time series.

- Include calibration factors and correct for cross-talk.

- Calculate mean value and subtract the mean drag force in IL direction.

- Subtract the inertia force due to acceleration of the cylinder mass.

- Low-pass filter the hydrodynamic force signals

The mean values are calculated for an integer number of oscillation periods. The reason for calculating the mean value in CF direction, which is supposed to be zero, is to verify that there is no cross-talk or force sensor drift. The cut-off frequency of the low-pass filter is 4Hz and is chosen based on the eigenfrequencies of the apparatus determined by pluck tests. Low pass filtering of the force signals is performed in order to obtain accurate rms- and correlation coefficients. Filtering the force signals is not required, and hence not desirable, for calculating the hydrodynamic force coefficients ($C_{e,IL/CF}, C_{a,IL/CF}$). Comparing coefficients based on filtered and not filtered force signals has shown that the selected cut-off frequency does not influence the results.

4.4 Hydrodynamic force coefficients

The purpose of this section is to define all hydrodynamic coefficients used in this thesis, and specify how they are calculated from the measured force and motion signals.

4.4.1 Fourier-coefficient analysis

From basic fourier theory a continuous function, x(t), can be represented by a series of harmonic functions defined as:

$$x(t) = a_0 + \sum_{n=1}^{\infty}(a_n \cos(\omega_n t) + b_n \sin(\omega_n t)) \tag{4.1}$$

The coefficients a_0, a_n and b_n are defined as:

$$a_0 = \frac{1}{T}\int_0^T x(t)dt \tag{4.2}$$

$$a_n = \frac{2}{T} \int_0^T x(t) \cos(\omega_n t) dt \qquad (4.3)$$

$$b_n = \frac{2}{T} \int_0^T x(t) \sin(\omega_n t) dt \qquad (4.4)$$

In our case we are mainly concerned with the force at the oscillation frequency, ω_{osc}. In case of a harmonic oscillation, the force can be written:

$$F(t) = F_0 \sin(\omega_{osc} t + \phi) \qquad (4.5)$$

where ω_{osc} is the oscillation frequency. The oscillation period T_{osc} is then given by $\frac{2\pi}{\omega_{osc}}$. Expanding equation 4.5 we get

$$F(t) = F_0 \sin(\phi) \cos(\omega_{osc} t) + F_0 \cos(\phi) \sin(\omega_{osc} t) \qquad (4.6)$$

and we identify $F_0 \sin(\phi)$ with a_1 and $F_0 \cos(\phi)$ with b_1. The force amplitude, F_0, and phase angle, ϕ, are then given by:

$$F_0 = \sqrt{a_1^2 + b_1^2} \qquad (4.7)$$

and

$$\phi = atan(\frac{a_1}{b_1}) \qquad (4.8)$$

The coefficient a_0 (Eqn 4.2) is seen to represent the mean value of the load x(t), and will hence define the drag coefficient.

Methods for calculating the fourier coefficients, a_1 and b_1, are discussed in section 4.5.

4.4.2 Notation

There will be reported results from forced oscillations in two directions, both IL and CF, and since forced oscillations in IL direction has not previously been reported there is not an established practice on notation. It has hence been necessary to establish a notation for the hydrodynamic coefficients that is applicable in two directions. In order to achieve a consistent notation in both IL and CF directions, the proposed notation for CF is slightly changed compared to what traditionally has been used for pure CF experiments. The following notation will be used:

- C_D and C_L refer to static force in IL and CF direction respectively. There has not been measured any static forces in CF direction in these experiments. Hence, no C_L values are reported.

- $C_{t,IL/CF}$, coefficient referring to the total dynamic force in IL/CF direction.

- $C_{e,IL/CF}$, coefficient referring to the force in phase with velocity.

- $C_{a,IL/CF}$, coefficient referring to the force in phase with acceleration.

4.4.3   Definition of Hydrodynamic Coefficients

The hydrodynamic coefficients are defined in the following:

Drag coefficient, C_D

The drag coefficient is defined as:

$$C_D = \frac{1}{T} \int_t^{t+T} \frac{F_{IL}(t)}{\frac{1}{2}\rho DLU_0^2} \tag{4.9}$$

where F_{IL} is the force in IL direction and T is taken as an integer number of oscillation periods.

Dynamic excitation coefficient, $C_{e,IL/CF}$

The dynamic excitation coefficient is defined as:

$$C_{e,IL/CF} = \frac{F_{hydro,0,IL/CF}\sin(\phi)}{\frac{1}{2}\rho DLU_0^2} \tag{4.10}$$

Where $F_{hydro,0,IL/CF}sin(\phi)$ is the hydrodynamic force in phase with velocity, in IL or CF direction. This coefficient is analogous to the C_{L_V} coefficient that traditionally has been used when reporting results from pure CF experiments, see Gopalkrishnan [15] and others.

The reason for using e as identifier for the component in phase with velocity is that this component will define energy exchange between the fluid and the cylinder. A positive C_e will excite the cylinder, while a negative value will provide damping.

Added mass coefficient, $C_{a,IL/CF}$

The added mass coefficient is defined as:

$$C_{a,IL/CF} = \frac{F_{hydro,0,IL/CF}\cos(\phi)}{\frac{\pi D^2}{4}\rho L\omega_{osc}^2 x_0} \tag{4.11}$$

where ω_{osc} is the oscillation frequency and x_0 is the oscillation amplitude. The added mass coefficient is based on the force in phase with acceleration normalized with respect to the mass of the displaced water and the acceleration amplitude of the harmonic oscillation, $\omega_{osc}^2 x_0$.

Total dynamic force coefficients, $C_{t,n,IL/CF}$

The total dynamic force coefficient is defined as:

$$C_{t,n} = \frac{\sqrt{a_n^2 + b_n^2}}{\frac{1}{2}\rho DLU_0^2} \tag{4.12}$$

where

$$a_n = \frac{2}{T} \int_t^{t+T} F_{hydro}(t)\cos(n\omega_{osc}\cdot t)dt \tag{4.13}$$

and

$$b_n = \frac{2}{T} \int_t^{t+T} F_{hydro}(t) \sin(n\omega_{osc} \cdot t) dt \tag{4.14}$$

The coefficient can be calculated both in IL and CF direction. The letter n refers to which multiple of the oscillation frequency, ω_{osc}, the coefficient is calculated for. Hence, n=1 refers to the total dynamic force at the oscillation frequency, in general referred to as $C_{t,IL/CF}$.

In a similar manner the total dynamic force coefficient at the Strouhal frequency is estimated in CF direction, C_{t,S_t}. The Strouhal number, S_t, is estimated from fixed cylinder tests and a shedding frequency, f_s, for the given test condition is found from the relation $f_s = \frac{S_t U}{D}$. The coefficient is defined as:

$$C_{t,S_t} = \frac{\sqrt{a_{f_s}^2 + b_{f_s}^2}}{\frac{1}{2}\rho D L U^2} \tag{4.15}$$

RMS coefficients, $C_{rms,IL/CF}$

An rms-coefficient, C_{rms}, is defined for the total hydrodynamic force:

$$C_{rms} = \frac{\sqrt{2 \cdot \frac{1}{n} \sum_{i=1}^{n}(F_{hydro,i} - \bar{F}_{hydro})^2}}{\frac{1}{2}\rho D L U_0^2} \tag{4.16}$$

Where $\bar{F}_{hydro}$ is the mean value of the hydrodynamic force and $F_{hydro,i}$ refers to the hydrodynamic force at time step i. The summation is performed for the n time steps in the steady state region of the time series.

The rms-coefficient is linked to the magnitude of the oscillating force, but does not refer to a given oscillation frequency or phase component relative to motions. For a purely harmonic force, i.e. single frequency, equal values for C_{rms} and C_t will be calculated. For force signals containing more than one frequency, the value of C_{rms} will be higher. The ratio between C_{rms} and C_t may hence be used to investigate if there are significant force components at other frequencies than the oscillation frequency.

The rms-coefficient is calculated for the oscillating force in both IL and CF direction.

Correlation coefficient, $\rho_{xy,IL/CF}$

Forces are measured at both ends of the cylinder. The correlation coefficient is defined as:

$$\rho_{xy} = \frac{\frac{1}{n} \sum_{i=1}^{n}(x_i - \bar{x})(y_i - \bar{y})}{SD(x)SD(y)} \tag{4.17}$$

where SD(x) is the standard deviation of x, defined as:

$$SD(x) = \frac{1}{n-1} \sqrt{\sum_{i=1}^{n}(x_i - \bar{x})^2} \tag{4.18}$$

x and y represents the hydrodynamic forces at the two ends, and $\bar{x}$ and $\bar{y}$ is the mean value of the force. The summation is made over the n time steps in the steady state region of the time series.

The range of the correlation coefficient is -1 to 1. A large positive coefficient indicate that the two parameters are strongly correlated in phase.

4.5   Decomposition of the hydrodynamic force

In this section four methods used to decompose the hydrodynamic force into a component in phase with velocity and a component in phase with acceleration are described. The power transfer method, see 4.5.1, is used as the base case method and the three other methods are used in the uncertainty analysis, see chapter 5, to estimate the uncertainty in the force decomposition.

4.5.1   The Power Transfer Method

The method considers the power transfer, i.e. energy pr. unit time, between the fluid and the cylinder.

The power transfer, P(t), is given by

$$P(t) = F_{hydro}(t) \cdot \frac{d}{dt}x(t) = F_{hydro}(t) \cdot \dot{x}(t) \tag{4.19}$$

where x(t) is the cylinder motion. $\dot{x}(t)$ is hence the cylinder velocity. The average power transfer, $\bar{P}$, can be written as:

$$\bar{P} = \lim_{T \to \infty} \frac{\int_t^{t+T} F_{hydro}(t) \cdot \dot{x}(t)dt}{T} \tag{4.20}$$

Assuming that a forced harmonic oscillation gives a harmonic hydrodynamic force, a second expression for the average power transfer is given by:

$$\bar{P} = \frac{1}{nT_{osc}} \int_0^{nT_{osc}} F_{hydro,0}sin(\omega_{osc}t + \phi) \cdot x_0\omega_{osc}cos(\omega_{osc}t)dt$$

$$\bar{P} = \frac{F_{hydro,0} \cdot x_0\omega_{osc}}{nT_{osc}}[cos(\phi) \int_0^{nT_{osc}} cos(\omega_{osc}t)sin(\omega_{osc}t)dt + sin(\phi) \int_0^{nT_0} cos^2(\omega_{osc}t)dt]$$

$$\tag{4.21}$$

Recognizing the first integral as $\int_0^{nT_{osc}} cos(\omega_{osc}t)sin(\omega_{osc}t)dt = 0$ and the second as $\int_0^{nT_{osc}} cos^2(\omega_{osc}t)dt = \frac{nT_{osc}}{2}$ we get:

$$\bar{P} = \frac{F_{hydro,0} \cdot x_0\omega_{osc}}{nT_{osc}}[sin(\phi)\frac{nT_{osc}}{2}] = \frac{1}{2}x_0\omega_{osc}F_{hydro,0}sin(\phi) \tag{4.22}$$

Hence, from equation 4.20 and 4.22 the force in phase with velocity, $F_{hydro,0}sin(\phi)$, is given by:

$$F_{hydro,0}sin(\phi) = \frac{2}{x_0\omega_{osc}} \lim_{T \to \infty} \frac{\int_t^{t+T} F_{hydro}(t) \cdot \dot{x}(t)dt}{T} \tag{4.23}$$

By applying the same technique, but without linking it to a physical quantity such as $\bar{P}$, a similar expression can be derived for the force in phase with acceleration, $F_{hydro,0}cos(\phi)$.

$$F_{hydro,0}cos(\phi) = -\frac{2}{x_0\omega_{osc}^2}\lim_{T\to\infty}\frac{\int_t^{t+T}F_{hydro}(t)\cdot\ddot{x}(t)dt}{T} \tag{4.24}$$

As the time series from the experiments are of limited length, i.e. $T \to \infty$ not valid, the limit functions in Eqn. (4.23) and (4.24) are approximated by integrating over an integer number of oscillation periods, $T = nT_{osc}$.

4.5.2 The Fourier-average Method

In the Fourier average method it is assumed that the hydrodynamic force is harmonic, with the same frequency as the oscillation, ω_0. The hydrodynamic force is then given by:

$$F_{hydro}(t) = F_{hydro,0}sin(\omega_{osc}t + \phi) \tag{4.25}$$

Where ϕ is the phase angle between the force and the cylinder motion. The cylinder motion, or oscillation, is given by $x(t) = x_0sin(\omega_{osc}t)$. The force in phase with velocity can then be found by pre-multiplying by $cos(\omega_{osc}t)$ and integrate over an integer number of periods, nT_{osc}.

$$\int_t^{t+nT_{osc}}F_{hydro}\cdot cos(\omega_{osc}t)dt =$$

$$F_{hydro,0}cos(\phi)\int_t^{t+nT_{osc}}sin(\omega_{osc}t)\cdot cos(\omega_{osc}t)dt + \tag{4.26}$$

$$F_{hydro,0}sin(\phi)\int_t^{t+nT_{osc}}cos^2(\omega_{osc}t)dt$$

Since $\int_t^{t+nT_{osc}}sin(\omega_{osc}t)\cdot cos(\omega_{osc}t)dt = 0$ and $\int_t^{t+nT_{osc}}cos^2(\omega_{osc}t)dt = \frac{nT_{osc}}{2}$ we get:

$$F_{hydro,0}sin(\phi) = \frac{2}{nT_{osc}}\int_t^{t+nT_{osc}}F_{hydro}(t)\cdot cos(\omega_{osc}t)dt \tag{4.27}$$

Correspondingly, pre-multiplying by $sin(\omega_{osc}t)$, the force in phase with the acceleration is given by:

$$F_{hydro,0}cos(\phi) = \frac{2}{nT_{osc}}\int_t^{t+nT_{osc}}F_{hydro}(t)\cdot sin(\omega_{osc}t)dt \tag{4.28}$$

The calculated phase angle, ϕ, refers to the time step, t, where the integration starts. As the phase angle of interest is the phase between the force and the body motion, the starting point of the integration is taken at the zero up-crossing of the displacement signal. Coefficients are calculated for all zero up-crossing periods in the steady state region, i.e. n=1, and the reported value is the mean value of the individual coefficients.

An alternative method for estimating the correct phase between motion and force is to select a starting point t, e.g. the start of the steady state region, and then use Eqn. (4.27) and Eqn. (4.28) to calculate the phase angle for both the force- and motion signal relative to this point. The phase angle between force and motion is then the difference between the two phase angles.

4.5.3   The Transfer Function Method

The Transfer Function Method is a frequency domain method. The basic assumptions is hence that there is a linear relationship between the input signal (frequency and amplitude of the cylinder motion) and the output signal (the hydrodynamic force).

A transfer function, $H_{xy}(\omega)$, is estimated using the well known relation $S_{xy}(\omega) = H_{xy}(\omega)S_{xx}(\omega)$. The cross spectrum, $S_{xy}(\omega)$, between displacement and hydrodynamic force, and the auto spectrum, $S_{xx}(\omega)$, of displacement signal is calculated from the measured time series. The transfer function is then given by:

$$H_{xy}(\omega) = \frac{S_{xy}(\omega)}{S_{xx}(\omega)} \tag{4.29}$$

The phase angle between the two signals is the argument of the complex transfer function. The phase angle of interest is that of the oscillation frequency, ω_{osc}

$$\phi = tan^{-1}\left(\frac{imag(H_{xy}(\omega_{osc}))}{real(H_{xy}(\omega_{osc}))}\right) \tag{4.30}$$

The amplitude ratio between the hydrodynamic force signal and the displacement signal is found by:

$$\frac{F_{hydro,0}}{x_0} = \sqrt{(real(H_{xy}(\omega_{osc})))^2 + (imag(H_{xy}(\omega_{osc})))^2} \tag{4.31}$$

As the oscillation amplitude, x_0, is known, the hydrodynamic force in phase with velocity, $F_{hydro,0}sin(\phi)$, and acceleration, $F_{hydro,0}cos(\phi)$, may be calculated.

4.5.4   The "Least Square Fit" Method

The method is based on a "built-in" least square fit routine in Matlab and the basic assumption is that the hydrodynamic force may be represented by a linear combination of the acceleration and velocity signal.

$$C_1 \cdot \dot{x}(t) + C_2 \cdot \ddot{x}(t) = F_{hydro}(t) \tag{4.32}$$

Rewritten:

$$Cx = F \tag{4.33}$$

where $C = \begin{vmatrix} C_1 & C_2 \end{vmatrix}$ and $x = \begin{vmatrix} \dot{x}(t) \\ \ddot{x}(t) \end{vmatrix}$

The coefficients in C are then estimated by:

$$minimize \ \ ||Cx - F|| \tag{4.34}$$

Assuming that an harmonic oscillation ,$x(t) = x_0 \sin(\omega_{osc}t)$, gives an harmonic force, see Eqn. (4.25), Eqn. (4.32) is given by:

$$C_1 x_0 \omega_{osc} \cos(\omega_{osc}t) - C_2 x_0 \omega_{osc}^2 \sin(\omega_{osc}t) = F_{hydro,0} \sin(\phi) \cos(\omega_{osc}t) + F_{hydro,0} \cos(\phi) \sin(\omega_{osc}t) \tag{4.35}$$

The two force components are then easily identified as:

$$F_{hydro,0}sin(\phi) = \omega_{osc}x_0 \cdot C_1 \tag{4.36}$$

$$F_{hydro,0}cos(\phi) = -\omega_{osc}^2 x_0 \cdot C_2 \tag{4.37}$$

Chapter 5

Uncertainty Analysis

In this chapter the method used for estimating the confidence interval for the hydrodynamic coefficients found in the experiments will be presented. The chapter is closely linked with to the previous chapter on data analysis and Appendix A where the results from calibration of force and motion sensors are reported.

5.1   Introduction to Uncertainty Analysis

The aim of an uncertainty analysis is to give a quantitative estimate of how reliable a measured or calculated value is. Here this will be given as a 95% confidence interval, i.e. the probability that the true value is within the interval is 0.95. Even if an uncertainty analysis is performed, parts of the analysis will be open to discussion and possible major error sources may be overlooked. On the other hand, concluding on experimental results without at least trying to estimate the reliability of the data, seems at best optimistic.

This chapter presents the uncertainty analysis carried out for the experimental data. The theoretical background is mainly based on Coleman & Steele [8] and some theory will be included to explain the various steps of the uncertainty analysis. Ersdal [11] has used the methodology for a towing tank experiment, and some of the error estimates are based on his work.

5.1.1   Error and Uncertainty

In the following the term error will be used as the distance between a measured and a true, but unknown, value. The total error is the sum of a precision (random) error and the bias (systematic) error. Using the calibration of force sensors as an example, the precision error would typically be given by the variation in calibration coefficient found from different calibration series, while the bias error would be given by the possible error in the mass of the weights used for performing the calibration.

Uncertainty will be used as the statistical estimate of the error.

5.1.2   The Concept of Replication Level

When discussing errors and uncertainties in measurements there is a clear distinction between the words repetition and replication. Repetition is used in its common sense, something is repeated. When repeating an experiment the replication level describes exactly what is repeated. Three orders of replication will be used.

- *Zeroth-order replication level* describes a condition where the measured quantity is assumed constant in time, i.e. only the variations inherent in the measurement system contributes. An example of a zeroth-order replication level is measuring the length and diameter of the test cylinder.

- *First-order replication level* describes a condition where the instrumentation and setup is fixed but time is running. An example of first-order replication level is force measurements during fixed cylinder tests.

- *N'th order replication level* would include all other changes. This includes performing a second test at a later time or performing a similar experiment in a different laboratory. In this thesis repeating a test at a later time is considered 2nd order replication, while repeating a test in a later experimental phase is referred to as higher order replication.

A more practical distinction between precision and bias error can then be given as follows: The precision error is given by the variation of the data at a given replication level, while the bias error is constant for the same level. Hence, the precision error can be estimated by repeating the experiment while this is not the case for bias error without increasing the replication level.

5.2   Hydrodynamic Coefficients

The hydrodynamic coefficients for which the uncertainty is estimated are the drag coefficient, Eqn. (5.1), the dynamic excitation coefficient, Eqn. (5.2), and the added mass coefficient, Eqn. (5.3).

- Drag coefficient

$$C_D = \frac{F_{IL,mean}}{\frac{1}{2}\rho DLU_0^2} \tag{5.1}$$

- Dynamic excitation coefficient

$$C_{e,IL/CF} = \frac{F_0 \sin(\phi)}{\frac{1}{2}\rho DLU_0^2} \tag{5.2}$$

- Added mass coefficient

$$C_{a,IL/CF} = \frac{1}{\frac{\pi D^2}{4}L\rho}\left(\frac{F_0 \cos(\phi)}{a_0} - M\right) \tag{5.3}$$

The definition of the drag coefficient is the same as presented in chapter 4, Eqn. (4.9), and has been included here for completeness. In the uncertainty analysis the measured force F has been used when calculating $C_{e,IL/CF}$ and $C_{a,IL/CF}$ instead of F_{hydro} as used in chapter 4. The reason for the change is that this method makes it straight forward to include a phase error in the motion signal, which is needed in the total uncertainty estimate. The implications of using the measured force is that the mass of the cylinder has to be subtracted after the force has been decomposed, see Eqn. (5.3), and that the calculated phase angle, ϕ, would not be comparable with other experiments as it depends on the mass of the cylinder.

5.3 Data Reduction Equations

As seen in the previous section the measured parameters are not the final result of the experiment. The propagation of elemental errors into the final experimental result is given by the data reduction equation, DRE.

5.3.1 General

Given an experimental result, r, which is a function of n measured variables.

$$r = r(X_1, X_2, ..., X_n) \tag{5.4}$$

The influence coefficient, κ, defines how the result is influenced by one specific measurement.

$$\kappa_i = \frac{\partial r}{\partial X_i} \tag{5.5}$$

The uncertainty in the result is then given by (Coleman & Steele [8]):

$$
\begin{aligned}
U_r^2 &= (\frac{\partial r}{\partial X_1})^2 U_{X_1}^2 + (\frac{\partial r}{\partial X_2})^2 U_{X_2}^2 + ... + (\frac{\partial r}{\partial X_n})^2 U_{X_n}^2 \\
&= \sum \kappa_i^2 U_{X_i}^2
\end{aligned}
\tag{5.6}
$$

5.3.2 DRE for the hydrodynamic coefficients

In this section the influence coefficients are found for the three hydrodynamic coefficients.

Drag coefficient. In order to get a transparent expression for the uncertainty in drag coefficients the expression for uncertainty, U_{C_D}, has been divided by the drag coefficient, C_D. The uncertainty can then be expressed as:

$$(\frac{U_{C_D}}{C_D})^2 = (\frac{U_{F_{IL,mean}}}{F_{IL,mean}})^2 + (\frac{U_\rho}{\rho})^2 + (\frac{U_D}{D})^2 + (\frac{U_L}{L})^2 + (\frac{2U_{U_0}}{U_0})^2 \tag{5.7}$$

For both the dynamic excitation coefficient, C_e, and the added mass coefficient, C_a, the coefficients can get the value of zero. Hence, it would not give any meaning to express the uncertainty as a fraction of the coefficient itself.

Dynamic excitation coefficient, C_e

$$(U_{C_e})^2 = (\kappa_{F_0 sin(\phi)})^2 (U_{F_0 sin(\phi)})^2 + (\kappa_\rho)^2 (U_\rho)^2 + (\kappa_D)^2 (U_D)^2 + (\kappa_L)^2 (U_L)^2 + (\kappa_{U_0})^2 (U_{U_0})^2 \quad (5.8)$$

Where the influence coefficients are given as:

$$\kappa_{F_0 sin(\phi)} = \frac{\partial C_e}{\partial (F_0 sin(\phi))} = \frac{1}{\frac{1}{2}\rho D L U_0^2} \quad (5.9)$$

$$\kappa_\rho = \frac{\partial C_e}{\partial \rho} = -\frac{F_0 sin(\phi)}{\frac{1}{2}\rho^2 D L U_0^2} \quad (5.10)$$

$$\kappa_D = \frac{\partial C_e}{\partial D} = -\frac{F_0 sin(\phi)}{\frac{1}{2}\rho D^2 L U_0^2} \quad (5.11)$$

$$\kappa_L = \frac{\partial C_e}{\partial L} = -\frac{F_0 sin(\phi)}{\frac{1}{2}\rho D L^2 U_0^2} \quad (5.12)$$

$$\kappa_{U_0} = \frac{\partial C_e}{\partial U_0} = -2\frac{F_0 sin(\phi)}{\frac{1}{2}\rho D L U_0^3} \quad (5.13)$$

Added mass coefficient, C_a

$$(U_{C_a})^2 = (\kappa_{F_0 \cos(\phi)})^2 (U_{F_0 \cos(\phi)})^2 + (\kappa_M)^2 (U_M)^2 + (\kappa_{a_0})^2 (U_{a_0})^2 \\ + (\kappa_D)^2 (U_D)^2 + (\kappa_L)^2 (U_L)^2 + (\kappa_\rho)^2 (U_\rho)^2 \quad (5.14)$$

Where the influence coefficients are given as:

$$\kappa_{F_0 \cos(\phi)} = \frac{\partial C_a}{\partial (F_0 cos(\phi))} = \frac{1}{\frac{\pi D^2}{4} L \rho}\left(\frac{1}{a_0}\right) \quad (5.15)$$

$$\kappa_M = \frac{\partial C_a}{\partial M} = -\frac{1}{\frac{\pi D^2}{4} L \rho} \quad (5.16)$$

$$\kappa_{a_0} = \frac{\partial C_a}{\partial a_0} = -\frac{1}{\frac{\pi D^2}{4} L \rho}\left(\frac{F_0 \cos(\phi)}{a_0^2}\right) \quad (5.17)$$

$$\kappa_D = \frac{\partial C_a}{\partial D} = -\frac{2}{\frac{\pi D^3}{4} L \rho}\left(\frac{F_0 \cos(\phi)}{a_0} - M\right) \quad (5.18)$$

$$\kappa_\rho = \frac{\partial C_a}{\partial L} = -\frac{1}{\frac{\pi D^2}{4} L^2 \rho}\left(\frac{F_0 \cos(\phi)}{a_0} - M\right) \quad (5.19)$$

$$\kappa_\rho = \frac{\partial C_a}{\partial \rho} = -\frac{1}{\frac{\pi D^2}{4} L \rho^2}\left(\frac{F_0 \cos(\phi)}{a_0} - M\right) \quad (5.20)$$

In the basic data reduction equations, Eqn. (5.8) and Eqn. (5.14), the force component in phase with velocity, $F_0 \sin(\phi)$, and in phase with acceleration, $F_0 \cos(\phi)$, has been kept as one uncertainty component even though it consist of a force component and a phase component. The reason for this is that there are several factors that influence the uncertainty in the product rather than the two individual parameters.

5.4 Uncertainties in the DRE

In this section the individual uncertainties, U_i, in the data reduction equation are addressed. Both bias- and precision errors will be considered, and the notation for the two types of errors are B and P respectively. The DRE is used to calculate B and P individually, and then the total uncertainty, U, is estimated according to: $U = \sqrt{B^2 + P^2}$.

5.4.1 Uncertainty in water density

The water in the towing tank is fresh water and the density is a function of the water temperature. The temperature was measured several times and at several locations during the experiments and the table used to find the water density for a given temperature is taken from Faltinsen [12]. The mean value and error in water density was found by linear interpolation between the table values $\rho = 999.1@15^0C$ and $\rho = 998.2@20^0C$. The variation in temperature give the water density precision error while a possible error in the temperature vs. density table represents the bias error. As a constant density will be used for each of the three experiment phases the density error will be treated as a bias error.

Table 5.1: Error in water density, U_ρ.

Experiment	Mean value, temperature	Std, temperature	t-value	Mean value, density	Density error, B_ρ
PhaseIII	18.2	0.263	3.18	998.5	0.2
PhaseII	15.9	0.363	2.45	998.9	0.2
PhaseI	17.4	0.082	2.57	998.7	0.1

5.4.2 Uncertainty in cylinder diameter and length

The diameter of the cylinder was measured by a slide caliper at random locations and the estimated bias error is given in Table 5.2.

The length of the cylinder was measured by a tape measure. Several readings were performed and all were found to be within 1mm of the mean value. An estimated error of 5mm have been chosen due to a possible error in the alignment of the end plates. The error in cylinder diameter and length are treated as bias errors in the error analysis.

Table 5.2: Error in cylinder diameter, B_D, and length, B_L.

Experiment	D [mm]	B_D [mm]	L [mm]	B_L [mm]
PhaseIII & II	100.0	0.1	2000	5
PhaseI	150.0	0.2	2987	5

5.4.3   Uncertainty in towing velocity

The towing velocity, U_{U_0}, is found from the tow carriage position measurements. Both an average velocity (given by start and stop position and time) and an instant velocity vector (the derivative of the displacement signal) is calculated. The first is used in the force coefficient calculation and the latter is used to estimate the precision error. The bias error in the tow velocity is related to the calibration factor used in the motion control system and has been estimated by stop-watch tests and by PIV measurements for various tow velocities.

Bias error: Error in calibration factor, $B_{U_0}/U_0 = 0.01$.
Precision error: Variation over length of time series. The standard deviation, S_{U_0}, is calculated for each case and the precision error is taken as $P_{U_0} = 2 \cdot S_{U_0}/\sqrt{N}$.

5.4.4   Uncertainty in drag force

The mean value of the IL force, $F_{IL,mean}$, is used to calculate the drag coefficient. The mean value is found for the steady state region of the time series. For cases where only IL oscillations are present, the mean value is taken over an integer number of IL oscillations and when CF oscillations are present, an integer number of CF oscillations are used. The bias error consists of an error in the force calibration factor and an error in the cross-talk angle, while the variation in mean force over the length of the time series represent the precision error. The expression used for estimating the bias error ($B_{F_{IL,mean}}$) is shown in Eqn. (5.21) and the errors in calibration coefficient and cross-talk angles are given in Appendix A. Table 5.3 summarizes the bias error for the three phases.

$$\frac{B_{F_{IL,mean}}}{F_{IL,mean}} = \sqrt{(\frac{B_{k_{IL}}}{k_{IL}})^2 + (1 - \cos(B_\alpha))^2} \tag{5.21}$$

In Eqn. (5.21) k_{IL} is the IL force calibration factor and B_α is the error in cross-talk angle.

Table 5.3: Error in drag force, $B_{F_{IL,mean}}$.

Experiment	$(\frac{B_{k_{IL}}}{k_{IL}})_{SB}$	$(B_\alpha)_{SB}$	$(\frac{B_{F_{IL,m}}}{F_{IL,m}})_{SB}$	$(\frac{B_{k_{IL}}}{k_{IL}})_{Port}$	$(B_\alpha)_{Port}$	$(\frac{B_{F_{IL,m}}}{F_{IL,m}})_{Port}$
PhaseIII	0.015	2.2	0.015	0.058	2.8	0.058
PhaseII	0.021	6.0	0.022	na	na	na
PhaseI	0.027	2.3	0.027	na	na	na

The precision error is calculated for each case according to $P_{F_{IL,mean}} = 2S_{F_{IL,mean}}/\sqrt{N}$. $S_{F_{IL,mean}}$ is the standard deviation of the mean IL force and a measure of the variation over the length of the time series. For each zero up-crossing period the mean value of the IL force is calculated, giving N individual values. $S_{F_{IL,mean}}$ is based on these values.

5.4.5   Uncertainty in the decomposed force

This subsection addresses the error in the decomposed force, given in Eqn. (5.8) and Eqn. (5.14) as $U_{F_0 \sin(\phi)}$ and $U_{F_0 \cos(\phi)}$ for the force in phase with velocity and acceleration
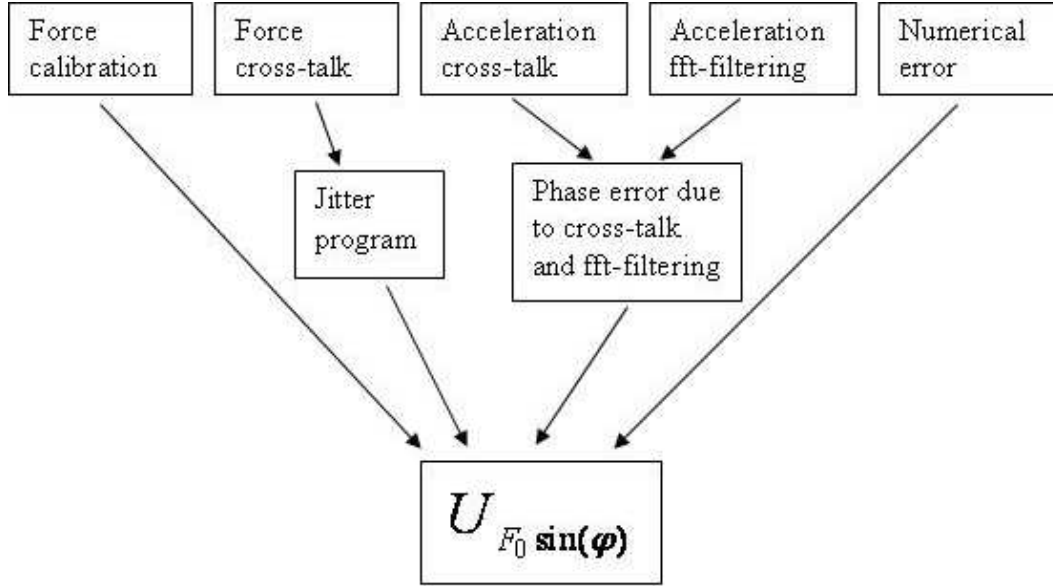
Figure 5.1: Schematic overview of the errors contributing to the uncertainty in the parameter $F_0 sin(\phi)$.

respectively. The method used to find the error is the same for both components and $U_{F_0 \sin(\phi)}$ is used to describe the method.

The phase angle ϕ is defined as the phase between the force and the cylinder motion. As the force and motion signals are recorded at different channels, see Table 3.2, it is important to correct for the time lag between the sampling of the two channels in question. In this project the data acquisition card NI PCI6221, with a sampling rate of 250kHz, has been used. For the oscillation frequencies and the channels used in these experiments, this sampling rate corresponds to a maximum error in phase angle of 0.007deg, or an error in the force in phase with velocity of $1.1 \cdot 10^{-4}$N. This error is insignificant, thus no correction for sampling rate has been performed.

The following parameters are found to contribute to the error in the decomposed force (see also Figure 5.1):

1. Error in force calibration factor.

2. Error in force cross-talk angle.

3. Error in acceleration cross-talk angle.

4. Error due to fft filtering of the acceleration signal.

5. Numerical error in the method used to calculate $F_0 sin(\phi)$.

Only the numerical error is contributing to the precision error. The bias error is calculated as a root-sum-square combination of the elemental bias errors:

$$B_J = \sqrt{\sum_{k=1}^{M} (B_{J,k})^2} \tag{5.22}$$

Error in Force Calibration Factors

The errors in calibration factors are shown in Table 5.4, and are based on the calibration procedure reported Appendix A.

Table 5.4: Error in force calibration factor (relative to mean value) and cross-talk angle, α

Experiment	IL_{SB}	CF_{SB}	α_{SB}	IL_{Port}	CF_{Port}	α_{Port}
PhaseIII	0.015	0.038	2.23 deg	0.058	0.033	2.84 deg
PhaseII	0.021	0.025	6.0 deg	-	-	-
PhaseI	0.027	0.025	2.3 deg	-	-	-

Error in Force Cross-talk Angle

The estimated uncertainty in cross-talk angle is based on results from the force sensor calibration. A method known as a "jitter program" is used to determine how this uncertainty transfers into an uncertainty in the decomposed force. The idea behind a jitter program is to use the data reduction algorithm to calculate the effect on the final result due to an error in the input parameter, for details see Coleman & Steele [8].

The effect of an error in cross-talk angle is calculated as follows: First the error in the cross talk angle is estimated, see Appendix A. Then the cross talk angle is included in the force signal and the coefficient, $F_0 sin(\phi)$, is calculated. This is carried out for both positive and negative cross-talk angle. The maximum error is used when the uncertainty in the force in phase with velocity, $F_0 \sin(\phi)$, is estimated. The error in cross-talk angles for the three experimental phases are summarized in Table 5.4.

Error in the Acceleration Cross-talk angle and fft-filtering

Two of the errors identified to contribute to the uncertainty in the decomposed force are related to a phase error in the motion signal. For the cases where acceleration measurements have been used as motion signals, the errors are related to incorrect correction for cross-talk and to band-pass filtering of the signals. As seen in Figure 5.1 the combined effect of these errors is considered. This has been done by investigating synthetic signals where cross-talk has been included and filtering performed, see Appendix A.1.2 for details.

The investigation gave a phase error of B_ϕ=0.04deg for a 95% confidence interval. No correlation was found between phase angle and acceleration amplitude or frequency. Hence, this error has been used for all cases. The string potentiometer signal was used as motion signal in CF direction for Phase III. The phase error due to signal processing of these signals has been investigated and reported in Appendix A.1.2 and for a confidence level of 95% a phase error of B_ϕ=0.02deg was found.

Numerical Error in Force Decomposition

The numerical error is estimated based on the four methods of force decomposition described in chapter 4.5. The power transfer method is considered to be the most robust and accurate method for this type of experiment and is therefore used as the base case method. The numerical error, which is a precision error, is then estimated by calculating a standard deviation based on the mean value given by the power transfer method. In the following the errors related to the four methods are discussed:

The *The Power Transfer Method* is defined by Eqn. (4.23) and Eqn. (4.24). The method uses the velocity and acceleration signal, and the integration is performed over the full length of the steady state region. For most of the analyzed cases the velocity signal is calculated by integration of the measured acceleration signal in frequency domain, see 4.3.2. Both the acceleration and velocity signal is band-pass filtered. The error in this method is related to how accurate the numerical integration in Eqn. (4.23) and Eqn. (4.24) is performed, the error in the velocity- and acceleration amplitude ($x_0\omega_0$ and $x_0\omega_0^2$ respectively) and a possible phase error in the calculated velocity signal.

The *"Least Square Fit" Method* is characterized by Eqn. (4.32) and uses the same input signals as the power transfer method. The difference is that this method uses a Matlab built-in least square fit algorithm for the force decomposition instead of the numerical integration used in the base case method. Comparing the results from the two methods will give an indication of how sensitive the result is to the numerical method used.

The *Fourier Average Method* is characterized by Eqn. (4.27) and Eqn. (4.28) and the filtered acceleration signal is used to find the integration limits. The force decomposition is then performed for all zero up-crossing periods in the steady state region. Only the filtered acceleration signal is used in the force decomposition which excludes possible errors in the phase of the velocity signal and errors in velocity- and acceleration amplitude which are included in the two previous methods. The fourier average method can be used to calculate dynamic excitation- and added mass coefficients for all zero up-crossing periods and also the individual oscillation periods. The error in the method is related to finding the correct integration limits and to the numerical integration.

In the *Transfer Function Method*, see Eqn. (4.29), the force decomposition is performed in frequency domain and only the force signal, acceleration signal and oscillation amplitude are included in the analysis. The method is very robust but the main contribution to the error is the frequency resolution. The full length of the steady state region is used in the analysis but this is only approximately 70 seconds in the PhaseIII experiments.

From the discussion above it is seen that there are different sources of errors in the four methods and they are therefore found well suited to be the basis for the estimated uncertainty. The transfer function method is however found to give the less accurate result and the inclusion of this method is believed to give a conservative result. It is, however, a robust method and if it is found to give a very different result from the other methods the test case would need to be further investigated.

5.4.6 Uncertainty in cylinder mass

The mass of the cylinder has been found by a Marintek calibrated digital weight measuring equipment with two digit accuracy. In addition to the mass of the cylinder the design of the force sensor cross must be considered. The IL force sensor is the sensor connected to the force sensor housing. Hence the inertia force due to the weight of the CF sensor will be measured in the IL sensor. The mass of this force sensor, HBM PW2GC3, is 0.25kg. In addition there are some connection brackets. The mass causing the measured inertia force and the estimated uncertainty for the two directions are summarized in Table 5.5.

Table 5.5: Error in cylinder mass, B_M.

Experiment	M_{IL} [kg]	$B_{M,IL}$ [kg]	M_{CF} [kg]	$B_{M,CF}$ [kg]
PhaseIII & II	10.38	0.10	9.78	0.03
PhaseI	16.02	0.10	15.42	0.03

5.4.7 Uncertainty in Acceleration Amplitude

The acceleration amplitude is estimated based on the filtered acceleration time series, also used in the force decomposition. The acceleration amplitude is found for each zero up-crossing period and mean value and precision error ($P_{a_0} = 2S_{a_0}/\sqrt{N}$) are estimated based on the individual amplitudes. The bias error is estimated from the accelerometer calibration, see Appendix A, and the bias error relative to the acceleration amplitude is given in Table 5.6.

Table 5.6: Acceleration amplitude bias error, (B_{a_0}/a_0).

Experiment	$(B_{a_0}/a_0)_{IL,SB}$	$(B_{a_0}/a_0)_{CF,SB}$	$(B_{a_0}/a_0)_{CF,Port}$	$(B_{a_0}/a_0)_{CF,Port}$
PhaseIII	0.013	0.020	0.010	0.020
PhaseII	0.009	0.072	0.018	0.022
PhaseI	0.031	0.036	0.022	0.026

5.5 Additional Error Sources

In this section some additional potential error sources are addressed. These have not been included in the uncertainty estimate because the experiments were designed to limit them to the extent that they are found negligible for the reliability of the hydrodynamic coefficients.

5.5.1 Residual flow

The relative motion between the cylinder and the fluid was generated by towing the cylinder. In order to perform the experiment for the desired flow conditions it is essential that
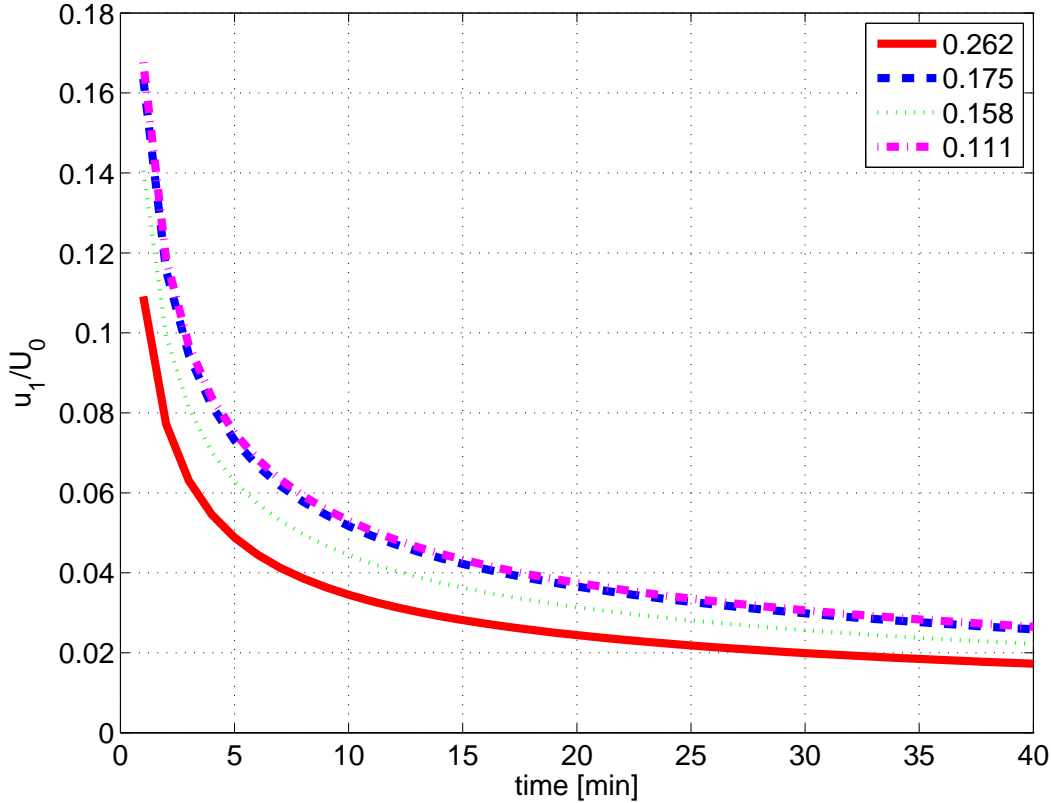
Figure 5.2: Estimated residual velocity vs. waiting time. The graphs refer to the tow velocity, U_0, in m/s.

the fluid is at rest before a new test is performed. Ersdal [11] has published the following equation for estimation of residual flow, based on far wake theory:

$$\frac{u_1}{U_0} = 1.2(\frac{U_0 t}{C_D D})^{-\frac{1}{2}} \tag{5.23}$$

The residual flow relative to the tow velocity, for the four towing speeds used in these experiments, is show in Figure 5.2.

The tow carriage was returned to its starting position immediately after each run. This should reverse the residual flow and hence reduce needed waiting time. Taking this into account would however not change the results significantly. After 10min the equation gives a residual flow of between 3.5 and 5% of the towing speed for all actual cases.

In order to get a hands-on feeling with the fluid conditions at the depth of the cylinder a drifter was placed into the towing tank after the tow carriage had returned to its starting position. After approximately 6 minutes it was not possible to see any movement of the drifter. Also, the runs performed after longer breaks, more than two hours, gave the same results as tests performed after 10 minutes. It was therefore concluded that waiting 10 minutes after each run was sufficient for the residual flow to die out.

5.5.2   End conditions

End plates were installed in order to avoid three dimensional end effects due to the finite length of the cylinder. The end plates were made of plexiglass and were structurally attached to the force sensor housing, with a small gap between the end plates and the cylinder so that the end plates would not influence the measured hydrodynamic forces. The end plates were constructed according to specifications given by Stansby [50], with dimension 7D mounted asymmetric fore and aft, extending 2.5 diameters upstream and 4.5 diameters downstream. The height of the end plates were 5 diameters.

5.5.3   Blockage effect

Forces measured on a cylinder in a finite body of water is different from the forces expected in an infinite stream. This effect is referred to as the "blockage effect" and is caused by the presence of the walls and free surface in the towing tank.

The blockage ratio is defined by the diameter of the cylinder divided by the water depth (D/D_t) and Zdravkovich [67], stated that no correction of forces is necessary for blockage ratios $< 1/10$ for $Re > 300$. In these experiments the blockage ratio is $1/10$ for the PhaseI experiments and $1/15$ for Phase II and III. Re is $2.4 \cdot 10^4$.

5.5.4   Wave generation

The force coefficients from this project is produced to be valid for a cylinder in an infinite volume of water, i.e. no cylinder free surface interaction was tolerated in the experiments. Bishop & Hassan [4] uses the Froude number to evaluate if surface wave effect is important to the experiment. The Froude number is the ratio between inertia forces and gravitation forces and is given on the following form:

$$F_{n,max} = \frac{U_0}{\sqrt{gh_{min}}} \tag{5.24}$$

where h_{min} is the minimum depth of submergence. For the free-surface effects to be neglected, Bishop & Hassan stated that the $F_{n,max}$ was to be much less than unity. In their experiments $F_{n,max}$ was calculated to be 0.375, which was considered sufficiently low. Gopalkrishnan [15] and Vikestad [61] have reported $F_{n,max}$ of 0.181 and 0.29 respectively, which they found sufficiently low for neglecting the effect of free surface.

In the experiments presented in this thesis the $F_{n,max}$ is 0.06 for the Phase I experiments and 0.11 for Phase II and III. The free-surface effect is hence deemed negligible.

Transverse waves were however observed for the largest oscillation amplitudes for the Phase I experiments. By observing the wash on the tank wall it was found that the maximum wave height was approximately 2cm. Comparison with validation experiments performed in phase II, where no waves were observed, showed no effect on the hydrodynamic coefficients.

5.5.5 Limited towing tank length

The duration of the time series obtained by the experiments are limited by the length of the towing tank and the towing velocity. As transient effects are present both at the start up and end of each run it is important that the steady state part of the time series contains a number of load cycles sufficient to calculate an average value with acceptable standard deviation.

For these experiments steady state conditions are expected to cover approximately 23m of the total length. The lowest frequency used in the in-line experiments were $\hat{f}_{IL} = 0.2$, giving approximately 30 load cycles for a run. For the Phase II and III experiments the lowest CF frequency were $\hat{f}_{CF} = 0.11$, which gives 25 load cycles. This was found to be sufficient for calculating force coefficients and the limited length of the towing tank is not considered contributing to the uncertainty in the hydrodynamic coefficients.

5.5.6 Flexibility in apparatus

It is vital for the results of the experiments that the apparatus has a high stiffness, i.e. can be considered rigid. The lowest natural frequency of the apparatus was therefore estimated by exciting the system by a rubber mallet and perform a spectral analysis of the measured forces. The measured natural frequencies are given in Appendix A and are found to be outside the region of interest.

Chapter 6

Results from IL Experiments

This chapter presents the results from the forced IL oscillation experiments, valid for the pure IL VIV regime. The chapter is divided into five parts where results from fixed cylinder tests in uniform flow are presented in the first part. In the second part hydrodynamic coefficients for IL direction are presented while the oscillating forces measured in CF direction for the same experiments are presented in the third part. The fourth part addresses the reliability of the presented results, based on results from the uncertainty analysis, comparison with previously reported results from free vibration experiments and comparison with results from tests performed at lower Reynolds number. The fifth part discusses how the results can be applied for estimating response amplitudes and frequencies for cylindrical structures subjected to VIV.

6.1 Stationary cylinder results

Tests with stationary cylinder in uniform flow were performed to determine drag coefficient and Strouhal number. A large number of runs were performed, especially during the Phase III experiments, where more than 50 repetitions were made. These results will serve as a sound statistical basis for the estimation of the coefficients. Histograms of Strouhal number and drag coefficient are shown in Figure 6.1 and Figure 6.2 respectively. Figure a and b shows the results from measurements at starboard (a) and port (b) side of the cylinder. The mean value of the Strouhal number is 0.188, with a standard deviation of 0.004, for the measurements at both ends of the cylinder. When interpreting the results for the Strouhal number it is important to keep in mind that the duration of the steady state condition was approximately 70 seconds, which gives a spectral resolution of 0.014Hz, corresponding to a resolution in the Strouhal number of 0.005.

Figure 6.2 shows that there is a significant difference between the drag coefficient estimated from force measurements at the two ends of the cylinder. The mean values are 1.325 for starboard side and 1.265 for port side, which represents a difference of 4.5%. From the uncertainty analysis, see Table 5.3, it is seen that there is a relatively large bias error related to the IL force at port side (5.8%). The IL results presented in this thesis will hence be based on the starboard measurements.

The majority of the IL experiments were performed in Phase I, where the cylinder diameter was 150mm compared to 100mm for phase II and III (the Reynolds number for
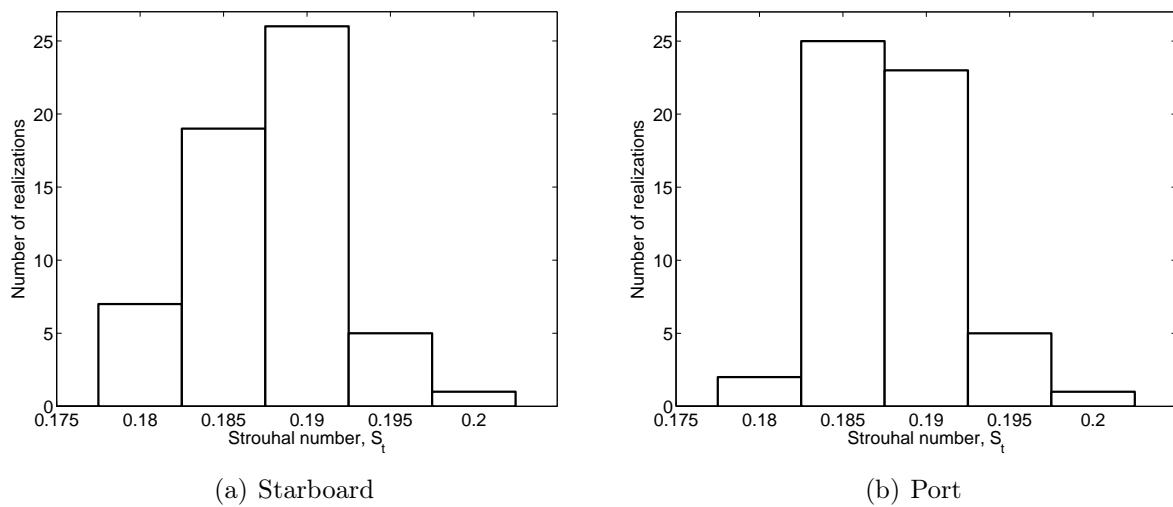
(a) Starboard   (b) Port

Figure 6.1: Histogram of Strouhal number, estimated based on the the frequency representing the peak value of the power spectrum. Based on a total of 58 realizations.
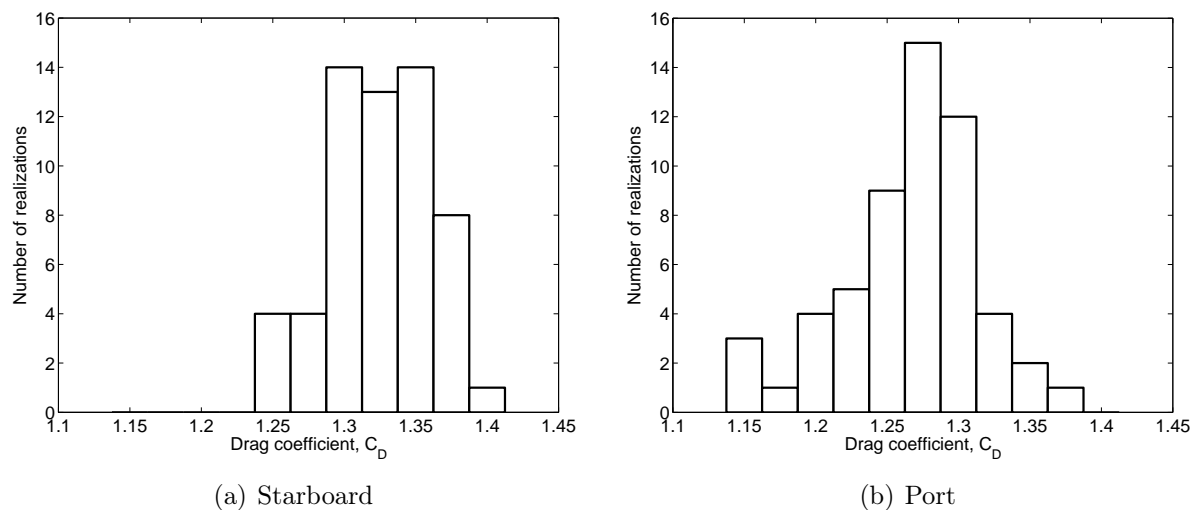

(a) Starboard   (b) Port

Figure 6.2: Histogram of drag coefficient, estimated based on the mean value of the force in IL direction in the steady state region of the time series. Based on a total of 58 realizations.
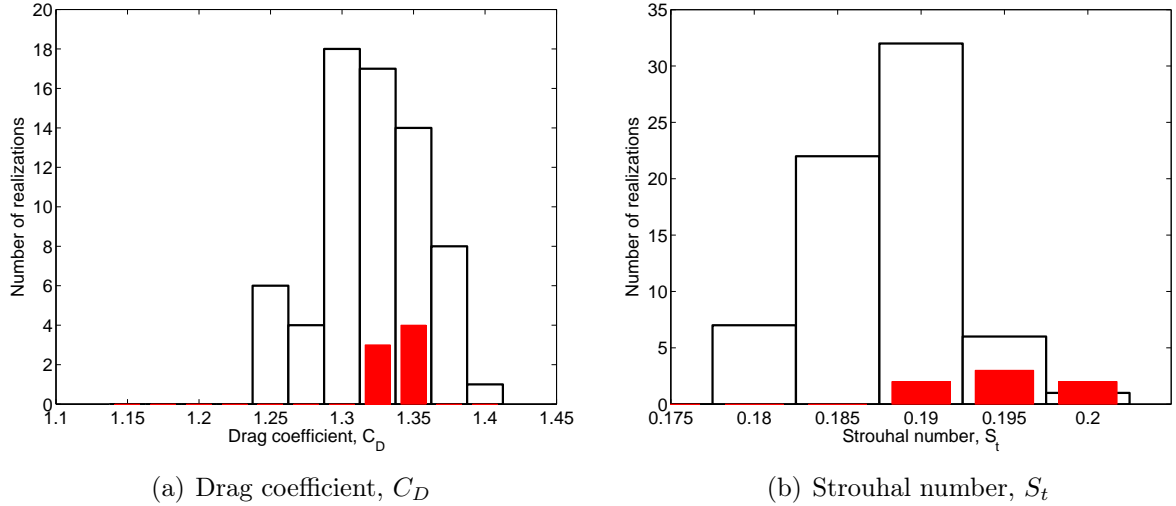
(a) Drag coefficient, C_D

(b) Strouhal number, S_t

Figure 6.3: Histogram of Strouhal number and drag coefficient. Comparison between PhaseI results, 7 realizations shown as solid bars, and the combined results from Phase II and III (68 realizations).

the various experimental phases were the same). In total 7 stationary cylinder tests were performed during Phase I and these are compared with the stationary cylinder results from Phase II and III in figure 6.3. The figure indicates that the drag coefficient given by the two diameters is similar, while it indicates a slightly higher Strouhal number for the Phase I experiment.

The results from the stationary cylinder runs are summarized in Table 6.1. For the Phase III results a correlation coefficient of 0.63 ($\rho_{xy,CF}$), with a standard deviation of 0.24 ($\sigma_{\rho_{xy,CF}}$), was found in CF direction. In IL direction the corresponding results were $\rho_{xy,IL}$=0.77 and $\sigma_{\rho_{xy,IL}}$=0.14. The results from Phase I show higher oscillating forces in both CF (approx-

Table 6.1: Results from stationary cylinder runs. μ represents the mean value and σ the standard deviation.

Phase	No	C_D		S_t		$C_{rms,CF}$		$C_{rms,IL}$		C_{t,S_t}	
		μ	σ	μ	σ	μ	σ	μ	σ	μ	σ
III, SB	58	1.325	0.036	0.188	0.004	0.603	0.128	0.126	0.040	0.460	0.144
III, Port	58	1.265	0.048	0.188	0.004	0.598	0.133	0.115	0.040	0.461	0.147
II	10	1.300	0.029	0.189	0.003	0.600	0.072	0.093	0.008	0.459	0.110
I	7	1.342	0.017	0.195	0.004	0.669	0.110	0.406	0.058	0.509	0.139

imately 11%) and IL direction(a factor of 4!) compared to the results from Phase II and III. From inspection of the force time series it appears that there is a more stable vortex shedding process for the the Phase I tests, which also results in a slightly higher drag coefficient. Unfortunately only the force transducers at one side of the cylinder worked for this phase. Hence, no information with regard to correlation of the vortex shedding process along the length of the cylinder can be gained. The reason for the higher oscillating forces is

not known, but this observation is not important for the main results from the experiments.

Comparing these results with the fixed cylinder results reported by Norberg [39], see chapter 2.1.5, excellent agreement between the Strouhal number results is seen. In order to compare the oscillating lift force, $C_{rms,CF}$, with the results shown in Figure 2.5(b), the results presented in Table 6.1 must be divided by $\sqrt{2}$. The reason for this is the way the coefficients are defined, see Eqn. 2.5 and Eqn. 4.16. Comparing our value for the oscillating lift force coefficient of 0.42 with the results in Figure 2.5(b), it is seen that it is in the lower region of reported values for Re=$2.4 \cdot 10^4$. This is expected as the results in Norbergs figure are normalized based on an "vanishingly small length", l_c, while the results presented herein are normalized with respect to the cylinder length. The correlation coefficient shows that the oscillating lift forces are not correlated, and a lift coefficient normalized with respect to the full length of the cylinder must hence be expected to be lower.

6.2 Hydrodynamic force in IL direction

In this section the hydrodynamic forces measured in IL direction during forced IL oscillation experiments will be presented. Contour plots of dynamic excitation coefficient, $C_{e,IL}$, added mass coefficient, $C_{a,IL}$, and drag coefficient, C_D, will be shown in the first part. Then the forces in the two excitation regions, referred to as 1st and 2nd IL instability region in the literature, will be addressed and contour plots of higher order force components will be shown. The effect of mass ratio and structural damping is addressed in the following two parts, where the concept of nondimensional damping is introduced as a method to estimate the effect of structural damping. In the last part the response amplitude of a flexible beam is addressed.

6.2.1 Contour Plots

The main motivation for performing the IL experiments has been to produce hydrodynamic coefficients $C_{e,IL}$, $C_{a,IL}$ and C_D for the regions where pure IL VIV are expected. The results are presented as contour plots in Figure 6.4, 6.5 and 6.6. The figures contain results from approximately 150 runs with nondimensional frequencies ranging from 0.2 to 0.9 and amplitude ratios from 0.01 to 0.3. The contours are based on linear interpolation between the results and no attempt has been made to smooth the curves. Results for amplitude ratio of 0.5 and nondimensional frequencies of 1.0 and 1.2 are given in Appendix C. Flow visualization by PIV is presented in Appendix D.

Dynamic excitation coefficient, $C_{e,IL}$. Figure 6.4 represents the oscillating force, in IL direction, in phase with velocity as defined in Eqn. (4.10). The zero contour, i.e. the line representing the separation between positive and negative values of the coefficient, is shown as the thick black line. The zero contour line defines the IL response amplitude for a cylinder without mechanical damping. The dynamic excitation coefficient represents the energy transfer between the fluid and the cylinder. Hence, the two areas of positive excitation coefficient represent the excitation regions and the zero contour is the boundary of these regions. The two excitation regions for pure IL VIV, known in the literature as 1st and 2nd instability region, are clearly defined from the zero contour. The 1st instability
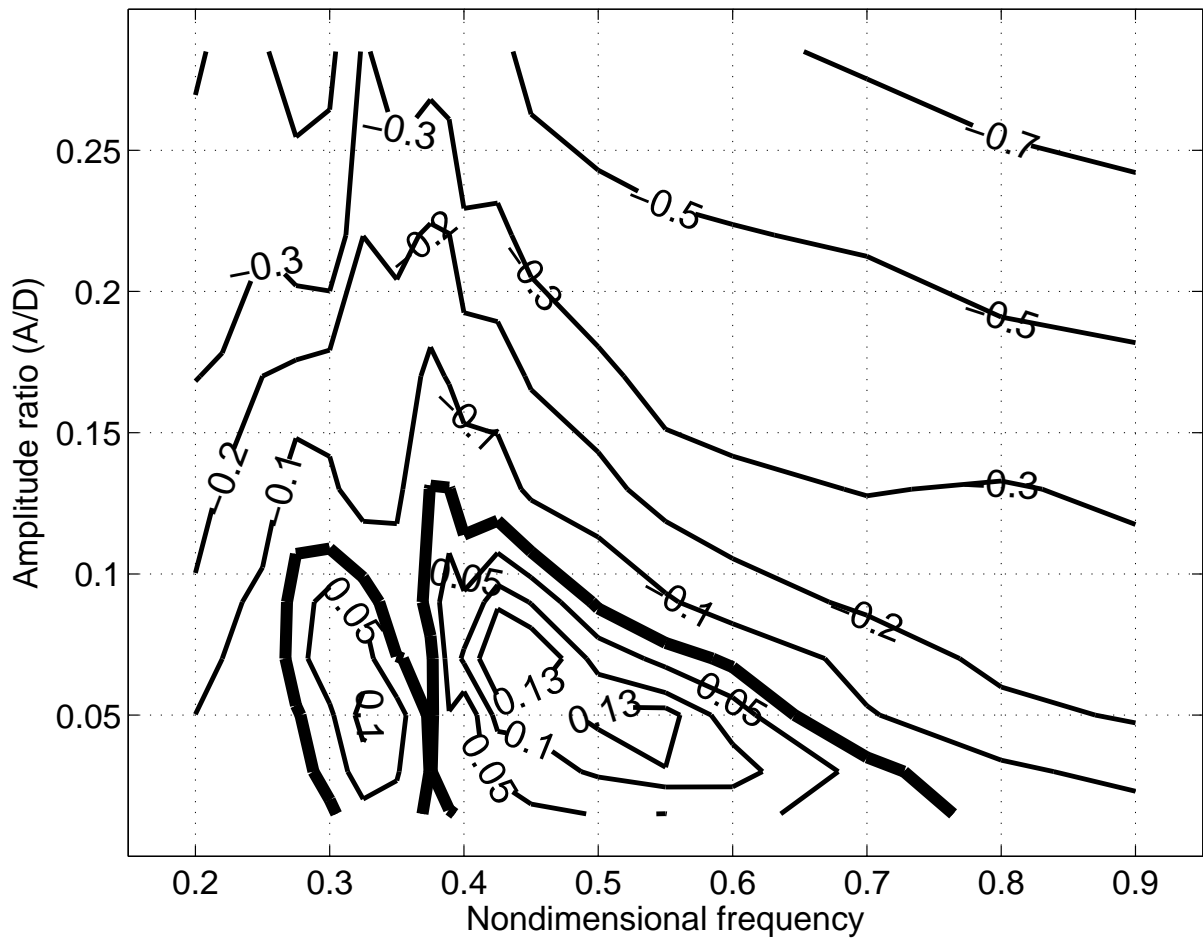
Figure 6.4: Contour plot of dynamic excitation coefficient in IL direction.
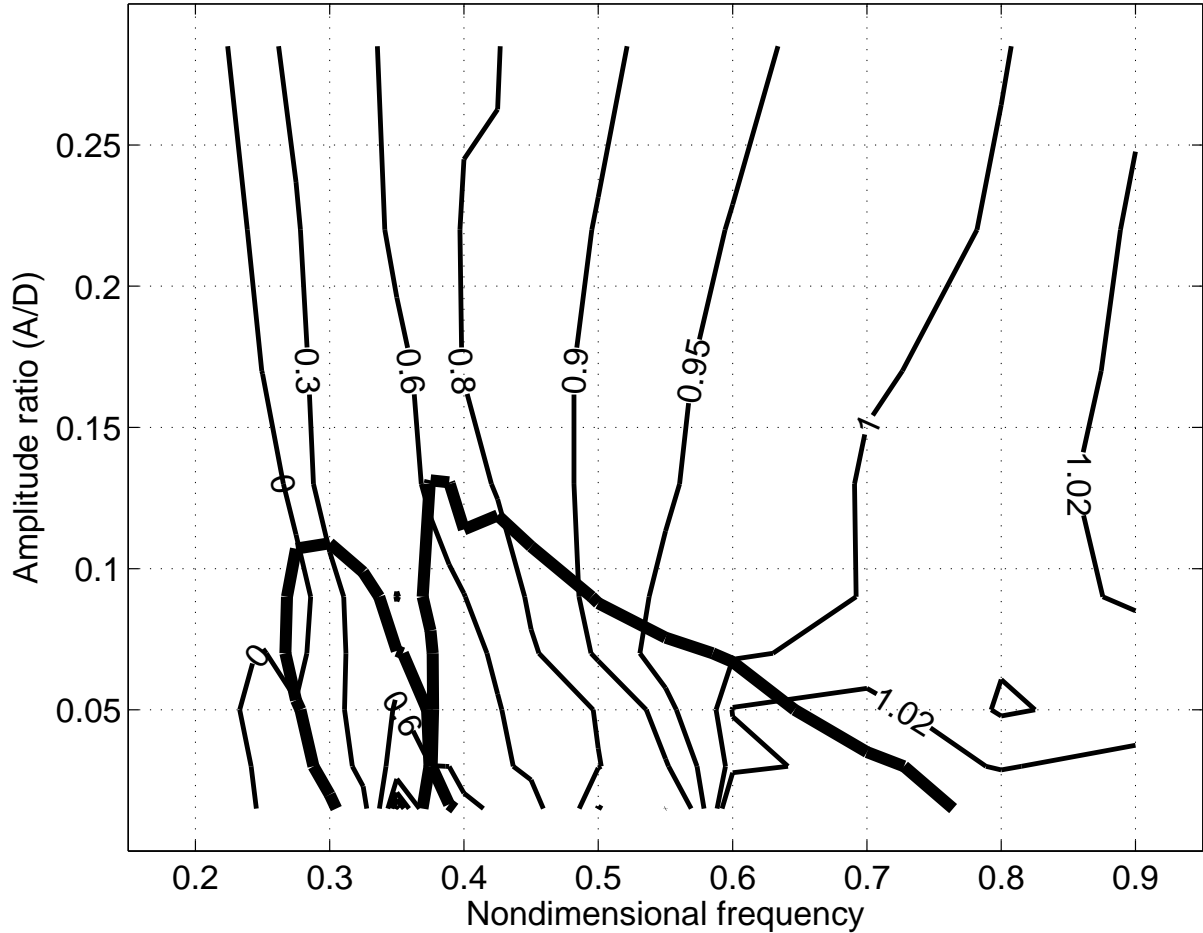
Figure 6.5: Contour plot of added mass coefficient in IL direction. The thick black line is the zero contour of the dynamic excitation coefficient, Figure 6.4, included to illustrate the excitation regions.

region ranges from nondimensional frequency 0.375 to 0.76 with a maximum amplitude ratio of 0.13, while the 2nd instability region ranges from 0.27 to 0.375 with a maximum amplitude ratio of 0.11.

Added mass coefficient, $C_{a,IL}$. Figure 6.5 shows a contour plot of the added mass coefficient which is based on the force in phase with acceleration as shown in Eqn. (4.11). The thick black line shows the zero contour of the dynamic excitation coefficient and has been included to indicate the two excitation regions. The figure shows that the added mass coefficient is mainly dependent on the nondimensional frequency and less influenced by the amplitude. This is especially the case if we look at the added mass coefficient along the zero contour, which can be considered as an estimate of the oscillation amplitude for free vibrations.

Drag coefficient, C_D. Contours of the drag coefficient are shown in Figure 6.6. Also in this figure the zero contour of the dynamic excitation coefficient is included, as a thick black line, to indicate the two excitation regions. The drag coefficient is defined from the mean value of the force in IL direction, see Eqn. (4.9). Note that the mean value
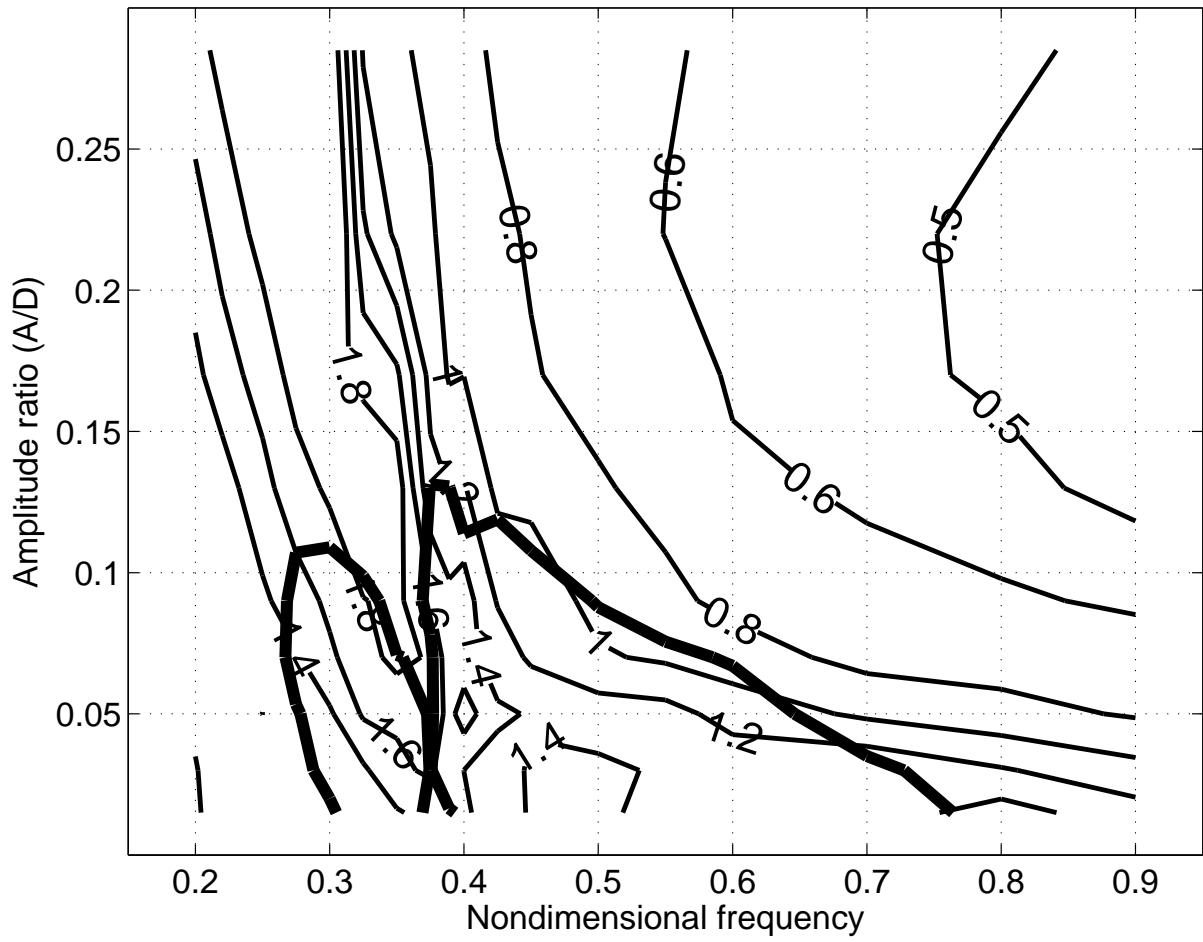
Figure 6.6: Contour plot of drag coefficient. The thick black line is the zero contour of the dynamic excitation coefficient, Figure 6.4, included to illustrate the excitation regions.

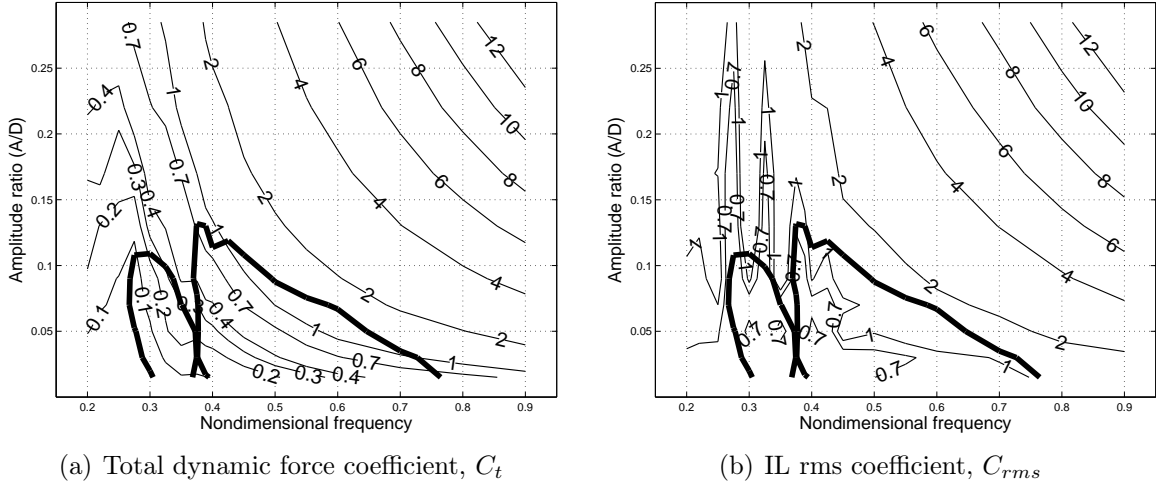(a) Total dynamic force coefficient, C_t

(b) IL rms coefficient, C_{rms}

Figure 6.7: Contour plot of total dynamic force coefficient and IL rms coefficient. The thick black line represents the zero contour of the dynamic excitation coefficient ($C_{e,IL} = 0$).

of the drag coefficient found in the stationary cylinder experiments was 1.33. Figure 6.6 shows a significant variation of the drag coefficient for combinations of amplitude ratio and nondimensional frequency. Low values of the drag coefficient are seen in the high frequency - high amplitude corner of the figure while a drag amplification peak is seen for a nondimensional frequency of approximately 0.32. Following the zero contour it is seen that the 1st instability region can be associated with reduced drag, compared to the stationary results, and the 2nd instability region can be associated with drag amplification. Closer inspection of the results actually shows that the drag amplification peak falls in between the two excitation regions. Also worth noticing is that Gopalkrishnan [15] reported a drag amplification peak for CF oscillations at a nondimensional frequency of 0.32.

6.2.2   IL force components

The dynamic excitation- and added mass coefficients, presented in Figure 6.4 and 6.5, are based on the hydrodynamic force components at the oscillation frequency. In Figure 6.7 contours of the total dynamic force coefficient (figure a), which also is based on the force at the oscillation frequency, and the rms-coefficient (figure b) are shown. The definitions of the coefficients are given in Eqn. (4.12) and (4.16) respectively.

Figure 6.7 shows that the values of $C_{t,IL}$ and $C_{rms,IL}$ are very close for the high frequency - high amplitude cases. However, for the low frequency - low amplitude cases the difference is more pronounced, which indicates that there are significant force components at other frequencies than the oscillation frequency. Especially for the second instability region the difference is large. Figure 6.8 shows the power spectrum of one case in the 1st (a) and one case in the 2nd instability region. The two cases show that there are forces at multiples of the oscillation frequency. These components will in the following be referred to as higher order harmonic forces.

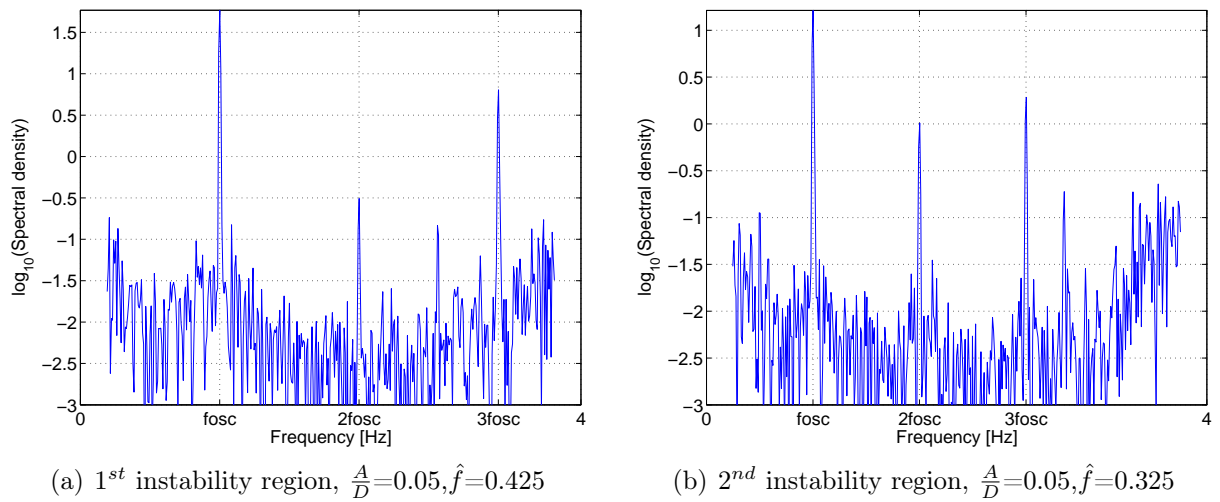Figure 6.9 shows contours of the total dynamic force coefficients at two- ($C_{t2,IL}$) and three

(a) 1st instability region, $\frac{A}{D}$=0.05,$\hat{f}$=0.425

(b) 2nd instability region, $\frac{A}{D}$=0.05,$\hat{f}$=0.325

Figure 6.8: Power spectrum of IL hydrodynamic force.

(a) Contours of $\frac{C_{t2,IL}}{C_{t,IL}}$
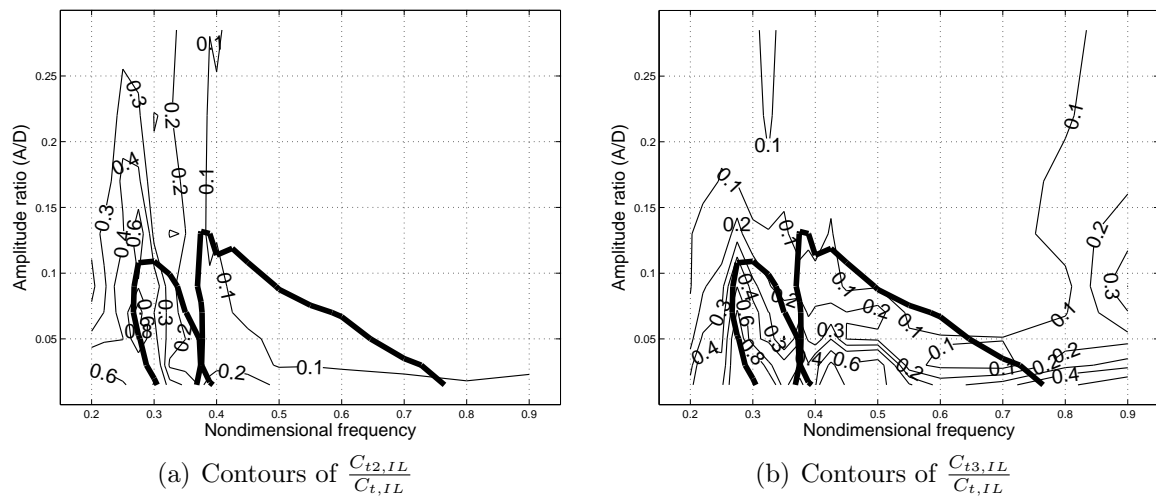
(b) Contours of $\frac{C_{t3,IL}}{C_{t,IL}}$

Figure 6.9: Higher harmonic forces relative to $C_{t,IL}$. The thick black line represents the zero contour of the dynamic excitation coefficient ($C_{e,IL} = 0$).

($C_{t3,IL}$) times the oscillation frequency, see Eqn. (4.12), relative to $C_{t,IL}$. The figure shows that the higher order harmonic forces are mainly related to the second instability region. In the first instability region a force component at three times the oscillation frequency is seen for very low amplitude ratios, but along the $C_{e,IL} = 0$ contour the ratio is less than 0.1. In the second instability region ratios of 0.6 and 0.4 are seen for the second and third harmonic respectively. These forces are seen for the highest response amplitudes, i.e. amplitude ratios of approximately 0.11.

6.2.3 Effect of mass ratio

VIV results from free vibration experiments are normally presented as oscillation amplitude versus reduced velocity, V_r. By finding the added mass coefficient along the $C_{e,IL} = 0$ contour (as indicated by the inclusion of the $C_{e,IL} = 0$ contour in the added mass contour plot in Figure 6.5) and assuming that the added mass coefficient for the natural frequency in still water (f_0) is $C_{a,IL} = 1.0$, the nondimensional frequency can be transformed to reduced velocity by:

$$V_r = \frac{1}{\hat{f}}\sqrt{\frac{\bar{m}+1}{\bar{m}+C_a}} \tag{6.1}$$

In the following, amplitude ratio, frequency ratio and drag coefficient will be shown as function of reduced velocity for varying mass ratio.
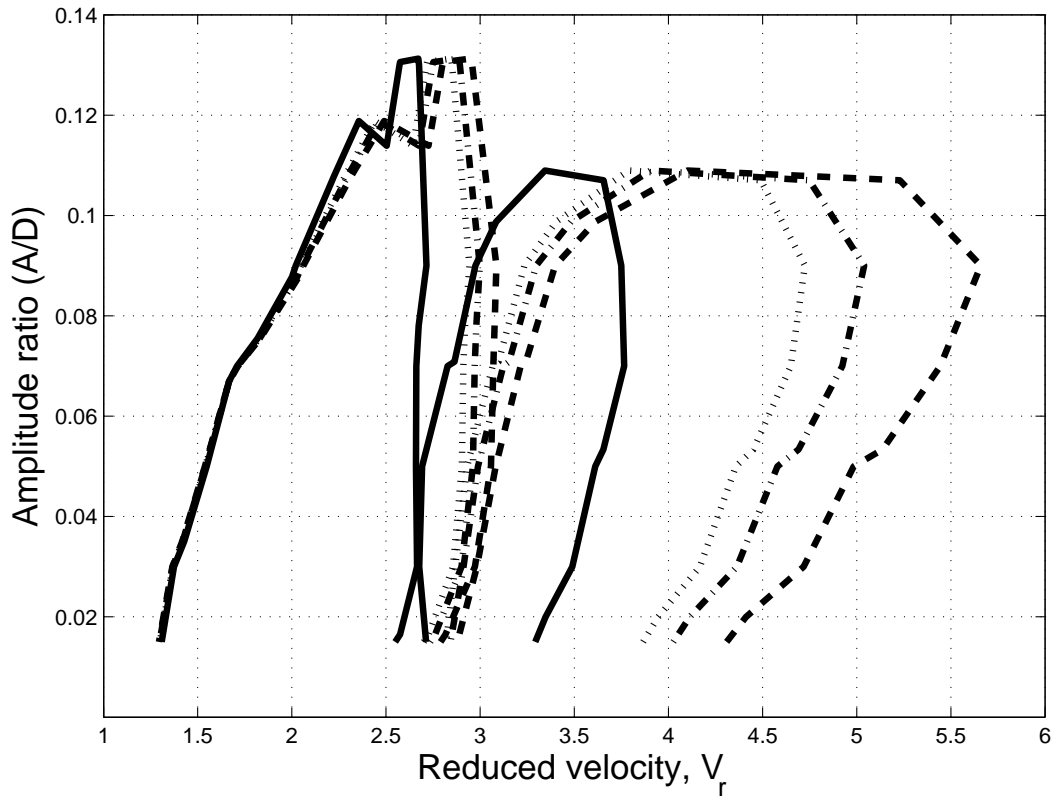
Amplitude ratio

In Figure 6.10 (a) the amplitude ratio (A/D) given by the $C_{e,IL} = 0$ contour is shown as a function of reduced velocity. The transformation from nondimensional frequency to reduced velocity has been performed for four mass ratios. It is seen that when reducing the mass ratio the response region is stretched out over a larger range of reduced velocities. A mass ratio of 100 would typically represent a cylinder in air while a mass ratio of 1.5 to 2.0 would be relevant for a pipeline or riser in water. Figure 6.10 (a) shows that the effect of mass ratio is stronger for the 2nd instability region, compared to the 1st. For the first instability region the highest amplitude ratio appears at a reduced velocity of approximately 2.6 for a mass ratio of 100 while it appears at V_r=2.9 for a mass ratio of 1. The second instability region spans from V_r=2.6 to V_r=3.7 for $\bar{m}$=100 and from V_r=3.0 to V_r=5.6 for $\bar{m}$=1.
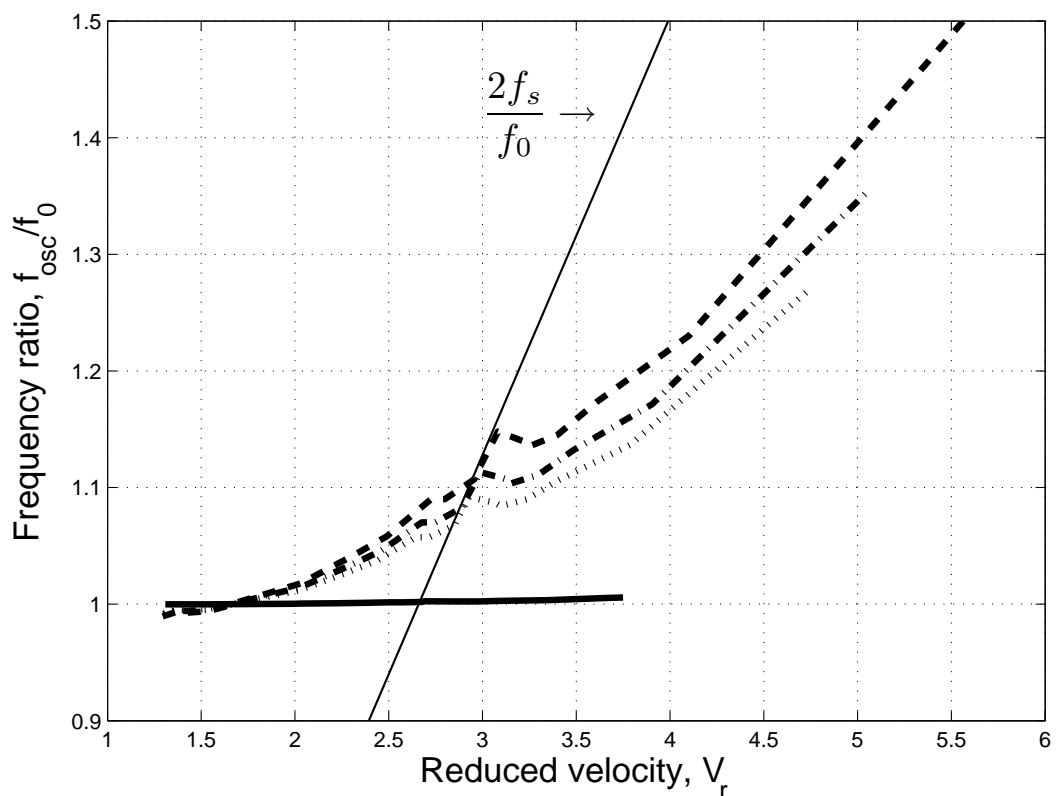
Frequency ratio

Knowing the added mass along the $C_{e,IL} = 0$ contour it is possible to calculate the ratio between the response, or oscillation, frequency and the eigenfrequency of a cylinder subjected to VIV. Figure 6.10 (b) shows this frequency ratio as a function of reduced velocity for the four mass ratios used in Figure 6.10 (a). The frequency ratio is calculated by substituting for V_r and $\hat{f}$ in Eqn. (6.1), which gives the following expression:

$$\frac{f_{osc}}{f_0} = \sqrt{\frac{\bar{m}+1}{\bar{m}+C_a}} \tag{6.2}$$

Figure 6.10 (b) also shows the ratio between the frequency given by two times the Strouhal number and the eigenfrequency in still water for increasing reduced velocity. The following

(a) Amplitude ratio

(b) Frequency ratio

Figure 6.10: Figure (a) shows the amplitude ratio (given by the $C_{e,IL} = 0$ contour) and figure (b) shows the frequency ratio as a function of reduced velocity for four mass ratios. Solid line: $\bar{m} = 100$; Dotted line (..): $\bar{m} = 2$; Dashdot line (-.-.): $\bar{m} = 1.5$; Dashed line (- -): $\bar{m} = 1.0$.

expression can be derived from the definition of St and V_r:

$$\frac{2f_s}{f_0} = 2St \cdot V_r \tag{6.3}$$

The factor 2 is included because the Strouhal number is defined based on the shedding frequency, for a stationary cylinder, in CF direction. The frequency of the force from vortex shedding in IL direction is two times the frequency in CF direction. The Strouhal number found from the stationary cylinder tests is 0.19.

Figure 6.10 (b) clearly shows the importance of mass ratio. The high mass ratio case, $\bar{m}=100$, shows a response frequency equal to the eigenfrequency in still water for the full range of the excitation region. This shows that the forces in phase with acceleration are not strong enough to change the response frequency for this condition. For the low mass ratio cases the response frequency increases for increasing V_r. It is seen that the slope is different from the slope given by the Strouhal number and that the slope changes for the various mass ratios.

Figure 6.10 (b) also shows that the two excitation regions are divided by the frequency corresponding to two times the Strouhal frequency $(2f_s)$. For the low mass ratio cases the response frequency apparently follows the Strouhal frequency between the two excitation regions. It should also be noted that the IL excitation region starts at a ratio between forcing frequency and eigenfrequency in still water, i.e. $2f_s/f_0$, of approximately 0.5.

Lock-in or wake capture is, as discussed in chapter 2.2.1, one of the characteristic properties of VIV. Figure 6.10 (b) demonstrates what this phenomenon looks like in free vibration experiments of varying mass ratio.

Drag coefficient

Figure 6.11 (a) shows the drag coefficient as function of reduced velocity for four mass ratios. The values for the drag coefficient has been found for the first and second instability region as indicated by the thick black line in Figure 6.11 (b), representing the $C_{e,IL} = 0$ contour. The transformation from nondimensional frequency to reduced velocity has been performed by using Eqn. (6.1) for the added mass values corresponding to the $C_{e,IL} = 0$ contour.

Figure 6.11 (a) clearly shows the difference in drag coefficient between the 1st and 2nd instability region. The average drag coefficient for the stationary cylinder cases was 1.33 and it is seen that the first instability region give a reduction in drag coefficient, while drag amplification is seen for the second instability region. The minimum value is 0.9, found for a reduced velocity of 1.7, and the maximum value is 1.85 for reduced velocities of approximately 3. For $\bar{m}=1.5$ and oscillation amplitude A/D=0.1 (Figure 6.11 (b)) it is seen that there is almost a factor of 2 in drag force depending on which vortex shedding mode is causing the vibration, see also discussion given in Appendix D.

(a) Drag coefficient, C_D, vs. V_r
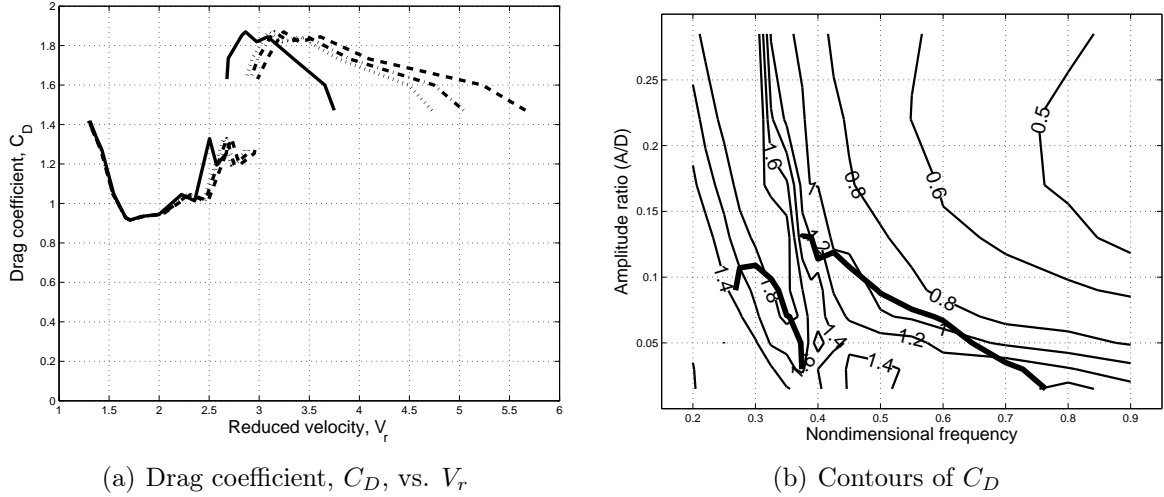
(b) Contours of C_D

Figure 6.11: Drag coefficient as function of reduced velocity for varying mass ratio (figure a). Solid line: $\bar{m} = 100$; Dotted line (..): $\bar{m} = 2$; Dashdot line (-.-.): $\bar{m} = 1.5$; Dashed line (- -): $\bar{m} = 1.0$. Figure b shows the C_D contours and the $C_{e,IL} = 0$ contours, thick black line, that figure a is based on.

6.2.4 Effect of structural damping

Structural damping will extract energy from the system. Hence, when structural damping is present the zero contour will no longer represent the oscillation amplitude. Energy from the fluid will have to balance the energy extracted from the system by structural damping. The new balance will be achieved by a reduction of the response amplitude, which will give a positive dynamic excitation coefficient.

In the following the concept of nondimensional damping will be introduced as a method for predicting the oscillation amplitude for a system with structural (external) damping. Application of the method for prediction of IL response amplitudes is shown in section 6.5.2.

Nondimensional damping

A cylinder subjected to VIV in in-line or cross flow direction can be described by the equation of motion:

$$m\ddot{x} + c\dot{x} + kx = F_{hydro}(t) \tag{6.4}$$

Where m is the dry mass of the cylinder, c is the structural damping coefficient and k is the stiffness. $F_{hydro}(t)$ is the hydrodynamic force component in IL or CF direction and x is the corresponding cylinder motion. As shown in previous chapters we have assumed that the VIV response is harmonic and takes place at resonance. We may then further assume that the hydrodynamic force is harmonic, $F_{hydro}(t) = F_{hydro,0}\sin(\omega_0 t + \phi)$. Using the known general property:

$$F_0 \sin(\omega t + \phi) = F_0 \cos(\phi)\sin(\omega t) + F_0 \sin(\phi)\cos(\omega t) \tag{6.5}$$

Eqn. (6.4) can be written as (at resonance):

$$(m + \frac{F_{hydro,0}\cos(\phi)}{x_0\omega_{osc}^2})\ddot{x} + (c - \frac{F_{hydro,0}\sin(\phi)}{x_0\omega_{osc}})\dot{x} + kx = 0 \qquad (6.6)$$

We readily identify $F_{hydro,0}\sin(\phi)$ from the definition of the dynamic excitation coefficient, C_e Eqn. (4.10), and in order to achieve a steady state situation the excitation term must balance the damping term, i.e. the oscillation amplitude is given by the amplitude where there is a balance between damping and excitation.

$$(c - \frac{F_{hydro,0}\sin(\phi)}{x_0\omega_{osc}}) = 0 \qquad (6.7)$$

Making the substitutions $F_{hydro,0}\sin(\phi) = C_e \cdot \frac{1}{2}\rho DU_0^2$, $\omega_{osc} = 2\pi U_0\hat{f}/D$ and $\frac{x_0}{D} = \frac{A}{D}$ we have:

$$c = \rho U_0 D \frac{C_e}{4\pi \frac{A}{D}\hat{f}} \qquad (6.8)$$

The nondimensional damping coefficient pr. unit length, $\hat{c}$, can now be defined as:

$$\hat{c} = \frac{c}{\rho U_0 D} = \frac{C_e}{4\pi \frac{A}{D}\hat{f}} \qquad (6.9)$$

Referring to IL oscillations (Figure 6.12) we may divide the dynamic excitation coefficient, $C_{e,IL}$, by $4\pi\frac{A}{D}\hat{f}$ and then draw contours for varying level of nondimensional damping. In other words, the oscillation amplitude is determined by the nondimensional frequency, $\hat{f}$, and the nondimensional damping, $\hat{c}$. Again, no attempt has been made to smooth the contours of Figure 6.12. Only linear interpolation has been used between the measured values.

Transformation to reduced velocity

In order to better illustrate the effect of damping, amplitude ratios for levels of nondimensional damping are shown as a function of reduced velocity in Figure 6.13 (a). The mass ratio chosen for the figure is 1.3.

In Figure 6.13 (a) the transformation to V_r is performed by choosing added mass values along the actual $\hat{c}$-contour line. These added mass values are plotted as a function of nondimensional frequency in Figure 6.13 (b). The figure shows that added mass for varying $\hat{f}$ is almost independent on $\hat{c}$ and hence also on amplitude ratio.

Nondimensional damping and the response parameter, S_G

The concept of nondimensional damping is, to the best of our knowledge, introduced for the first time in this thesis. Previously the effect of damping in VIV experiments has been evaluated by various parameters containing the product of mass ratio and relative damping, ζ. Halse [17] has given a thorough discussion on the various versions of the response parameter, and the following is based on his discussion.

Gopalkrishnan [15] proposed a simple method for estimating CF response based on the
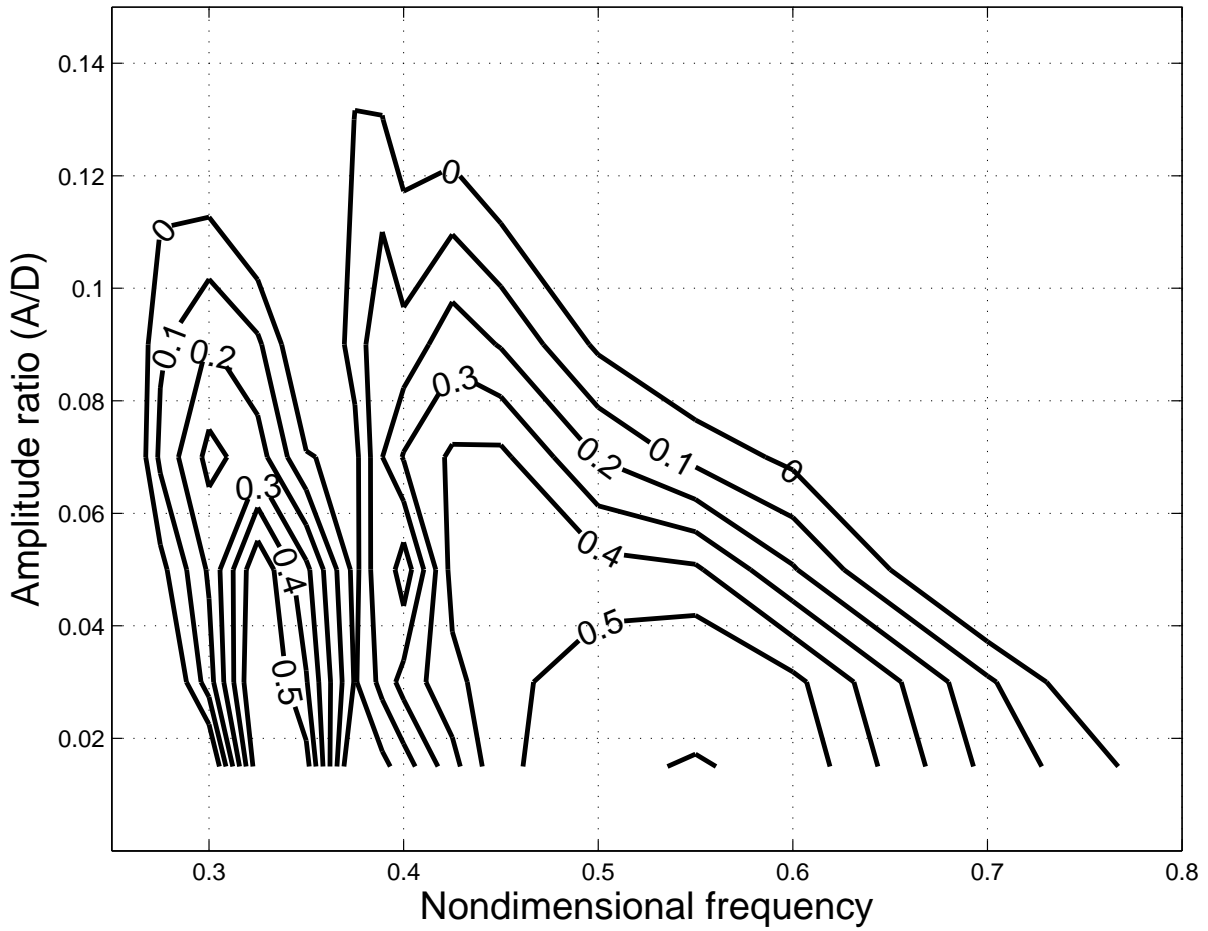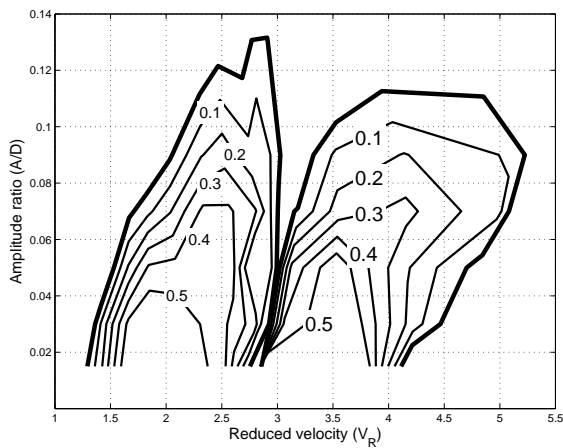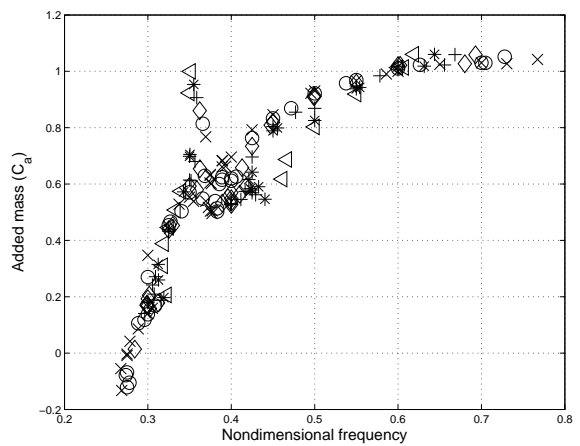
Figure 6.12: Contours of nondimensional damping, $\hat{c}$.

(a) Response amplitude as function of V_r and $\hat{c}$.

(b) Added mass, C_a, as function of $\hat{f}$ and $\hat{c}$.

Figure 6.13: (a): Similar curve as for Figure 6.12, but use of V_r instead of $\hat{f}$. The transformation from $\hat{f}$ to V_r has been performed according to Eqn. (6.1) and the C_a values used are shown in figure (b) where $\times$ represent $\hat{c} = 0$, $\circ$ for $\hat{c} = 0.1$, $\diamond$ for $\hat{c} = 0.2$, $+$ for $\hat{c} = 0.3$, $\star$ for $\hat{c} = 0.4$ and $\triangleleft$ for $\hat{c}=0.5$.

response parameter, S_G. The basic assumptions for the method was that the oscillation could be described by the equation of motion, Eqn. (6.4), and that the hydrodynamic force could be described as harmonic, Eqn. (6.5), giving a harmonic response at the same frequency (denoted ω_n which is analogous to ω_{osc} used in this thesis). For this situation the oscillation amplitude is a result of a balance between the damping and the hydrodynamic lift coefficient in phase with velocity, C_{L_V} (analogous to the dynamic excitation coefficient, $C_{e,CF}$, used in this thesis):

$$2m\zeta\omega_n\frac{dy}{dt} \Longleftrightarrow \frac{1}{2}\rho D U_0^2 C_{L\_V}\cos(\omega_n t) \tag{6.10}$$

The symbol $\Longleftrightarrow$ has been used to denote "in balance with". By substituting $y = y_n\sin(\omega_n t)$ and $\omega_n = 2\pi\hat{f}U_0/D$, canceling common terms and rearranging Gopalkrishnan ended up with the expression:

$$2\{2\pi\hat{f}^2\left(\frac{2m(2\pi\zeta)}{\rho D^2}\right)\}\frac{y_n}{D} \Longleftrightarrow C_{L\_V} \tag{6.11}$$

From Eqn. (6.11) we recognize the expression within the curly braces $\{...\}$ as the response parameter S_G (used by among others Gopalkrishnan, Sarpkaya and Griffin) and the expression within the "normal" braces $(...)$ as the stability parameter K_S, or Scruton number, used by e.g. Blevins and DNV. We also recognize the ratio $\frac{m}{\rho D^2}\zeta$ know as the mass damping parameter.

By substituting $\hat{f} = \frac{\omega_n D}{2\pi U_0}$ and $c = 2m\zeta\omega_n$ in the expression for S_G we get the expression published by Vandiver [58].

$$S_G = \frac{c\omega_n}{\rho U_0^2} \tag{6.12}$$

Vandiver used this expression to show that S_G is independent of mass and that the parameter is a statement of dynamic equilibrium between the average energy input injected into the oscillating system by the fluid through lift force, and the energy dissipated by damping. This is the same reasoning used when defining the nondimensional damping parameter, and by using Eqn. (6.12) in Gopalkrishnans expression we have:

$$2\{S_G\}\frac{y_n}{D} \Longleftrightarrow C_{L\_V} \tag{6.13}$$

Substituting $\omega_n = 2\pi\frac{\hat{f}U_0}{D}$ and rearranging we get

$$\frac{c}{\rho U_0 D} \Longleftrightarrow \frac{C_{L\_V}}{4\pi\hat{f}\frac{y_n}{D}} \tag{6.14}$$

Which again is the definition of the nondimensional damping.

As seen from the discussion above, the nondimensional damping is essentially the same as the stability parameter, S_G. Given the large number of nondimensional parameters related to VIV it is not desirable to introduce new ones. We have, however, chosen to introduce the nondimensional damping in order to emphasize that variation of damping and mass ratio causes different effects as pointed out in this chapter. Also, the fact that

S_G traditionally has been associated with mass ratio justifies the replacement. As pointed out by Vandiver [58]: *"The common erroneous conclusion is that low-density cables, hence cables with small mass ratio, are likely to respond more than high density ones"*.

Relationships between the nondimensional damping parameter and the most frequently used parameters describing damping in VIV experiments are summarized in the expressions below.

Response parameter, S_G:

$$\hat{c} = \frac{S_G}{2\pi\hat{f}} \tag{6.15}$$

Mass-damping parameter, $\bar{m}\zeta$:

$$\hat{c} = (\bar{m} + C_a)\zeta \cdot \pi^2\hat{f} \tag{6.16}$$

Stability parameter, K_s, as defined in DNV-OS-F105 [10]:

$$\hat{c} = K_s\hat{f} \tag{6.17}$$

Vandiver [59] has introduced a variation of the S_G parameter given in Eqn. 6.12 named S_u, universal reduced damping parameter. This parameter can be used for both uniform and non-uniform flow conditions, and the parameter is intended to be used to estimate modal response of flexible beams.

Nondimensional damping and Reynolds number

There has been an ongoing discussion on the importance of Reynolds number in VIV experiments, i.e. which Reynolds number is sufficient in experiments for capturing the effect of VIV of a full scale free spanning pipeline or riser. It is seen from the definition of the nondimensional damping, see Eqn. (6.9), that it contains the inverse of the product $U_0 D$ which is also included in the definition of the Reynolds number. Substituting $\nu = \frac{\mu}{\rho}$, where μ is the viscosity and ν the kinematic viscosity, the nondimensional damping can be written as:

$$\hat{c} = \frac{c}{\rho U_0 D} = \frac{c}{Re}\mu \tag{6.18}$$

As seen from Eqn. (6.18) it can be very easy to interpret a reduced oscillation amplitude caused by damping as a Reynolds number effect. Also, it is seen that the importance of damping inherent in the experimental apparatus is much higher for low Reynolds numbers than for higher values.

Nondimensional damping in free vibration experiments

The nondimensional damping parameters importance for the response amplitude is clearly shown for the pure IL regime in Figure 6.12. When performing free vibration experiments

it is hence important to keep this in mind when the results are interpreted and applied for prediction of VIV for full scale risers and free spanning pipelines. For instance, when performing free vibration tests in a water tunnel it is common to select a fixed spring stiffness, giving the desired eigenfrequency, and then increase the current speed to cover the desired region of reduced velocities, V_r. Assuming that the structural damping is close to constant over the tested range of frequencies and amplitudes, the oscillation amplitudes measured will represent different levels of nondimensional damping. High values of nondimensional damping for low reduced velocity results and lower values for the high reduced velocity results.

When free vibration experiments are used to investigate the effect of Reynolds number, the same experimental setup will typically be used for various flow velocities. For the tests performed the damping level in still water will be the same, but the nondimensional damping will be reduced for increasing Re. An increased response amplitude observed in such experiments may then be interpreted as a Re effect. However, the increased response may actually be caused by a reduced effect of the structural damping in the apparatus. The effect of Re in VIV experiments has also been discussed in section 2.3.4.

6.2.5   Response amplitude of a flexible beam

As discussed in section 2.3.4 the maximum response amplitude of a flexible beam is expected to be larger than the maximum response amplitude given by an elastically mounted rigid cylinder experiment.

The concept of nondimensional damping and the assumption that strip theory is valid may be used to estimate the maximum response amplitude of a flexible beam. For a given mode shape, Φ, the modal nondimensional damping coefficient is given by Eqn. (6.19).

$$\hat{c}_{modal,IL} = \frac{\int_0^L \hat{c}_{IL}(y)\Phi_{IL}^2(y)\ dy}{\int_0^L \Phi_{IL}^2(y)\ dy} \tag{6.19}$$

For each position along the length of a flexible beam the oscillation amplitude is given by the maximum response amplitude and the mode shape. For a given mode shape and oscillation frequency, $\hat{c}_{modal,IL}$ may be calculated for given values of maximum response amplitude. To demonstrate the effect, the mode shape of a pinned-pinned beam is assumed ($\Phi = (\frac{A}{D})_{max}\sin(\pi\frac{y}{L})$). Modal values of nondimensional damping are calculated for $(\frac{A}{D})_{max}$ from 0.02 to 0.16, and for nondimensional frequency values between 0.25 and 0.80. The results are presented as contours in Figure 6.14.

It is seen that the shapes of the contours in Figure 6.14 are similar to those in Figure 6.12, but the amplitudes are increased.

The ratio between maximum response amplitude of a flexible beam and that of a rigid cylinder is know as the geometric shape factor, or γ-factor (see section 2.3.4). Figure 6.15 shows the geometric shape factor as a function of nondimensional frequency for nondimensional damping values from 0 to 0.3.
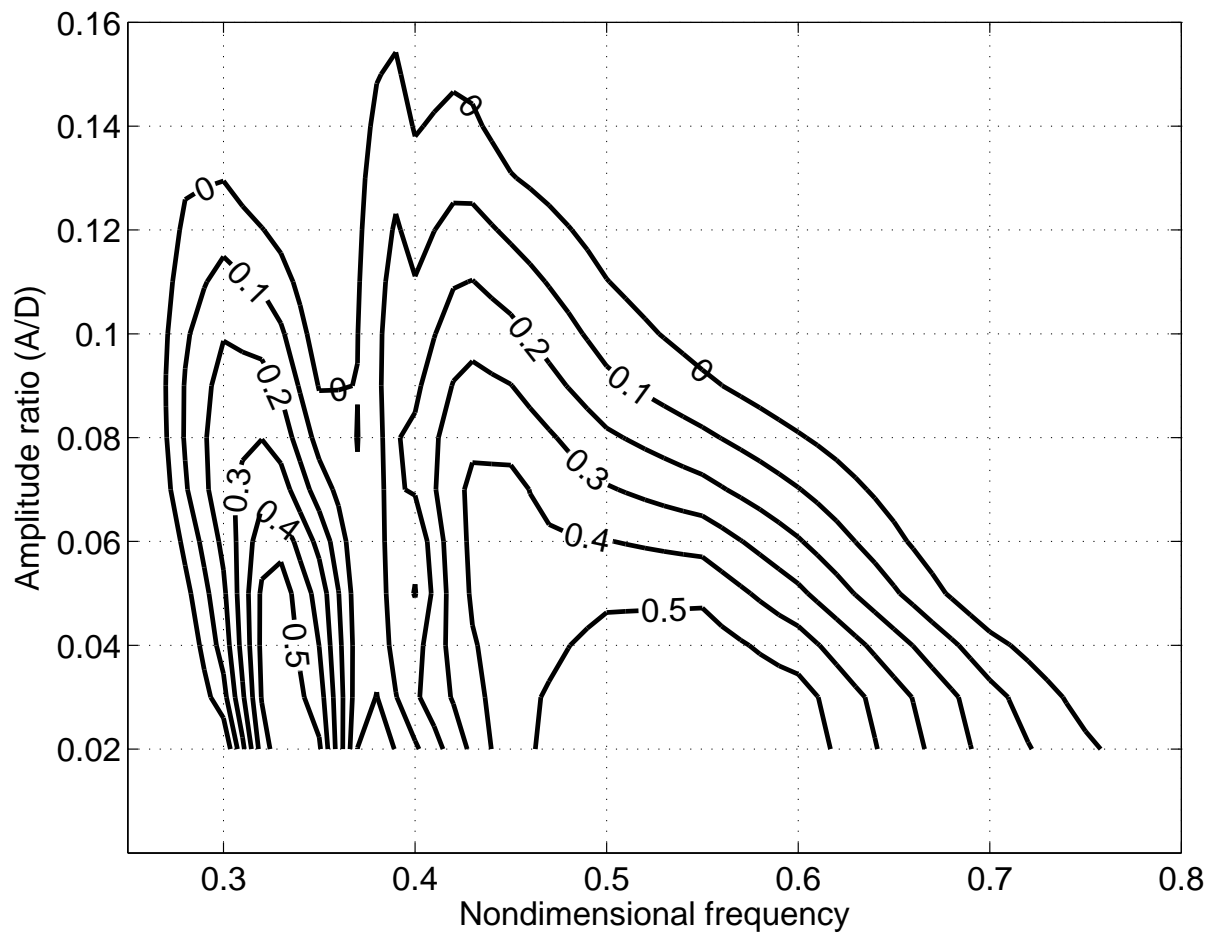
Figure 6.14: Modal $\hat{c}$ values for a pinned-pinned beam. Amplitude ratio (y-axis) refers to maximum amplitude ratio at midspan.
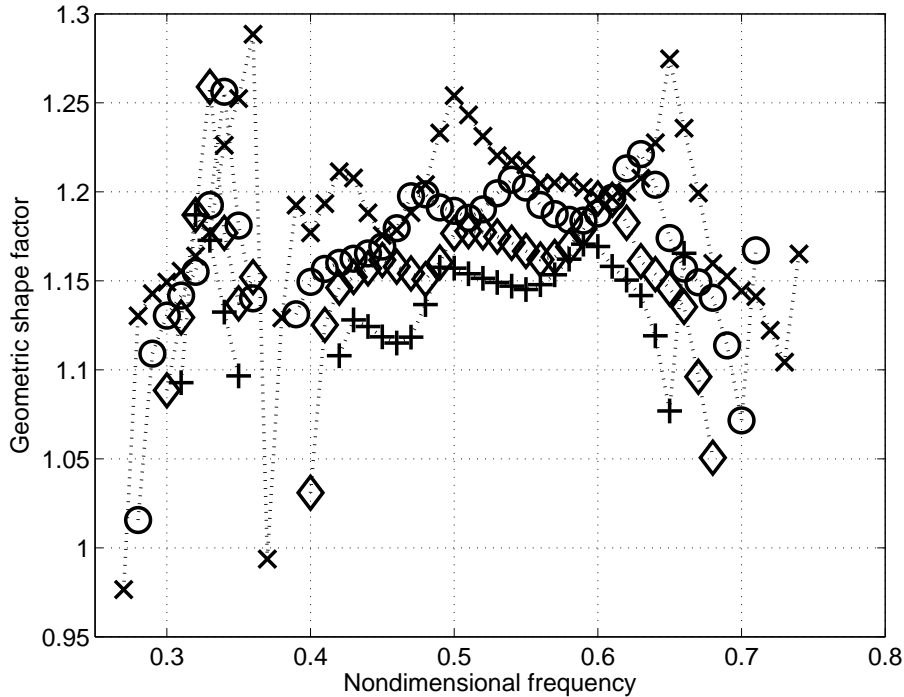
Figure 6.15: Geometric shape factor for a flexible beam with pinned - pinned boundary conditions. $\times$ represent $\hat{c} = 0$, $\circ$ represent $\hat{c} = 0.1$, $\diamond$ represent $\hat{c} = 0.2$ and $+$ represent $\hat{c} = 0.3$.

For a beam with pinned-pinned boundary conditions, Reid [42] has proposed a geometric shape factor of 1.18 for IL VIV. For this mode shape Blevins [5] has proposed a geometric shape factor of 1.16, but this factor is based on a hydrodynamic load model valid for CF direction. Figure 6.15 shows that one single factor will not cover all conditions, but values similar to the previously published factors are seen. The figure shows that for most frequencies an increased $\hat{c}$ level will reduce the geometric shape factor.

In order to use the contours of Figure 6.14 for predicting response amplitude, a modal structural damping coefficient for the given flexible beam is required. This coefficient must be established from a damping analysis.

6.3   Oscillating force in CF direction

This section addresses the forces measured in CF direction, when oscillating the cylinder in IL direction. The objective is to show that there are significant CF force components at 0.5 and 1.5 times the IL oscillation frequency. These force components may excite response in CF direction, both at $\omega_{CF} = 0.5\omega_{IL}$ and at a higher order harmonic frequency.

6.3.1   CF force components

In Figure 6.16 (a) contours of the $C_{rms,CF}$ coefficient are shown. The value of $C_{rms,CF}$ obtained from the stationary cylinder cases was approximately 0.6, and we readily see that
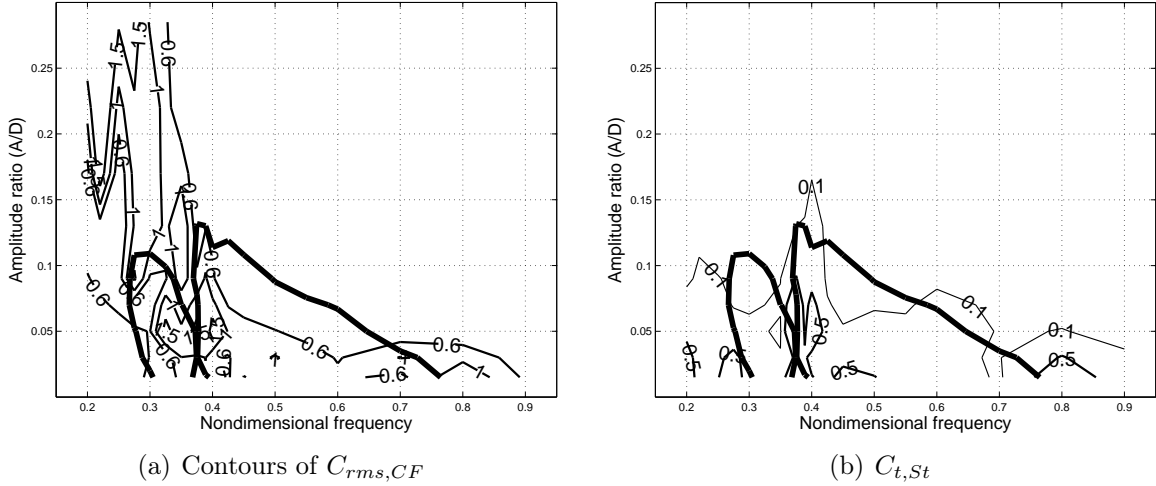
(a) Contours of $C_{rms,CF}$

(b) $C_{t,St}$

Figure 6.16: Figure a shows contours of the $C_{rms,CF}$ coefficient during forced IL oscillations. The $C_{rms,CF}$ value for the stationary cylinder tests was 0.6. Figure b shows the oscillating force in CF direction at the Strouhal frequency. Stationary cylinder value is 0.5. The two instability regions are indicated by the thick black line.

IL oscillations influence the oscillating force in CF direction. The $C_{rms,CF}$ values are increased in the 2nd instability region and reduced in the 1st instability region, compared to the stationary cylinder results. Comparing Figure 6.16 (a) with the contours of the drag coefficient, see Figure 6.6, it is evident that there is a correlation between the oscillating force in CF direction and drag force. In Figure 6.16 (b) contours of the force coefficient at the Strouhal frequency, $C_{t,St}$, is shown. The $C_{t,St}$ value for the stationary cylinder cases was approximately 0.5, and it is seen from Figure 6.16 (b) that $C_{t,St}$ for the IL oscillation cases only exceeds this value in the close region of where $\hat{f}_{IL}$ is two times the Strouhal number. This indicates that the CF force frequency locks on to the IL oscillation frequency, i.e. a wake capture phenomenon. In order to investigate this further the power spectra of the CF hydrodynamic force for one case in the 1st and one case in the 2nd instability region are inspected, see Figure 6.17.

The spectral density peaks in Figure 6.17 show forces at 0.5 and 1.5 times the IL oscillation frequency for the second instability region. The case shown for the first instability region is at the boarder line of where increased $C_{rms,CF}$ is seen. The spectrum (Figure. 6.17 (a)) shows that the frequency band of the force components are wider than for the 2nd instability region case. The total dynamic force coefficient for the two frequency components $0.5 \cdot f_{osc,IL}$ and $1.5 \cdot f_{osc,IL}$ is shown as contours in Figure 6.18.

For the second instability region, Figure 6.18 shows total dynamic force coefficient values (Eqn. (4.12)) of up to 1 at frequency 0.5 times the IL oscillation frequency and 0.5 at a frequency of 1.5 times the IL oscillation frequency. $C_{t,IL}$ values for the second instability region are in the region of 0.1-0.3, see Figure 6.7.
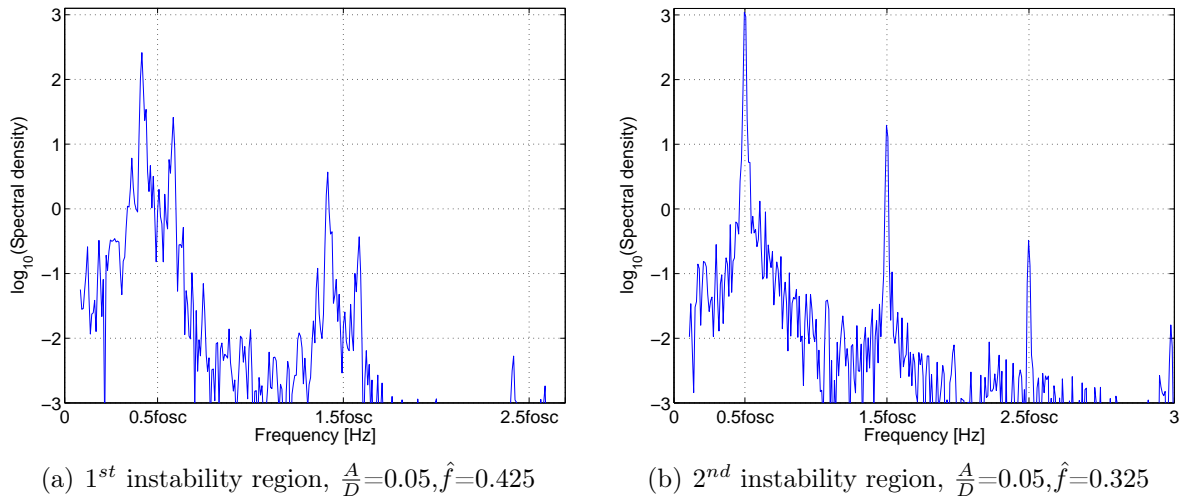
(a) 1st instability region, $\frac{A}{D}=0.05, \hat{f}=0.425$

(b) 2nd instability region, $\frac{A}{D}=0.05, \hat{f}=0.325$

Figure 6.17: Power spectrum of CF hydrodynamic force. f_{osc} is the oscillation frequency in IL direction.
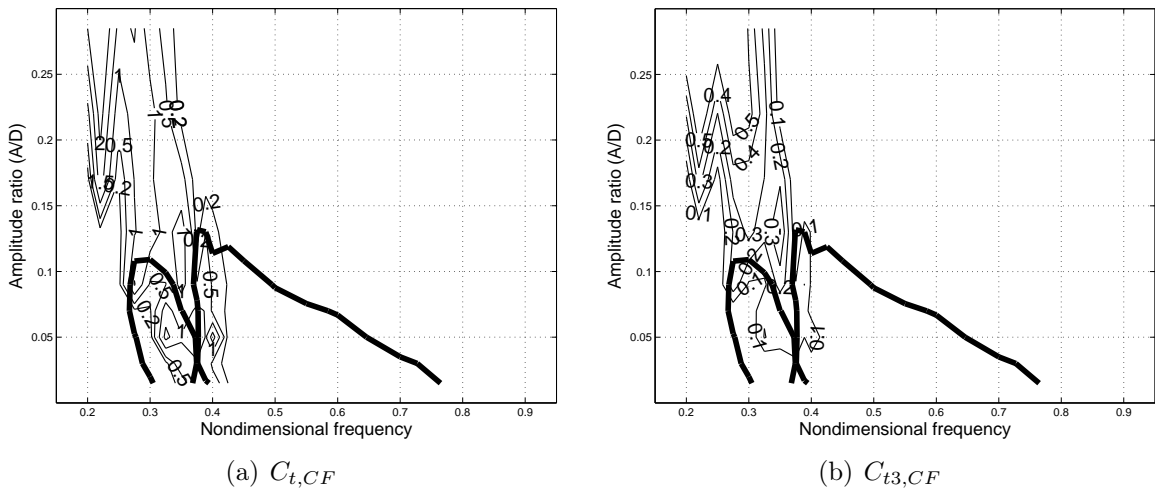

(a) $C_{t,CF}$

(b) $C_{t3,CF}$

Figure 6.18: Figure a shows contours of the $C_{t,CF}$ coefficient, forces at 0.5 times the IL oscillation frequency. Figure b shows contours of oscillating CF forces at 1.5 times the IL oscillation frequency, $C_{t3,CF}$. The two instability regions are indicated by the thick black line.

6.3.2 CF results as function of reduced velocity

In this section force components in CF direction are shown as a function of reduced velocity, V_r. The reduced velocity is calculated by the method described in section 6.2.3, and relates as such to an eigenfrequency in IL direction. For a free spanning pipeline of low mass- and L/D ratio, the first eigenfrequency in CF direction will be very similar to the first eigenfrequency in IL direction. E.g. for the flexible beam experiment presented in Figure 1.1, the first eigenfrequency in the two directions are almost identical.

CF forces at 0.5 and 1.5 times the IL oscillation frequency are shown as a function of reduced velocity in Figure 6.19 (a) and Figure 6.20 respectively. The values presented are taken along the $C_{e,IL} = 0$ lines for the 1st and 2nd instability region as shown in Figure 6.11 (b). Both figures show significant force components in the second instability region. Keeping in mind that the total dynamic force coefficient in IL direction ($C_{t,IL}$) for the second instability region is approximately 0.1-0.3, significant CF forces at both frequencies are also seen in the first instability region.

Figure 6.19 (b) shows the frequency of the CF force component $C_{t,CF}$, relative to the IL eigenfrequency in still water. Included in the figure is also the Strouhal frequency relative to the IL eigenfrequency. Figure 6.19 shows the two instability regions, 1st and 2nd, as separate curves in (a), while in (b) the two regions are divided by the point where the line representing the Strouhal frequency crosses the curves representing the force frequency. It is clearly seen that there are CF forces also in the 1st instability region. In IL direction response is observed when the forcing frequency, i.e. $2f_s$, is 0.5 times the eigenfrequency in still water. For conditions where the eigenfrequencies in the two directions are equal, the figure shows that once the CF forces occur the ratio between the forcing frequency and the eigenfrequency is at least 0.5.

These forces may explain why CF response occur at a lower reduced velocity in experiments where the cylinder is allowed to oscillate in both IL and CF direction, compared to experiments where IL motions are restricted. Also, it may explain why the drop in response amplitude between the first- and second IL instability region is not seen in flexible beam experiments (CF vibrations are present). It could hence be correct to talk about an IL induced CF vibration.

6.3.3 CF correlation

Figure 6.21 (a) shows the correlation coefficient based on the CF forces measured at the two ends of the cylinder for two frequencies, $\hat{f}$=0.325 and $\hat{f}$=0.425. In Figure 6.21 (c) the total dynamic force coefficient at 0.5 times the IL oscillation frequency is shown. The amplification of CF forces in the 2nd instability region (line with $\times$ markers) is easily seen from the figure. Comparing Figure 6.21 (c) with the correlation coefficient it is seen that the correlation is very high for the high CF forces, indicating that there is a fully developed vortex shedding mode over the length of the cylinder. The result for amplitude ratio 0.09 ($\hat{f}$=0.325) does however stand out as the correlation coefficient changes sign (-0.7) and the CF force drops. Looking at Figure 6.21 (d) it is seen that this case $((A/D)_{IL} = 0.09)$ is on the border line of the IL excitation region, i.e. $C_{e,IL}$ close to zero. There is however
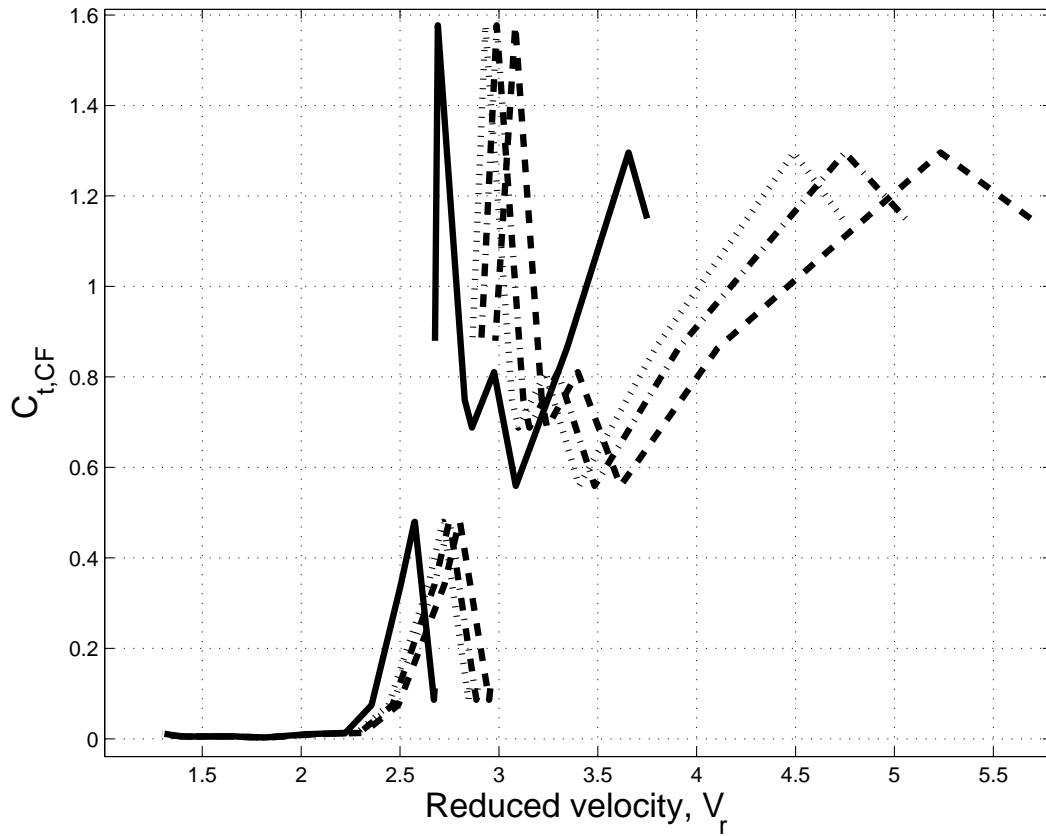
(a) $C_{t,CF}$
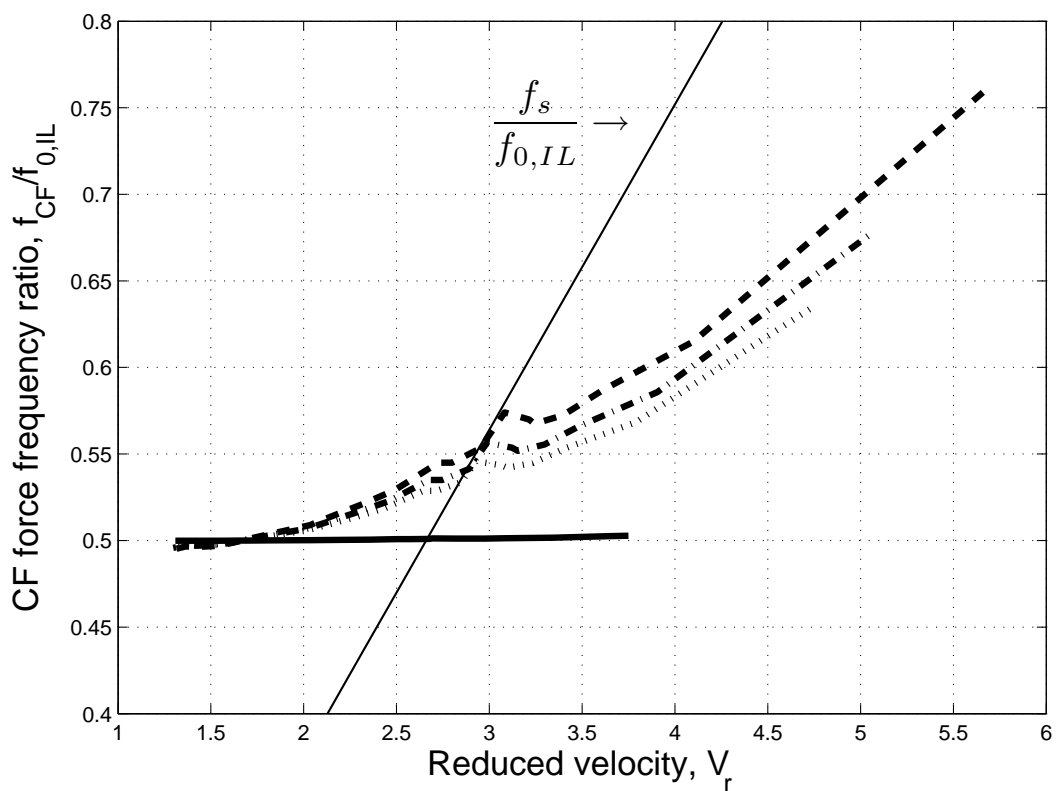
(b) Frequency ratio

Figure 6.19: Figure (a) shows the amplitude ratio (given by the $C_{e,IL} = 0$ contour) and figure (b) shows the frequency ratio as a function of reduced velocity for four mass ratios. Solid line: $\bar{m} = 100$; Dotted line (..): $\bar{m} = 2$; Dashdot line (-.-.): $\bar{m} = 1.5$; Dashed line (--): $\bar{m} = 1.0$.
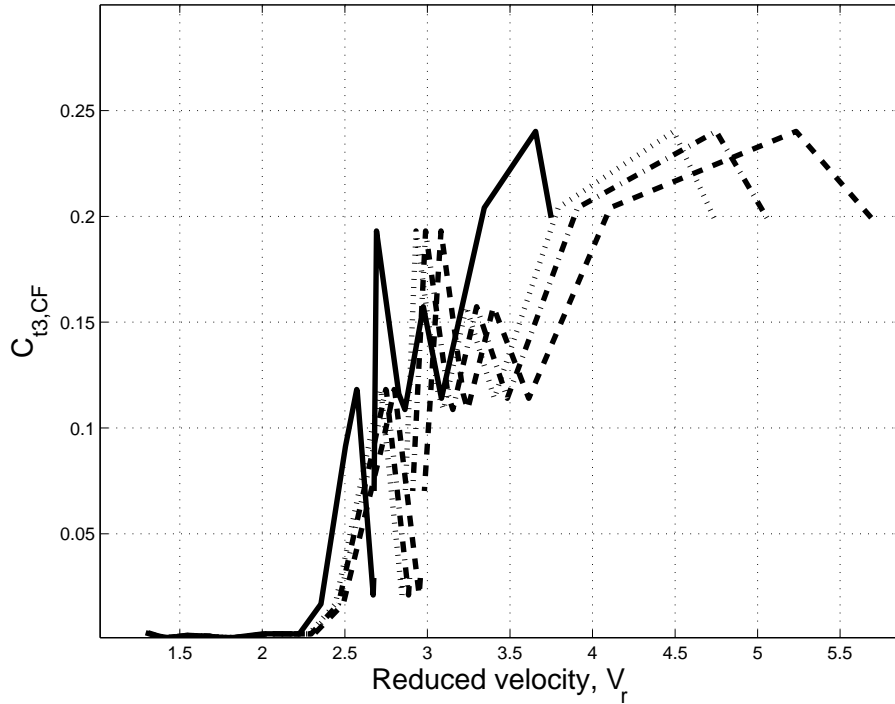
Figure 6.20: Total dynamic force coefficients at 1.5 times the IL oscillation frequency. Values taken along the $C_{e,IL} = 0$ lines for the 1st and 2nd instability region as shown in (6.18b). Solid line: $\bar{m} = 100$; Dotted line (..): $\bar{m} = 2$; Dashdot line (-.-.): $\bar{m} = 1.5$; Dashed line (- -): $\bar{m} = 1.0$.

no drop in correlation in IL direction as shown in 6.21 (b) and due to problems with the apparatus for the first two experimental phases there are no other relevant cases available to further investigate the observation.

6.4 Validation

In this section the reliability of the IL results is discussed. The section is divided into three parts where the first part discusses the main results from the error analysis presented in chapter 5. In the second part results for some cases performed for a Reynolds number of $1.0 \cdot 10^4$ are compared with the Re=$2.4 \cdot 10^4$ results in order to get some idea of how sensitive the results are with respect to Re. In the last part of this section the results are compared with free vibration results found in the literature.

A very important part of the quality control was the daily routines in the lab. All experiments and calibrations were performed by the author and care was taken for each experimental run to be performed according to specifications. An important part of the data processing quality control was the result sheets that were produced for each case, see Appendix B. In the first sheet intermediate results are presented in order to select the appropriate steady state region and verify that the filter limits are doing its job. The "final result" sheet, see Figure B.2, is used to verify that stable values for the hydrodynamic coefficients are achieved. In the error analysis result sheet, see Figure B.3, the importance
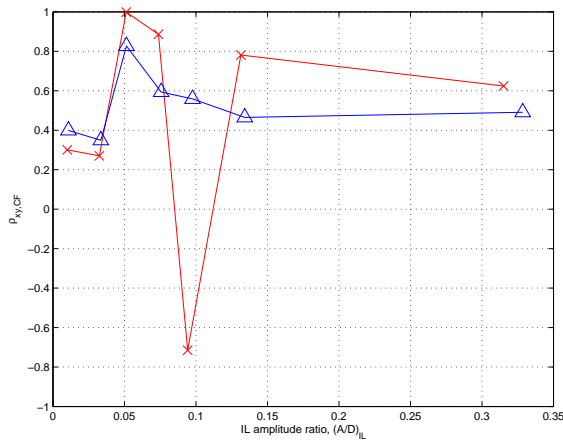
(a) Correlation coefficient CF, $\rho_{xy,CF}$
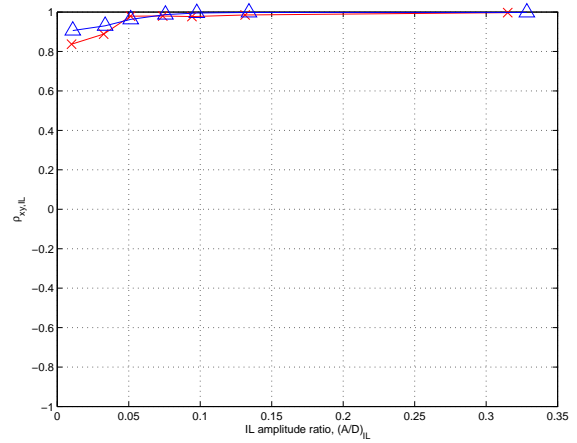
(b) Correlation coefficient IL, $\rho_{xy,IL}$
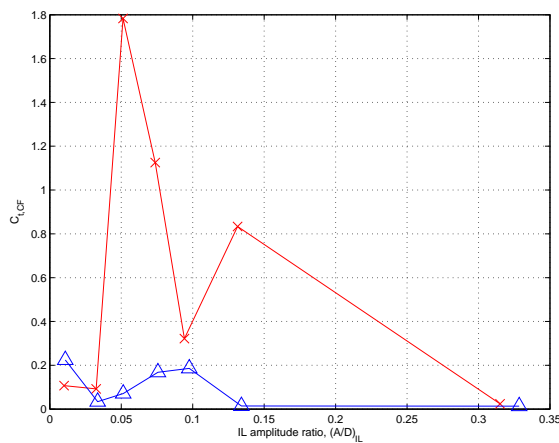
(c) $C_{t,CF}$
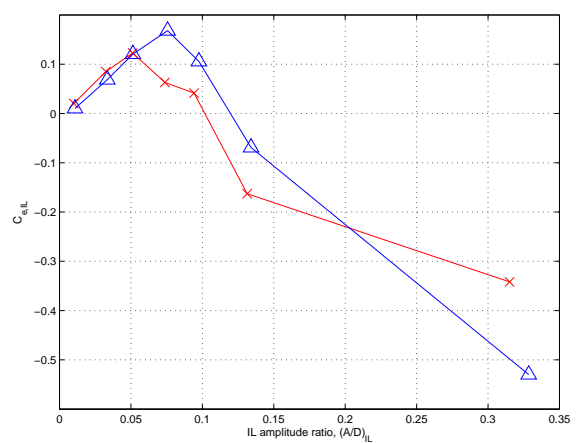
(d) $C_{e,IL}$

Figure 6.21: Correlation coefficient, as defined by Eqn. (4.17), for CF and IL direction in figure a and b respectively. Figure c shows the total dynamic force coefficient for a frequency of 0.5 times the IL oscillation frequency. Figure d shows the dynamic excitation coefficient. The results are plotted as function of IL oscillation amplitude ratio. $\times$ represents result for $\hat{f}$=0.325 and $\triangle$ for $\hat{f}$=0.425.

of the various error sources is seen.

6.4.1 Uncertainty

The methodology used for estimating the 95% confidence interval of the hydrodynamic coefficients is presented in chapter 5. Performing the error analysis proved to be important for understanding the possible errors in the experiments and also for gaining confidence in the results. Due to the large number of cases performed for the IL VIV investigation, it is not feasible to report detailed results from the error analysis for each case. The uncertainty analysis results are therefore presented as a summary where the important factors for the three hydrodynamic coefficients, C_D, $C_{e,IL}$ and $C_{a,IL}$, are discussed. Then repeated cases, 2nd order replication, is presented to investigate the repeatability and also whether the uncertainty analysis can capture the real uncertainties. The results from three frequencies performed in Phase I were repeated in Phase II. These are compared, and the bias errors from force sensor and accelerometer calibration are addressed. For Phase I and II the force sensors at one end of the cylinder did not work properly. The results from both ends are hence compared only for tests performed in Phase III.

Error analysis

Drag coefficient, C_D. For the drag coefficient the error in cylinder dimensions (L and D) and water density (ρ) is negligible. The important contributions to the bias error is error in tow velocity and error in calibration of the IL force sensors. A bias error of 1% is assumed for the tow velocity, see section 5.4.3, and as seen from the data reduction equation, Eqn. (5.7), this will lead to a 2% error in the result. The bias error in the force calibration factor is given in Table 5.3 and is between 1.5 and 2.7% at starboard side for the various experimental phases. The bias error at port side, Phase III, is 5.8%. The main contribution to the precision error for the drag coefficient is the variation in mean value from the individual zero up-crossing periods as described in section 5.4.4. A histogram of the precision error relative to the drag coefficient is shown in Figure 6.4.1.

Dynamic excitation coefficient, $C_{e,IL}$. Also for the dynamic excitation coefficient the error in dimensions and water density give negligible contribution to the total error. The dynamic excitation coefficient describes the energy transfer between the fluid and the cylinder. Thus, the sign of the coefficient represents the direction of the energy transfer. As seen from the presentation of the IL results in earlier sections of this chapter, the oscillation amplitude where the dynamic excitation coefficient changes sign is one of the important findings from the experiments. These amplitudes define the boundary of the excitation region. At the point where the coefficient changes sign the force in phase with velocity is zero. It is seen from the influence coefficient of the tow velocity, Eqn. (5.13), that this approaches zero as the force approaches zero. The bias error of the tow velocity is proportional to the force and is hence important for the magnitude of the dynamic excitation coefficient, but not for the error in the phase of the force and hence not important for the boundary of the excitation region (the $C_{e,IL} = 0$ contour). The error in the decomposed force, $F_0 \sin(\phi)$, is discussed in section 5.4.5. As for the error in tow velocity, the bias error from calibration of the force sensors is important for the magnitude of the dynamic excitation coefficient, but not for the phase of the force and thus not for the sign of the
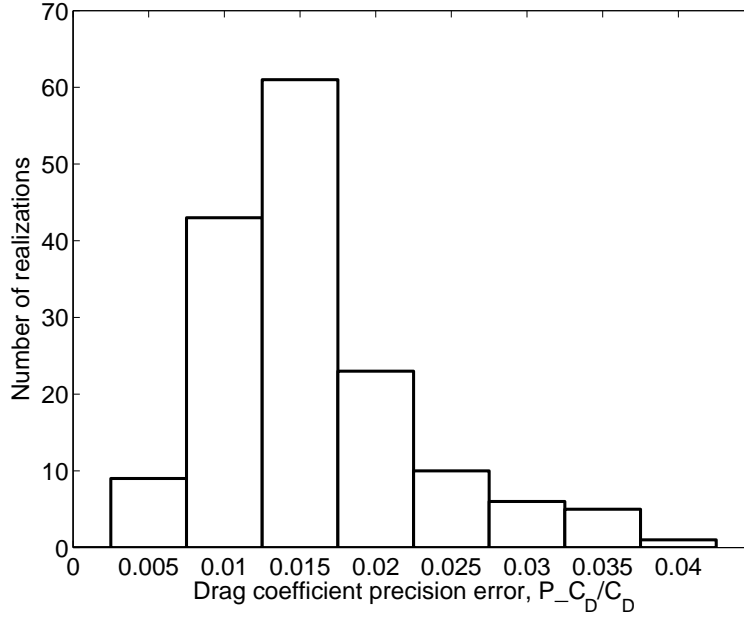
Figure 6.22: Histogram of estimated precision error relative to drag coefficient, $\frac{P\_C_D}{\bar{C}_D}$.

coefficient. The error due to cross-talk is found to be negligible for these experiments, and the estimated phase error due to cross-talk and FFT filtering of the acceleration signal is 0.04deg, see 5.4.5. Hence, there is a marginal contribution from cross-talk to the total error for cases where the phase angle is close to zero. The main contribution to the precision error is the numerical error from data processing. The precision and bias errors estimated for $C_{e,IL}$ are shown in Figure 6.23 (a) and the figure indicates a precision error for the $C_{e,IL} = 0$ region of less than 0.02. In Figure 6.23 (b) the contours for $C_{e,IL} = -0.015$ and $C_{e,IL} = 0.015$ are shown to indicate an error band for the estimated zero contour $C_{e,IL} = 0$. The bias error is approximately 4% of $C_{e,IL}$.

Added mass coefficient, $C_{a,IL}$.
The error analysis shows that the added mass coefficients for the lowest amplitude ratios in the test matrix (A/D=0.01) are too unreliable to be included in the results. The data reduction equation for the estimation of uncertainty in the added mass coefficient is given in Eqn. (5.14), and the calculated bias and precision errors are shown in Figure 6.24. The figure shows that the bias error is a function of the added mass value and the trend is indicated by two black lines. The two lines represent the results from Phase I and Phase III where the relative bias error (B_{C_a}/C_a) is higher for Phase I (approximately 4%) compared with Phase III (approximately 1.8%). The main contribution to the bias error is error in the force calibration coefficient, see table 5.4, and error in accelerometer calibration coefficient, see table 5.6. The tables show that the error in both calibration coefficients is higher for Phase I. It is seen that the bias error is not zero for zero added mass due to a bias error in cylinder mass and cross-talk. The relative error in mass is larger for the smaller cylinder, Phase III. The bias error is expected to increase for increasing negative values of the added mass and it is not clear why this is not the case. The bias errors in dimensions and water density are found negligible.

(a) $B_{C_{e,IL}}$ and $P_{C_{e,IL}}$ vs. $C_{e,IL}$

(b) Zero contour boundary
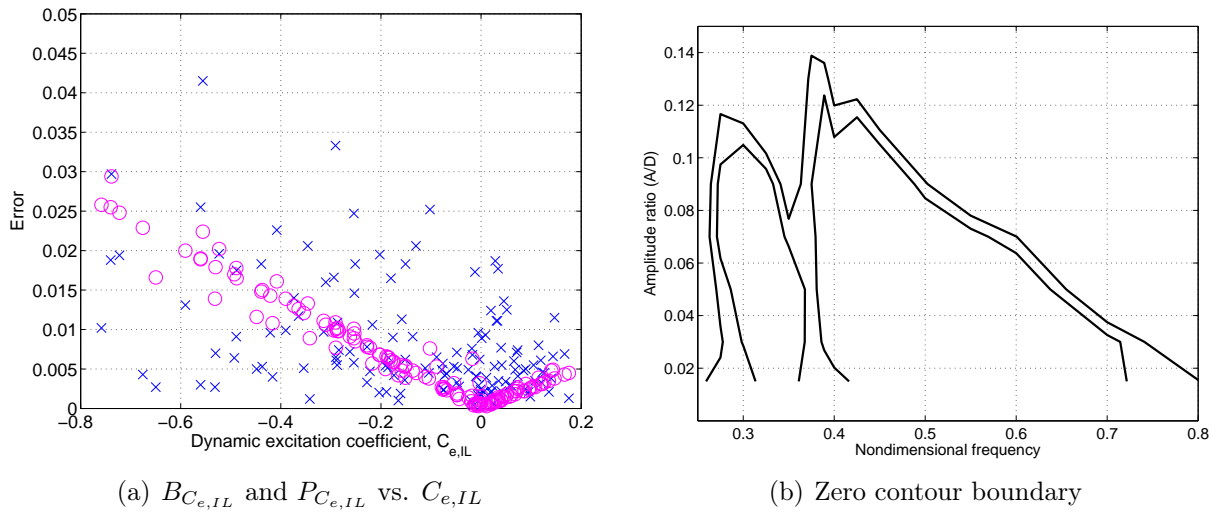
Figure 6.23: (a) shows estimated errors for the dynamic excitation coefficient, $C_{e,IL}$. $\times$ indicate precision error, P_{C_a}, and $\circ$ indicate bias error, B_{C_a}. Figure (b) shows the zero contour for an error in $C_{e,IL}$ of $\pm\,0.015$.

(a) B_{C_a} and P_{C_a} vs. C_a
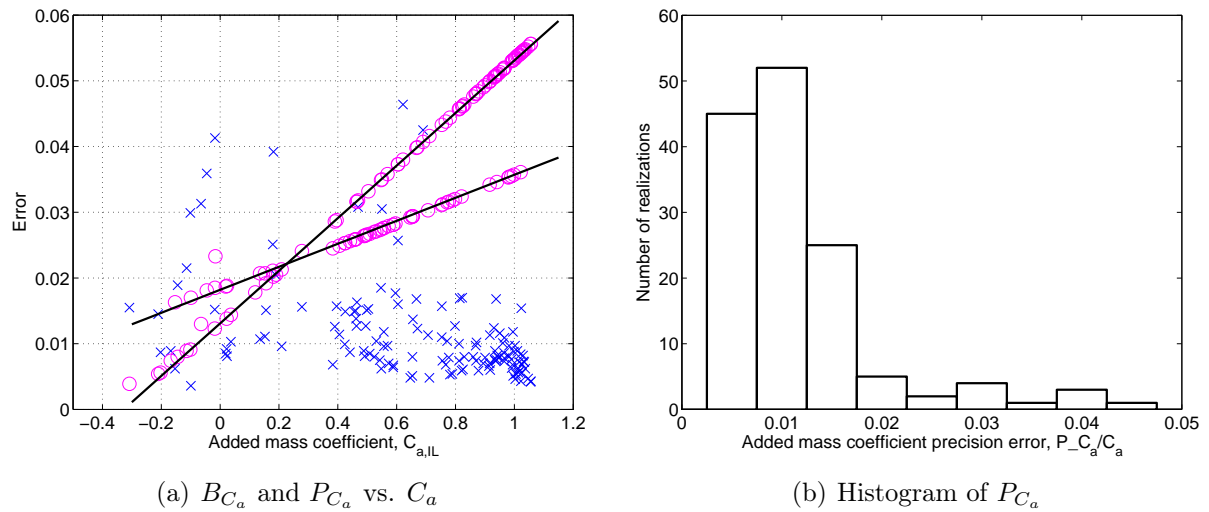
(b) Histogram of P_{C_a}

Figure 6.24: Estimated errors for the added mass coefficient, $C_{a,IL}$. In Figure a: $\times$ indicate precision error, P_{C_a}, and $\circ$ indicate bias error, B_{C_a}.

(a) Drag coefficient, C_D

(b) Dynamic excitation coefficient, $C_{e,IL}$

(c) Added mass coefficient, $C_{a,IL}$
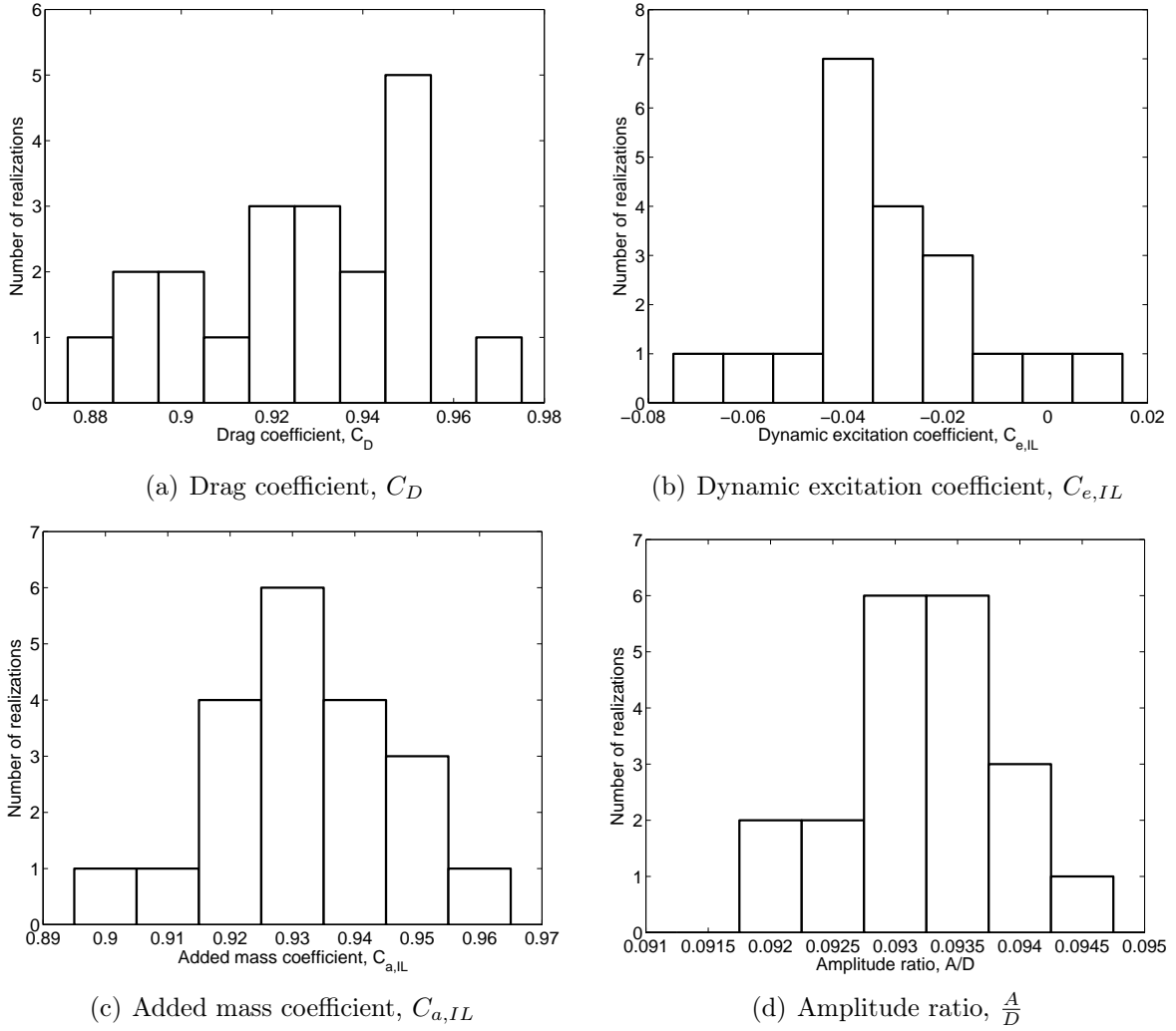

(d) Amplitude ratio, $\frac{A}{D}$

Figure 6.25: Histograms of results for case $\hat{f} = 0.5$, $\frac{A}{D} = 0.09$.

In general the highest precision errors are seen for the low frequency - low amplitude cases. Numerical error and precision error in acceleration amplitude contribute to the reported precision error. A histogram of the precision error is shown in Figure 6.24 (b). The estimated precision error for two cases of nondimensional frequency 0.2 exceeds the scale of Figure 6.24 (a) and are not considered in the discussion as they are taken as outliers.

Repeatability

Over the course of Phase I, case (A/D)=0.09 and $\hat{f}$=0.5 was repeated 20 times. The results for drag coefficient, dynamic excitation coefficient, added mass coefficient and measured amplitude ratio are presented as histograms in Figure 6.25. In Table 6.2 the mean values and standard deviations, based on these 20 repetitions, are compared with the nominal value and precision error estimated from a single case (the one used in the result matrix). As the experimental setup is the same for all repetitions, the results represent an estimate of the actual precision error of the coefficients. The bias errors are the same for all 21 cases.

Table 6.2: Results from repeatability investigation, Phase I.

	C_D	$C_{e,IL}$	$C_{a,IL}$	$\frac{A}{D}$
mean	0.927	-0.033	0.932	0.093
std	0.025	0.018	0.014	0.001
Nominal	0.932	-0.025	0.931	0.093
Precision	0.012	0.005	0.012	0.001

Table 6.3: Results from repeatability investigation, Phase II.

	C_D	$C_{e,IL}$	$C_{a,IL}$	$\frac{A}{D}$
mean	0.863	-0.060	0.923	0.092
std	0.019	0.008	0.014	0.001

Table 6.2 confirms that the precision error of the measured oscillation amplitude is small. The added mass coefficient for the selected case is approximately 0.9, and Figure 6.24 (a) shows that the precision error is expected to be low. This is confirmed by the standard deviation of the 20 cases, even though the repetitions gave a 95% confidence interval of $\pm$0.028 (P=2S) compared with the $\pm$0.012 found from the error analysis. For the drag coefficient and especially the dynamic excitation coefficient the error analysis underestimates the precision error. By inspecting the evolution of the hydrodynamic coefficients during one test run (an example is shown in Figure B.2), it is seen that for several of the tests a stationary value is not reached. This indicates that the length of the towing tank is not sufficient even though the number of oscillation periods in the steady state region is approximately 65. The method for estimating precision error, used in the error analysis, is based on the assumption that stationary condition is obtained for all tests.

Higher order replication

Tests for three nondimensional frequencies, $\hat{f}$, (0.35, 0.5 and 0.7) were repeated in Phase II. The cylinder diameter was reduced from 15cm to 10cm and all the calibrations were redone. This represents a higher order replication level, and by comparing these results with the results from Phase I the bias error estimated in the error analysis can be investigated. The results from Phase II are compared with Phase I in Figure 6.26. The case used for investigating the precision error (A/D=0.09, $\hat{f}$=0.5) was also repeated in Phase II. In total 10 repetitions were carried out and the results are summarized in Table 6.3.

In Figure 6.26 it is seen that there is a large discrepancy in drag coefficient for the $\hat{f}$=0.35 case at A/D=0.13 and 0.17. From Figure 6.5 it is seen that these two cases are at the border of the drag amplification region. The stationary cylinder tests show that there is a small deviation between the Strouhal number obtained for the two cylinder diameters. The results indicate that this small difference cause the Phase II results to be outside the
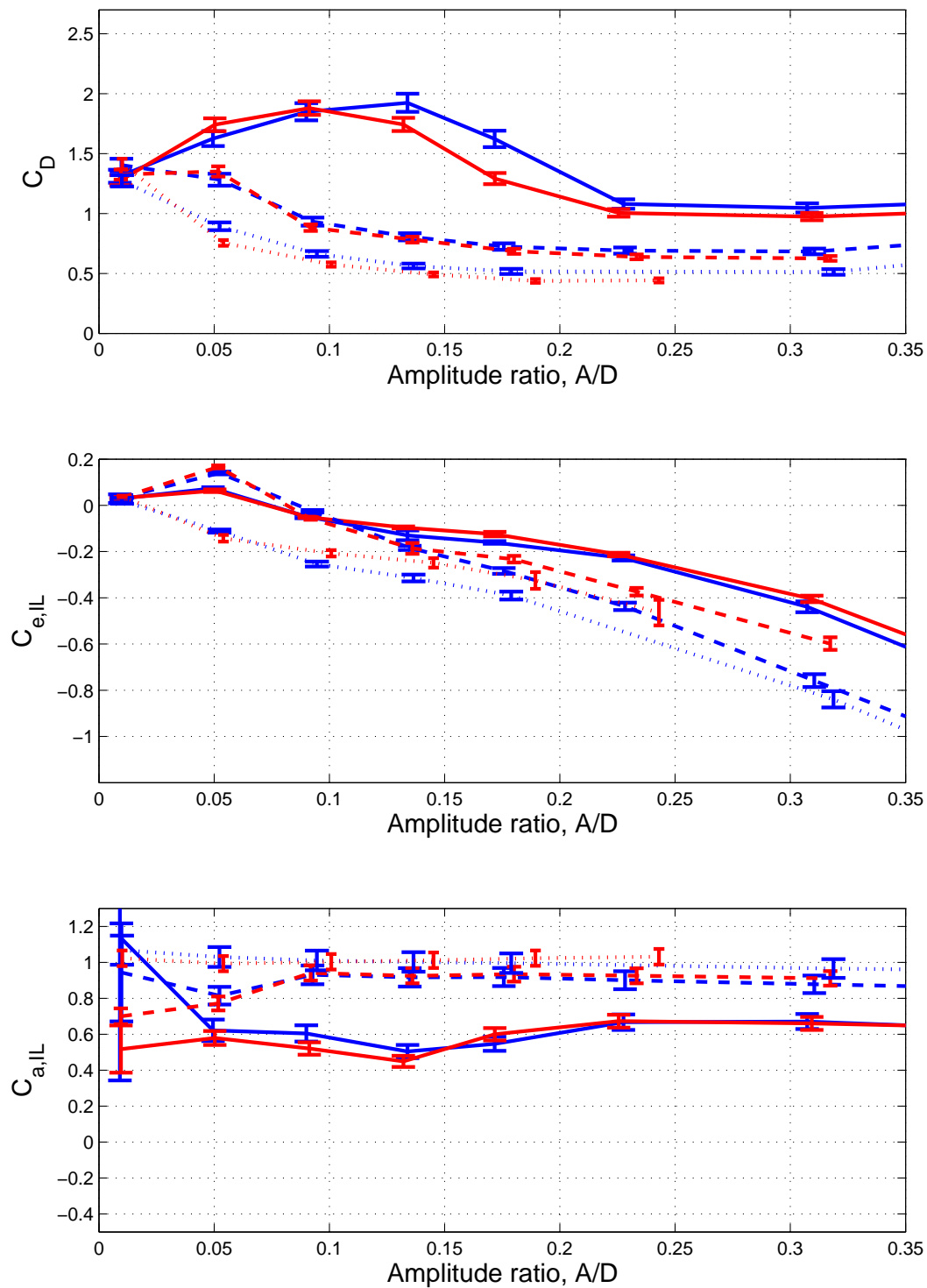
Figure 6.26: Comparison of results from Phase I (blue lines) and Phase II (red lines). Solid line show results for $\hat{f}$=0.35, dashed line (- -) show results for $\hat{f}$=0.5 and dotted line ($\cdots$) show results for $\hat{f}$=0.7.

Table 6.4: Results from repeatability investigation, Phase I and II.

	$C_{e,IL}$	$C_{t,IL}$	ϕ [deg]
mean, Phase I	-0.033	1.341	-1.40
std, Phase I	0.018	0.017	0.77
mean, Phase II	-0.060	1.315	-2.64
std, Phase I	0.008	0.016	0.36

drag amplification region. As pointed out in an earlier section the added mass results for A/D=0.01 are highly unreliable. This is confirmed by the results presented in Figure 6.26. Apart from the A/D=0.01 cases the results for added mass coefficient show good agreement. Investigating the results for the dynamic excitation coefficient it is seen that the difference between the results from Phase I and II increases for increasing A/D ratio. A closer look at the results reveal that the oscillating forces are of the same magnitude but there is a difference in phase angle. As the oscillation amplitude increase, the total force increase and a constant difference in phase cause an increasing difference in dynamic excitation coefficient. The same effect is also seen when the three different frequencies are compared. The total oscillating force increases for increasing frequency, and it is also seen that the difference between Phase I and II results increases for increasing frequency. The results indicate that the bias error for phase angle is larger than estimated in the error analysis, see chapter 5 and Appendix A.

The results from the 10 repetitions of case A/D=0.09-$\hat{f}$=0.5, given in Table 6.3, show similar trends for measured amplitude and added mass coefficient as seen for the 20 repetitions performed in Phase I. However, the differences in drag coefficient and dynamic excitation coefficient is significant and indicate that there are larger bias errors related to these parameters than estimated in the error analysis. The mean value of the drag coefficient is 7% lower than predicted in Phase I, while the estimated bias error based on calibration and cross-talk were 3.4% and 3.0% for Phase I and II respectively. The stationary cylinder tests gave a difference of 3%. This indicates that there are additional bias errors related to the drag coefficient that are not accounted for in the error analysis.

The dynamic excitation coefficient is based on the force in phase with velocity and relates to the total dynamic force coefficient as $C_{e,IL} = C_{t,IL}\sin(\phi)$. Table 6.4 shows the mean and standard deviation of $C_{t,IL}$ and ϕ. The results clearly show that the difference in dynamic excitation coefficient is due to the difference in phase angle (ϕ). Based on the standard deviation, the 95% confidence interval for the mean value of ϕ can be estimated ($P_{\bar{\phi}} = 2S_\phi/\sqrt{N}$). The result shows that for Phase I $\phi = -1.40 \pm 0.34$ and for Phase II $\phi = -2.64 \pm 0.24$. This indicate that there is a bias error in ϕ. The bias error is however small, and is not considered to influence the main conclusions drawn from the experiments.

Correlation

In Phase I and II only forces at one side of the cylinder could be measured. The reported results from these two experiments have therefore been based on the assumption that using half the cylinder length when estimating the hydrodynamic coefficients would give the same result as adding the forces from the two sides and useing the full length of the cylinder.

In Phase III forces were measured at both sides of the cylinder and the results for the two sides are compared in Figure 6.27. The figure shows drag coefficient, dynamic excitation coefficient and added mass coefficient as a function of amplitude ratio for nondimensional frequency 0.425. It is seen that there are some differences in the results for the drag coefficient, but (apart from A/D=0.05) the general trend is that the two sides give the same result. From the stationary cylinder results it should be expected that the drag coefficient at port side is between 4 and 5% lower than the drag coefficient measured at starboard side. For the dynamic excitation coefficient and the added mass coefficient there is, however, a systematic difference between the two sides. The results for $C_{e,IL}$ indicate a systematic phase difference and the results for $C_{a,IL}$ indicate a systematic difference in the magnitude of the oscillating force. This is further investigated by plotting the correlation coefficient, the ratio of the total dynamic force coefficients and the difference in calculated phase angle between cylinder motion and hydrodynamic force, see Figure 6.28.

Results for nondimensional frequency 0.375 and 0.325 are also included in Figure 6.28. For $\hat{f}$=0.425 it is seen that there is indeed a difference between the port and starboard phase angle, between 1.5 and 3 degrees for the various A/D ratios. This trend can also be seen for the two other nondimensional frequencies, but the variation is larger. Comparing the phase difference with the correlation coefficient it is seen that both seem to become stable for higher amplitude ratios. The correlation coefficient is approaching 1 and the phase difference seems to approach -3. For low values of A/D the correlation is poor and low correlation is also seen for low values of the nondimensional frequency. The reason for this is that the total dynamic force for these cases are low and the correlation seems to drop for low values of the force. The influence on the dynamic excitation coefficient is, however, not very large due to the large phase angles for these cases, i.e. the majority of the oscillating force is i phase with velocity which give low values for the added mass. Figure 6.28 also confirms that the oscillating force at port side is lower than at starboard side. The calibration of the port side force sensor showed larger uncertainty in the calibration coefficient, and for the stationary cylinder cases the port side give lower values. The difference between the two sides seem to increase for low values of total dynamic force.

6.4.2 Reynolds number dependance

As discussed in section 2.3.4 Re is an important parameter in VIV experiments. For pure CF VIV experiments indicate that both response amplitudes and hydrodynamic coefficients approaches stable values within the subcritical flow regime when Re exceeds $1.5 \cdot 10^4$-$2.0 \cdot 10^4$. For Re below $1.5 \cdot 10^4$ the hydrodynamic coefficients are significantly influenced by varying Re.

In order to investigate if the hydrodynamic coefficients are significantly different below
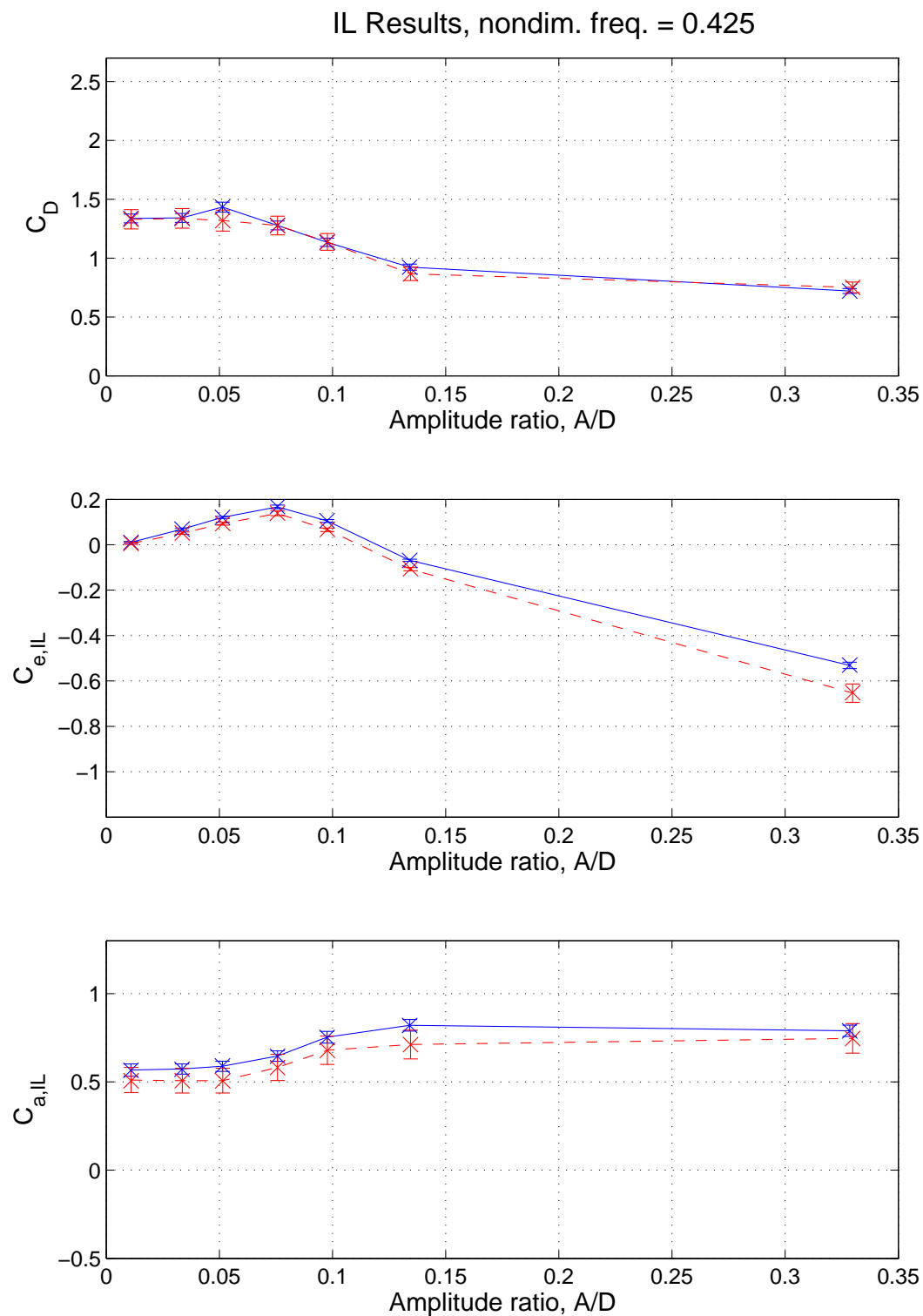
Figure 6.27: Results for $\hat{f} = 0.425$. Solid line show results for starboard side and dashed line (- -) indicate the results from port side.
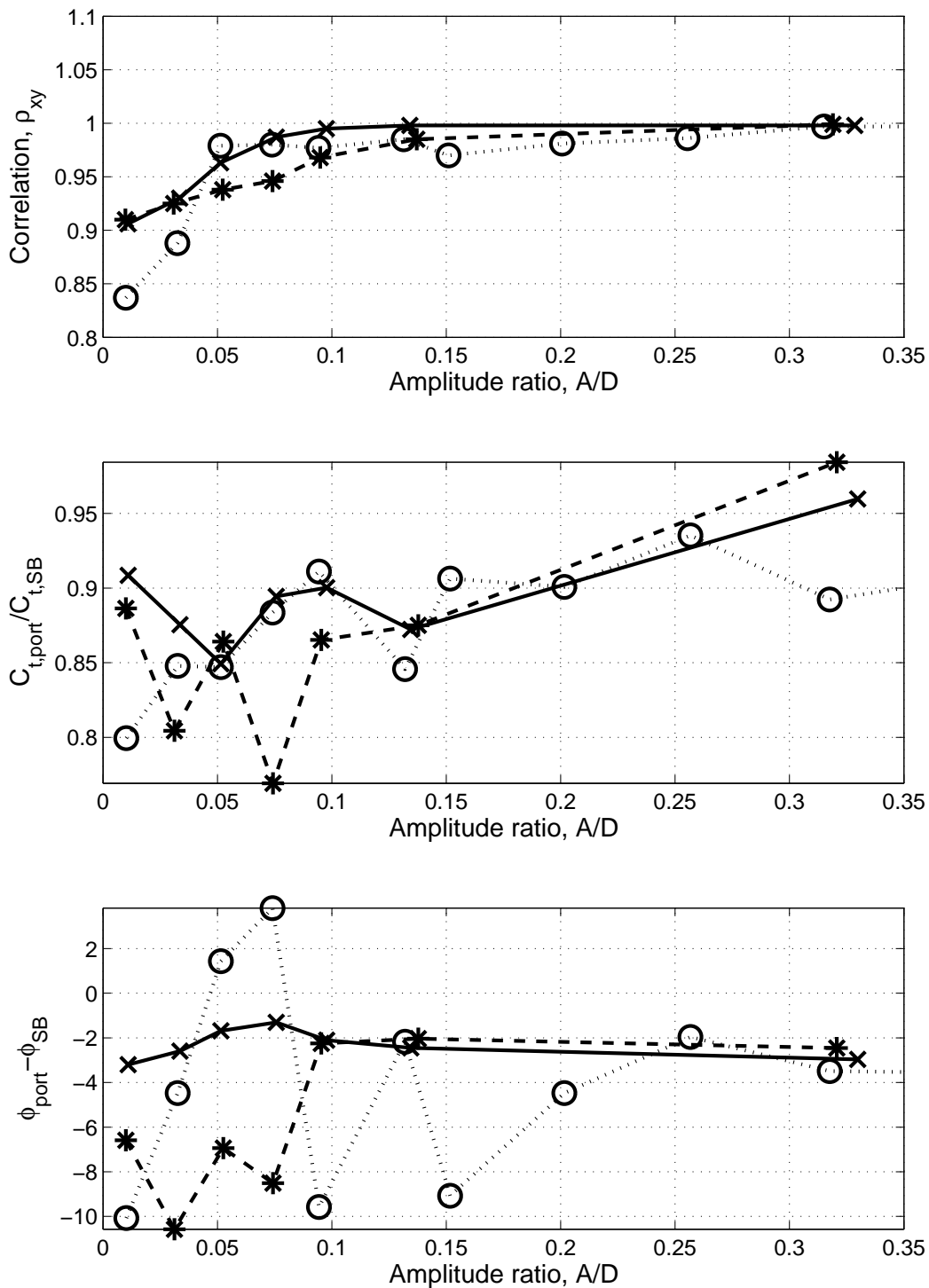
Figure 6.28: The figure shows correlation coefficient, ρ_{xy}, ratio between between port and starboard total dynamic coefficient, $C_{t,IL}$, and difference between port and starboard phase angle, ϕ. ϕ is the phase angle between the cylinder displacement and the hydrodynamic force. Solid line with $\times$ markers show results for $\hat{f}$=0.425, dashed line (- -) with $\star$ markers show results for $\hat{f}$=0.375 and dotted line ($\cdots$) with $\circ$ markers show results for $\hat{f}$=0.325.

this limit also for IL VIV, experiments were performed at Re=$1.0 \cdot 10^4$. A motivation for these tests was to investigate if the results from the forced vibration experiments could be used to predict the response of the flexible beam experiments shown in Figure 1.1. The pure IL tests of the flexible beam experiment were performed at Re below $1.5 \cdot 10^4$.

Figure 6.29 shows results for $\hat{f}$=0.4 and 0.8 performed at Re=$1.0 \cdot 10^4$, compared with the corresponding Re=$2.4 \cdot 10^4$ results. The figure shows good agreement for the added mass coefficient for $\hat{f}$=0.8, while the other results show significant discrepancies. Too few cases are tested in order draw any conclusions regarding the importance of Re for IL VIV experiments, performed within the subcritical flow regime. The results do, however, indicate that the results from the Re=$2.4 \cdot 10^4$ experiment can not be expected to compare well with the pure IL results of the flexible beam experiment.

6.4.3 Comparison with Other Experiments

Even tough the vast majority of experimental results on VIV are related to CF oscillations, there have been several research programs investigating IL VIV by free vibration experiments. Classical work on the topic is published by Wootton et. al. [64] and King et. al [27], see Figure 6.30 (a) and (b) respectively.

Figure 6.30 (a) shows the two instability regions and also indicates the dominating vortex shedding pattern related to the two regions. The figure shows maximum A/D values of 0.14 for the first instability region and 0.13 for the second instability region. Comparing Figure 6.30 (a) with the response amplitude given by the $C_{e,IL} = 0$ contour presented in Figure 6.10 it is seen that the maximum response amplitude is similar for both instability regions, and that the response curve is shifted to higher reduced velocities in Figure 6.10 compared to Figure 6.30 (a). The reason for this is that Wootton performed his experiments at a Strouhal number of 0.23 (see Sarpkaya [53]), while the Strouhal number for this project is 0.19. It is also seen that the high mass ratio curve in Figure 6.10 give the best approximation to the Wootton results.

King presented IL response diagrams for various values of the stability parameter k'_s based on results from a model pile mounted as a vertical cantilever in a water flume. The response was presented in terms of base bending moment as a function of reduced velocity. The results are discussed by Naudascher [36] where the base bending moment is converted to a tip displacement, and Figure 6.30 (b) is taken from this publication. k'_s is defined as

$$k'_s = 2m_r\delta_s \ with \ m_r = \frac{\rho_e}{\rho} \tag{6.20}$$

where m_r is the reduced mass, δ_s is the logarithmic decrement from structural damping, ρ_e is the equivalent body density and ρ is the fluid density. Figure 6.30 (b) shows two figures where the levels of k'_s have been achieved by two different methods. In the figure to the left k'_s values from 0.48 to 1.41 have been achieved by varying the tip mass of the model pile while in the figure to the right k'_s values from 0.15 to 1.35 have been achieved by varying the water level of the flume. It is seen from Figure 6.30 (b) that the levels of k'_s resembles the effect of increased nondimensional damping illustrated in Figure 6.13 (a). However, the experimental methods used by King make it difficult to compare the results
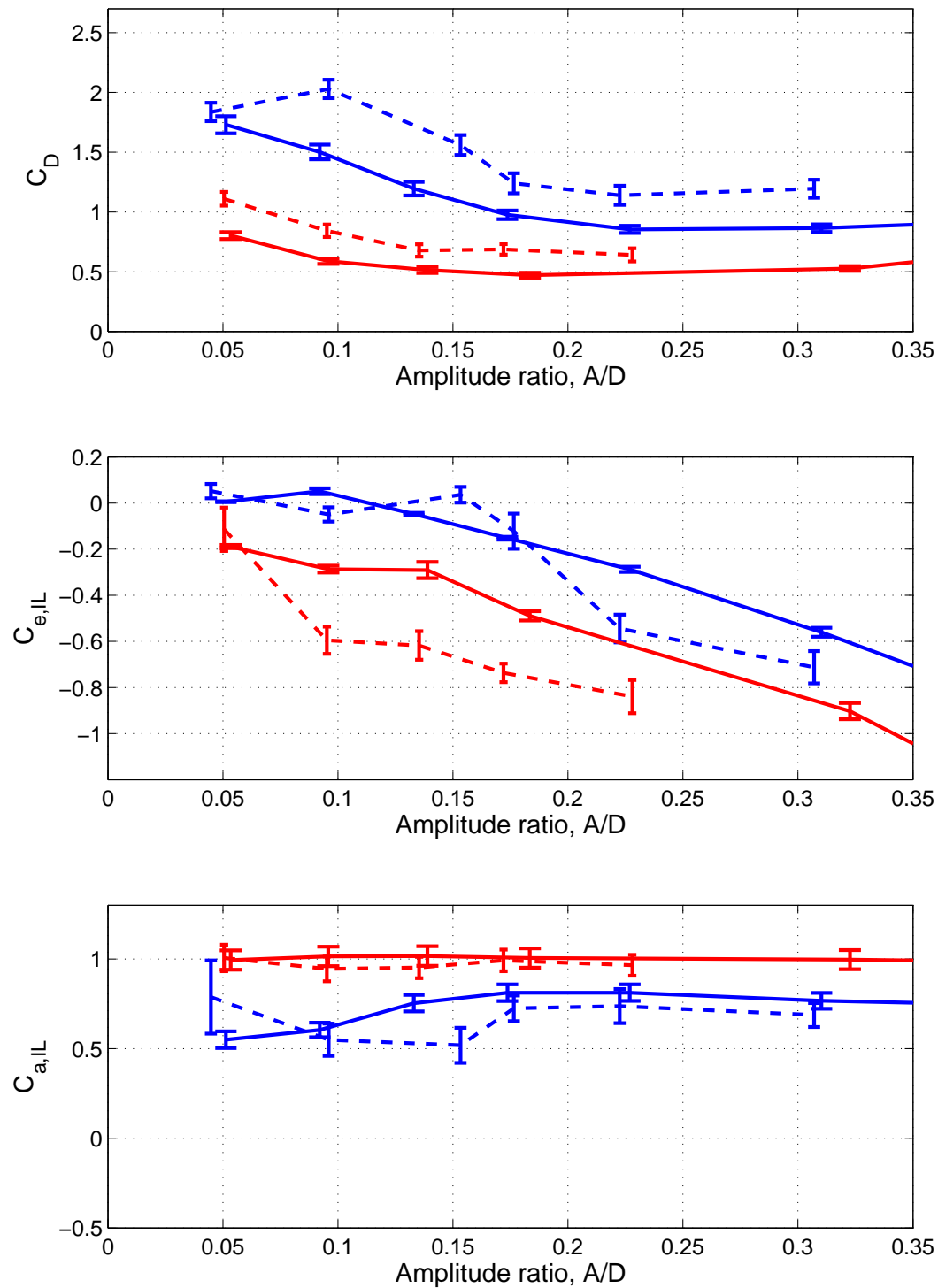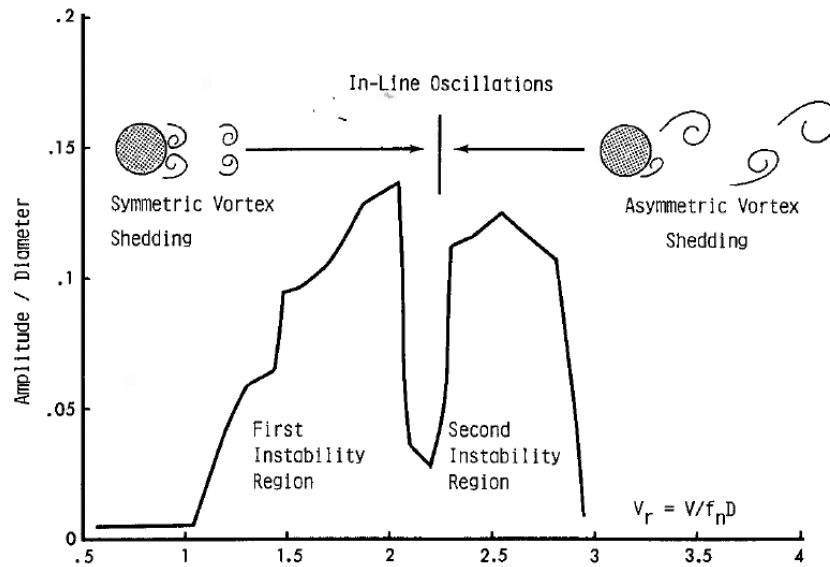
Figure 6.29: The figure compare results for Re=$1.0 \cdot 10^4$ with the corresponding results for Re=$2.4 \cdot 10^4$. The blue lines represent $\hat{f}$=0.4 and red lines represent $\hat{f}$=0.8. Solid lines for the Re=$2.4 \cdot 10^4$ results and dashed lines (- -) for the Re=$1.0 \cdot 10^4$ results.

(a) Results from Wootton [64]. Figure from Sarpkaya and Isaacson [53].
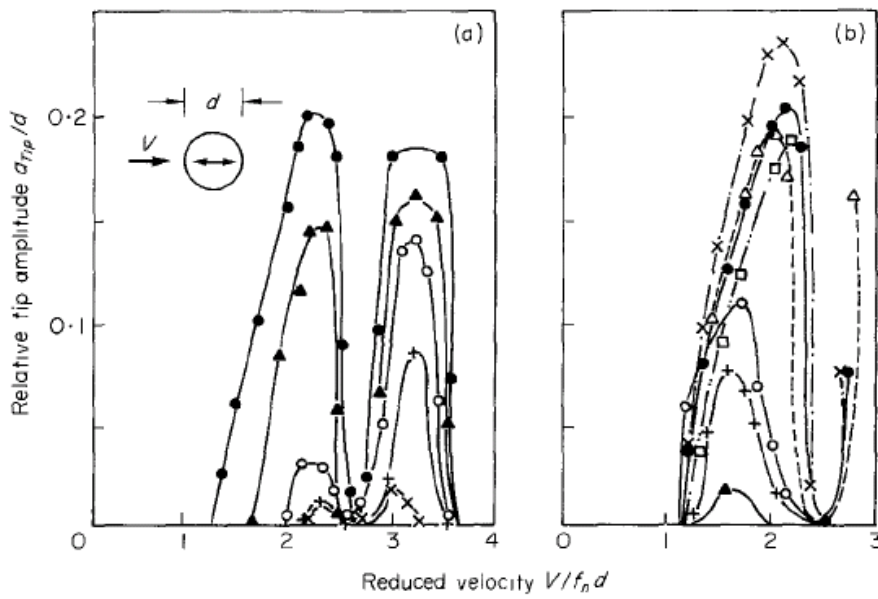
(b) Results from King [27]. Figure from Naudascher [36]. Left figure varying tip mass, right figure varying water level.

Figure 6.30: IL VIV response.

(a) DNV, $K_S=0$ (b) Johansen/Huse

Figure 6.31: Comparison between literature results given by solid line and $C_{e,IL}=0$ contour given by dashed (- -) line.
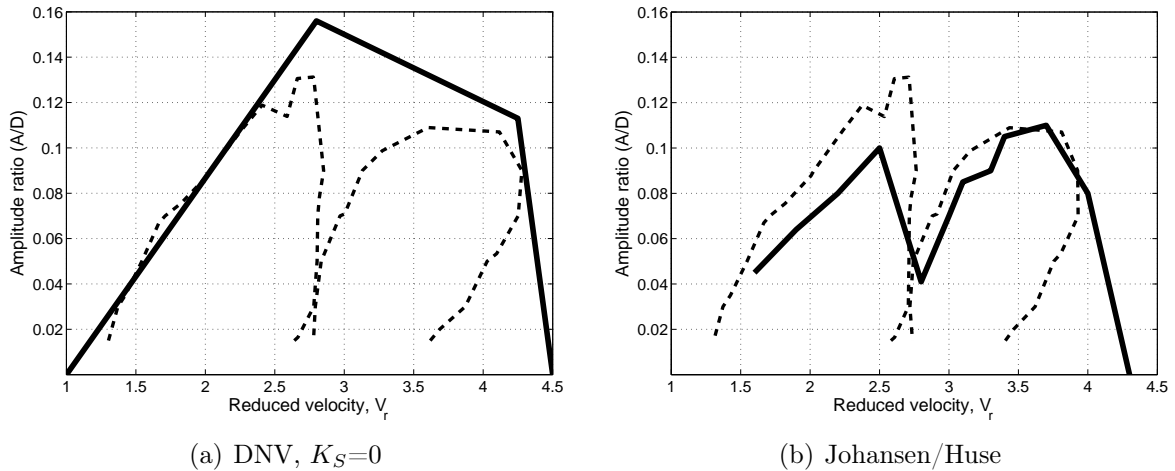
directly with our results.

The main findings related to IL VIV from several research and development projects carried out from 1984 to 1995 have been summarized in two articles by Bryndum et. al [7] and Tørum et. al. [55]. These results are also the basis for the response curves used in DNV's recommended practice "Free Spanning Pipelines" (DNV-RP-F105) [10]. The response amplitudes given by the $C_{e,IL} = 0$ contour is compared with the DNV response curve for $K_s = 0$ in Figure 6.31 (a). When converting the nondimensional frequency to reduced velocity a mass ratio of 3.7 gives the closest fit to the DNV curve. The response amplitudes in DNV-RP-F105 refer to the maximum response amplitude of a uniform beam or cable. In order to compare these values with the rigid cylinder results presented in this thesis, the DNV curve is divided by $\gamma = 1.16$, see Blevins [5]. It is seen that the slope of the two curves compares very well for the first instability region and that the maximum response amplitude occur at approximately the same reduced velocity. The maximum amplitude given by the DNV curve is, however, higher than given by the $C_{e,IL} = 0$ contour, $(A/D)_{max}=0.155$ vs. $(A/D)_{max}=0.13$.

A series of IL pendulum tests were performed in the towing tank at Marintek in 2003/2004, and the results from the experiments were reported in a technical report by Huse [19], and in a MSc thesis by Johansen [26]. The experiment was performed as excitation and decay runs where the transient phase was utilized to extract hydrodynamic coefficients, $C_{e,IL}$ and $C_{a,IL}$. The results from the decay tests are compared with the $C_{e,IL}=0$ contour in Figure 6.31 (b). It is seen that the Johansen/Huse results show very similar response amplitudes in the second instability region, while the response is lower for the first instability region. The reason for this is expected to be mechanical damping.

In order to compare the response amplitudes from the pendulum experiment with the results from the forced oscillation experiment, the structural damping in the pendulum tests must be estimated. The damping reported in the Huse/Johansen experiment is the
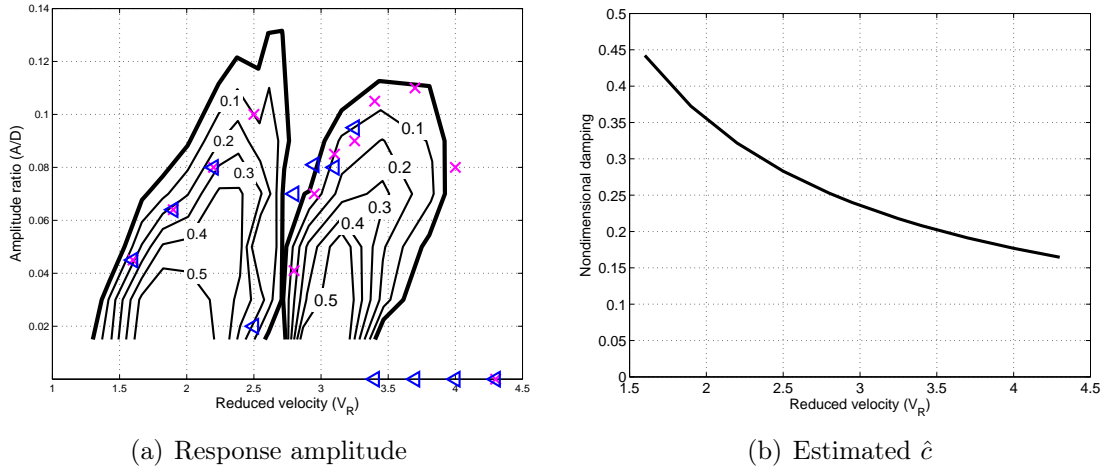
(a) Response amplitude

(b) Estimated $\hat{c}$

Figure 6.32: Figure (a) compares response amplitudes from Huse/Johansen with contours for nondimensional frequency. × indicate decay run and ◁ indicate excitation run. Figure (b) shows the estimated nondimensional frequency vs. reduced velocity.

relative damping from decay tests in still water. A relative damping of ζ=0.0081 is reported for an oscillation period of 0.803s and an oscillating mass of 73.91kg. A cylinder length of 1.4m give a damping coefficient pr. unit length of $c = \zeta \cdot 2m\omega = 6.6\ [N/(m/s^2)]$. This value does, however, include the damping due to fluid forces acting on the cylinder, which is not a part of the structural damping. The relative damping of a cylinder in viscous fluid can, for small amplitudes, be estimated by Eqn. 6.21, see Blevins [5].

$$\zeta_{cyl} = \frac{\pi}{2} \frac{\rho D^2}{m} \sqrt{\frac{\nu}{\pi f D^2}} \tag{6.21}$$

Substituting Eqn. 6.21 into the definition of relative damping, $\zeta = \frac{c}{2m\omega}$, the following expression for the damping coefficient due to forces acting on the cylinder is obtained (pr. unit length).

$$c = 2\pi\rho D \sqrt{\pi f \nu} \tag{6.22}$$

Subtracting the value given by Eqn. 6.22 from the damping coefficient given by the decay tests gives a structural damping coefficient pr. unit length of 5.6 [N/(m/s)]. Nondimensional damping values can hence be calculated for the towing velocities used in the pendulum experiment, see Figure 6.32 (b).

In Figure 6.32 (a) nondimensional damping contours from $\hat{c}$ =0.0 to $\hat{c}$ =0.5 are shown as functions of reduced velocity. The transformation from nondimensional frequency to reduced velocity is carried out for a mass ratio of 10.5, which is the mass ratio for the pendulum experiment. Looking more closely at the decay results it is seen that for V_r between 1.6 and 2.2 the amplitudes lay between $\hat{c}$=0.3 and 0.2. For V_r=2.5 the response amplitude from the decay test is located between $\hat{c}$=0.2 and 0.1. In the second instability region the response amplitudes follow the $\hat{c}$=0.1 contour until V_r=3.5 where the amplitudes approach the $\hat{c}$=0 contour. Figure 6.32 (b) shows the estimated nondimensional damping. It is readily seen that the $\hat{c}$ estimated from the structural damping given by decay tests

in still water is higher than indicated by comparing the response amplitudes with the contours for nondimensional damping. However, the encouraging result from this comparison is that the concept of nondimensional damping seems to capture the physical effect related to damping in IL VIV experiments, i.e. the influence from damping increases for lower current velocities. For further validation of the nondimensional damping concept against free vibration experiments, better estimates of the actual structural damping for the various oscillation frequencies and amplitudes are required. The results for the two highest reduced velocities indicate that experiments should have been carried out for more nondimensional frequencies. The maximum response amplitude in the second instability region seems to be between $\hat{f}$=0.275 and 0.3, and lower boundary of the second instability region seems to be between $\hat{f}$=0.25 and 0.275. By performing experiments at nondimensional frequencies between these values, a better representation of the boundary of the second instability region may have been found.

Figure 6.32 (a) shows the response amplitudes from the excitation and decay tests in the pendulum experiment by Huse/Johansen. The results for the lowest reduced velocities in both the first and the second instability region show similar values for both types of tests. However, for V_r=2.5 in the first instability region and the highest reduced velocities of the second instability region, the excitation runs do not give any response. Huse/Johansen have concluded that this is a hysteresis effect. The same effect can also be predicted by investigating the nondimensional damping contours from the forced oscillation experiments. In the second instability region it is clearly seen that the boundary of the excitation region is at a lower V_r for low oscillation amplitudes compared to higher amplitudes, V_r=3.4 for A/D=0.015 and V_r=3.9 for A/D=0.08. In decay runs the pendulum was held at an excursion higher than the expected response amplitude and then released after the tow carriage had been accelerated to the desired velocity. The oscillations would then be damped until equilibrium was reached in the excitation region. In the excitation runs the pendulum was fixed at its mean position until the tow carriage had reached the desired speed and then released. For any oscillations to occur for this type of experiment there must be an energy transfer from the fluid to the cylinder in order to start the oscillation. It is seen that cases with a reduced velocity of more than 3.4 and an A/D less than 0.015 are outside the excitation region. The same can be seen for the highest reduced velocities in the first instability region. For V_r=2.5 and a nondimensional damping level of more than 0.1 the forced oscillation experiments predicts a response amplitude close to zero for an excitation experiment. In Figure 6.32 (a) it is seen that the response amplitude from the excitation run at V_r=2.8 exceeds the response given by the decay run by a large margin. It is also outside the excitation region given by the forced oscillation experiments.

Okajima et.al [40] have published results from IL free vibration experiments performed in a water tunnel. The experiments were performed for varying values of the mass-damping parameter Cn. Results from tests with a duraluminum cylinder are shown in Figure 6.33. The figure clearly shows the two instability regions and it also shows that the response is reduced for increasing values of the mass-damping parameter Cn. Okajima has defined Cn as:

$$Cn = 2M\delta_w \qquad (6.23)$$

where M is defined as $\frac{m}{\rho d}$ with m as the structural mass pr unit span length and d as the diameter of the cylinder. δ_w is the logarithmic decrement in still water. The different levels
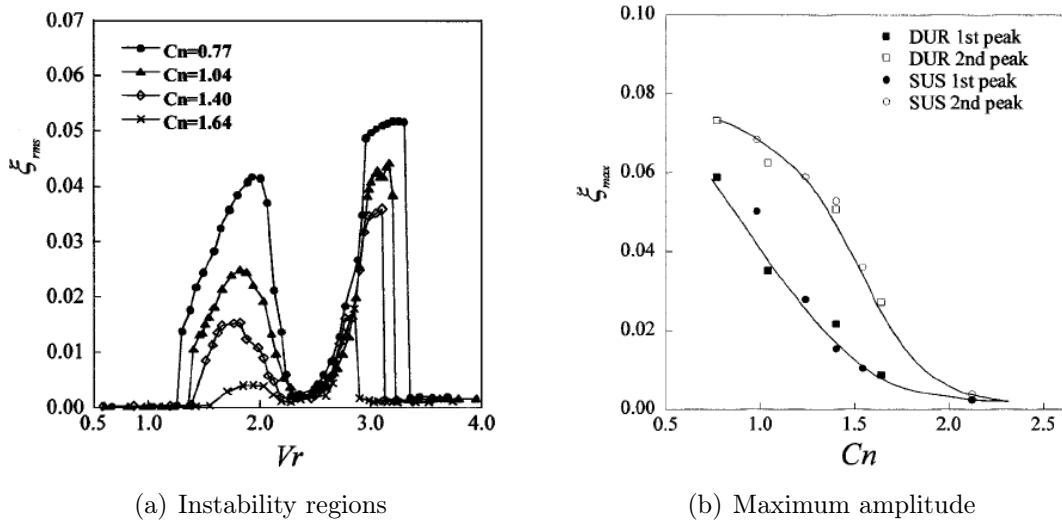
(a) Instability regions

(b) Maximum amplitude

Figure 6.33: Results presented by Okajima et.al. [40].Figure (a) shows rms values of the measured response as a function of reduced velocity. In figure (b) the maximum response amplitude for the 1st and 2nd instability region is shown as function of the mass-damping parameter Cn. Figure (a) corresponds to the DUR results in figure (b).

of Cn were obtained by changing the width of the plate springs used as elastic support. Using this method the mass and the natural frequency were kept relatively constant for all levels of Cn. In order to compare the results from Okajima with the results from the forced oscillation experiment, the various levels of Cn has to be converted to nondimensional damping, $\hat{c}$. M=10.5 is reported for the duraluminum case shown in Figure 6.33, and using the definition of M an oscillating mass of 0.69kg is found. A natural frequency in still water of 24Hz is reported and using the relation $\delta = 2\pi\zeta$ and the definition of the damping ratio ($\zeta = \frac{c}{2m\omega}$), the total damping coefficient in still water can be estimated for the various Cn levels. The structural damping is found by subtracting the damping due to the fluid forces on the cylinder given by Eqn. 6.22. The estimated nondimensional damping for Cn=0.77 and 1.04 (dashed line) are shown as functions of reduced velocity in figure 6.34 (b).

Figure 6.34 (a) shows the contours of nondimensional damping as function of reduced velocity. The transformation to reduced velocity has been carried out for a mass ratio corresponding to the Okajima experiments. The response amplitudes given by Figure 6.33 (b) for the reduced velocities given by Figure 6.33 (a) are included as circles for Cn=0.77 and squares for Cn=1.04. It is seen that the response amplitudes from Okajima's experiments are very close to the nondimensional damping contours corresponding to the estimated $\hat{c}$. However, for the Cn=0.77 case (circles) the $\hat{c}$ contours predicts an increased amplitude for higher V_r. The reason for this discrepancy is not known and can only be investigated by measuring the actual structural damping for the different oscillation frequencies and amplitudes.

Hysteresis effects in the second IL instability region were also reported in Okajima's article.

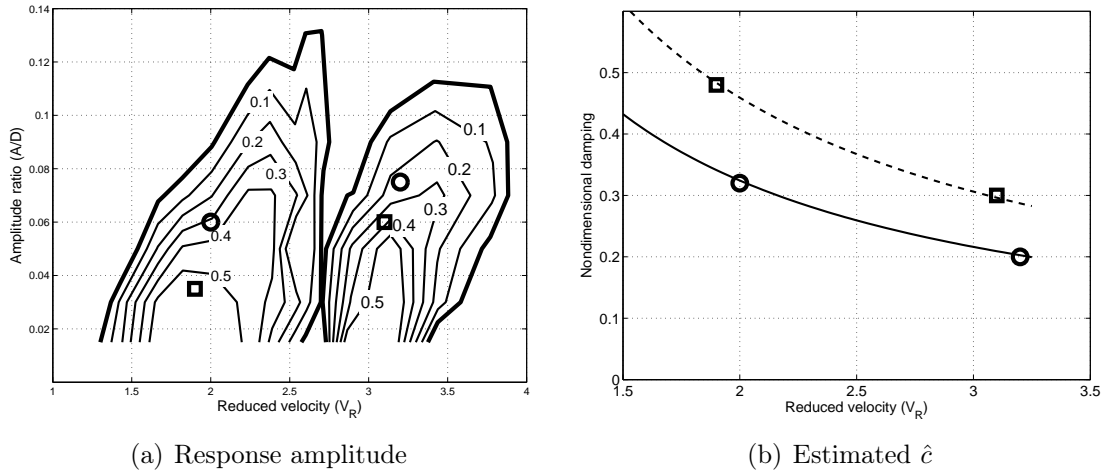(a) Response amplitude   (b) Estimated $\hat{c}$

Figure 6.34: Figure (a) shows response amplitudes for two tests reported by Okajima et.al. 2002 [40] and contours for nondimensional damping. Figure (b) shows estimated nondimensional damping for the same tests.

The damping was too high for any hysteresis to be observed in the first instability region.

6.5   Application of IL results

The results reported in this chapter can be applied to predict response amplitudes and response frequencies for pure IL VIV. As discussed in chapter 2 there are two methods commonly used for prediction of fatigue damage from VIV. These are methods based on empirical force coefficients, such as VIVANA and Shear7, and parametric response models as found in DNV-RP-F105. In the following it is shown how the results from the forced IL oscillation experiments can be utilized in the two VIV prediction methods.

6.5.1   Empirical force coefficient methods

The method implemented in VIVANA for prediction of CF VIV has been discussed in chapter 2.4.2. The hydrodynamic coefficients extracted from the experiments presented in this thesis contain all the information required to implement a similar model for IL VIV.

The contour plot of the added mass coefficient, see Figure 6.5, and also the added mass vs. nondimensional frequency plot for levels of nondimensional damping, see Figure 6.13, indicate that an amplitude independent model of the added mass can be applied. The proposed added mass model is shown in Figure 6.35 (a). The model shows a similar trend as the added mass values from a forced IL oscillation experiment for a fixed amplitude ratio of 0.05, reported by Nishihara et. al [38].

Contours of the dynamic excitation coefficient are presented in Figure 6.4. In the model for CF VIV, implemented in VIVANA, mathematical functions described by the maximum value of the excitation coefficient and the amplitude of the zero contour has been fitted to the data. This method can also be used for an IL VIV model. As an example, shown

(a) Added mass, $C_{a,IL}$
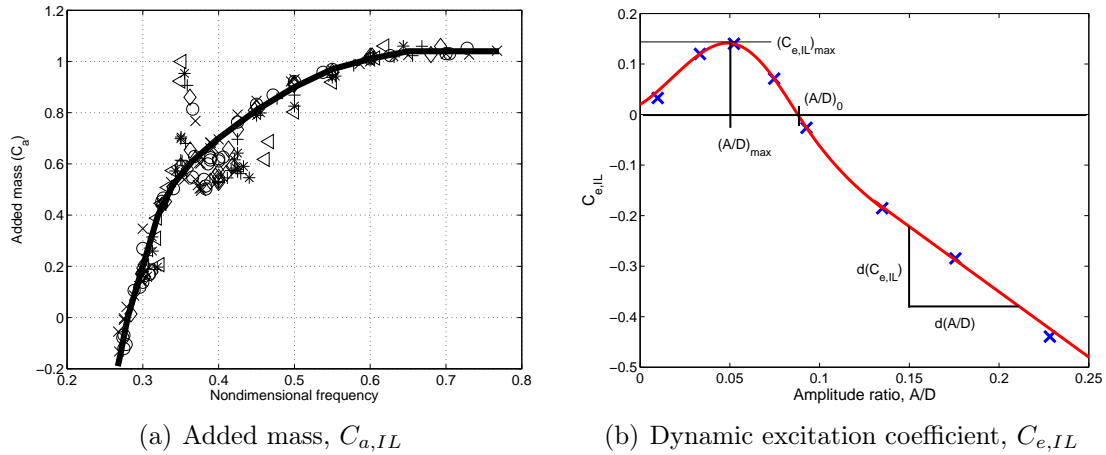

(b) Dynamic excitation coefficient, $C_{e,IL}$

Figure 6.35: Figure (a) shows the proposed added mass model, thick black line, for implementation in empirical force coefficient methods. Markers indicate results for different levels of $\hat{c}$, see FIG 6.13b. Figure (b) indicate how the dynamic excitation coefficient can be modeled. The figure shows results for $\hat{f}$=0.5.
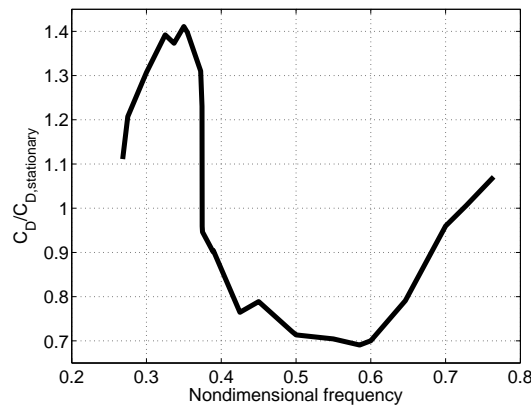

Figure 6.36: Proposed drag amplification/reduction curve. Based on $C_{D,stationary} = 1.325$.

in Figure 6.35 (b), cubic splines are fitted to the measured data points in the excitation region and a straight line is fitted to the large amplitude data points. Figure 6.35 (b) is based on $\hat{f}$=0.5 and similar curves can be created for the other nondimensional frequencies.

Drag amplification is normally included as a function of CF oscillation amplitude. As seen in Figure 6.6 the drag amplification and reduction is both frequency and amplitude dependent for IL oscillations. For low values of the nondimensional damping parameter, which often is the case for free spanning pipelines, it should, however, be sufficient to use a frequency dependent model for drag correction. The proposed nondimensional frequency dependent drag amplification /reduction curve is shown in Figure 6.5.1.

The models for the hydrodynamic coefficients presented in Figure 6.35 are valid for the Strouhal number of the IL experiments, i.e. $S_t = 0.19$. The Strouhal number is however a function of the Reynolds number, as shown in several publications (e.g. Sumer & Fredsøe

[52]). The hydrodynamic models presented herein are valid for St=0.19 and when used for conditions giving a different Strouhal number, it is the ratio between $\hat{f}$ and St that must used in the calculations.

$$(\frac{\hat{f}}{0.19})_{model} = (\frac{\hat{f}}{S_t})_{actual} \tag{6.24}$$

A model for IL VIV, similar to the one described in this section, has recently been included in the computer program VIVANA, see Larsen et. al [31].

6.5.2   Response model

As discussed in chapter 2, response models have traditionally been based on results from free vibration experiments. However, by introducing the concept of nondimensional damping it is possible to establish a response model for pure IL VIV from the forced oscillation results presented herein.

In previous sections it has been shown how the results can be compared to results from experiments of flexibly mounted rigid cylinders. This section presents a method for predicting response frequency and maximum response amplitude of a flexible beam, such as a free spanning pipeline, subjected to uniform current. The proposed response model is shown in Figure 6.38 and consists of two steps:

1. The eigenfrequency of the pipe is converted to a response frequency through an added mass model, where the mass ratio of the pipe is an important parameter.

2. The response amplitude is then predicted based on the level of structural damping.

The parameter chosen for the response model is $\frac{2S_t}{\hat{f}}$. This parameter represents the ratio between the loading frequency for a stationary cylinder (i.e. two times the vortex shedding frequency) and the response frequency, $\frac{2S_t}{\hat{f}} = \frac{2\hat{f}_s}{f_{osc}}$.

In the following the method is first described by addressing the steps of the prediction, and then the method is used to predict response amplitudes and response frequencies of the three pure IL cases of the flexible beam experiment shown in Figure 1.1.

Establish the eigenfrequency of the span
The eigenfrequency of a free spanning pipeline may be estimated by performing a FE-analysis. Note that the static drag force should be included in this analysis. The drag coefficient of a stationary cylinder should be used in order to determine whether the frequency of the span is within the excitation region. Based on this eigenfrequency, the flow velocity and the diameter of the pipe, the parameter $V_r \cdot 2S_t$ can be calculated. The parameter represents the ratio between the loading frequency and the eigenfrequency, $V_r \cdot 2S_t = \frac{2f_s}{f_0}$.

Convert eigenfrequency to response frequency
By using Figure 6.38 (a) the eigenfrequency is converted to a response frequency by choosing the curve corresponding to the appropriate mass ratio. From this figure it can be determined whether the span will respond due to pure IL VIV. If the span is found to

(a) Drag amplification model
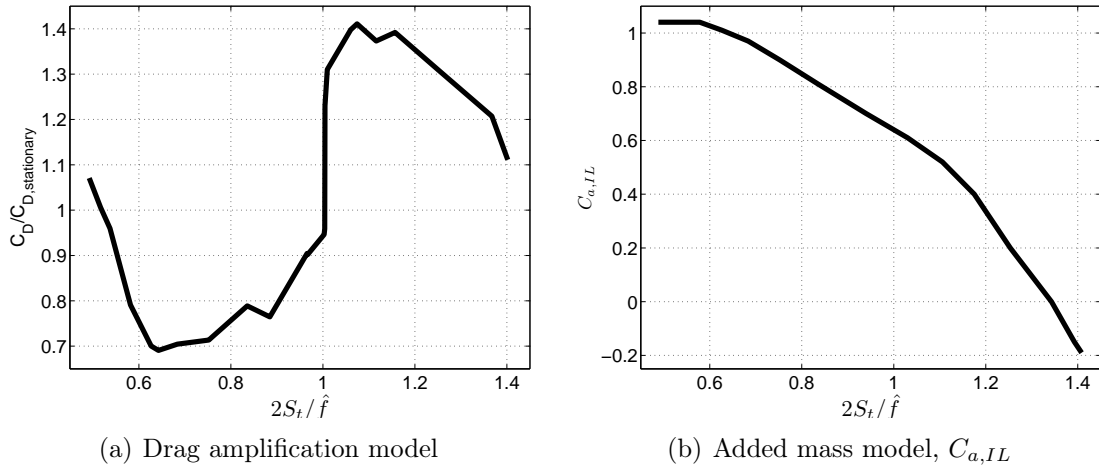

(b) Added mass model, $C_{a,IL}$

Figure 6.37: Drag amplification(a) and added mass shown as a function of the ratio between the loading frequency and the response frequency.

respond the eigenfrequency should be recalculated based on an updated drag coefficient, see Figure 6.37 (a). A value for $\frac{2S_t}{\hat{f}}$ is then established and the oscillation frequency, f_{osc}, may be found.

Establish response amplitude

For the given $\frac{2S_t}{\hat{f}}$, the response amplitude is estimated by using Figure 6.38 (b). The nondimensional damping is given by $\hat{c} = \frac{c}{\rho U_0 D}$, where c is the modal structural damping coefficient which in general must be found from a damping analysis. For free spanning pipelines the level of modal structural damping is often given by the damping ratio, ζ. The nondimensional damping may then be estimated by $\hat{c} = (\bar{m} + C_a)\zeta \cdot \pi^2 \hat{f}$, see Eqn. 6.16. Figure 6.37 (b) gives the added mass required in the expression. Damping from pipe-soil interaction at the span shoulders should also be included in the modal damping coefficient.

Flexible beam example

Figure 1.1 shows results from a flexible beam experiment performed for the Ormen Lange pipeline project, and it is seen that three of the flow velocities tested gave pure IL response. In the following the proposed response model is used to predict response amplitude and response frequency for these flow velocities, and the results are then compared with the measured values. Characteristic properties of the flexible beam:

D=0.0351m
$\bar{m}$=1.36
f_0=2.563

Establish eigenfrequency of the span:
In the flexible beam experiment the eigenfrequency in still water was determined experimentally by performing pluck tests. This eigenfrequency is also used here. The Strouhal number for the various flow velocities may be estimated from Figure 2.5 (a). This figure

is however based on results from smooth cylinders. The flexible beam is not expected to be smooth, and a Strouhal number of 0.2 is therefore assumed. The values in column 2 of Table 6.5 ($V_r \cdot 2S_t$) is then calculated.

Convert eigenfrequency to response frequency:
Figure 6.37 (a) is used to convert the eigenfrequency to response frequency, giving the values in column 3 of Table 6.5 ($2S_t/\hat{f}$). The mass ratio of the beam is 1.36 which is in between the line for 1.0 and 1.5 (for the three cases investigated the two lines are almost identical).

Establish response amplitude:
The response amplitude is estimated from Figure 6.37 (b), and an estimate for the structural damping is hence required. This value is not known, but typical structural damping ratios for flexible beam experiments are between 1 and 2%. A damping ratio of 1.5% is assumed. In order to estimate the nondimensional damping, $\hat{c} = (\bar{m} + C_a)\zeta \cdot \pi^2 \hat{f}$, values for C_a are found from Figure 6.37 (b) and values for $\hat{f}$ are known since values for $2S_t/\hat{f}$ have already been established. These values are given in column 4 and 5 in Table 6.5. The estimated values for nondimensional damping are given in column 6 and the corresponding response amplitudes are given in column 7. The response frequency is calculated from the definition of $\hat{f}$.

Table 6.5: Results from response model example.

| U_0 [m/s]	$V_r \cdot 2S_t$	$\frac{2S_t}{\hat{f}}$	C_a	$\hat{f}$	$\hat{c}$	$\frac{A}{D}$	f_{osc} [Hz]
0.135	0.60	0.60	1.02	0.67	0.24	0.045	2.56
0.181	0.80	0.78	0.87	0.51	0.17	0.095	2.64
0.226	1.00	0.94	0.70	0.43	0.13	0.10	2.74

Comparison with measured results:
The measured values for response frequency and response amplitude are given in Table 6.6. It is seen that the predicted values are in very close agreement with the measured values with one exception. This is the response amplitude for the highest flow velocity. Looking at the response curves for $2S_t/\hat{f}$=0.94, it is seen that the results at this frequency ratio deviate from the general trend of the response curves. This result highlights that there may be errors related to the experimental results that are not captured by the error analysis. Interpolating between the neighboring frequency ratios, it is seen that a response amplitude close to the measured will be predicted.

Table 6.6: Measured values from the flexible beam experiment.

U_0 [m/s]	$\frac{A}{D}$	f_{osc} [Hz]
0.135	0.040	2.59
0.181	0.095	2.63
0.226	0.12	2.73
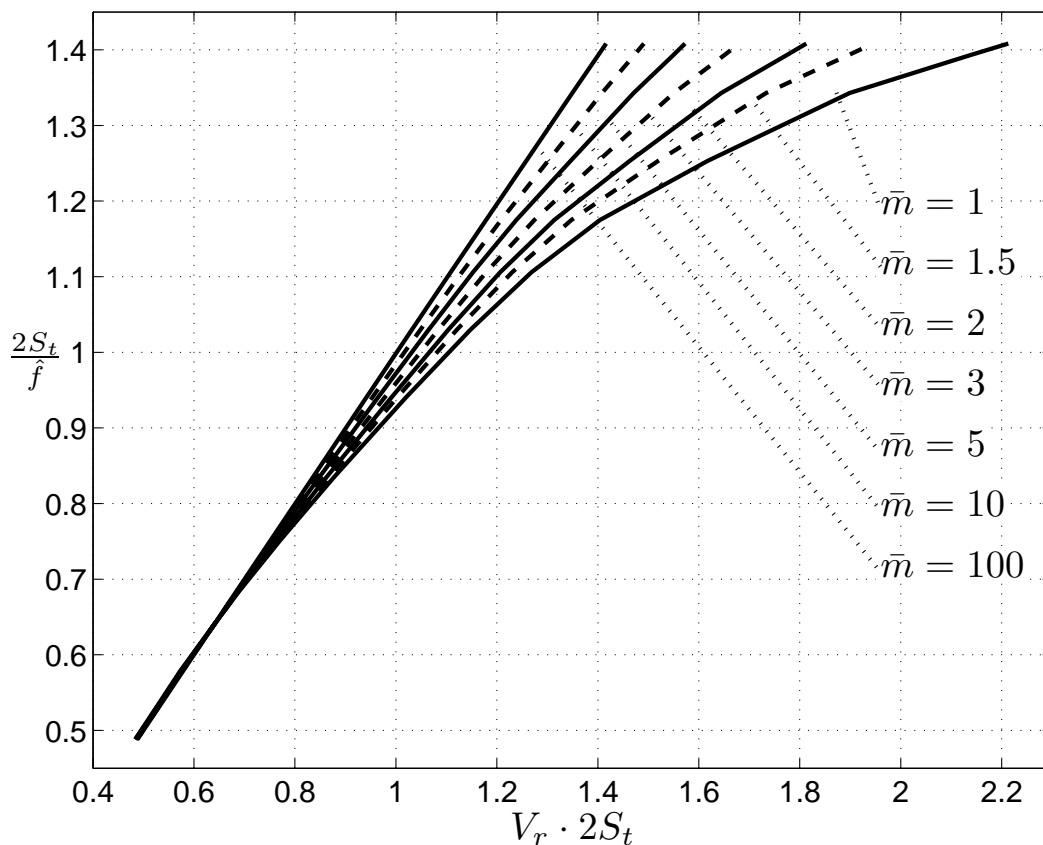
(a) Transformation from eigenfrequency to response frequency
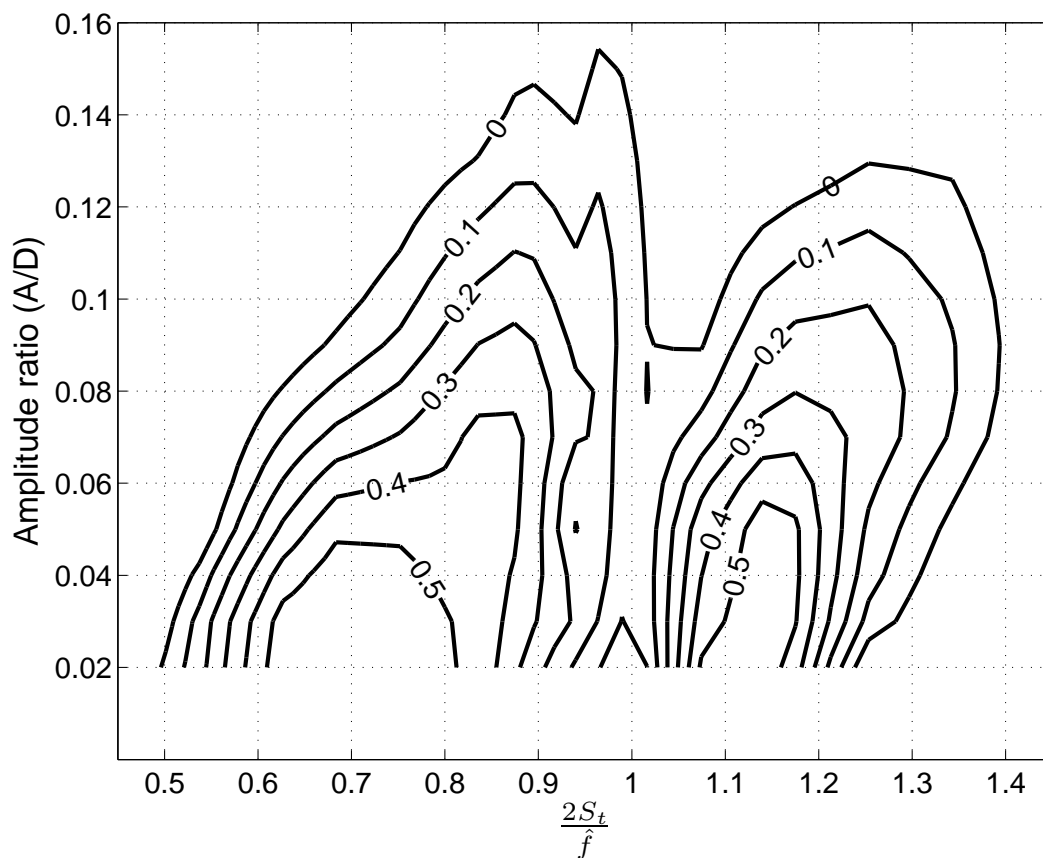
(b) Flexible beam, pinned-pinned boundary conditions

Figure 6.38: Proposed curves for estimation of response amplitude for levels of nondimensional damping, $\hat{c}$.

Chapter 7

On the Validity of Strip Theory in VIV modeling

This chapter presents results from an investigation performed in order to determine whether results from forced oscillation experiments in two degrees of freedom can be used to model VIV for flexible beams by a strip theory approach.

7.1 Background - Aim of Investigation

Chapter 6 showed that results from forced IL oscillation experiments are well suited for predicting response of a freely oscillating cylinder in the pure IL regime. This chapter goes one step further, by also including CF oscillations. While the pure IL regime could be described by two parameters, A/D and $\hat{f}$, the two degrees of freedom motion requires 5 parameters if harmonic motions are assumed in both directions. These are A/D and $\hat{f}$ in both IL and CF and a phase angle α, see Figure 3.5.

The aim of this chapter is to investigate if forced oscillation experiments in two degrees of freedom give results that can be used to model VIV of flexible beams, i.e. slender marine structures such as free spanning pipelines. The method used is summarized in the following:

- Results from a relevant and well documented oscillating beam experiment are collected. The results required are time series of response, in addition to structural data and eigenfrequencies in both IL and CF.

- Trajectories of IL-CF oscillation are identified for 9 cross sections along the length of the flexible beam.

- Orbits are constructed by fitting harmonic functions to the observed trajectories. It is important that the orbital directions correspond to the observed directions.

- The orbits are used in forced oscillation experiments of a rigid cylinder, and hydrodynamic forces valid for each orbit are found.

- The excitation coefficients in IL and CF direction for all orbits are calculated in order to determine the total energy transfer between the pipe and the fluid.

- Added mass in both directions are calculated in order to determine whether these values can explain the difference between the still water eigenfrequency and the observed oscillation frequency for the flexible beam in the two directions.

The method is based on two main assumptions:

- Strip theory is valid, i.e. the fact that there is communication in the water between adjacent sections experiencing different oscillation amplitudes would not change the hydrodynamic forces on the cylinder compared to the forces from 2D flow conditions.

- The difference between the actual response of the flexible beam and the orbits tested does not significantly change the hydrodynamic forces on the cylinder.

7.2 Experiments Performed

The flexible beam experiment presented in Figure 1.1 for V_r=5.0 has been chosen for this investigation. From the flexible beam results, trajectories for 9 cross sections evenly distributed over the length of the span, from y/L=0.1 to y/L=0.9, has been chosen. The trajectories are shown in Figure 7.1 together with the fitted orbits. The figure clearly shows that the flexible beam results contain more than one frequency in each direction and can not be very accurately represented by harmonic orbits. The CF amplitude ratios (A/D) are between 0.1 and 0.5, and the CF amplitude is two times the IL amplitude for all 9 cases. The phase angle, α, vary from 73 degrees for the smallest amplitudes close to the two ends, to 85 degrees for the highest amplitude at mid span. The oscillation frequency in CF represents a nondimensional frequency of 0.147. The IL frequency is two times the CF frequency.

Two sets of experiments were performed. The first set was carried out during experimental phase II at Re=2.4 · 10^4 and the second set was carried out during phase III at Re=1.46 · 10^4. This is the same Re as for the flexible beam experiment.

7.3 Data analysis

The experimental results from each individual test are analyzed by the methods presented in chapter 4 and 5. In the following the methods used to estimate the power transfer, added mass and damping ratio are outlined.

7.3.1 Energy Balance

The coordinate x refers to IL direction, z is the CF direction and y the axial direction along the beam. The average power transfer pr. unit time ($\bar{P}_{fluid}$) between the fluid and the pipe for an infinitesimal length and oscillation in IL and CF is given as:

$$d\bar{P}_{fluid} = \lim_{T \to \infty} \int_{t}^{t+T} (F_z(t)\dot{z}(t) + F_x(t)\dot{x}(t)) \, dt \qquad (7.1)$$
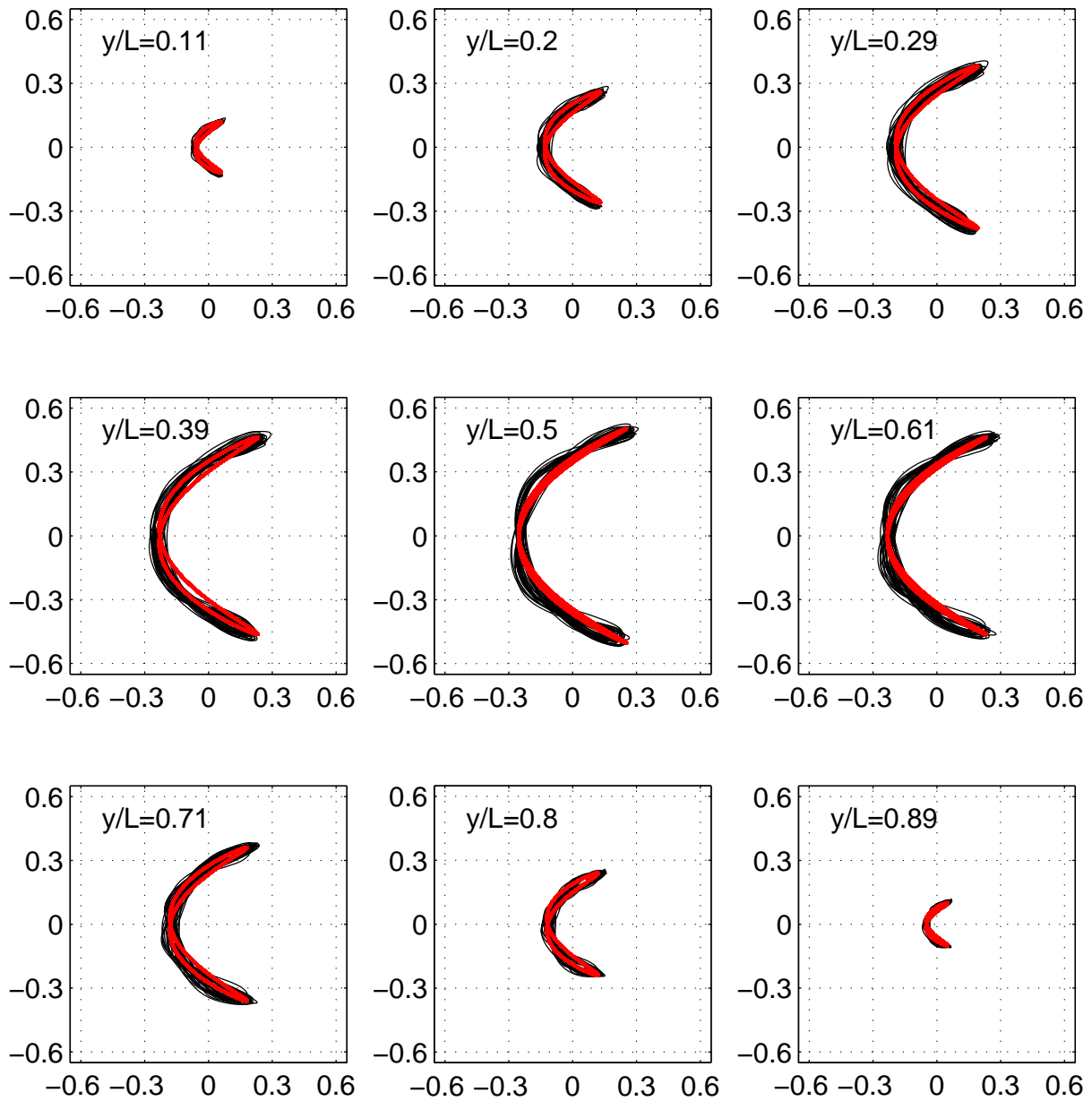
Figure 7.1: Cases analyzed. Black lines indicate results from flexible beam experiments. Red lines indicate the orbits tested (forced oscillation experiments).

Using the properties of Eqn. (4.22) and the definition of the excitation coefficient, $C_{e,IL/CF}$ (Eqn. (4.10)), the average power transfer in CF direction may be expressed as :

$$d\bar{P}_{fluid,CF} = \lim_{T \to \infty} \int_t^{t+T} F_z(t)\dot{z}(t)\ dt = \frac{1}{2}\omega_{osc}z_0(F_0 \sin \phi)_{CF} = \frac{1}{4}\rho DU^2\omega_{osc}z_0C_{e,CF} \quad (7.2)$$

A similar expression is also valid for IL direction. Further, using the expression found in Eqn. (7.2) and substituting for $\omega_{osc} = 2\pi U \hat{f}/D$, Eqn. (7.1) can be expressed as:

$$d\bar{P}_{fluid} = \frac{\pi}{2}\rho DU^3 \left[\hat{f}_{CF}\left(\frac{A}{D}\right)_{CF} C_{e,CF} + \hat{f}_{IL}\left(\frac{A}{D}\right)_{IL} C_{e,IL} \right] \quad (7.3)$$

For the flexible beam the power transfer integrated over the length of the beam is the quantity of interest. Substituting for $\hat{f}_{IL} = 2\hat{f}_{CF}$ and $(A/D)_{CF} = 2(A/D)_{IL}$ the power transfer for this particular case may be written as:

$$\bar{P}_{fluid} = \int_0^L dP_{fluid}(y)\ dy = \frac{\pi}{2}\rho DU^3\hat{f}_{CF} \int_0^L \left(\frac{A}{D}\right)_{CF}(y)\ [C_{e,CF}(y) + C_{e,IL}(y)]\ dy \quad (7.4)$$

For the 9 discrete results available, the integral is approximated by a sum. The expression used to calculate the reported results is:

$$\bar{P}_{fluid} = \frac{\pi}{2}\rho DU^3\hat{f}_{CF} \sum_{i=1}^{9} (A/D)_{CF,i}\ [C_{e,CF,i} + C_{e,IL,i}] \cdot 0.1 \quad (7.5)$$

A free oscillation can only exist if the value of $\bar{P}_{fluid}$ is positive. The power transfer from the fluid to the cylinder balances the energy dissipation through structural damping. In order to get a better understanding of the magnitude of the estimated power transfer, equivalent values of the overall excitation and nondimensional damping coefficients can be estimated:

$$\bar{C}_{e,CF} = \frac{\sum_{i=1}^{9} (A/D)_{CF,i}\ [C_{e,CF,i} + C_{e,IL,i}] \cdot 0.1}{(A/D)_{CF,characteristic}} \quad (7.6)$$

$$\hat{c}_{CF,equivalent} = \frac{\bar{C}_{e,CF}}{4\pi\hat{f}_{CF}(A/D)_{CF,characteristic}} \quad (7.7)$$

The characteristic oscillation amplitude ratio is taken as the maximum amplitude ratio divided by the γ-factor for a pinned-pinned beam (γ=1.16), given by Blevins [5].

7.3.2   Added mass

There is no coupling between the two directions, IL and CF, in the mass matrix for the flexible beam experiment. Hence, the added mass is found by using modal analysis and calculating the added mass independently in the two directions. The expression giving added mass pr. unit length is:

$$\bar{C}_{a,IL/CF} = \frac{\int_0^L C_{a,IL/CF}(y)\Phi_{IL/CF}^2(y)\ dy}{\int_0^L \Phi_{IL/CF}^2(y)\ dy} \quad (7.8)$$

Φ is the modeshape of the span. The equivalent added mass from the 9 cross sections tested is estimated by:

$$\bar{C}_{a,IL/CF} = \frac{\sum_{i=1}^{9} C_{a,IL/CF,i}(A/D)^2_{IL/CF,i}}{\sum_{i=1}^{9}(A/D)^2_{IL/CF,i}} \tag{7.9}$$

The ratio between the eigenfrequency in still water, f_0, and the oscillation frequency, f_{osc}, is given by the added mass and the mass ratio:

$$\left(\frac{f_0}{f_{osc}}\right)^2_{IL/CF} = \frac{\bar{m} + \bar{C}_{a,IL/CF}}{\bar{m} + 1} \tag{7.10}$$

7.3.3   Damping ratio

Knowing the nondimensional damping and the added mass, the damping ratio, ζ, can be calculated. The damping ratio is defined in Eqn. (2.11) and substituting for oscillation frequency ($\omega_n = 2\pi \cdot U\hat{f}/D$) and the corresponding oscillating mass ($m_n = \frac{\pi D^2}{4}\rho(\bar{m} + C_a)$) the damping ratio is given as:

$$\zeta = \frac{c}{\rho DU\pi^2 \hat{f}(\bar{m} + C_a)} = \frac{\hat{c}}{\pi^2 \hat{f}(\bar{m} + C_a)} \tag{7.11}$$

Using the estimated equivalent value for nondimensional damping, and nondimensional frequency and added mass in CF direction, an estimate of the damping ratio for the flexible beam experiment can be calculated:

$$\zeta_{CF,equivalent} = \frac{\hat{c}_{CF,equivalent}}{\pi^2 \hat{f}_{CF}(\bar{m} + \bar{C}_{a,CF})} \tag{7.12}$$

7.4   Results

The hydrodynamic coefficients from forced oscillation tests at Re=$2.4 \cdot 10^4$ are presented in Figure 7.2. The coefficients are calculated according to the definitions in Chapter 4 and the 95% confidence intervals are estimated by the methodology presented in Chapter 5. The figure shows high values for the excitation coefficient, $C_{e,CF}$, close to the two ends, i.e. for low oscillation amplitudes. Note that these values are significantly higher than for pure CF experiments. For the highest oscillation amplitudes the excitation coefficient is negative. The added mass coefficient, on the other hand, has a relatively constant value except for the smallest oscillation amplitudes. Both coefficients behave as expected for an oscillating beam. In IL direction the excitation coefficient is negative, but the values are small. The added mass is also negative, indicating an oscillation frequency higher than the eigenfrequency.

For the Re=$2.4 \cdot 10^4$ case the results presented for y/L=0.2 and 0.3 are based on the same orbits as for y/L=0.8 and 0.7. Hence, only 7 different cases have been analyzed. The differences in oscillation amplitude between the the two sides are, however, small (less than 8%). Only measurements at one side of the cylinder are available from Phase II. Also, due to some problems with the control system the phase angles are lower than intended. The

largest difference is seen for the lowest oscillation amplitudes where the phase angle is 10 degrees lower than intended, while at midspan the oscillation amplitude is 3 degrees lower than intended.

The hydrodynamic coefficients obtained for Re=$1.46 \cdot 10^4$ are shown in Figure 7.3. This is the same Re as for the flexible beam experiment. The oscillation amplitudes and phase angles achieved during this experimental phase (phase III) are as given by the fitted orbits. Force measurements are also available at both ends. The results show a very close agreement between the two sides of the cylinder. The trends of the coefficients are very much the same as for the Re=$2.4 \cdot 10^4$ case. However, the CF excitation coefficient shows higher values and only the maximum amplitude give $C_{e,CF} < 0$.

In Table 7.1 the equivalent coefficients, representing the oscillating beam, are presented. The table shows that both cases have a positive equivalent excitation coefficient, which indicate that vibrations can take place. However, the excitation coefficient, especially for the Re=$1.46 \cdot 10^4$ case, seems high. The added mass coefficients show good agreement for the two cases.

Table 7.1: Results strip theory validation. Hydrodynamic force coefficients.

| Coefficient	Re=$2.4 \cdot 10^4$	Re=$1.46 \cdot 10^4$
$\bar{C}_{e,CF}$	0.28	0.51
$\hat{c}_{CF,equivalent}$	0.35	0.63
$\bar{C}_{a,CF}$	3.77	3.58
$\bar{C}_{a,IL}$	-0.13	-0.19

The mass ratio, $\bar{m}$, of the flexible beam experiment is 1.36, and the frequency ratios in IL and CF direction are $(f_0/f_{osc})_{IL}$=0.673 and $(f_0/f_{osc})_{CF}$=1.364 respectively. The damping ratio and frequency ratios estimated based on the forced oscillation experiments are given in Table 7.2.

Table 7.2: Results from strip theory validation. Mass ratio used in the calculations is $\bar{m}$=1.36.

Coefficient	Re=$2.4 \cdot 10^4$	Re=$1.46 \cdot 10^4$
$\zeta_{CF,equivalent}$	4.7%	8.8%
$(f_0/f_{osc})_{CF}$	1.48	1.45
$(f_0/f_{osc})_{IL}$	0.72	0.70

7.5   Discussion

Table 7.2 shows damping ratios corresponding to ζ=4.7% and ζ=8.8% for Re=$2.4 \cdot 10^4$ and Re=$1.46 \cdot 10^4$ respectively. Damping has not been reported for the flexible beam experi-
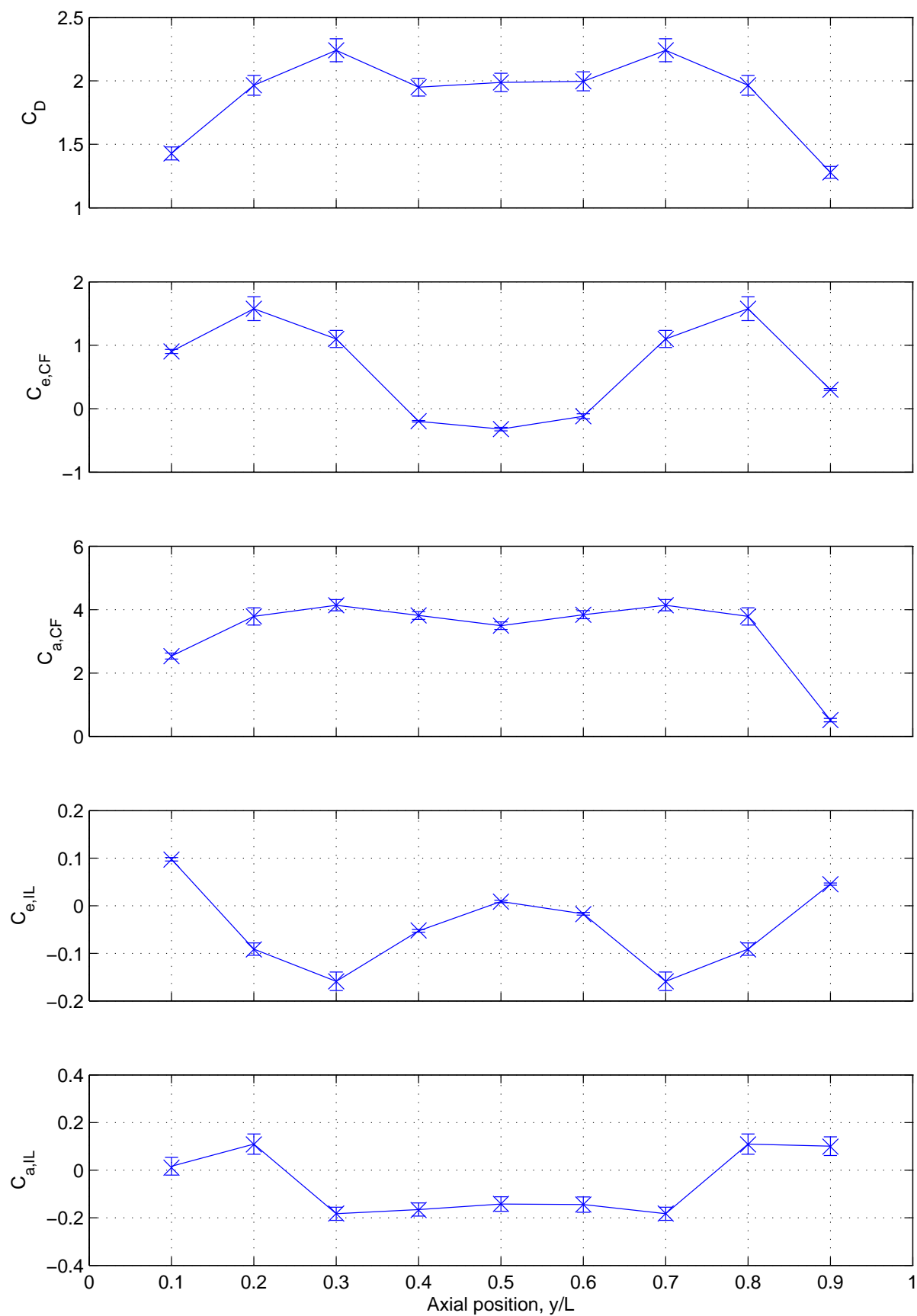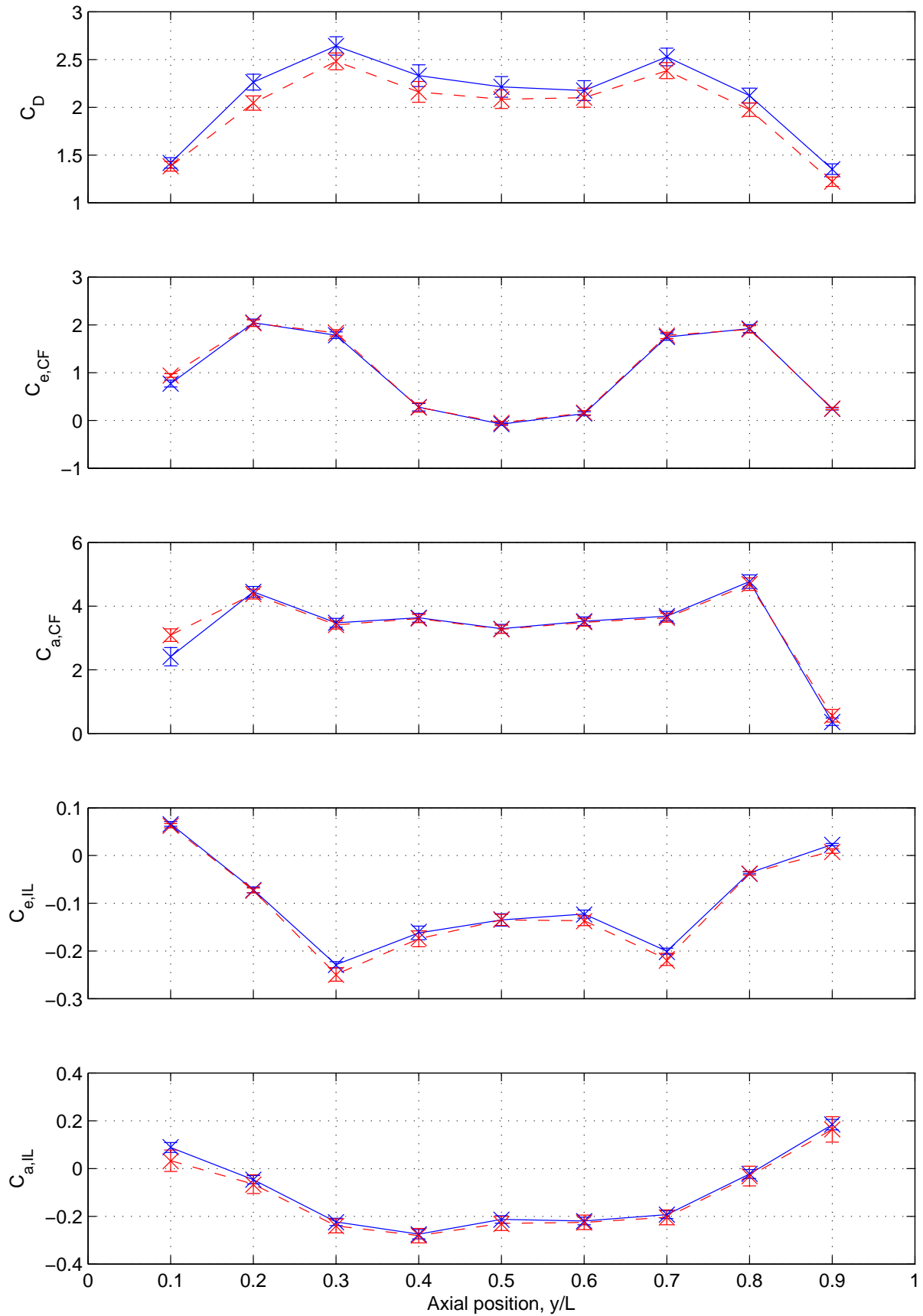
Figure 7.2: Results for Re=$2.4 \cdot 10^4$.

Figure 7.3: Results for Re=$1.46 \cdot 10^4$. Dashed lines represent Port side and solid lines represent Starboard side.

ment, but is expected to be very low for such an experiment. In particular the damping ratio estimated for the Re=$1.46 \cdot 10^4$ case is too high. This is also the experiment expected to give the better approximation to the flexible beam results. However, the excitation coefficient seems to be very sensitive to oscillation amplitude. A small increase in oscillation amplitude should hence give an excitation coefficient corresponding to a more realistic damping ratio. The encouraging result is the trend of the excitation coefficient with respect to increased oscillation amplitude.

The ratios between the eigenfrequency and oscillation frequency, f_0/f_{osc}, estimated from the equivalent added mass values (see Eqn. (7.10)) corresponds reasonably well with the ratios reported for the flexible beam experiment. The difference is only 4 to 8%. A reason for this difference can be that the eigenfrequency of the span is changed when the static drag forces are considered, compared to the still water case. As seen from Figure 7.2 and 7.3 the drag coefficient is relatively high, approximately 2. This will add tension and hence also geometric stiffness and the eigenfrequency will increase. The added mass from this type of forced oscillation experiment refers to the eigenfrequency of the span experiencing VIV, i.e. included static drag forces.

As discussed in section 2.3.4 the Reynolds number is an important parameter in VIV experiments. The Re of the flexible beam experiment is close to the region where a transition to turbulence in the free shear layer is seen and the force coefficients are Re dependent. However, the force coefficients for the two Re values are similar, and the Re is considered high enough for the transition in the free shear layer not to be a factor. The measured Strouhal number for Re=$1.46 \cdot 10^4$ was slightly higher than for Re=$2.4 \cdot 10^4$, St=0.195 compared to St=0.188. Correcting for this difference in the cases performed at Re=$2.4 \cdot 10^4$, by changing the nondimensional frequency to 0.142, should give closer agreement between the two sets of results.

The results indicate that the IL direction extract energy, i.e. causes damping, while the excitation is in CF direction. More results are required to determine if this is the case for all oscillations in two degrees of freedom, but the results show the importance of investigating the energy balance by taking both IL and CF direction into account. The two directions can not be treated independently.

The results show some robustness with respect to phase angle. For the Re=$2.4 \cdot 10^4$ results the phase angle was up to 10 degrees lower than intended, without a major change to the hydrodynamic coefficients. The sensitivity with respect to phase is discussed in Chapter 8.

The experiment was performed in order to investigate if two degrees of freedom forced oscillation experiments and strip theory can be used to model VIV of a flexible beam oscillating both in IL and CF. The results are promising. Even if the response of the flexible beam is not exactly reproduced by the selected orbits, the results indicate that such a parametrization provides useful insight into the response of a flexible beam.

It should also be noted that an attempt was made to reproduce the flexible beam results observed for V_r=3.5, see Figure 1.1, during the Phase II experiment. The same methodol-

ogy as presented in this chapter was used, but the results gave a negative energy balance. The reason for this is not known, but the difference in Re between the two experiments may be one explanation (Re=$1.03 \cdot 10^4$ for the flexible beam experiment and Re=$2.4 \cdot 10^4$ for the forced oscillation experiment).

Chapter 8

Systematic Variation of Orbital Shape and Amplitude Ratio

8.1   Introduction

The motivation for performing a systematic variation of orbital shape and amplitude ratio is to investigate the influence of these parameters on the hydrodynamic forces acting on a cylinder. This information is vital for understanding the behavior of a flexible beam subjected to VIV.

The results presented in Chapter 7 indicate that coefficients from forced oscillation experiments and the strip theory assumption can be used to model the response of a flexible beam. It would therefor make sense to continue with a more systematic variation of orbital shape and amplitude ratio in order to investigate how flexible beams respond to VIV.

The tests performed are defined in Chapter 3.3 and hydrodynamic coefficients for all these tests are reported in Appendix E. Included are also the results from pure CF tests. These are included to serve as a reference for the two degree of freedom cases, and also for comparison with literature results.

This chapter is organized in sections presenting the main findings from the investigation. The test matrix consists of more than 300 cases, and a compact way of presenting all the results is not found. Some of the results are however presented in detail in order to illustrate the findings by a detailed discussion of as few examples as possible. The cases chosen are the crescent shaped orbits discussed in chapter 7 ($\hat{f}$=0.147) and two figure of eight shaped orbits at $\hat{f}$=0.163 for which flow visualization is available. Detailed results for the two latter cases are tabulated in order to demonstrate the reliability of the data. The two cases are considered to be representative for the complete data set. The data processing is performed using the methodology outlined in chapter 4, 5 and Appendix A. See also data sheets in Appendix B.
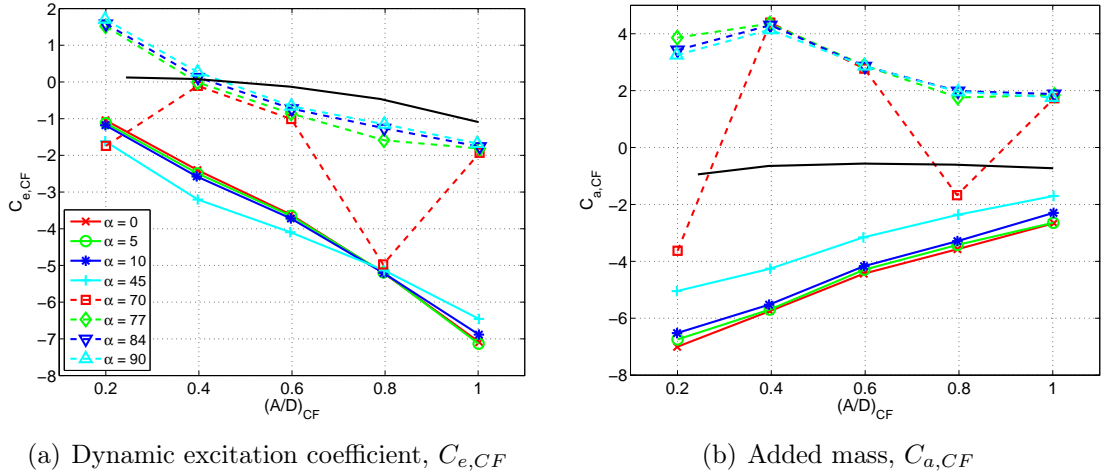
(a) Dynamic excitation coefficient, $C_{e,CF}$ (b) Added mass, $C_{a,CF}$

Figure 8.1: Results for $\hat{f}$=0.147, phase angles (α) between 0 and 90. Solid black line shows the results for pure CF.

8.2 Sensitivity with respect to orbital shape

The results presented in chapter 7 indicate that hydrodynamic coefficients obtained from forced oscillation experiments and the strip theory assumption may be used to model VIV of flexible beams. However, the results predicted a structural damping level higher than what can be expected from a flexible beam experiment. In order to investigate how sensitive the hydrodynamic coefficients are with respect to orbital shape and amplitude ratio, a systematic variation of these parameters has been performed. The results for $C_{e,CF}$ and $C_{a,CF}$ are presented in Figure 8.1 for amplitude ratios from 0.2 to 1.0 and phase angles (α) between 0 and 90. The two figures for excitation coefficient and added mass coefficient show that there are two distinct branches. One branch consists of the phase angles representing a crescent or "half moon" shaped orbit, α from 77 to 90°, where the excitation coefficient is positive for low amplitude ratios and the added mass coefficient is positive. The second branch, representing orbital shapes close to a "figure of eight", shows negative values for both the excitation coefficient and the added mass coefficient. The results for α=70 seem to be jumping between the two branches. The large difference in hydrodynamic coefficients indicates that there are different vortex shedding modes present for the two branches. Flow visualization of the wake would, however, be necessary to determine if this is the case, but such data are not available.

From the flexible beam experiment discussed in chapter 7 it was seen that the phase angle between CF and IL motions was between 70° and 85°. The results for the dynamic excitation coefficient in Figure 8.1 (a) show that such phase angles give excitation for low amplitude ratios. The figure also shows the strong sensitivity with respect to amplitude ratio. This indicates that a marginally increased oscillation amplitude for the tests presented in chapter 7, would result in a realistic damping level.

Worth noticing is also the high values of the excitation coefficient for low amplitude ratios, compared to the values for the pure CF tests. This shows that a cylinder free to oscillate

in a two degree-of-freedom motion is less sensitive to damping, compared to a cylinder that oscillates in CF only.

The excitation coefficient in IL direction has not been included in this discussion. The reason for this is that the values of the IL excitation coefficient are small for all phase angles, and are thus not very important for the energy balance. The IL results are given in Figure E.3 in Appendix E.

8.3 On the importance of Orbital Direction

One of the main findings from the Ormen Lange experiments, discussed in the introduction to this thesis, see Nielsen et al. [37], was that for cases where the dominating IL mode had higher order than the dominating CF mode, the maximum response amplitude was significantly lower than found from pure CF tests. This conclusion was confirmed by a 2-D pendulum experiment that could investigate sections with figure of eight motions with different phase between IL and CF components, see Søreide [48] and Huse et al. [21].

The phenomenon may be further investigated by looking into the influence from orbital direction on the hydrodynamic coefficients. The importance of orbital direction is here demonstrated by looking into a 1st mode CF - 2nd mode IL scenario. Two scenarios are addressed, based on two hypotheses on what determines the orbital shape.

- The first hypothesis is that the orbit is controlled by the eigenfrequency ratio between the IL and CF direction.

- The second hypothesis is that the orbit is controlled by the hydrodynamic forces, i.e. the cylinder is forced into a certain oscillation pattern. This "preferred" orbital shape must then be expected to be the crescent shape observed in the flexible beam experiment discussed in chapter 7.

8.3.1 Orbit controlled by eigenfrequency ratio

A beam with low bending stiffness and high tension will have the same dynamic behavior as a cable. The second eigenfrequency will then be close to two times the first. Since the IL excitation frequency is two times the CF, the second mode will dominate IL response for conditions where the first mode will dominate for CF. The orbital directions of two symmetrically positioned cross sections will hence become opposite, see Figure 8.2 (a). Hydrodynamic forces on the two half length sections must therefore be expected to become different, not only with respect to phase but also magnitude. Hence, the perfect combination of first mode CF and second mode IL response must be expected to be disturbed. Results from two cases of opposite orbital direction (see Figure 8.2 (b)), but with identical nondimensional frequency ($\hat{f}_{CF}=\hat{f}_{IL}/2=0.163$) and amplitude ratio ($(A/D)_{CF}=2(A/D)_{IL}=0.3$) are presented in the following. These results are compared with results from pure IL and pure CF experiments. Detailed results for the hydrodynamic coefficients C_D, $C_{e,IL/CF}$, $C_{a,IL/CF}$, defined in chapter 4.4, are presented in Table 8.1 and 8.2 for CF and IL direction respectively. The coefficients are presented separately for the two ends of the cylinder, and the 95% confidence interval is given as U_{C_D}, U_{C_e}, U_{C_a}. Detailed result are included to
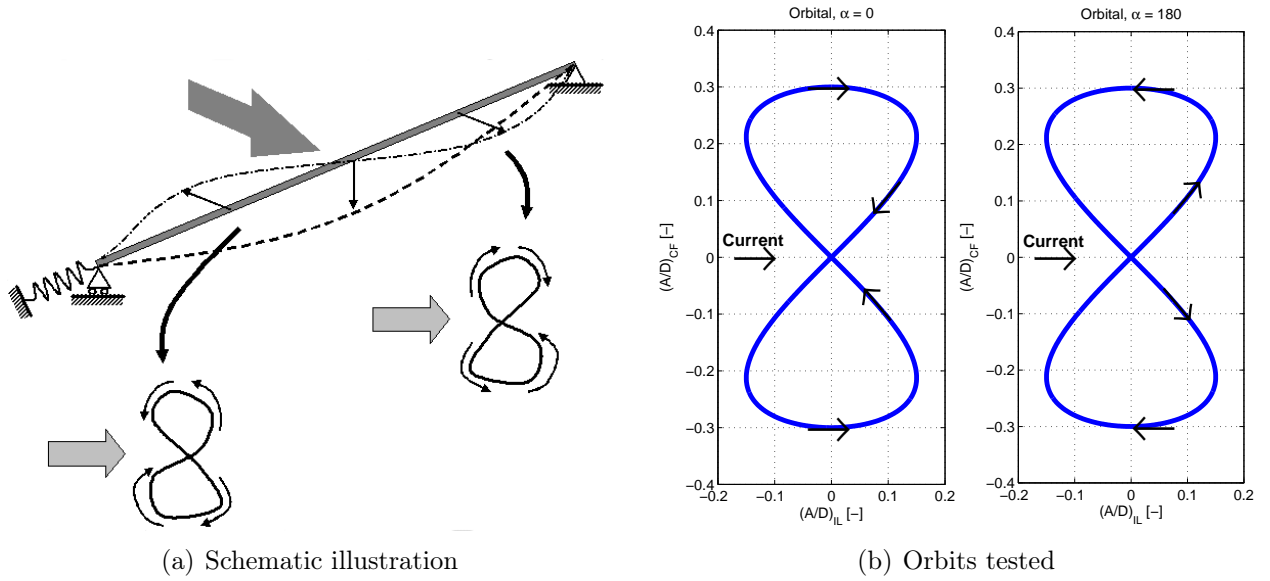
(a) Schematic illustration

(b) Orbits tested

Figure 8.2: Illustration of the 1st CF - 2nd IL scenario.

demonstrate the reliability of the reported coefficients.

The results presented in chapter 7 show that the response of a flexible beam is determined by a balance between the energy transferred through the vortex shedding process and the energy dissipated through damping. Also for the scenario 1st mode CF - 2nd mode IL, described in Figure 8.2 (a), there must be an energy balance over the length of the beam. The results in chapter 7 showed that the highest CF amplitudes, in the mid section of the beam, gave damping, while the excitation regions were seen for lower CF amplitudes closer to the ends. The two "figure of eight" cases presented in this section have moderate oscillation amplitudes, $(A/D)_{CF}$=0.3, and are chosen to represent the excitation regions somewhere between the mid segment of each half span and the two ends. The pure CF case tested confirms that this combination of frequency ($\hat{f}_{CF}$=0.163) and amplitude ratio is in the CF excitation region. Table 8.1 shows a positive dynamic excitation coefficient ($C_{e,CF}$=0.64), which is in agreement with results reported by Gopalkrishnan [15] and others. However, looking at the excitation coefficient for the two "figure of eight" cases it is seen that for the α=0 case the excitation coefficient is negative ($C_{e,CF}$=-1.4), while the excitation coefficient for α=180 is positive ($C_{e,CF}$=0.9). The same trend is also seen for the excitation coefficients in IL direction reported in Table 8.2.

Even though the two cases represent only two cross sections along the length of the oscillating beam, the results highlight the importance of orbital direction. It is seen that if the combination of first mode CF and second mode IL response (see Figure 8.2) appears, one half of the span is forced into an orbital direction that extracts energy from the system and thus reduces the oscillation amplitude for free vibrations. This finding is in agreement with the above mentioned publications. The results presented herein indicate that the

Table 8.1: Hydrodynamic coefficients CF.

Case	C_D	U_{C_D}	$C_{e,CF}$	$U_{C_{e,CF}}$	$C_{a,CF}$	$U_{C_{a,CF}}$
1dof CF , SB	1.725	0.067	0.648	0.027	3.180	0.123
1dof CF , Port	1.640	0.061	0.640	0.026	3.202	0.115
$\alpha = 0$, SB	1.662	0.065	-1.384	0.073	3.922	0.221
$\alpha = 0$, Port	1.653	0.058	-1.460	0.056	4.192	0.155
$\alpha = 180$, SB	1.956	0.079	0.916	0.036	3.171	0.126
$\alpha = 180$, Port	1.962	0.074	0.927	0.034	3.249	0.117

Table 8.2: Hydrodynamic coefficients IL.

Case	C_D	U_{C_D}	$C_{e,IL}$	$U_{C_{e,IL}}$	C_{aIL}	$U_{C_{a,IL}}$
1dof IL, SB	1.866	0.056	-0.150	0.008	0.426	0.028
1dof IL, Port	1.899	0.109	-0.195	0.014	0.360	0.066
$\alpha = 0$, SB	1.662	0.050	-0.193	0.008	-0.117	0.031
$\alpha = 0$, Port	1.653	0.095	-0.209	0.012	-0.159	0.034
$\alpha = 180$, SB	1.956	0.062	0.105	0.004	0.357	0.024
$\alpha = 180$, Port	1.962	0.115	0.063	0.005	0.322	0.063

physical explanation is that one half of the span is forced into an oscillation orbit that causes damping. Hence, the results show that the orbital direction of the "figure of eight" response is an important factor for the fluid structure interaction, in addition to oscillation amplitude and frequency in the two directions.

8.3.2   Orbit controlled by the hydrodynamic force

The second hypothesis on what determines the orbital shape is that the hydrodynamic forces from the vortex shedding process will force a flexible beam to oscillate in a certain pattern; i.e. the orbital shape is controlled by the hydrodynamic force. The flexible beam experiment discussed in chapter 7 showed a crescent shaped oscillation orbit with lobes facing downstream which means that the phase angle, α, is close to 90° (see definition in Eqn. 3.1). Continuing the investigation of the reduced response amplitude for the combination second mode IL and first mode CF, based on the second hypothesis, it must be expected that the part of the span where where excitation takes place must have this crescent shape. The second half of the span would then be forced into a pattern given by α-values close to 270°, i.e. a crescent shape with lobes facing upstream. The scenario
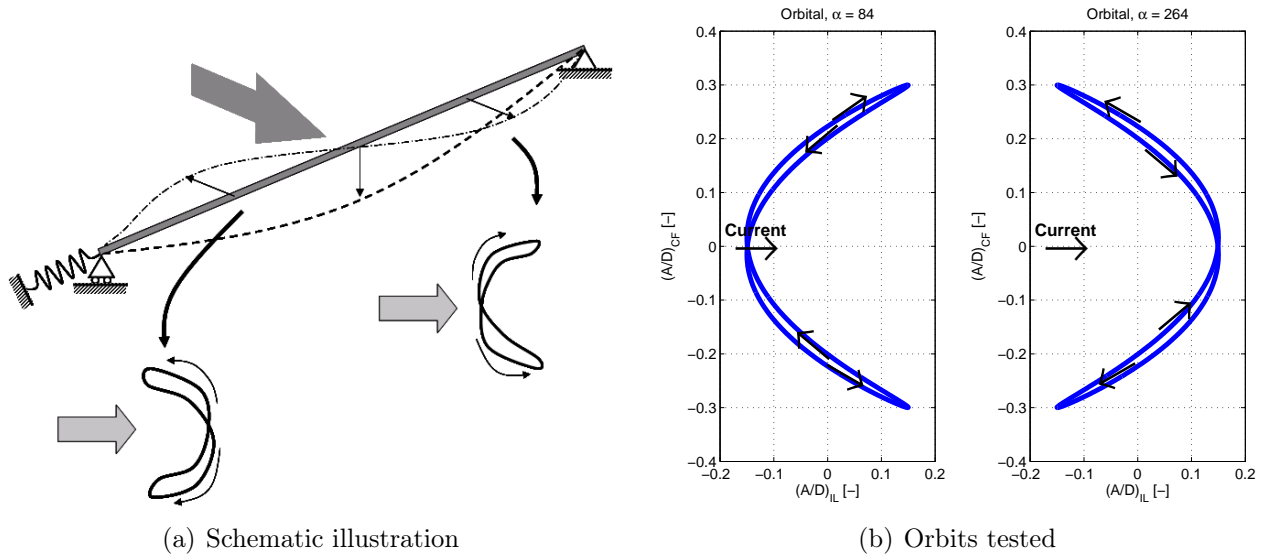
(a) Schematic illustration

(b) Orbits tested

Figure 8.3: Illustration of the 1st CF - 2nd IL scenario.

is illustrated in Figure 8.3 (a) and the tested oscillation patterns, α=84 and α=264, are shown in Figure 8.3 (b).

The excitation coefficients in CF direction, $C_{e,CF}$, for phase angles, α, between 0 and 90 are given in Figure 8.1 (a). For phase angles close to α=90 it is seen that the excitation coefficient is positive for amplitude ratios up to approximately 0.4. The results for phase angles representing the second half of the span are shown in Figure 8.4. Figure 8.4 (a) shows that the excitation coefficient for phase angles close to α=270 is positive for moderate oscillation amplitudes. This does not support the finding from the Ormen Lange experiment, i.e. different oscillation mode in IL and CF direction causes reduced oscillation amplitude. However, a closer look at the added mass coefficient reveal that the added mass coefficient has a negative value of high magnitude. The large change in added mass means that the oscillation frequency for the scenario illustrated in Figure 8.3 (a) will require a much higher reduced velocity, V_r, than the span discussed in chapter 7 and section 8.2, for the same eigenfrequency, f_0.

8.4   Extreme negative values of added mass

Figure 8.4 (b) shows added mass values as low as $C_{a,CF} = -7$ for phase angles giving positive values of the excitation coefficient. This section discusses the implication of negative added mass for a cylinder subjected to VIV.

8.4.1   Physical interpretation of added mass

The added mass coefficient, defined in Eqn. (4.11), is based on the hydrodynamic force in phase with the acceleration of the oscillating cylinder. This force component is then divided by the acceleration amplitude of the harmonic oscillation and normalized with respect to the mass of the displaced water. A positive added mass means that there is
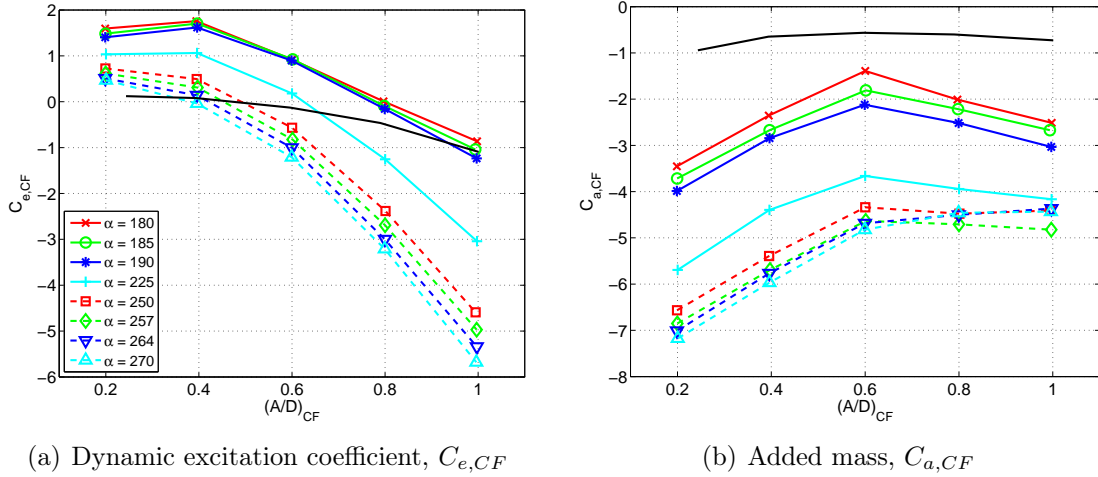
(a) Dynamic excitation coefficient, $C_{e,CF}$

(b) Added mass, $C_{a,CF}$

Figure 8.4: Results for $\hat{f}=0.147$, phase angles (α) between 180 and 270. Solid black line shows the results for pure CF.

a hydrodynamic force acting on the cylinder in the opposite direction of the acceleration. Hence, increasing values of the added mass coefficient has the same effect on an oscillating cylinder as increasing value of the mass ratio of the cylinder. Increasing the mass ratio or the added mass of a body oscillating at resonance reduces the oscillation frequency.

For negative values of added mass the hydrodynamic force in phase with acceleration will act in the same direction as the acceleration of the cylinder, i.e. in the opposite direction of the inertia force caused by the acceleration of the dry mass of the cylinder. The effect of a negative added mass coefficient, for a body oscillating at resonance, is the same as reducing the mass ratio of the oscillating system, i.e. the oscillation frequency will increase.

If a negative added mass coefficient approaches the magnitude of the mass ratio of the oscillating body, the eigenfrequency will approach infinity, i.e. if $C_a \rightarrow -\bar{m}$ then $f_{osc} \rightarrow \infty$.

8.4.2 The existence of a critical mass ratio

The existence of a critical mass ratio, for which high amplitude CF response extends to infinite values of reduced velocity (V_r), is discussed in a paper by Govardhan and Williamson [16]. The discussion is based on results from free vibration experiments where the IL motion is restrained and the product of mass ratio ($\bar{m}$) and damping ratio (ζ) is low. Response from such experiments consists of three branches; the Initial-, the Upper- and the Lower branch (see Figure 8.5 (a)). It is well known that the Lower branch is associated with an added mass coefficient of approximately -0.6, and the paper demonstrates the effect of mass ratios approaching this value ($\bar{m} \rightarrow 0.6$).

Govardhan and Williamson found a critical mass ratio of 0.54. For mass ratios lower that this value, the upper branch extends to infinite values of reduced velocity, and the lower branch ceases to exist. In the paper this is demonstrated by reporting results from an experiment with a mass ratio lower than the critical value, see Figure 8.5 (b), and
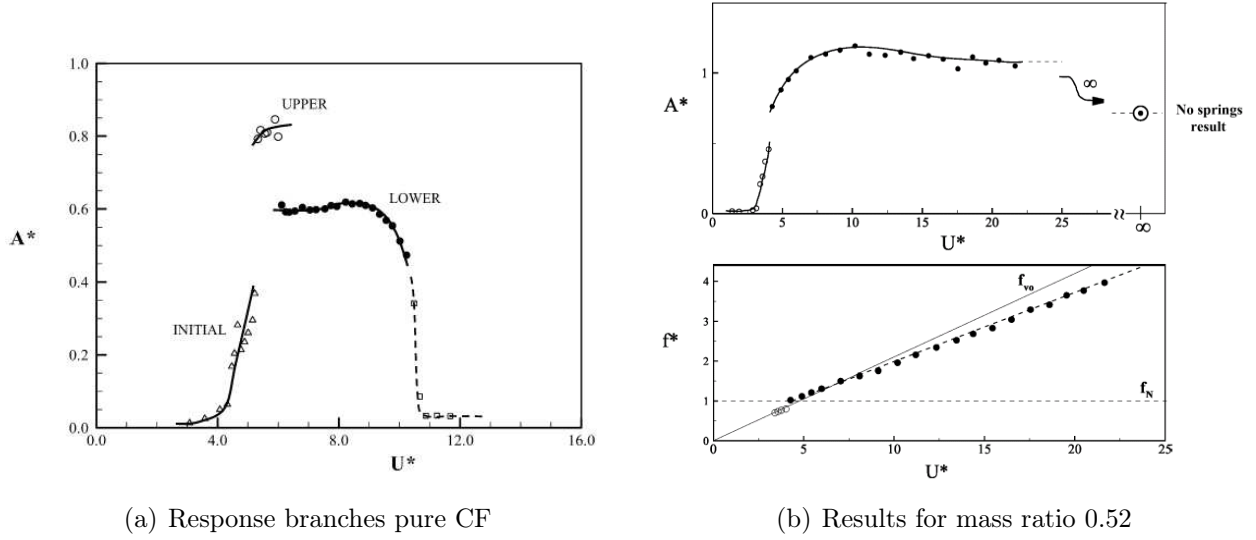
(a) Response branches pure CF

(b) Results for mass ratio 0.52

Figure 8.5: Results from Govardhan and Williamson [16]. Notation: $A^* = (A/D)_{CF}$, $U^* = V_r$, $f^* = f_{osc}/f_0$ and $f_{vo} = f_s$.

from an experiment with zero restoring force. Zero restoring force, resulting in $f_0 \approx 0$ and $V_r \rightarrow \infty$, was achieved by removing the springs used to generate the eigenfrequency of the experiment.

The pure CF results presented herein, see Figure 8.6 (b) for $(A/D)_{CF}$=0.3, show an added mass coefficient of -0.7 for the nondimensional frequencies corresponding to the Lower branch. The results also show that the added mass coefficient drops from approximately 3 for $\hat{f} = 0.163$ to -0.7 for $\hat{f} = 0.15$, a large change in added mass for a small change in oscillation frequency. The relationship between $\hat{f}$ and V_r is given by Eqn. (8.1) and it is seen that for small mass ratios, $\bar{m}$, a small change in $\hat{f}$ represents a large change in V_r for this $\hat{f}$-region.

$$V_r = \frac{1}{\hat{f}} \sqrt{\frac{\bar{m} + 1}{\bar{m} + C_a}} \qquad (8.1)$$

From Eqn. (8.1) and the definitions of the non-dimensional parameters $U^* = V_r$ and $f^* = f_{osc}/f_0$, we have the following relationships for $\hat{f}$ and C_a:

$$\hat{f} = \frac{f^*}{U^*} \qquad (8.2)$$

$$C_a = \frac{\bar{m} + 1}{(f^*)^2} - \bar{m} \qquad (8.3)$$

These relations makes it possible to compare the results from Govardhan and Williamson, Figure 8.5 (b), with the pure CF added mass results shown in Figure 8.6 (b). In Figure 8.5 (b) it is seen that the upper branch, shown as dots ($\bullet$ $\bullet$), stretches from reduced velocity 5 to 22. Using the expressions in Eqn. (8.2) and Eqn. (8.3) and the mass ratio used in the experiment, this corresponds to $\hat{f}$ from 0.2 to 0.18 and C_a from 1 to -0.425. A large change in added mass is observed for a small change in oscillation frequency. In Figure 8.6 (b) it

(a) Excitation coefficient, $C_{e,CF}$
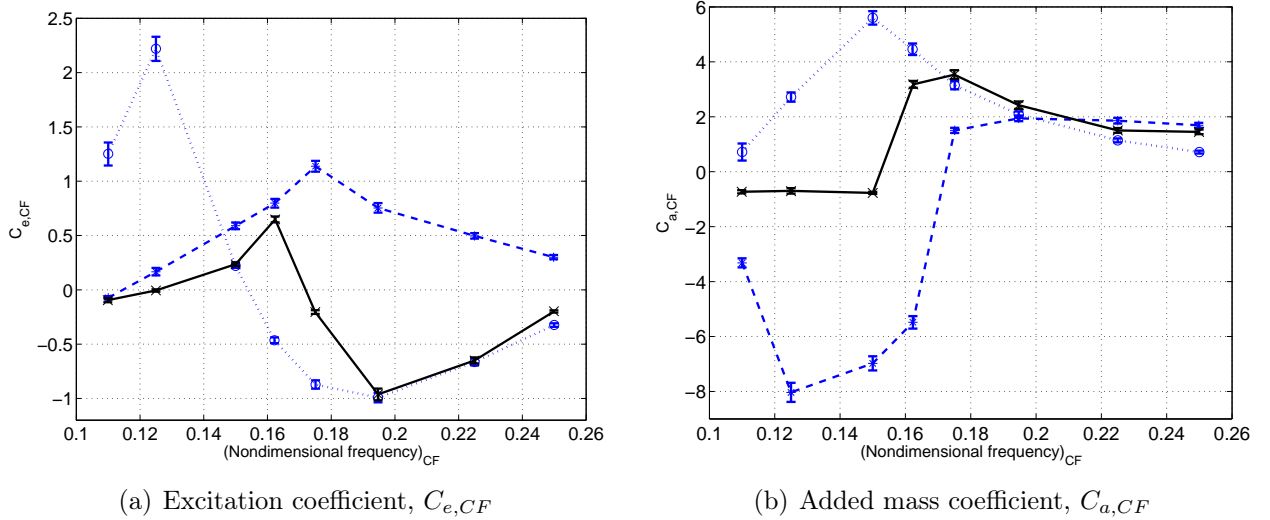
(b) Added mass coefficient, $C_{a,CF}$

Figure 8.6: Hydrodynamic coefficients for $(A/D)_{CF} = 0.3$ found from forced oscillation tests. Dotted line $(\cdot \cdot \cdot)$ represents $\alpha = 84$, dashed line (- -) represents $\alpha = 264$ and solid line represent pure CF results.

is seen that the large change in C_a takes place between $\hat{f}$=0.15 and $\hat{f}$=0.163 and that the change in C_a is from 3.1 ($\hat{f}$=0.163) to -0.7 ($\hat{f}$=0.15). Comparing the results of Govardhan and Williamson with our pure CF results show a similar trend. However, there is a shift in frequency for where the drop in added mass takes place and there is also a significant difference in the magnitude of the added mass coefficient. Some of these differences may be explained by the discussion on Reynolds number in VIV experiments given in section 2.1.5. The difference is, however, larger than expected.

The phenomenon discussed in this section, for pure CF experiments, is the same phenomenon seen as a widening of the second instability region for pure IL VIV, demonstrated in chapter 6.2.3. For the pure IL results a minimum added mass of $C_{a,IL}$=-0.2 is seen in the excitation region. Hence, the critical mass ratio in IL direction i 0.2.

8.4.3 Effect of extreme negative added mass

In the previous section the existence of a critical mass ratio, for which response will extend to infinite values of reduced velocity, for both pure CF and pure IL VIV is discussed. Based on results from the experiments presented in this thesis the critical mass ratios are 0.7 and 0.2 for pure CF and pure IL respectively. Mass ratio less than unity means that the buoyancy force exceeds the weight, which is not relevant for offshore pipelines. The critical mass ratio as such is hence not relevant to the present study, but may become important for other applications.

The results shown in Figure 8.4 (b) does, however, give $C_{a,CF}$ values between -1.5 and -7. A mass ratio of 1.36, used in the flexible beam experiment referred in this thesis, is thus less than the critical mass ratio. Hence, a nondimensional frequency $(\hat{f}_{CF})$ of 0.147 can not be reached for an orbital shape characterized by α-values from 0 to 45 and from

180 to 270 degrees. In the following the effect of these extreme negative added mass values will be discussed based on two scenarios:

1. First mode response in IL and CF with orbital shape characterized by α=264.

2. 1st mode - CF 2nd mode IL scenario as illustrated in Figure 8.3.

The excitation coefficient, $C_{e,CF}$, and added mass coefficient, $C_{a,CF}$, for orbits characterized by $\alpha = 84$ and 264 are plotted for a wide range of nondimensional frequencies in Figure 8.6, for an amplitude ratio of 0.3. The figure shows that the added mass coefficient for $\alpha = 264$ and pure CF has the same trend. For high nondimensional frequencies both excitation and added mass coefficients are positive, and there is a large drop in added mass coefficient over an $\hat{f}$ range showing positive $C_{e,CF}$.

If an orbit characterized by $\alpha = 264$ should exist, the discussion given in section 8.4.2 and the added mass coefficient shown in Figure 8.6 (b) indicate that response may prevail till infinite values of V_r for mass ratios up to 7, which is a mass ratio that covers all relevant mass ratios for offshore risers or pipelines. However, the results shown in Figure 8.6 are valid for CF amplitude ratios of 0.3 and A_{CF}/A_{IL}=2 only. For pure CF it is well known that added mass varies insignificantly with amplitude, see e.g. Gopalkrishnan [15], but this is not necessarily the situation for two degree-of-freedom motion. Figure E.6 shows negative added mass for $(A/D)_{CF}$=0.2 for $\hat{f}$=0.175, while Figure 8.6 (b) $((A/D)_{CF}$=0.3) shows positive added mass at this frequency.

For a flexible beam the modal added mass coefficient, which determines the oscillation frequency of the span, is given by Eqn. (8.4) (see also chapter 7).

$$\bar{C}_{a,IL/CF} = \frac{\int_0^L C_{a,IL/CF}(y)\Phi^2_{IL/CF}(y)\ dy}{\int_0^L \Phi^2_{IL/CF}(y)\ dy} \qquad (8.4)$$

For the 1st mode CF - 2nd mode IL scenario illustrated in Figure 8.3 one half of the span will experience negative added mass. This will change the modal added mass coefficient significantly, and high reduced velocities will then be required in order to achieve the given oscillation frequency. Oscillation modes of higher order may therefor be excited at a lower flow velocity than the 1st mode CF - 2nd mode IL.

From the discussion above it is seen that for a span oscillating at higher order mode numbers, sections of the span may be forced into oscillation patterns giving large negative added mass values. These sections will then contribute significantly to the modal mass of the span, and thus change the oscillation frequency significantly. Eqn. (8.1) shows the relationship between the reduced velocity, which is based on the eigenfrequency of the span in still water (f_0), and the nondimensional frequency. For a low mass ratio condition, the equation shows that for decreasing values of added mass increasing values of the reduced velocity is required in order to keep the nondimensional frequency constant. For the 1st mode CF - 2nd mode IL scenario illustrated in Figure 8.3 (a) it is seen that half the span will oscillate in a pattern giving large negative $C_{a,CF}$. For a higher mode number scenario, e.g. 2nd mode CF - 3rd mode IL, a smaller portion of the span may be forced into orbits giving negative $C_{a,CF}$. Thus, even if this mode has a higher eigenfrequency in still water,
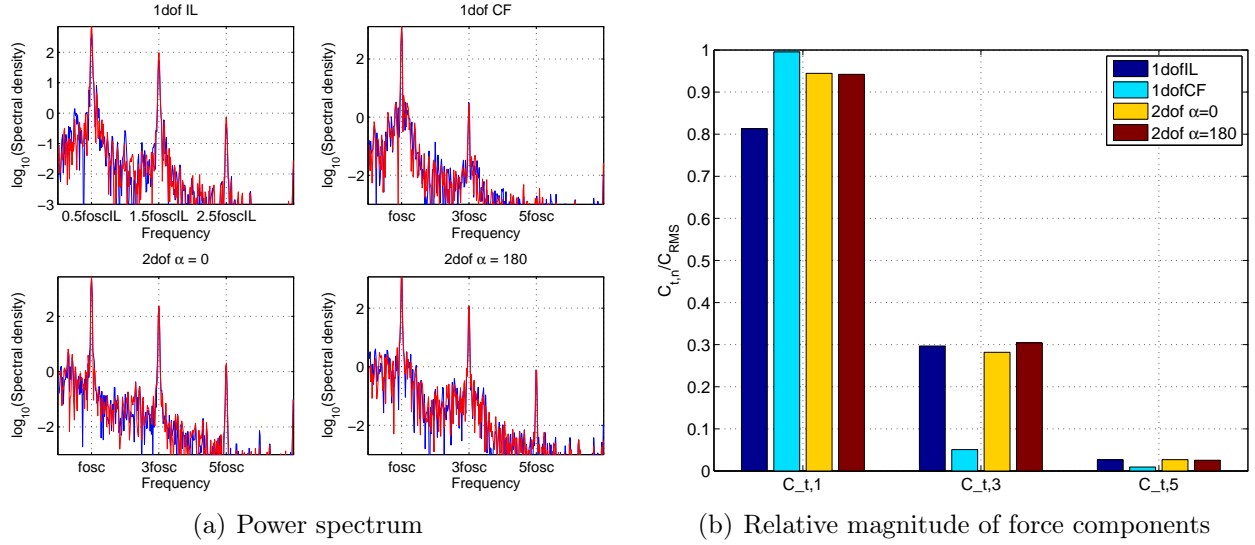
(a) Power spectrum

(b) Relative magnitude of force components

Figure 8.7: Force components in CF direction.

the V_r required to achieve a certain nondimensional frequency may be lower. The 1st mode CF - 2nd mode IL may therefore not be a stable oscillation mode.

8.5 Higher order harmonic forces

An important finding from the experiments presented in this thesis is the existence of significant hydrodynamic forces at multiples of the oscillation frequency. Forces at multiples of the oscillation frequency, also known as higher order harmonic forces, have been reported in two resent papers by Jauvtis and Williamson ([24] and [63]) and response due to higher order harmonic forces has been reported by Vandiver et al. [60]. Chapter 6 shows higher order harmonic forces also for pure IL vibrations. These forces are seen for the 2nd instability region which is associated with the 2S vortex shedding mode. In this section higher order harmonic forces are discussed based on the results from the combined IL and CF experiments.

Figure 8.7 (a) shows power spectra of CF force for 4 cases. These are a pure IL case (with label 1dof IL), a pure CF case (with label 1dof CF) and the two "figure-of-eight" cases illustrated in Figure 8.2 (b) (with labels 2dof α=0 and α=180). The four cases are characterized by nondimensional frequency $\hat{f}_{CF} = \hat{f}_{IL}/2$=0.163 and amplitude ratio $(A/D)_{CF} = 2(A/D)_{IL}$=0.3. For the three cases where there are CF oscillations, the frequencies corresponding to the oscillation frequency (f_{osc}), $3 \cdot f_{osc}$ and $5 \cdot f_{osc}$ are shown on the x-axis. For the pure IL case (1dof IL) the frequency corresponding to 0.5 times the IL oscillation frequency is the expected frequency of the CF force as it is well known that the frequency of the vortex shedding force in IL direction is twice the frequency in CF direction. The higher order components then correspond to $1.5 \cdot f_{osc,IL}$ and $2.5 \cdot f_{osc,IL}$. The power spectra show that there are force components at all three frequencies for the two "figure of eight" cases and the pure IL case, i.e. the three cases with IL oscillation. For the pure CF case there is a peak in the power spectrum at $3 \cdot f_{osc}$, but the spectral density

(a) Power spectrum

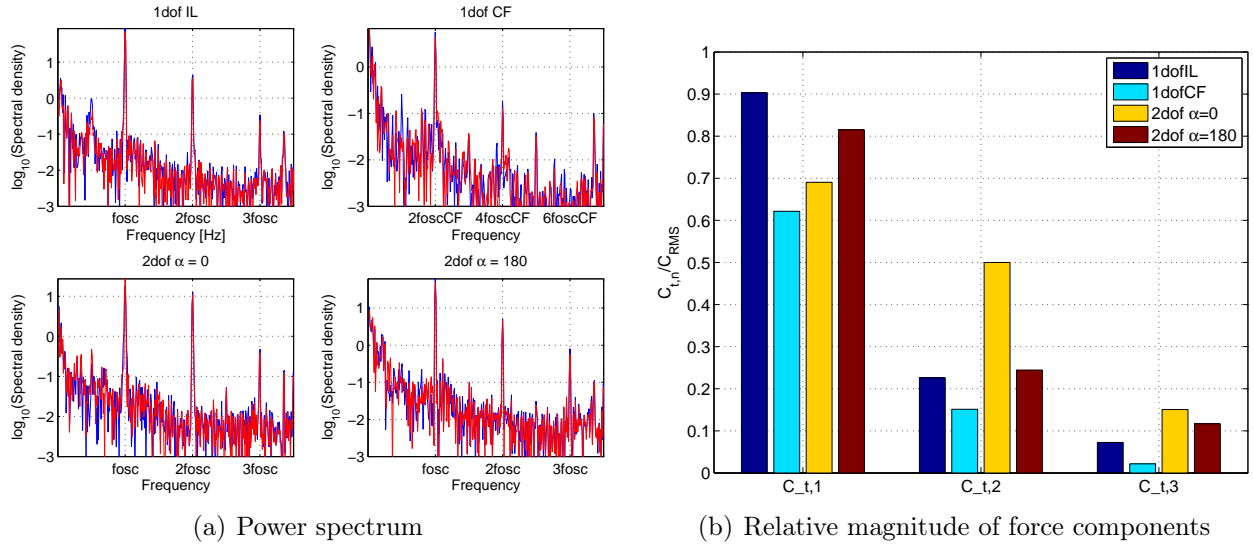(b) Relative magnitude of force components

Figure 8.8: Force components in IL direction.

is almost two order of magnitude lower than for the other cases.

In Figure 8.7 (b) the magnitude of the force components are shown relative to the RMS value of the oscillating force. The coefficients are defined in chapter 4.4 (see Eqn. (4.12) and Eqn. (4.16)), and the values are tabulated in Table 8.3. Figure 8.7 (b) shows that the magnitude of the force component at three times the oscillation frequency is approximately 30% of the force component at the oscillation frequency, for the three cases where IL oscillations are present. For the pure CF case the relative magnitude of the higher order component is only about 5%. The force component at 5 times the oscillation frequency shows negligible magnitude for all four cases.

Figure 8.8 shows the frequency components of the hydrodynamic force in IL direction, and the results are presented in a similar way as for the CF force in Figure 8.7. Note that f_{osc} here refers to the IL oscillation frequency, except for the pure CF case. The power spectra show higher order components also for the hydrodynamic force in IL direction. The frequencies of these higher order components are 2 and 3 times the IL oscillation frequency, corresponding to 4 and 6 times the CF frequency for the pure CF case. Figure 8.8 (b) and Table 8.4 show that the magnitude of the higher order components varies more between the four cases in IL direction than in CF direction. The ratio between the force component at two times the oscillation frequency and the force component at the oscillation frequency is approximately 25% for the pure IL case, approximately 70% for the α=0 case and approximately 30% for the α=180 case. The magnitude of the oscillating hydrodynamic force in IL direction for the pure CF case is small compared to the three other cases, see Table 8.4, and the higher order harmonic component is therefore negligible even if the relative magnitude is approximately 20%.

The discussion so far has shown that higher order harmonic forces seem to be related to IL oscillations, and that the main higher order force component is 3 times the oscil-
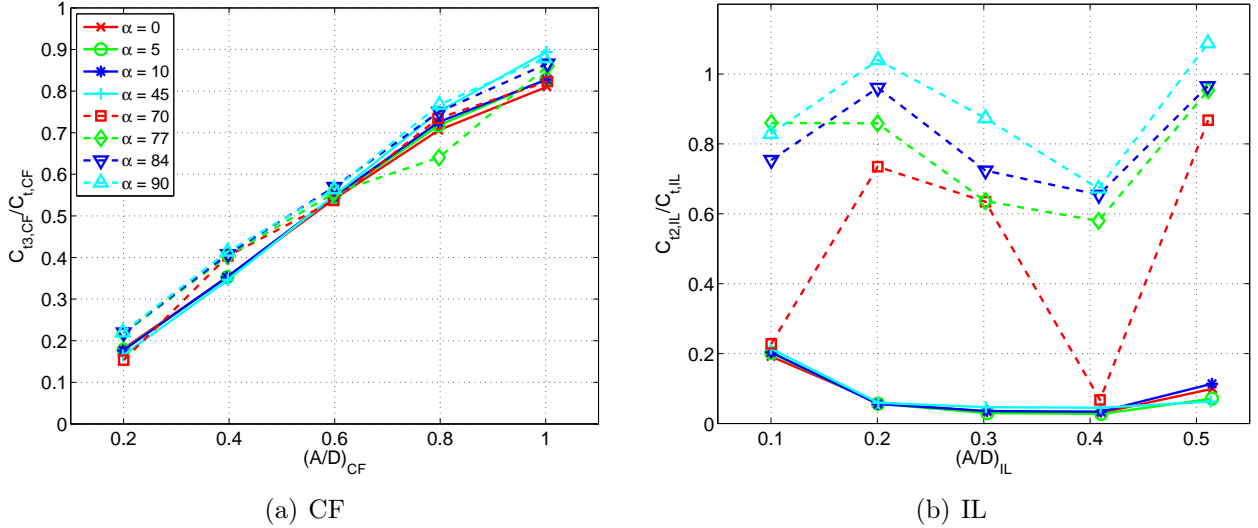
(a) CF

(b) IL

Figure 8.9: Higher order harmonic forces for $\hat{f}_{CF} = 0.147$.

lation frequency ($C_{t3,CF}$) in CF direction and 2 times the oscillation frequency ($C_{t2,IL}$) in IL direction. In Figure 8.9 $C_{t3,CF}/C_{t,CF}$ (a) and $C_{t2,IL}/C_{t,IL}$ (b) are shown for amplitude ratios from 0.2 to 1.0 and phase angles, α, between 0 and 90. The nondimensional frequency of 0.147 is the same $\hat{f}_{CF}$ as seen in the flexible beam experiment discussed in chapter 7. The figure clearly shows that the relative magnitude of the higher order CF force component increases with increasing amplitude ratio. It is, however, important to note that a fixed ratio of 2 between CF and IL oscillation amplitude has been used for all cases tested. From comparison with pure CF and pure IL results it is reasonable to believe that the increased relative magnitude of $C_{t3,CF}$ is due to increased IL oscillation amplitude (results for pure IL are given in Figure 6.18). Comparing Figure 8.9 (a) with the results for $(A/D)_{CF}$=0.3 in Figure 8.7 it is seen that also for $\hat{f}_{CF}$=0.147 the ratio $C_{t3,CF}/C_{t,CF}$ is approximately 0.3 for this amplitude ratio.

The results for $C_{t2,IL}/C_{t,IL}$ given in Figure 8.9 (b) show that only some orbital patterns give significant higher order forces. For these patterns the relative magnitude of the higher order forces seem to be independent of amplitude ratio. Interestingly, the orbits giving higher order IL forces corresponds to the shapes observed in the flexible beam experiment. It is also seen that the irregular behavior of the α=70 case corresponds to the jump between the two branches of $C_{e,CF}$ and $C_{a,CF}$ seen in Figure 8.1.

The higher order harmonic forces for all combined IL and CF motion tests performed are shown in Figures E.10 to E.15 in Appendix E. The observed trend is that the relative magnitude of the higher order harmonic force at 3 times the oscillation frequency in CF direction increases with increasing oscillation amplitude. For the higher order harmonic force in IL direction the picture is more complex, and a general trend is not seen. The higher order harmonic forces in both directions seem, however, to be related to IL oscillations as none of the 38 pure CF cases tested showed significant force components at other frequencies than the oscillation frequency. The vast majority of the publications on VIV

Table 8.3: Total dynamic force coefficients in CF direction.

Case	C_{RMS}	ϕ	$C_{t,1}$	$C_{t,3}$	$C_{t,5}$
1dof IL, SB	1.125	na	0.915	0.334	0.030
1dof IL, Port	1.513	na	1.274	0.464	0.039
1dof CF, SB	1.715	22.47	1.707	0.087	0.016
1dof CF, Port	1.730	22.01	1.720	0.086	0.016
$\alpha = 0$, SB	2.505	-35.70	2.366	0.706	0.067
$\alpha = 0$, Port	2.651	-35.36	2.517	0.761	0.073
$\alpha = 180$, SB	1.933	30.46	1.821	0.588	0.049
$\alpha = 180$, Port	1.968	30.15	1.859	0.596	0.048

are based on pure CF experiments, both free and forced vibration, and this is probably the reason why higher order harmonic forces only recently have attracted attention.

For a free vibration experiment where an elastically mounted rigid cylinder (in two degrees-of-freedom) is tested in constant flow velocity, the higher harmonics are expected to be seen in the measured force only. As VIV is a resonance phenomenon and the apparatus has only one eigenfrequency in each direction, there are no other eigenfrequencies "available" to be excited by the higher order harmonic force. Hence, only small components of higher order harmonic response are expected to be seen. For a flexible beam, on the other hand, there are several eigenfrequencies related to the various eigenmodes of the beam. The flexible beam discussed in chapter 7 has an eigenfrequency for the second mode of approximately 3 times the eigenfrequency corresponding to the first mode. For this situation it is possible for the 3rd harmonic force component to excite the second CF mode, even if the first CF mode is the dominating one. This is seen as a plausible explanation to the presence of higher order modes seen from modal analysis of the experiment.

If a free spanning pipeline or riser subjected to VIV responds to higher order harmonic forces, Vandiver et al. [60] has shown that this is very important for the fatigue life of the structure. As both the frequency and the mode number is higher than for the dominating mode, the higher order harmonics contribute significantly to fatigue damage. The next step of the investigation of higher order harmonic forces should be to investigate for which conditions these forces injects energy to- and extracts energy from the system. In order to investigate this by forced oscillation experiments an oscillation amplitude at the higher order harmonic frequency must be included so that the force can be decomposed into one component in phase with velocity and one component in phase with acceleration.

Table 8.4: Total dynamic force coefficients, IL.

Case	C_{RMS}	ϕ	$C_{t,1}$	$C_{t,2}$	$C_{t,3}$
1dof IL, SB	0.496	-19.71	0.448	0.112	0.036
1dof IL, Port	0.453	-28.80	0.406	0.103	0.032
1dof CF, SB	0.185	na	0.115	0.028	0.004
1dof CF, Port	0.164	na	0.103	0.024	0.006
$\alpha = 0$, SB	0.352	-121.47	0.243	0.176	0.053
$\alpha = 0$, Port	0.352	-127.30	0.267	0.165	0.052
$\alpha = 180$, SB	0.454	16.64	0.370	0.111	0.053
$\alpha = 180$, Port	0.409	11.15	0.328	0.105	0.048

8.6 Drag amplification due to VIV

Returning to the four cases used when discussing the 1st mode CF - 2nd mode IL scenario in Figure 8.2, it is seen from Table 8.1 and Table 8.2 that also the drag coefficient varies between the cases. The tables show that the pure IL case gives a higher drag coefficient than the pure CF case, the α=180 case gives a higher drag coefficient than the α=0 cases and that the pure IL case gives the best approximation to α=180 while the pure CF case gives the best approximation to α=0. The latter observation is, however, likely to be a coincidence. Looking at Figure E.7 in Appendix E it is seen that the drag coefficient ratio between the two orbital directions is a function of the oscillation amplitude.

Figure 8.10 shows the drag coefficient for all cases tested at $\hat{f}_{CF}$=0.147. The figure shows that orbits characterized by α between 180 and 270 (figure b) give higher drag coefficient than the orbits characterized by α between 0 and 90 (figure a). The flexible beam results show orbits corresponding to α values between 70 and 90. In Figure 8.10 it is seen that these shapes give the lowest drag coefficient. In chapter 7 the orbits representing the lowest response amplitudes were approximated by $\alpha \approx 70$, while the highest response amplitudes (close to the mid section of the span) were approximated by $\alpha \approx 85$. It is seen that these are the orbits that give the lowest drag coefficient.

Looking at the results for all cases tested, see Appendix E, the general trend is that orbits characterized by α close to 90 give the lowest drag coefficient.

For the two 1st mode CF - 2nd mode IL scenarios illustrated in Figure 8.2 and 8.3, the results presented in this section predict an unsymmetrical static drag force over the span. This may influence the the modeshape of the oscillation, the eigenfrequency and also the ratio between the eigenfrequencies in IL and CF directions.

Several models for drag amplification due to VIV have been proposed. Blevins [5] and
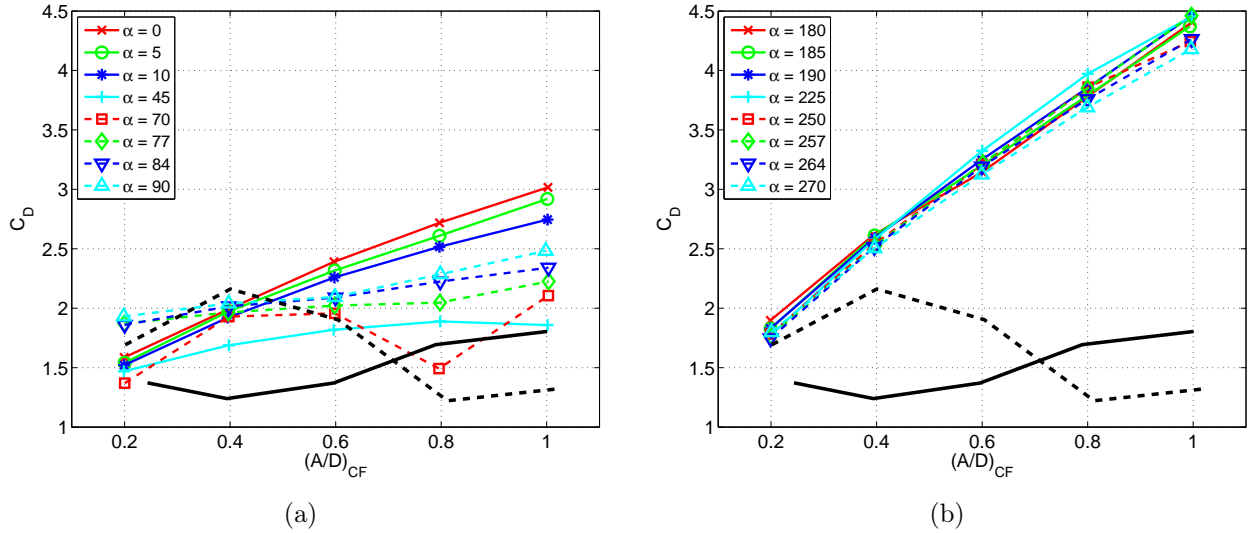
(a)

(b)

Figure 8.10: Drag coefficients for $\hat{f}_{CF} = 0.147$. Results for pure IL is shown as a dashed black line (- -), and results for pure CF as a solid black line.

Vandiver [57] have proposed two models for drag amplification based on the CF oscillation amplitude, while Skop [46] has proposed a model containing the oscillation frequency and Strouhal frequency in addition to the amplitude. The results presented herein do, however, indicate that also the shape and direction of the orbital path are important parameters for the drag coefficient.

8.7 Vortex shedding modes

Flow visualization by PIV has been carried out for the two "figure of eight" cases presented in detail in this chapter, see Figure 8.2 (b). Implementation of a new PIV system for use in the laboratories at NTNU was part of Dr. K.B. Skaugset's post. doc. project, and the experiment presented in this thesis (Phase III) was used as test case. The results shown in Figure 8.11 and Figure 8.12 are from a paper by Aronsen, Skaugset and Larsen [2].

Contour plots of vorticity are shown for the α=0 case in Figure 8.11 and for the α=180 case in Figure 8.12. The figures show the vorticity behind the cylinder at 6 time instances over one oscillation cycle. In addition to the vorticity plots, time traces of IL and CF forces have been included. The positions of the cylinder along the orbit, where the vorticity plots are taken, are also shown.

Comparing the two figures the most obvious observation is that the wake of the α=180 case is wider than the wake of the α=0 case. It looks like the vorticies in Figure 8.12 disappear out of the picture over the top and bottom boundary while the vorticies in Figure 8.11 to a larger extent line up behind the cylinder. In the following the vorticity plots are described with reference to the vortex shedding modes described in a paper by Williamson and Govardhan [62].
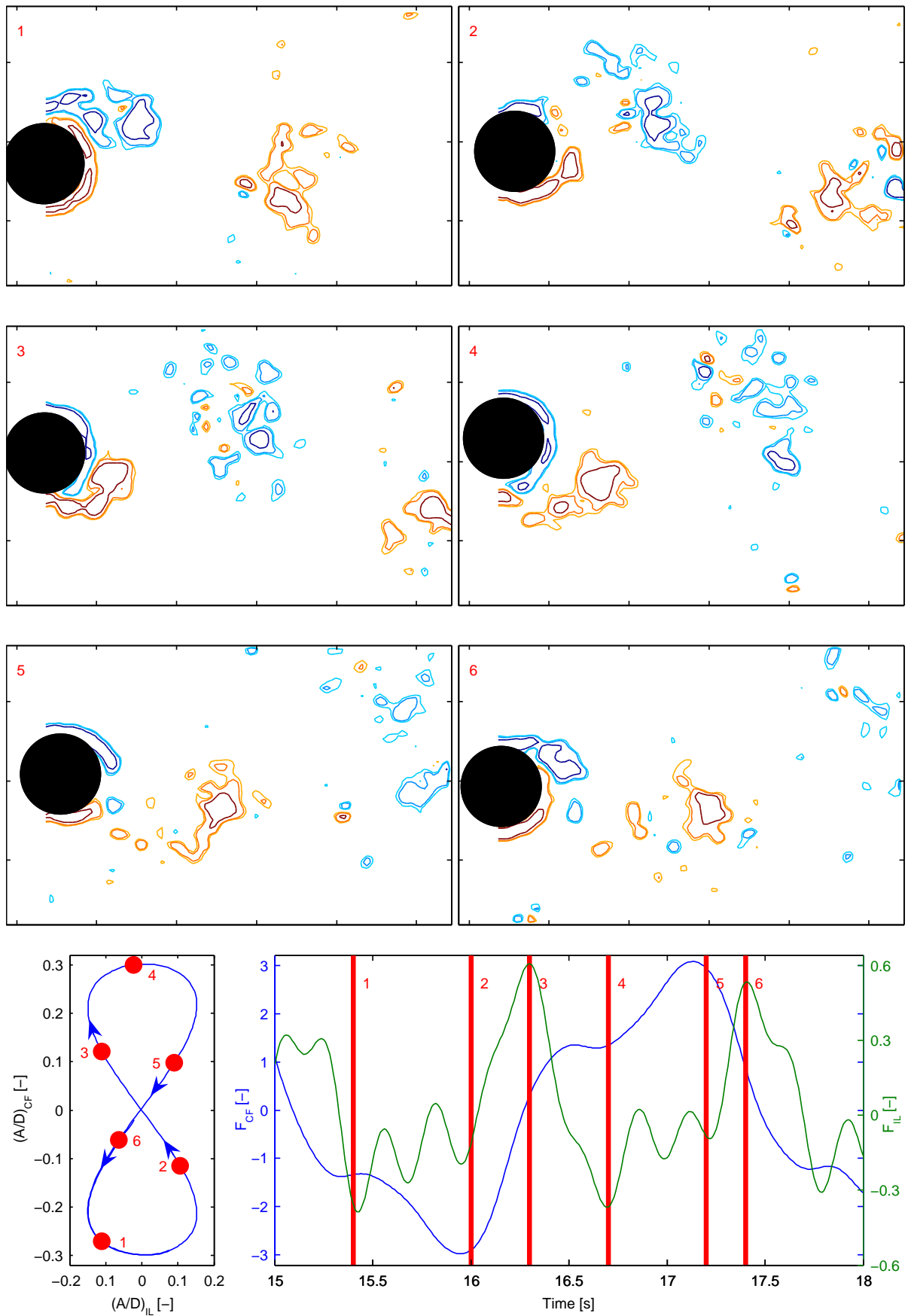
Figure 8.11: PIV results for α=0, $\hat{f}_{CF}$=0.163 and $(A/D)_{CF}$=0.3.
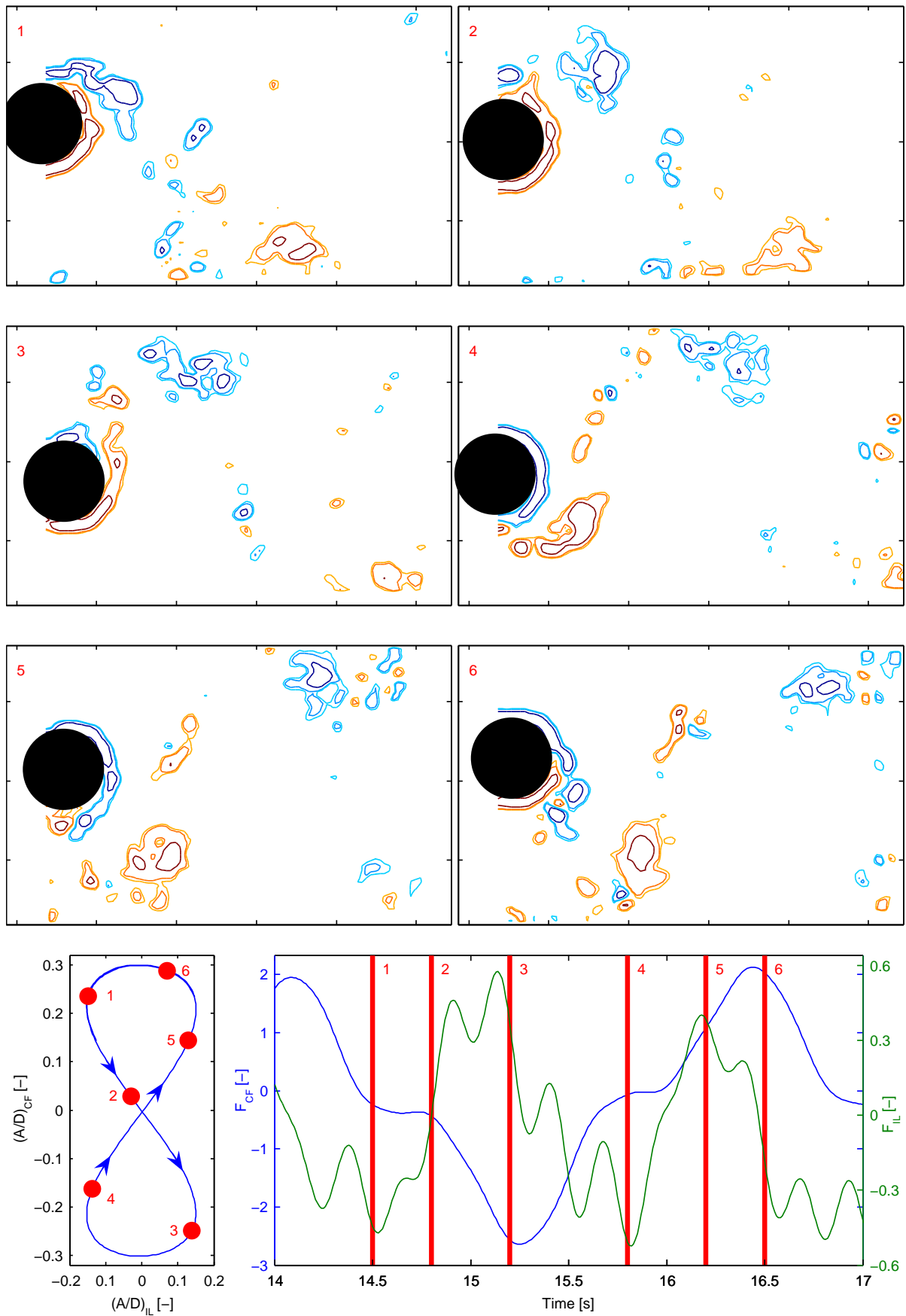
Figure 8.12: PIV results for α=180, $\hat{f}_{CF}$=0.163 and $(A/D)_{CF}$=0.3.

The $\alpha = 0$ case (Figure 8.11) resembles the 2C vortex shedding mode. Picture 1 shows the vorticity behind the cylinder when the cylinder is close to the lower dead end of the CF motion. The picture indicate that two vortices, with the same rotational direction, have just been shed from the top of the cylinder. The CF force is slightly negative and the formation of a vortex can be seen under the cylinder. In picture 2 the cylinder is moving upwards and in the opposite direction of the flow, giving high relative velocity. The vortex developing under the cylinder is stronger than in picture 1 and the CF force is at a minimum. The two vortices that were shed from the top of the cylinder in picture 1 can still be seen in picture 2. In picture 3 two vortices are about to be shed under the cylinder. The CF force is approximately zero and the cylinder is still moving upwards but with a component in the opposite direction of the flow. It is seen that vortices have been shed close to the center of the orbit, which explains the narrow wake. The two vortices shed under the cylinder are best seen in picture 4. Picture 4 to 6 is similar to picture 1 to 3 but the vortex shedding takes place at the top and underneath the cylinder respectively.

The $\alpha = 180$ case (Figure 8.12) resembles the 2T vortex shedding mode. The formation of the mode is best seen in picture 1 through 3. In picture 1 the cylinder is close to the top dead end of the CF motion, moving downwards and in the direction of the flow, i.e. low relative velocity. A vortex has just been shed from the top of the cylinder and the CF force is close to zero. It is seen that the vortex is shed close to the maximum CF oscillation amplitude, giving a wide wake. In picture 2 the cylinder is still moving downwards and in the direction of the flow. The position is close to the center of the orbit. It is seen that the shear layer under the cylinder extends all the way to the top of the cylinder. Both the IL and CF force are close to zero for this condition. In picture 3 it is seen that two additional vortices, of opposite rotational direction, have been shed from the top of the cylinder. The 2T mode is seen in this picture. The position of the cylinder is close to the minimum CF oscillation amplitude. A vortex is formed under the cylinder giving a negative CF force.

For both phase angle cases, $\alpha = 0$ and $\alpha = 180$, it is seen that the vortices are shed where the relative velocity between the flow and the cylinder is close to maximum. In the $\alpha = 180$ case a vortex is formed at the top of the cylinder when the cylinder is moving in positive CF direction, giving excitation. For the $\alpha = 0$ case the vortex is formed on the other side, giving damping. As pointed out by Jeon and Gharib [25], the IL oscillation is controlling the phase of the shedding. But as seen from the present study, also the vortex shedding mode can be changed by changing the phase of the IL oscillation relative to CF.

The force measurements are taken on each end of the cylinder while the pictures used to generate the vorticity plots are from the center of the cylinder. For general use of force coefficients and interpretation of the vorticity plots, it is important to prove that the vortex shedding process is correlated along the full length of the test cylinder. Table 8.5 shows the correlation coefficient (see Eqn. (4.17)) in IL and CF direction. The table shows that there is a high correlation coefficient in CF direction ($\rho_{xy,CF}$=0.99), while the correlation in IL direction is slightly lower ($\rho_{xy,IL}$=0.92). The hydrodynamic coefficients in IL direction also show a larger difference between the two sides compared with the corresponding coefficients in CF direction. In the discussion of the vorticity plots given above, the focus has hence been on the force in CF direction.

Table 8.5: Correlation coefficients.

Case	ρ_{IL}	ρ_{CF}
1dof IL	0.970	0.974
1dof CF	0.853	0.993
2dof, $\alpha = 0$	0.919	0.988
2dof, $\alpha = 180$	0.951	0.994

8.8 Implications for a flexible beam subjected to VIV

The motivation for performing the forced oscillation experiments reported in this thesis is to gain knowledge of the hydrodynamic forces acting on a cylinder in order to increase the understanding of the response of a flexible beam, such as a riser or a free spanning pipeline, subjected to VIV. The data set is far from large enough to build a model for prediction of VIV, but a number of findings important for the response of a flexible beam has been addressed in the preceding sections. These can be summarized in the following:

1. Large CF excitation forces. $C_{e,CF}$ values in excess of what is previously known from pure CF experiments.

2. Importance of shape and direction of the orbital path.

3. Large variation in added mass, for shapes and directions of the orbital path. Extreme negative values are observed. The added mass seems to have a stronger dependency on amplitude than observed for pure CF experiments.

4. Higher order harmonic forces for cases where IL oscillations are present.

5. Variation of drag coefficient.

These are all findings that have implication for the response of a flexible beam. These implications are addressed in the subsequent sections.

8.8.1 On orbital shape

Figure 8.13 shows results from a free vibration experiment reported by Dahl et al. [9]. The figure shows the orbits observed for ratios of the eigenfrequency in IL and CF between 1.0 and 1.9 for increasing reduced velocity. The observed oscillation patterns indicate that the ratio between the eigenfrequencies in the two directions is an important parameter for the shape of the orbit. The figure indicates that crescent shaped orbits are more likely for frequency ratios close to 1 while "figure of eight" shaped orbits are more likely for frequency ratios close to 2. However, the shape of the orbital path changes with reduced velocity.

Results from an experiment reported by Jauvtis and Williamson [24] are shown in Figure 8.14. The eigenfrequency ratio in this experiment is 1 and the figure shows a large variation of orbital shape for increasing reduced velocity. An important difference between the two experiments reported in Figure 8.13 and 8.14 is the mass ratio. The mass ratio for
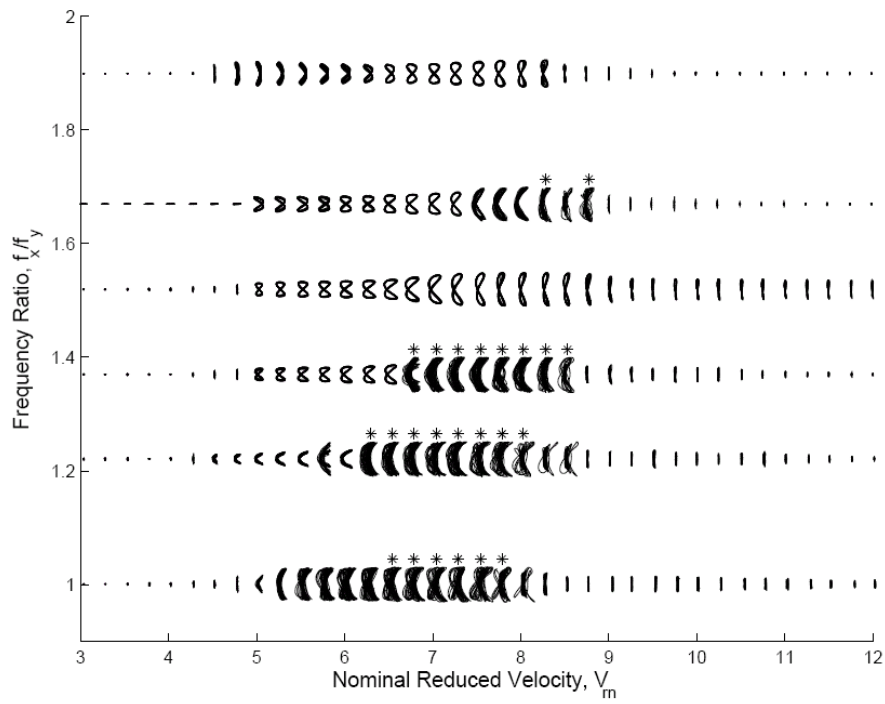
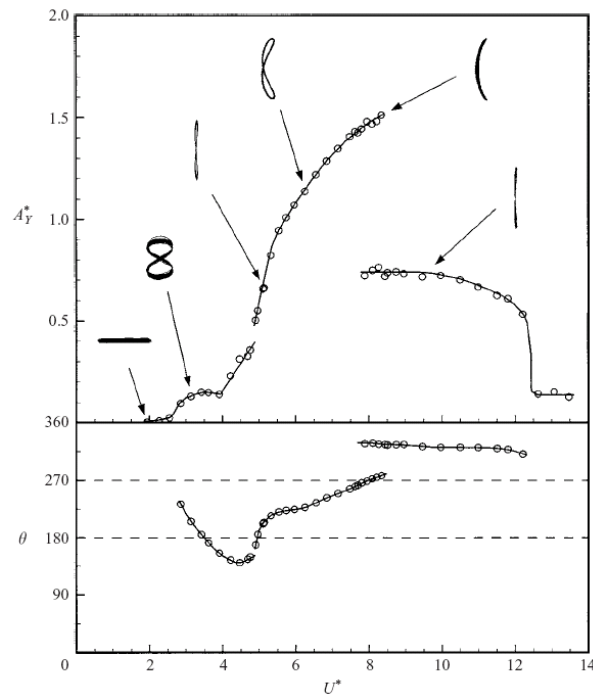Figure 8.13: Orbits from a free vibration experiment by Dahl et al. [9].

Figure 8.14: Orbits from a free vibration experiment by Jauvtis and Williamson [24]. Notation: $U^* = V_r$.

the results in Figure 8.13 is approximately 5 while the the results in Figure 8.14 are for a mass ratio of approximately 1. The latter results are thus more influenced by a change in added mass.

The results presented in this thesis show that there are some orbital shapes that can not exist for rigid cylinder experiments due to a negative excitation coefficient. However, the results also show the importance of both the shape and direction of the orbital path, for the hydrodynamic force acting on a cylinder subjected to VIV. Understanding what determines the response orbit would therefore be important for being able to predict the response of a flexible beam. In the following some of the important factors are highlighted.

In chapter 6 it is shown how the IL response frequency, for pure IL oscillation, controls the frequency of the CF hydrodynamic force. For response in CF direction it can be expected that the CF response frequency controls the hydrodynamic force frequency in IL direction. This is because the hydrodynamic forces are significantly stronger in CF than for IL. The hydrodynamic force frequency in IL direction is then two times the CF response frequency. Whether this IL force will excite the system and cause IL response must then be expected to depend on several factors; two important ones are eigenfrequency ratio and mass ratio:

- VIV is a resonance phenomenon and the frequency of the IL force must thus interact with the eigenfrequency in IL direction in order for IL response to take place.

- Added mass is changing the oscillation frequency, in both directions, from the eigenfrequency in still water. The effect of added mass, i.e. how much the oscillation frequency changes relative to the eigenfrequency, depends on the mass ratio of the cylinder.

The two bullet points highlight that both eigenfrequency ratio and mass ratio should be important parameters for whether IL excitation will occur or not. The results in Figure 8.13 and 8.14 indicate the same. For pure IL VIV, see Chapter 6, the nondimensional damping parameter determines the response amplitude in IL direction. Structural damping must be expected to be important for IL response amplitude also for combined IL - CF response. However, Chapter 7 indicates that there can be a transfer of energy between the two directions.

Once IL response takes place, and a "figure of eight" response motion is seen, the results presented in this thesis show that the hydrodynamic coefficients changes significantly from what is seen for pure CF response. From flow visualization of two orbits of opposite directions, see section 8.7, it is seen that it is in fact the IL motion that controls the phasing of the vortex shedding process. This is an observation also made by Jeon and Gharib [25].

For increasing values of the reduced velocity, V_r, the CF oscillation frequency is expected to change. Since the frequency of the hydrodynamic force in IL direction follows the response frequency of the CF motion, the orbit of the response must also be expected to change. As an interaction between the frequency of the IL force and the eigenfrequency in IL direction is required in order to get response, it is seen from Figure 8.13 and 8.14 that no IL response is seen for high reduced velocity associated with high CF oscillation frequency. A possible reason for this is that the frequency of the IL force is too high to

excite the IL eigenfrequency.

For a free spanning pipeline the mass ratio may change for various operational phases during its design life, i.e. empty in temporary phase after installation, water filled during system pressure test and various content densities during operation. A pipeline installed on uneven seabed may also have free spans with a large range of eigenfrequency ratios (between IL and CF direction) since the eigenmodes will be influenced by the boundary conditions and vertical displacements (sag). Varying pressure and temperature may also influence the effective axial force of the pipe and hence also the eigenfrequencies. As both mass ratio and eigenfrequency ratio seem to be important parameters for the response due to VIV, a better understanding of what causes the various oscillation patterns is important for being able to predict response and thus fatigue damage more accurately.

8.8.2   On dominating response mode

For a free vibration experiment of an elastically supported rigid cylinder, such as the one reported by Jauvtis and Williamson in Figure 8.14, there is only one eigenfrequency in each direction. For a flexible beam, such as a riser or free spanning pipeline, there are several eigenfrequencies and associated eigenmodes in the two directions that may be excited by the vortex shedding process. Which eigenmode that is excited is obviously important for the fatigue damage. From the results presented in this thesis it is seen that the hydro-dynamic coefficients are strongly dependent on both shape and direction of the response orbit. Hence, for flexible beams oscillating at other modes than 1st mode CF - 1st mode IL, there are sections of the span that will be forced into a pattern that is not seen in rigid cylinder experiments. The influence from such sections on the response of a flexible beam, will be addressed in the following.

The effect of the three basic hydrodynamic coefficients ($C_{e,IL/CF}$, $C_{a,IL/CF}$ and C_D), on the response of a flexible beam, is summarized below:

- The dynamic excitation coefficients ($C_{e,IL/CF}$) represent the energy transfer between the fluid and the cylinder. For a flexible beam responding to VIV there must be a balance over the span between the energy injected through the vortex shedding process and the energy extracted through damping. Chapter 7 indicates that there may be a transfer of energy between the two directions (IL and CF). Hence, in order to determine whether a certain mode can be excited and to determine the response amplitude, the total energy balance must be considered.

- Added mass ($C_{a,IL/CF}$) may change the response frequency so that the span does not oscillate at the still water eigenfrequency. Obviously the response frequency must be within the excitation region for response to take place.

- The drag force (C_D) may change the static configuration and thus the eigenmodes and eigenfrequencies of the span. It is seen from the results presented herein that the drag coefficient is a function of shape and direction of the response orbit, which may lead to an unsymmetrical drag force acting on a span. The eigenmode, at which oscillation takes place, is the eigenmode corresponding to the static configuration including the mean drag force in IL direction.
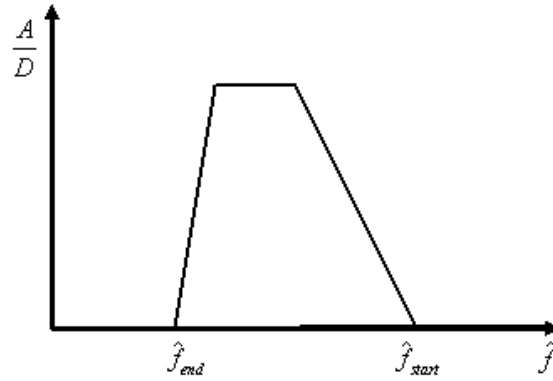
Figure 8.15: Principle sketch of the excitation region.

For higher order modes different vortex shedding modes must be expected over the length of the span, see section 8.7. Techet et al. [54] have shown vortex splitting between 2S and 2P vortex shedding modes for a tapered cylinder. It is thus reason to believe that more than one vortex shedding mode can exist over the length of a span oscillating at higher order modes.

In chapter 8.4 the effect of large negative values of the added mass coefficient is discussed. For higher order response modes, sections of the span may be forced into an orbit that gives negative added mass. As it is the modal added mass that must be considered in order to determine the response frequency of the span, there are reasons to believe that added mass is important for which combinations of IL and CF oscillation modes that can exist and also which modes that will be excited for varying current velocity.

Substituting for the reduced velocity ($V_r = U/(f_0 D)$) in Eqn. (8.1) the following expression can be derived for the current velocity (U) required to obtain a certain nondimensional frequency, $\hat{f}$.

$$ U = \frac{D}{\hat{f}} \cdot \sqrt{\frac{\bar{m}+1}{\bar{m}+\bar{C}_a}} \, f_0 \qquad (8.5) $$

The response region is characterized by the nondimensional frequency ($\hat{f}$), and extends over a range of $\hat{f}$, see Figure 8.15. It is seen from Eqn. (8.5) that the highest $\hat{f}$-values in the excitation region ($\hat{f}_{start}$) is reached for the lowest current velocity. Various response modes may have different excitation regions, but in the following a constant $\hat{f}$ is assumed to represent the upper boundary of the excitation region for all modes.

Each possible response mode represents a combination of f_0 (the eigenfrequency of the mode) and modal added mass, $\bar{C}_a$. Increasing mode order represents for most cases an increasing eigenfrequency, and it is seen from Eqn. (8.5) that for a higher eigenfrequency a higher current velocity is required in order to reach the response region. Hence, given a constant added mass, increasing response mode requires increasing current velocity. However, as seen in the previous sections of this chapter the added mass is a function of shape and direction of the orbital path. For response at higher order modes there may be sections of

the span that are forced into an orbit that gives a large negative C_a, which will contribute to a reduction of the modal added mass, $\bar{C}_a$. Eqn. (8.5) shows that for reduced values of $\bar{C}_a$ an increased current velocity is required in order to reach the excitation region. It is thus possible that, due to change in modal added mass, a CF mode of higher order may be excited at a lower current velocity than e.g. the 1st CF mode in combination with the 2nd IL mode.

8.8.3 On multimode response

The results from the experiments presented in this thesis have shown significant force components at multiples of the oscillation frequency. These forces, known as higher order harmonic forces, seem to be related to IL response as they are observed both in the second instability region for the pure IL experiments and in all combined IL and CF motion cases. No significant higher order harmonic forces are observed for the pure CF cases.

Response at modes higher than the dominating mode are observed in flexible beam experiments reported by Vandiver et al. [60] and are also observed in the results from the Ormen Lange experiments discussed in the introduction to this thesis. This response type is likely to be caused by the higher order harmonic forces, and since these forces are small resonance is a necessity. Hence, there must be eigenfrequencies available at approximately 3 and/or 5 times the dominating response frequency in CF direction. The eigenfrequencies corresponding to the eigenmodes of a flexible beam may be approximated by Eqn. (8.6) for tension dominated conditions and by Eqn. (8.7) for bending stiffness dominated conditions.

$$\omega_n^{cable} = n \cdot \pi \sqrt{\frac{T}{mL^2}} \tag{8.6}$$

$$\omega_n^{beam} = n^2 \cdot \pi^2 \sqrt{\frac{EI}{mL^4}} \tag{8.7}$$

For tension dominated conditions response in CF direction due to a force at 3 times the dominating response frequency is expected to occur at a mode number that is tree times the mode number of the dominating mode. The corresponding relation for bending stiffness dominated condition is $n_{3x,i} = \sqrt{3} \cdot n_{dominating,i}$. The relations are shown graphically in Figure 8.16 for dominating mode numbers from 1 to 20.

As seen from the figure the mode numbers excited by higher order harmonic force component become large even for moderate dominating mode numbers. In order to capture the response due to higher order harmonic forces in flexible beam experiments it is thus important that the model is instrumented with a sufficient number of motion sensors.

It is, however, important to note that the response frequency is the frequency that controls the higher order harmonic force components. As shown in previous chapters the response does not necessarily take place at a frequency corresponding to the eigenfrequency in still water. The response frequency is influenced by the added mass.

In the flexible beam experiment discussed in chapter 7 the eigenfrequency corresponding to the second mode, in both CF and IL direction, is approximately 3 times the first. The
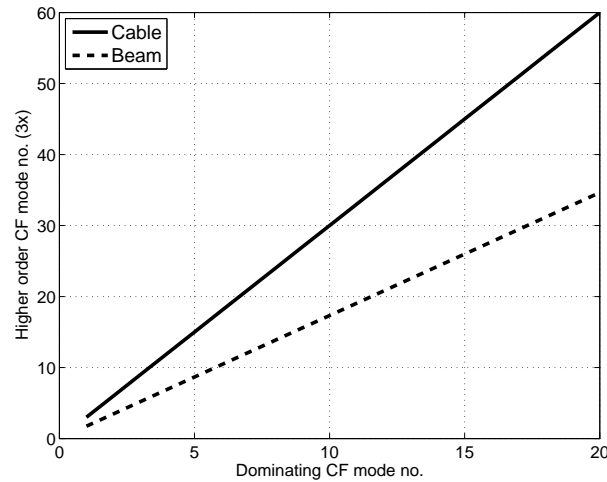
Figure 8.16: Higher order mode, 3x.

response trajectories clearly show that also the second mode is excited. However, chapter 7 also showed that excluding the response from the second mode in the orbits investigated by forced oscillation experiments, gave a good approximation of the hydrodynamic forces acting on the cylinder. I.e. the energy injected through the vortex shedding process corresponded reasonably well with the expected structural damping and the measured added mass corresponded reasonably well with the change in frequency from the eigenfrequency in still water to the response frequency.

The next step in the investigation of higher order harmonic forces should be to investigate how response from these forces influences the hydrodynamic forces at the primary frequency. By including oscillations at a frequency of 3 times the main frequency in forced oscillation experiments, the following questions may be answered:

- Does response due to higher order harmonic forces inject or extract energy?

- Is the response from higher order harmonic forces independent on the response of the primary frequency, or is there a transfer of energy between the frequencies?

- Can response from higher order harmonic forces disturb the vortex shedding process to such a degree that the vortex shedding pattern is disturbed and the primary response is reduced?

Response time series from flexible beams show that the response is significantly reduced from time to time, i.e it seems like there is some kind of slowly varying envelope effect that controls the amplitude at the primary frequency. An explanation for this reduced amplitude may be that the higher order response has become so large that it disturbs the vortex shedding process.

The force measurements reported in this thesis have not revealed significant force components at frequencies lower than the oscillation frequency. This suggests that multimode response will consist of a dominating mode and then up to two higher order modes in both

IL and CF direction. This should however be verified by investigating results from flexible beam experiments. Note that this refers to uniform current conditions.

Chapter 9

Conclusions and Recommendations for Further Work

The motivation for the present work has been to investigate pure IL VIV and the interaction between IL and CF response, primarily for improving prediction methods for free spanning pipelines. Forced oscillation experiments of a rigid cylinder in uniform flow has been carried out in order to measure the hydrodynamic forces acting on the cylinder. As a starting point pure IL oscillations were performed, and then the experiment was extended to include two degree-of-freedom motions.

9.1 Principal Contributions

The following list gives a summary of the main results. The list follows the chapters in this thesis, and is not a rating of the importance of the contributions.

1. Contour plots of hydrodynamic coefficients for the pure IL VIV regime:
   Dynamic excitation coefficient, $C_{e,IL}$, defines the first and second IL instability region, and gives a maximum response amplitude of A/D=0.13 for the first- and A/D= 0.11 for the second instability region. The maximum value found for the excitation coefficient is 0.13.
   The added mass coefficient, $C_{a,IL}$, changes with nondimensional frequency, but is less influenced by the oscillation amplitude. $C_{a,IL}$ ranges from 1.0 to -0.2 within the pure IL regime, and is gradually reduced for decreasing values of nondimensional frequency. The second instability region is hence associated with the lowest added mass values.
   The drag coefficient varies significantly within the pure IL VIV regime, ranging from a minimum value of 0.9 to a maximum value of 1.85. The drag coefficient for the fixed cylinder was 1.33 in these experiments. The first instability region is found to be associated with drag reduction while the second instability region is associated with drag amplification.

2. Higher order harmonic forces at 2 and 3 times the oscillation frequency are measured for pure IL oscillations. These forces are mainly associated with the second instability region. The magnitude of these forces are up to 60% of the force at the oscillation frequency for the second order component and up to 40% for the third order component.

3. Knowing the added mass it has been shown that for a freely vibrating cylinder the response regions will extend over a wider range of reduced velocities, V_r, as the mass ratio of the cylinder is reduced. It has also been demonstrated how the added mass changes the response frequency of a freely vibrating cylinder and that the mass ratio of the cylinder is important for the response frequency relative to the eigenfrequency in still water.

4. A novel approach for determining the response amplitude of a cylinder subjected to structural damping has been derived. A new nondimensional parameter representing the equilibrium between energy transferred from the fluid to the oscillating system and the energy dissipated by damping has been introduced. The parameter is referred to as nondimensional damping, $\hat{c}$. The magnitude of the coefficient is determined by the force in phase with the cylinder velocity, and the results from the forced oscillation experiments have been used to establish contours for $\hat{c}$ for the pure IL regime.

   The nondimensional damping coefficient is independent of the mass ratio of the cylinder. Hence, it has been possible to show the separate effects of mass ratio and damping on a cylinder subjected to VIV

5. The derivation of the nondimensional damping coefficient has highlighted the importance of Reynolds number in free vibration VIV experiments. If the same experimental setup is used to perform experiments at two different Reynolds numbers, the damping inherent in the apparatus becomes more important for the low Re case compared to the high Re case. A reduced oscillation amplitude will hence be measured for the low Re case. The introduction of $\hat{c}$ has thus given insight into scale effect of damping in VIV experiments.

6. It has been shown how $\hat{c}$ and modal analysis can be used to estimate maximum response amplitude of a flexible beam subjected to pure IL VIV. The method has been demonstrated by establishing contours of $\hat{c}$ valid for for a flexible beam with pinned-pinned boundary conditions. From these results it has been shown that the geometric shape factor, i.e. the ratio between the maximum response amplitude for the flexible beam and the response of a elastically mounted rigid cylinder, depends on both $\hat{c}$ and $\hat{f}$.

7. Comparison with literature results from free vibration IL experiments has shown that the data presented herein agrees well, and is hence well suited for predicting pure IL VIV.

8. Forces in CF direction, when oscillating the cylinder in IL direction, has been identified. The results show that the magnitude of this force is reduced in the first instability region and increased in the second instability region, compared to results from fixed cylinder tests. It has been shown that the IL oscillation frequency controls the frequency of the CF force for cases where significant force components are found at 0.5 and 1.5 times the IL oscillation frequency. Hence, higher order harmonic forces in CF direction exist for pure IL VIV.

9. The two significant CF force components are present for the lowest nondimensional frequencies of the first IL instability region. This is likely to be the reason why CF response is observed at a lower reduced velocity in experiments where the cylinder is free to oscillate in IL direction, compared to experiments where the IL direction is restrained.

10. IL hydrodynamic force models suited for inclusion in VIV prediction tools based on "empirical force coefficient methods" (such as VIVANA and Shear7) have been presented.

11. A response model for predicting response amplitude and response frequency of a flexible beam with pinned-pinned boundary conditions subjected to uniform flow has been presented.

12. A method for using results from two degree-of-freedom forced oscillation experiments to investigate results from flexible beam experiments has been outlined. The method considers energy balance and change in frequency, and has been demonstrated by an example. This example showed promising results as the trends of the results were as expected, and it indicated that the method gives valuable information on the forces acting on a flexible beam subjected to VIV. The predicted structural damping of the example was, however, unrealistically high.

13. The importance of orbital direction of two degree-of-freedom motion has been demonstrated. It has been shown that different vortex shedding modes will occur depending on the orbital direction. The change in vortex shedding mode is found to cause significant change in the force acting on the cylinder. This is important for the forces acting on flexible beams oscillating at higher order mode numbers, as the orbital direction will change over the length of the beam.

14. High negative values of the added mass coefficient has been measured for orbits of certain shapes and directions, with extreme values as low as $C_{a,CF}$=-7. For flexible beams oscillating at higher order mode numbers, sections of the span may be forced into orbits of such shapes and directions. These sections will then contribute significantly to the modal added mass. The modal added mass is important for modal response frequency at a certain flow velocity.

15. Higher order harmonic forces are measured, and the results show that these forces are strongly linked to IL oscillations. The trend of the data is that the relative magnitude of the higher order harmonic CF forces will increase for increasing IL oscillation amplitude.

16. The results have shown that both the shape and direction of the oscillation orbits are important parameters for the magnitude of the drag coefficient.

9.2 Recommendations for Further Work

Based on the experience from the present work the following recommendations are given for further work on this subject:

- For all future experimental work aimed at investigating the subcritical flow regime, it is recommended to perform the experiments at Reynolds numbers above $2 \cdot 10^4$.

- Validation of the proposed models for VIV prediction can be performed by flexible beam experiments for Reynolds numbers where the models are valid, i.e. for Re>$1.5 \cdot 10^4$ in the subcritical regime. In these experiments the structural damping should be known. The length of the span should be varied in order to obtain structural damping results for a range of oscillation frequencies. This is important as the oscillation frequency will change from the still water frequency due to added mass variation. When comparing the experimental results with the prediction model, it must also be kept in mind that the applied eigenfrequency should be based on the static configuration including drag forces.

- By performing free vibration experiments of a short rigid cylinder, e.g. using a pendulum set-up, it is possible to further investigate the start-up of CF oscillations, referred to in this thesis as IL induced CF. The ratio between the eigenfrequencies in the two directions should be varied in order to investigate if a certain ratio between the loading frequency (given by half the IL oscillation frequency) and the eigenfrequency is required for CF response to take place. It is also recommended to perform this experiment for various mass ratios to verify the assumption that it is the ratio between IL oscillation frequency and CF eigenfrequency that is of importance for when CF response is excited.

- With an experimental setup as proposed above, it is also recommended to investigate when the two degree-of-freedom response goes from being dominated by IL response to being dominated by CF response, referred to as IL induced CF and CF induced IL response respectively.

- In chapter 7 the eigenfrequency measured in still water was compared with the measured oscillation frequency of the flexible beam, in order to determine whether added mass results from forced oscillation experiments are suited for predicting the modal added mass of the beam. It is recommended to perform this exercise based on an eigenfrequency where the drag force is included in the static configuration on which the eigenfrequency is based.

- The orbits used in the experiments reported in chapter 7 were determined by a visual fit to the trajectories obtained from the flexible beam displacements. As time series of displacement are available it is possible to determine the phase angle between the two directions, IL and CF, from spectral analysis, considering only the dominating frequencies.

- The method described above may be extended to also include higher order displacement components. The higher order component can be represented by a harmonic function where amplitude and phase is determined from spectral analysis. An orbit is then established by superimposing the signal on the dominating component. By constructing the orbit in this manner, the techniques presented in chapter 4 may be used to analyze the results of a forced oscillation experiment for both the main and the higher order component. It is then possible to investigate if two components can be treated independently of each other and if not, how they then interact with respect

to excitation, damping and added mass. It is further possible to investigate the effect of frequency, phase and amplitude of the higher order component by systematically varying these parameters.

- One major limitation of the data from the two degree-of-freedom tests is that the ratio between CF and IL oscillation amplitudes has a fixed value of 2. The results have indicated that higher order harmonic forces are strongly dependent on the IL oscillation amplitude. In order to further investigate this, experiments should be performed with varying ratio between the oscillation amplitudes in the two directions.

Bibliography

[1] http://www.cesos.ntnu.no/research/MCLab.php.

[2] K.H. Aronsen, K.B. Skaugseth, and C.M. Larsen. Interaction between il and cf viv - on the importance of orbital direction. *Submitted to: Journal of Fluid and Structures*, October 2007.

[3] C. Barnardo. *Loads and Response Estimation and Model Recalibration Using Inverse Finite Element Methods*. Phd, University of Stellenbosch, South Africa, 2006.

[4] R.E.D. Bishop and A.Y Hassan. The lift and drag forces on a circular cylinder in a flowing fluid. *Proceedings of Royal Society of London*, Series A:32–75, 1964.

[5] R.D. Blevins. *Flow-Induced Vibration*. Krieger Publishing Company, Florida, Krieger drive, Florida, 2 edition, 1990.

[6] D. Brika and A. Laneville. Vortex-induced vibrations of a long flexible circular cylinder. *Journal of Fluid Mechanics*, 250:481–508, 1993.

[7] M.B. Bryndum, A. Tørum, L. Vitali, and R. Verley. Laboratory tests on in-line viv of pipes subjected to current loads. *OMAE1997*, 1987.

[8] H.W. Coleman and W.G. Steele. *Experimentation and Uncertainty analysis for Engineers*. John Wiley & Sons, 605 Third Avenue, NY, 2 edition, 1998.

[9] J.M. Dahl, F.S. Hover, and M.S. Triantafyllou. Two degree-of-freedom vortex-induced vibrations using a force assisted apparatus. *Journal of Fluids and Stuctures*, (22):807–818, 2006.

[10] DNV, Høvik, Norway. *DNV-RP-F105 Free Spanning Pipelines*, February 2006.

[11] Svein Ersdal. *An Experimental Study of Hydrodynamic Forces on Cylinders and Cables in Near Axial Flow*. Phd, Faculty of Marine Technology, Norwegian University of Science and Technology, Norway, 2004.

[12] O.M. Faltinsen. *Sea Loads on Ships and Offshore Structures*. Cambridge University Press, 1990.

[13] C.-C. Feng. The measurement of vortex induced effects in flow past stationary and oscillating circular and d-section cylinders. Master's thesis, Department of Mechanical Engineering, The University of British Columbia, Canada, 1968.

[14] I. Fylling, C.M. Larsen, N. Sødahl, E. Passano, A. Bech, A.G. Engseth, E. Lie, and H. Ormberg. *RIFLEX User Manual.* Marintek.

[15] R. Gopalkrishnan. *Vortex Induced Forces on Oscillating Bluff Cylinders.* PhD thesis, MIT, Dep. of Ocean Engineering, 1993.

[16] R. Govardhan and C.H.K. Williamson. Critical mass in vortex-induced vibration of a cylinder. *Journal of Mechanics B/Fluids*, (23):17–27, 2004.

[17] Karl Henning Halse. *On Vortex Shedding and Prediction of Vortex-induced Vibration of Circular Cylinders.* Phd, NTNU, 1997.

[18] F.S. Hover, A.H. Techet, and M.S. Triantafyllou. Forces on oscillating uniform and tapered cylinders in crossflow. *Journal of Fluid Mechanics*, 363:97–114, 1998.

[19] E. Huse. In-line viv excitation and mass coefficients. Technical report, MARINTEK, 2004.

[20] E. Huse, G. Kleiven, and F.G. Nielsen. Large scale model testing of deep sea risers. In *In: Proc. of Offshore Technology Conference, Houston, Texas*, number OTC8701, 1998.

[21] E. Huse, F.G. Nielsen, and T. Søreide. Coupling between in-line and transverse viv response. In *19th International Confrernce on Offshore Mechanics and Arctic Engineering, Lisboa*, number OMAE2002-28618, 2002.

[22] W.D. Iwan. The vortex induced oscillation of elastic structural elements. *Journal of Eng. Industry*, 97:1378–1382, 1975.

[23] N. Jauvtis and C. H. K. Williamson. Vortex-induced vibration of a cylinder with two degrees of freedom. *Journal of Fluids and Structures*, (17):1035–1042, 2003.

[24] N. Jauvtis and C. H. K. Williamson. The effect of two degrees of freedom on vortex-induced vibration at low mass and damping. *Journal of Fluid Mechanics*, 509:23–62, 2004.

[25] D. Jeon and M. Gharib. On circular cylinders undergoing two-degree-of-freedom forced motions. *Journal of Fluids and Structures*, (15):533–541, 2001.

[26] T. Johansen. Hydrodynamiske koeffisienter for virvelinduserte svigninger i strømmens retning. Master's thesis, Norwegian University of Science and Technology, 2004.

[27] R. King and D.J. Johns. On vortex excitation of model piles in water. *Journal of Sound and Vibration*, 29(2):169–188, 1973.

[28] C.M. Larsen, G.S. Baarholm, E. Passano, and K. Koushan. Non-linear time domain analysis of vortex-induced vibrations for free spanning pipelines. *OMAE2004*, 2004.

[29] C.M. Larsen, K. Koushan, and E. Passano. Frequency and time domain analysis of vortex induced vibrations for free span pipelines. *OMAE2002*, 2002.

[30] C.M. Larsen, K. Vikestad, R. Yttervik, and E. Passano. *VIVANA Theory Manual.* Marintek, 3.0 edition, January 2002.

[31] C.M. Larsen, R. Yttervik, and K.H. Aronsen. Calculation of in-line vortex induced vibrations of free span pipelines. *OMAE2007*, 2007.

[32] H. Lie and K.E. Kaasen. Modal analysis from a large-scale viv model test of a riser in linearly sheared flow. *Journal of Fluids and Structures*, (22):557–575, 2006.

[33] J.A. Mercier. *Large Amplitude Oscillations of a Circular Cylinder in a Low-speed Stream*. Phd, Stevens Institute of Technology, 1973.

[34] G. Moe and R.L.P. Verley. Hydrodynamic damping of offshore structures in waves and currents. *Proceedings of the 12th Ann. Offshore Techn. Conference, Houston, Texas*, 1980.

[35] G. Moe and Z.J. Wu. The lift force on cylinder vibrating in a current. *ASME Journal of Offshore Mechanics and Arctic Engineering*, 112:297–303, 1990.

[36] E. Naudascher. Flow-induced streamwise vibrations of structures. *Journal of Fluids and Structures*, 1:265–298, 1987.

[37] F.G. Nielsen, T.H. Søreide, and S.O. Kvarme. Viv response of long free spanning pipelines. *OMAE2002*, 2002.

[38] T. Nishihara, S. Kaneko, and T. Watanabe. Characteristics of fluid dynamic forces acting on a circular cylinder oscillated in the streamwise direction and its wake pattern. *Journal of Fluids and Structures*, (20):505–518, 2005.

[39] C. Norberg. Flow around a circular cylinder: Aspects of fluctuating lift. *Journal of Fluids and Structures*, (15):459–469, 2001.

[40] A. Okajima, T. Kosugi, and A. Nakamura. Flow-induced in-line oscillation of a circular cylinder in a water tunnel. *Journal of Pressure Vessel Technology*, 124:89–96, 2002.

[41] B. Pettersen. *Lecture Notes, Sin1501 - Marin Hydrodynamikk og Konstruksjonsteknikk*. Department of Marine Technology, NTNU, 2002.

[42] D.L Reid. A model for the prediction of in-line vortex-induced vibrations of cylindrical elements in a non-uniform steady flow. *Ocean Enineering*, 18(1):147–165, 1991.

[43] K. Mørk, O. Fyrileiv, M. Chezhian, F.G. Nielsen, and T. Søreide. Assessment of viv induced fatigue in long free spanning pipelines. *OMAE2003-37124*, 2003.

[44] T. Sarpkaya. A critical review of the intrinsic nature of vortex induced vibrations. Technical report, Naval Postgraduate School, Monterey, California, 2003.

[45] Kjetil B. Skaugset. *On the Suppression of Vortex Induced Vibrations of Circular Cylinders by Radial Water Jets*. Phd, NTNU, 2003.

[46] R.A. Skop, O. M. Griffin, and S. E. Ramberg. Strumming prediction for the seacon ii experimental mooring. *In Proc. of the 9th Annual Offshore Technology Conference, Houston, TX, pp. 61-66, OTC paper No. 2884*, 1977.

[47] Ø.N. Smogeli, F.S. Hover, and M.S. Triantafyllou. Force-feedback control in viv experiments. *OMAE03*, 2003.

[48] M. Søreide. On the coupling between in-line and cross-flow viv response. *IPC02*, 2002.

[49] P.K. Soni and C.M. Larsen. An experimental investigation of interaction between adjacent spans in pipelines. *Proc. of The Fourth International Conference on Hydroelsticity in Marine Technology, Wuxi, China*, 2006.

[50] P. K. Stansby. The effect of end plates on the base pressure coefficient of a circular cylinder. *Aeronautical Journal*, pages 36–37, January 1974.

[51] T. Staubli. Calculation of the vibration of an elastically mounted cylinder using experimental data from forced oscillation. *Journal of Fluide Engineering*, (105):225–229, 1983.

[52] B.M. Sumer and J. Fredsøe. *Hydrodynamic around cylindrical structures.*, volume 12 of *Advanced series on Ocean Engineering*. World Scientific, London, 1997.

[53] M. Isaacson T. Sarpkaya. *Mechanics of Wave Forces on Offshore Structures*. Van Nostrand Reinold Company, 1981.

[54] A.H. Techet, F.S. Hover, and M.S. Triantafyllou. Vortical patterns behind a tapered cylinder oscillating transversely to a uniform flow. *Journal of Fluid Mechanics*, 363:79–96, 1998.

[55] A. Tørum, G. Moe, J.V. Johansen, and E. Katla. On current induced in-line oscillation of pipelines in free spans. *OMAE1996*, 1986.

[56] M.S. Triantafyllou, A.H. Techet, F.S. Hover, and D.K.P Yue. Viv of slender structures in shear flow. *IUTAM Symphosium on Flow-Structure Interactions, Rutgers State University*, June 2003.

[57] J. K. Vandiver. Drag coefficients of long flexible cylinders. *In Proc. of the 15th Annual Offshore Technology Conference, Houston, TX, pp. 405-410, OTC paper No. 4490*, 1983.

[58] J.K. Vandiver. Dimensionless parameters important to the prediction of vortex-induced vibration of long, flexible cylinders in ocean current. *Journal of Fluid and Structures*, (7):423–455, 1993.

[59] J.K. Vandiver. A universal reduced damping parameter for prediction of vortex-induced vibration. *OMAE2002*, 2002.

[60] J.K. Vandiver, S.B. Swithenbank, V. Jaiswal, and V. Jhingran. Fatigue damage from high mode number vortex-induced vibration. *OMAE2006*, 2006.

[61] Kyrre Vikestad. *Multi frequency response of a cylinder subjected to vortex shedding and support motions*. Phd, Faculty of Marine Technology, Norwegian University of Science and Technology, Norway, 1998.

[62] C.H.K Williamson and R. Govardhan. Vortex-induced vibrations. *Annu. Rev. Fluid Mech.*, 2004.

[63] C.H.K Williamson and N. Jauvtis. A high amplitude 2t mode of vortex-induced vibration for a light body in xy motion. *European Journal of Mechanics*, B/Fluids(23):107–114, 2004.

[64] L.R Wootton, M.H. Warner, R.N. Sainsbury, and D.H. Cooper. Oscillation of piles in marine structures - a description of the full-scale experiments at immingham. *Technical note 40, CIRA*, 1972.

[65] R. Yttervik, E. Passano, J. Krogstad, and C.M. Larsen. *VIVANA Users Manual*. Marintek, 3.2 edition, April 2003.

[66] M.M. Zdravkovich. *Flow Around Circular Cylinders: Fundamentals*, volume 1. Oxford University Press, 1997.

[67] M.M. Zdravkovich. *Flow Around Circular Cylinders*, volume 2. Oxford Science Publications, 2002.

Appendix A

Calibration

In this appendix the calibration coefficients for force sensors and accelerometers for the three phases of experiments are given.

As experience was gained from one phase to the next, the methods used to calibrate the experimental setup was continuously improved. The first section of this appendix will therefore be a thorough description of the calibration process and the results for the last phase of experiments. Section A.2 and A.3 present the results from Phase II and Phase I respectively. The two sections also include a description of how the calibration methods deviate from what is reported in section A.1.

A.1 Calibration Phase III Experiments

A.1.1 Calibration of force sensors

The force sensors were of the strain gauge type (Hottiger PW2GC3), and the calibration of the sensors was performed in three steps. First each sensor was calibrated separately to find the calibration coefficient (in N/V). Then two and two sensors were mounted to form a "cross", enabling force measurements in two directions (90 degrees off). The mounted sensors were then calibrated to investigate if there was a transfer of forces between the two directions. The third step of the calibration was carried out after the assembly of the test rig. Weights were applied on the cylinder to see if the two sensor crosses were rotated when installed, and if so find the cross-talk angle. During these calibrations a constant force was applied in vertical direction to account for the buoyancy. The uncertainty in cross-talk angle was estimated by investigating the measurements from this calibration.

Force sensor calibration, Step I

The first step of the force sensor calibration is to find the calibration factors (from V to N) for each force sensor. This was done by applying known weights and recording the output voltage. Masses of 1, 2, 3, 5 and 7kg were used and a typical time series is shown in Figure A.1 (a). The load sequence was repeated two times in both positive and negative direction, giving a total of 44 data points. Results for a typical case is shown in Figure A.1 (b). As indicated in the Figure the calibration coefficient is estimated by linear
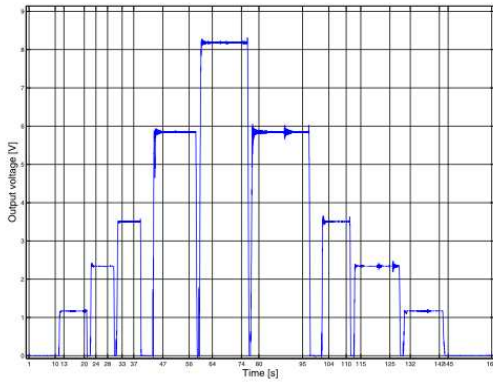
(a) Calibration time series
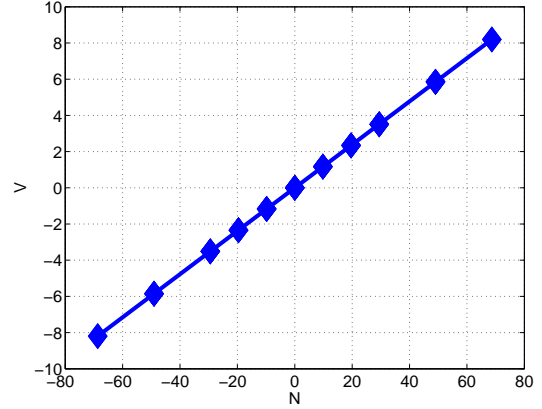
(b) Calibration results

Figure A.1: Step I, force calibration results.

regression. The general expression for a straight line regression is

$$Y(X) = mX + c \tag{A.1}$$

where m is the slope and c is the y-axis intercept. In the calibration procedure X represents the applied weight and Y the output voltage for the given weight. The parameter of interest is the slope m, which is the inverse of the calibration coefficient, and the standard deviation of the slope from the curve fit is given by (see Coleman & Steele [8], chapter 7):

$$S_m = \sqrt{\frac{S_Y^2}{Sxx}} \tag{A.2}$$

where

$$S_Y = \sqrt{\frac{1}{n-2} \sum_{i=1}^{n} (Y_i - mX_i - c)^2} \tag{A.3}$$

and

$$S_{xx} = \sum_{i=1}^{n} X_i^2 - \frac{(\sum_{i=1}^{n} X_i)^2}{n} \tag{A.4}$$

These expressions for regression uncertainty only apply when all random uncertainties are concentrated in the Y values (output voltage). The criteria is not formally met for these results as there are uncertainties related to the calibration weights. However, the uncertainties are found to be negligible. The confidence interval for the mean value of the slope is given by:

$$m - t_{95\%}S_m \leq \mu_m \leq m + t_{95\%}S_m \tag{A.5}$$

In the experiments the measured voltage is multiplied by the inverse of the slope, m, and the estimated uncertainty in the calibration coefficient is treated as a bias error in the force measurements. Calibration factors and estimated bias errors for the four force sensors are given in Table A.1.

Table A.1: Summary of force calibration factors.

Force sensor ID number	8346	8342	8354	8343
Mean value	8.396	8.444	33.567	8.380
Uncertainty, 95 % confidence interval	2.98E-04	4.14E-04	82.9E-04	3.03E-04

Force sensor calibration, Step II

In step II the force sensors ability to measure forces in two directions is tested. Two and two sensors were orthogonally mounted together. The "sensor cross" was then tested by applying known weights in four directions, negative and positive for both IL and CF. The output voltage was recorded for both sensors and the calibration factors found in step I was included. The result for one sensor cross is shown in Figure A.2. The figure shows that
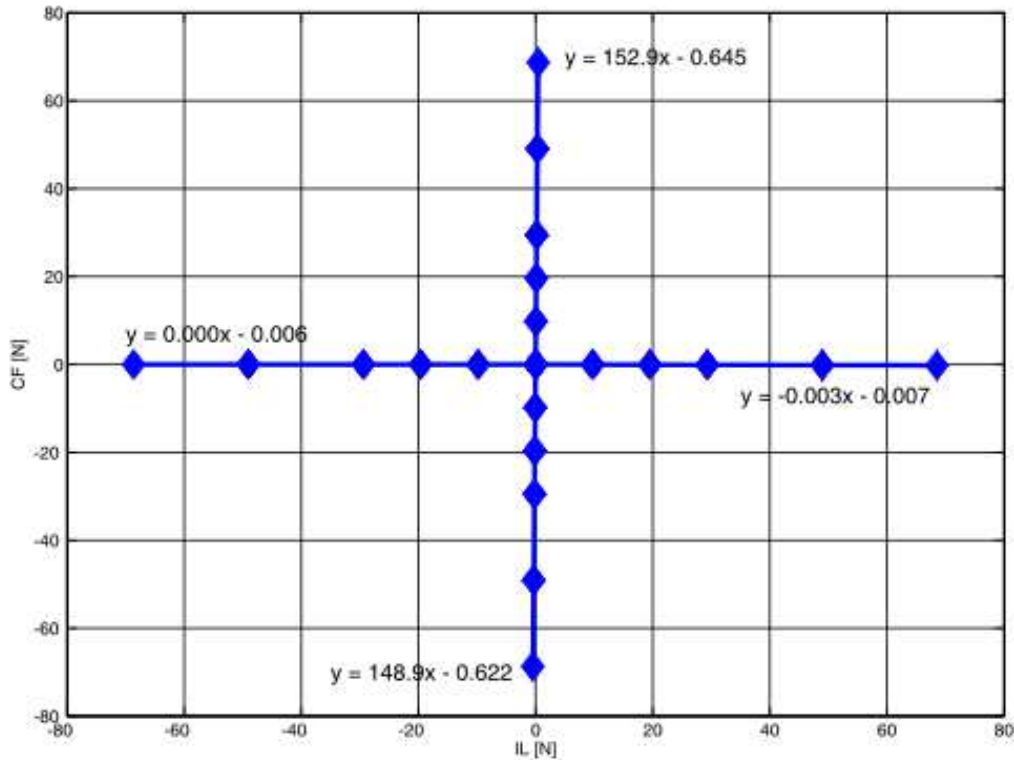
Figure A.2: Calibration step II, cross-talk.

when applying a force in CF direction a small force in IL direction will also be present. The magnitude of this force is estimated to 0.65% of the CF force, with an estimated 95% confidence interval from 0.62% to 0.69%. The reason for this cross-talk is the way the two sensors are connected. A force in CF direction cause a moment that has to be taken up by the IL sensor. The error seems to be linear and the two sensor crosses give the same

result.

Force sensor calibration, Step III

The purpose of force calibration step III is to:

1. Verify that there is no contact between the test cylinder and the sensor housing.

2. Investigate if the force sensor cross has been rotated during installation, and determine the cross-talk angle.

3. Verify that, corrected for cross-talk angle, the measured force comply with the force applied on the cylinder.

To ensure that the first condition was satisfied, a load equal to the buoyancy was applied in vertical direction. The maximum loads in each direction were higher than the maximum load expected in the experiment. The second condition was investigated by applying loads in four directions (positive and negative in CF and IL). Figure A.3 shows the results. Crosses represent results from the calibration and circles represent the same results after correction for cross-talk angle.

(a) Starboard   (b) Port
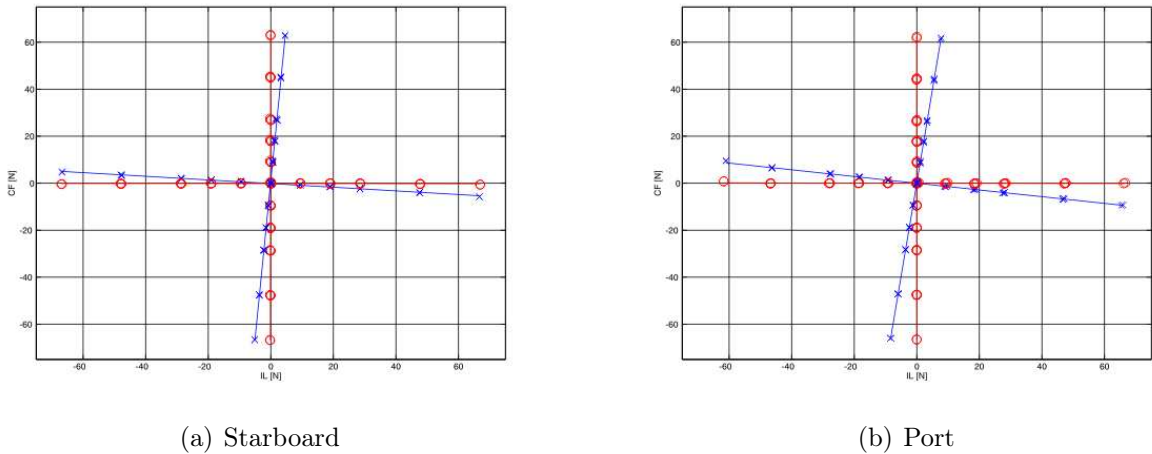
Figure A.3: Step III, estimation of cross-talk angle.

To verify that the measurements gave the correct forces the slope of the applied vs. measured load was calculated. The results show that the measured forces are slightly lower than the applied load, from 0.5 to 1.9%. The calibration method used in step III is however less accurate than the method used in the previous two steps. The deviation in measured load compared to the applied is therefore included in the error estimate, and not used to correct the calibration coefficient. Four load sequences were performed in each direction and the slope was estimated for every sequence. A standard deviation for the slope was then estimated based on a mean value of unity. The estimated relative error in the force coefficient was then taken as $t_{95\%}$ times the estimated standard deviation. Calibration coefficients and cross talk angels with estimated uncertainties for the two sides are summarized in Table A.2.

When calculating the slope in IL direction of the port force sensor the calibration results for the 7 kg external load in negative direction have been excluded. The two calibration results for this external load deviate by 6% compared to the remaining data set in IL direction (42 data points). The maximum IL force in the experiments is much smaller than this force.

Table A.2 shows that the correction factor for IL force from a force in CF direction is different for the two sides, and not the same as the factor found in step II. The reason for this is probably related to the cross-talk angle and to the direction of the rotation of the sensor cross. Rotation in one direction enhances the effect and rotation in the other direction reduces it. The cross-talk angle on the starboard side is approximately half the angle on the port side. Compared to the correction factor found in step II, 0.7%, the correction factor is approximately half of this for the starboard side and double for the port side.

Uncertainty in cross-talk angle

The cross-talk angle may also be estimated by investigating the frequency of the force in the two directions. The method is described by the following steps:

1. For an oscillation in e.g. IL direction of a given frequency, the force component at this frequency in CF direction is extracted.

2. A straight line is then fitted to the forces measured in the two directions by a "least square fit" method.

3. The cross-talk angle is then calculated from the estimated slope.

A typical result is shown in Figure A.4 (a). The full test matrix has been investigated and the uncertainty in cross-talk angle is estimated by: $B_\alpha = t_{95\%} \cdot S_{x-talk} + \mu_{x-talk}$. The estimated uncertainty in cross-talk angle is 2.23 [deg] at the Starboard side and 2.84 at the Port side. Figure A.4 (b) shows the calculated cross-talk angles for the port side, calculated in IL direction.

Some of the test series were excluded as a consequence of this exercise since it appeared that the vortex shedding process gave a force component at the CF frequency in IL direction. In future work tests should be performed in air to verify the calibrations. Performing the tests in air will exclude the fluid effects and the method will give a better estimate of the uncertainty in cross-talk angle.

A.1.2 Calibration of motion sensors

Two types of sensors were used, accelerometer and string potentiometer. The accelerometers were calibrated by using the acceleration of gravity, g=9.81 m/s^2. Cross-talk angles due to rotation of the sensor were determined based on the test series.

Accelerometer calibration

The accelerometers were calibrated by rotating the accelerometer so that the axis of interest would be horizontal (acceleration = 0), vertical pointing up (acceleration = -g) and vertical

(a) Cross-talk, single test

(b) Uncertainty in cross-talk angle
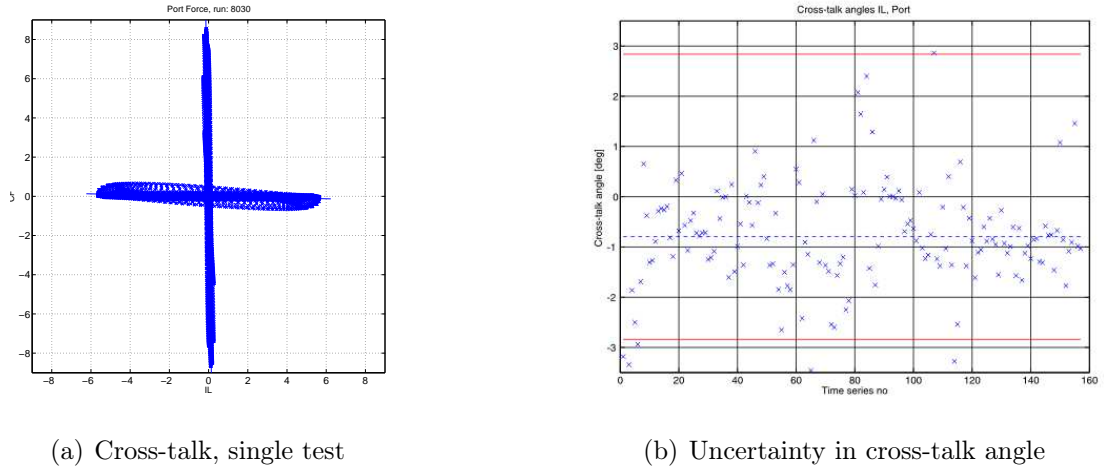
Figure A.4: Cross-talk angles estimated from experiment data. Force sensor at port side. Cross-talk angle based on IL oscillations.

pointing down (acceleration = g). Calibration coefficient and uncertainty were estimated in the same way as for the force sensors. The results are given in Table A.3.

Estimation of accelerometer cross-talk angle

The accelerometer cross-talk angles were estimated from the experiment time series in a similar manner as for the force sensors. The method should however work better for the accelerometers, since no hydrodynamic effects can influence the results. The calibration was performed in the following way: First all available time series were analyzed and an average cross-talk angle estimated for both ends of the cylinder. The estimated cross-talk angles were then included in the data reduction program and the the test matrix reanalyzed. The results showed that the cross-talk angle for the CF axis at the starboard side (accelerometer 6294z) deviated significantly from the IL axis, and a correction factor corresponding to a cross-talk angle of 7.4 degrees was included on this axis. The test matrix was then reanalyzed for a second time and based on these results the uncertainty in cross-talk angle was estimated. These were 0.8deg for the Starboard accelerometer and 2.2deg for the Port accelerometer. The results are given in Figure A.5, where the 95% confidence interval is included as solid lines. The results are summarized in Table A.4.

Phase error due to signal processing - accelerometer

In the data reduction analysis the acceleration signal is used as a reference signal for decomposition of the measured hydrodynamic force into components in phase with acceleration and in phase with velocity. Cross-talk between the two axes may cause a phase change in the acceleration signal which will give an error in the calculated force coefficients. Due to the combined uncertainty from this cross-talk angle and from noise, the acceleration signal had to be filtered. A digital fft band-pass filter was used.

To determine the possible phase change due to the combined effect of cross-talk and filtering an investigation with synthetic signals has been performed:

Table A.2: Summary of force calibration factors, Phase III.

Parameter	Mean Value	Uncertainty 95%
Calibration coefficient IL Starboard, sensor no 8342	8.444	0.130
Calibration coefficient CF Starboard, sensor no 8346	-8.396	0.316
Cross-talk angle Starboard	4.4 [deg]	2.23 [deg]
IL correction factor due to moment caused by CF force, Starboard	0.3 % [-]	-
Calibration coefficient IL Port, sensor no 8343	-8.380	0.483
Calibration coefficient CF Port, sensor no 8354	-33.567	1.115
Cross-talk angle Port	8.1 [deg]	2.84 [deg]
IL correction factor due to moment caused by CF force, Port	1.64 % [-]	-

Table A.3: Accelerometer calibration factors.

Accelerometer ID number	6294y	6294z	6293y	6293z
Mean value	12.944	-14.856	2.693	-2.264
Uncertainty, U, 95 % confidence interval	0.166	0.504	0.028	0.068

- Two synthetic acceleration signals, sinusoidal signals in IL and CF direction, were created based on the oscillation frequency and amplitude from the test matrix.

- New IL and CF signals were then created by introducing the cross-talk angle found in the previous section.

- The new IL and CF acceleration signals were then band-pass filtered with the same high-pass and low-pass frequency as used in the data reduction analysis for the given case.

- Finally the phase angles between the filtered signal and the original signal, in IL and CF direction, were calculated.

All test series from the two degree-of-freedom experiments have been included. It was not found to be a correlation between phase angle and acceleration amplitude or frequency. Therefore a constant phase error, due to cross-talk and filtering, will be used for all cases.

In some of the methods used to decompose the hydrodynamic force the velocity signal was used. The velocity signal was found by a frequency domain integration routine. The uncertainty in the velocity signal has been investigated in a similar manner.

The results from the calculations are shown in Figure A.6 and the uncertainty in both acceleration and velocity is found to be 0.04deg.

(a) Starboard   (b) Port
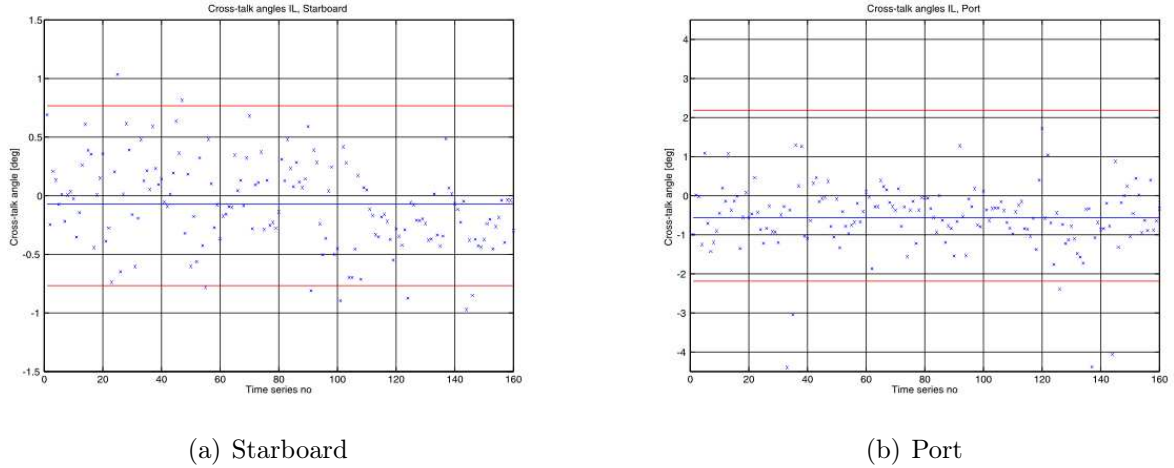
Figure A.5: Acceleration cross-talk angles estimated from experiment time series. 95% confidence interval included as solid lines.

Table A.4: Summary of accelerometer calibration factors.

Parameter	Mean Value	Uncertainty 95%
Calibration coefficient IL Starboard, sensor no 6294y	12.944	0.166
Calibration coefficient CF Starboard, sensor no 6294z	-14.856	0.508
Cross-talk angle Starboard	4.35 [deg]	0.77 [deg]
IL correction factor, Starboard	0.13 % [-]	-
Calibration coefficient IL Port, sensor no 6293y	2.693	0.028
Calibration coefficient CF Port, sensor no 6293z	-2.264	0.068
Cross-talk angle Port	1.3 [deg]	2.19 [deg]

String potentiometer calibration

The string potentiometers were factory calibrated and the calibration coefficients were verified by use of a standard ruler. The calibration showed that on average both string potentiometers over predicted the displacement by 1%. This was based on 10 measurements and the uncertainty in the calibration coefficient was 0.005 for both potentiometers. As the ruler had not been calibrated, it was decided to use an uncertainty of 2% (95% confidence interval) in the uncertainty analysis.

Phase error due to signal processing - string potentiometer

The displacement measured by the string potentiometers must be differentiated to get the velocity and acceleration signals. A time domain method has been used and the uncertainty in phase introduced by this method has been investigated in a similar manner as outlined in the previous section, but without cross talk. A constant band pass region between 0.1 and
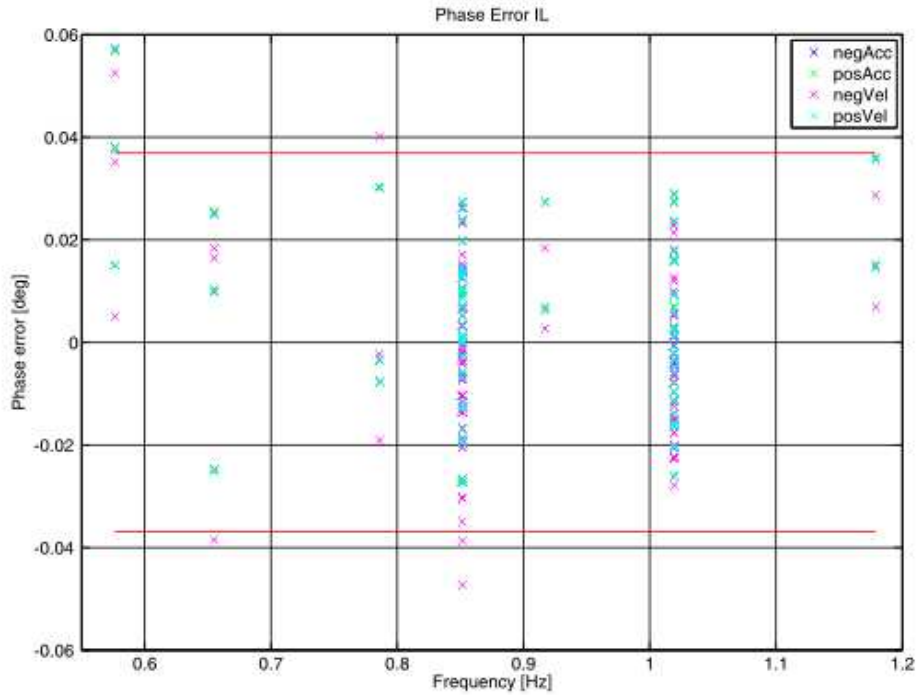
Figure A.6: Phase error in IL acceleration and velocity signal.

2.2Hz has been used for all cases. The phase uncertainty of the velocity- and acceleration signals were found to be 0.003deg and 0.022deg respectively.

A.1.3 Natural frequency

The natural frequency of the test rig was found by hitting the rig at different locations with a rubber mallet while measuring forces and accelerations. A spectral analysis showed the first eigenfrequency at approximately 4.5Hz in IL direction and at approximately 7Hz in CF direction. The power spectrums for the four force channels are show in Figure A.7.

A.2 Phase II Experiments

A.2.1 Calibration methods

The deviations from the method described in section A.1 are addressed in this section.

Force sensor calibration

Only force sensor calibration step III was performed for the phase II experiments. Step III was however performed three times as the model had to be taken down two times for modifications. Hence, the cross-talk angle had to be estimated each time the model was assembled.
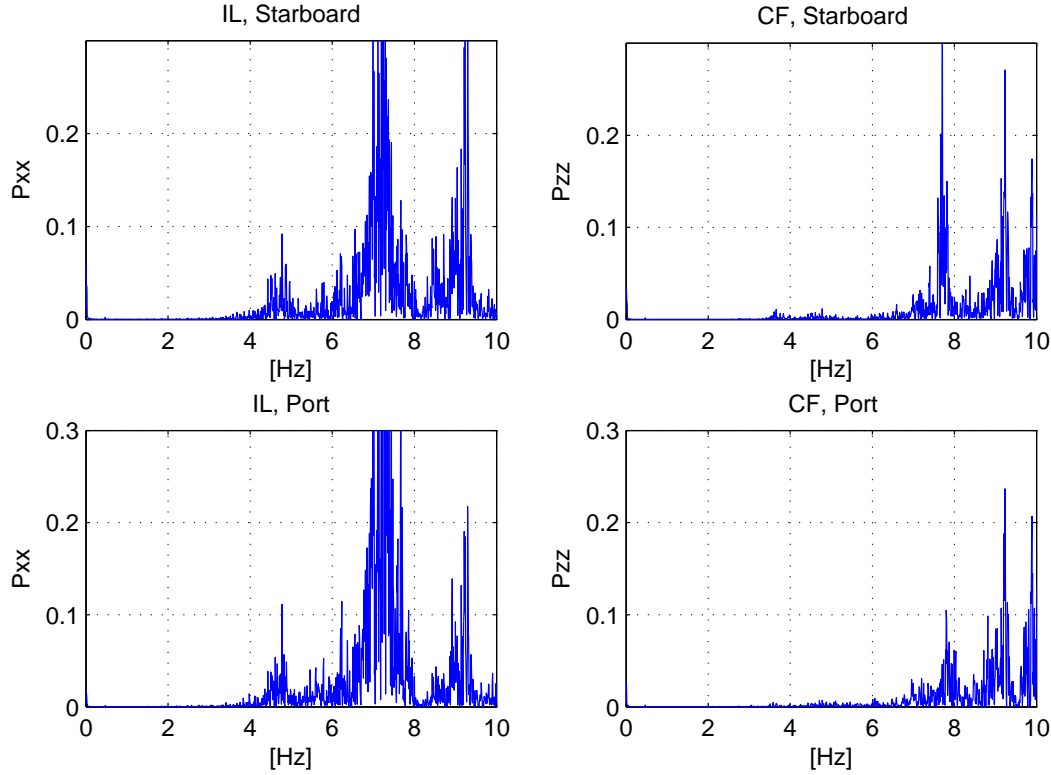
Figure A.7: Power spectral density of force measurements in natural frequency test, Phase III.

Only the results for Starboard side are reported, as there was contact between the test cylinder and the force sensor housing at port side. The calibration was performed in the following steps:

1. Each of the three data sets were analyzed so that calibration coefficients and cross talk angles were found.

2. An average value for the calibration coefficients in IL and CF direction, estimated for each of the three data sets, were used as force calibration coefficients in the post-processing. The uncertainty in the calibration coefficients were estimated based on the standard deviation of the three values. For a 95% confidence interval the uncertainty was found to be $P_{\bar{x}} = t\frac{S_x}{\sqrt{N}}$, where N=3 and t=4.303 (ν=2).

3. The cross-talk angle and IL correction factor found for the last data set were later used in the post-processing

The cross-talk angle was estimated from the time series as described in section A.1 and the results are shown in Table A.5.

Accelerometer calibration

The calibration of the accelerometers was performed in a similar manner as described in section A.1. There are however fewer data points available. For this phase the calibration factors are based on 5 to 9 data points, while the coefficients in phase III are based on 18 data points. The results are given in Table A.6.

A.2.2   Calibration results

The calibration results are summarized in Table A.5 and Table A.6 and the natural frequencies are shown in Figure A.8.

Table A.5: Summary of force calibration factors, Phase II.

Parameter	Mean Value	Uncertainty 95%
Calibration coefficient IL Starboard	34.142	0.734
Calibration coefficient CF Starboard	-8.661	0.213
Cross-talk angle Starboard	-2.4 [deg]	6.0 [deg]
IL correction factor due to moment caused by CF force, Starboard	-0.3% [-]	-

Table A.6: Summary of acceleration calibration factors, Phase II.

Parameter	Mean Value	Uncertainty 95%
Calibration coefficient IL Starboard	12.736	0.112
Calibration coefficient CF Starboard	-14.472	1.039
Cross-talk angle Starboard	3.70 [deg]	0.84 [deg]
IL correction factor, Starboard	0.13 [-]	-
Calibration coefficient IL Port	10.651	0.192
Calibration coefficient CF Port	-10.976	0.243
Cross-talk angle Port	-1.86 [deg]	1.73 [deg]

In Figure A.8 it is seen that there are force components at 1.7 and 3.3Hz. This is in the region where higher order harmonic forces are seen in the 2dof experiments and must be kept in mind when the results are evaluated.

A.3   Phase I Experiments

A.3.1   Calibration methods

The deviations from the method described in section A.1 are addressed in this section.

Force sensor calibration

The calibration was performed after the experiment and only step III in one direction was carried out. The test rig was also calibrated prior to the experiments, with loads in
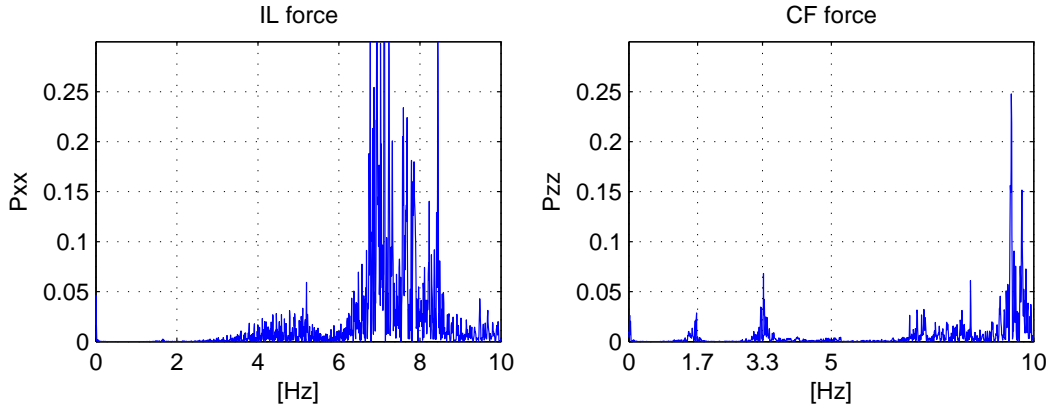
Figure A.8: Power spectral density of force measurements in natural frequency test, Phase II.

all four directions, and these calibrations showed no evidence of any difference between positive and negative direction. The calibration method was however less accurate than the method described in section A.1.1, and only the results from the calibration after the experiments have been used in the data processing. The error in force calibration coefficients was estimated as described in A.1.1. Since step I was not performed it has, however, been chosen to increase the error by 2%. Thus, if the calibration shows that the standard deviation (S_m) is 0.25% of the mean value and $t_{95\%} = 2$, the value used in the uncertainty analysis is 2.5% of the mean value. This is based on the experience gained from the Phase III experiments. Only the results for Starboard side are reported, as there was contact between the test cylinder and the force sensor housing at port side.

The cross-talk angle is estimated from the time series. In Phase I pure IL tests were performed and the cross-talk angle is therefore based on IL oscillations only.

Accelerometer calibration

The accelerometers were calibrated after the experiments and the results are summarized in Table A.8.

A.3.2   Calibration results

The calibration results are summarized in Table A.7 and Table A.8 and the natural frequencies are shown in Figure A.9.

A.4   Recommendations for future work

For future experiments it is strongly recommended to perform tests in air, i.e. oscillations in IL and CF direction, both prior to and after the experiment. This will be very useful for several reasons:

- The actual inertia force from the oscillating mass can be found.

Table A.7: Summary of force calibration factors, Phase I.

Parameter	Mean Value	Uncertainty 95%
Calibration coefficient IL Starboard	34.070	0.920
Calibration coefficient CF Starboard	8.871	0.222
Cross-talk angle Starboard	0.74 [deg]	2.3 [Deg]
IL correction factor due to moment caused by CF force, Starboard	0.3 % [-]	-

Table A.8: Summary of acceleration calibration factors, Phase I.

Parameter	Mean Value	Uncertainty 95%
Calibration coefficient IL Starboard	12.843	0.392
Calibration coefficient CF Starboard	-14.795	0.529
Cross-talk angle Starboard	-6.8 [deg]	1.0 [deg]
Calibration coefficient IL Port	10.852	0.236
Calibration coefficient CF Port	-11.008	0.284
Cross-talk angle Port	-1.2 [deg]	2.2 [deg]

- It can be verified that the force sensors at the two sides give the same result as there are no fluid forces present that can cause a difference in forces.

- The uncertainty in cross-talk angle can be estimated.

- The accuracy of the post-processor can be tested since we know that there are no forces in phase with velocity in the time series.

- It can be verified that calibration coefficients are valid for the duration of the experiment.

It is also recommended that force calibration step III is extended to include external load at the mid point of the test cylinder. This should be done in order to verify that the force is distributed evenly to each side of the cylinder.

Force calibration step II determines the magnitude of the measured force in IL direction due to a force in CF direction. In future work it is recommended to investigate how sensitive this transfer factor is to rotation of the sensor cross, i.e. cross-talk angle. In section A.1.1 it was found that the transfer factor was different for the two sides.
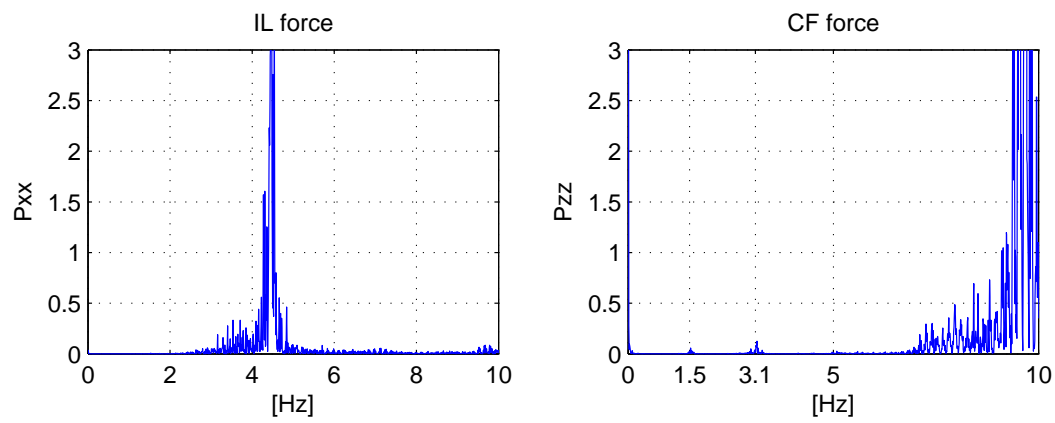
Figure A.9: Power spectral density of force measurements in natural frequency test, Phase I.

Appendix B

Data Sheets
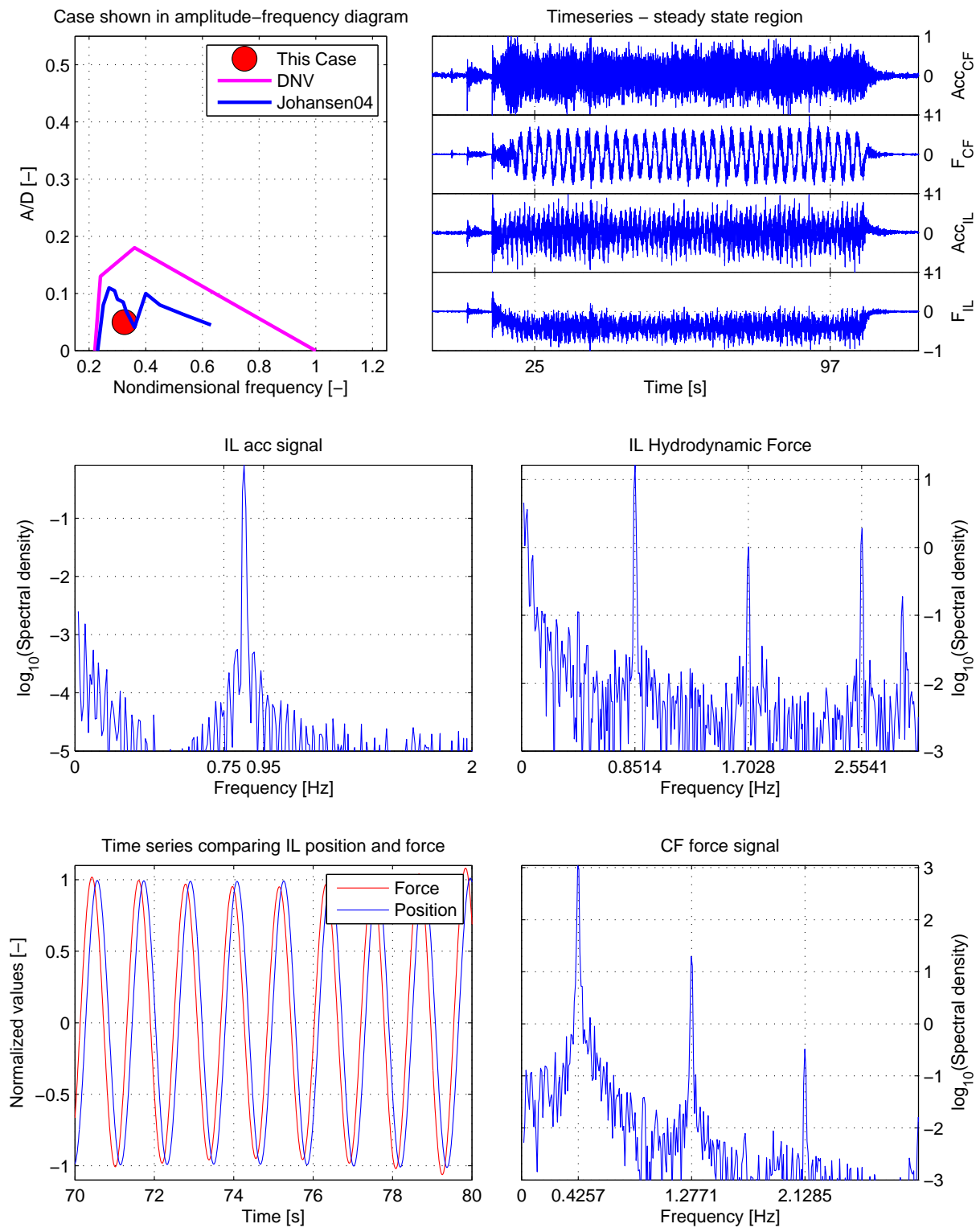
Figure B.1: Data sheet, intermediate results.
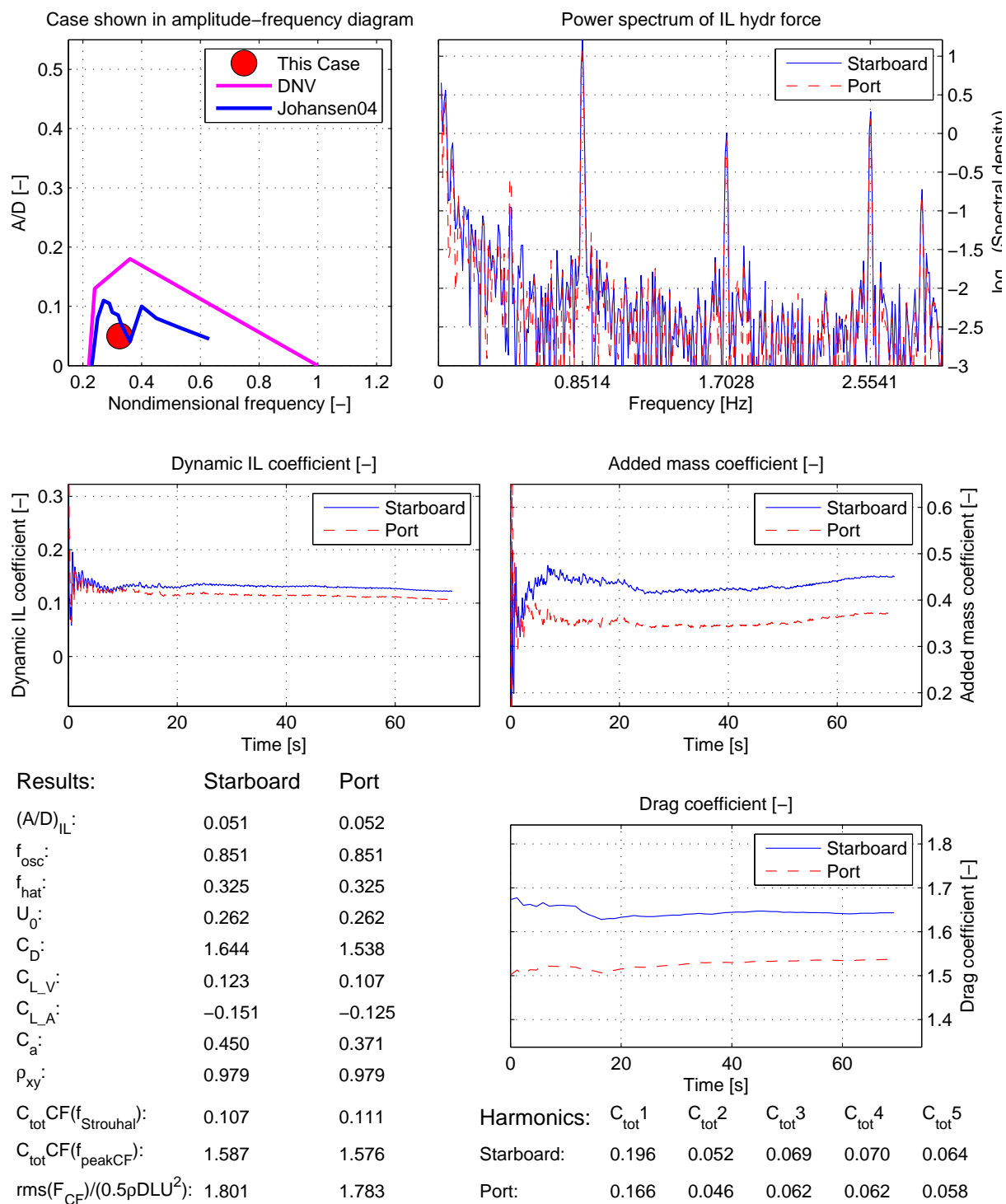
Figure B.2: Data sheet, final results.

Case: 7310. A/D = 0.05, f_{hat}= 0.325, IL Starboard

Measured: A/D_m = 0.051 ± 0.001, $f_{hat,m}$ = 0.325 ± 0.003

Figure B.3: Data sheet, results from error analysis.

Appendix C

Additional IL results
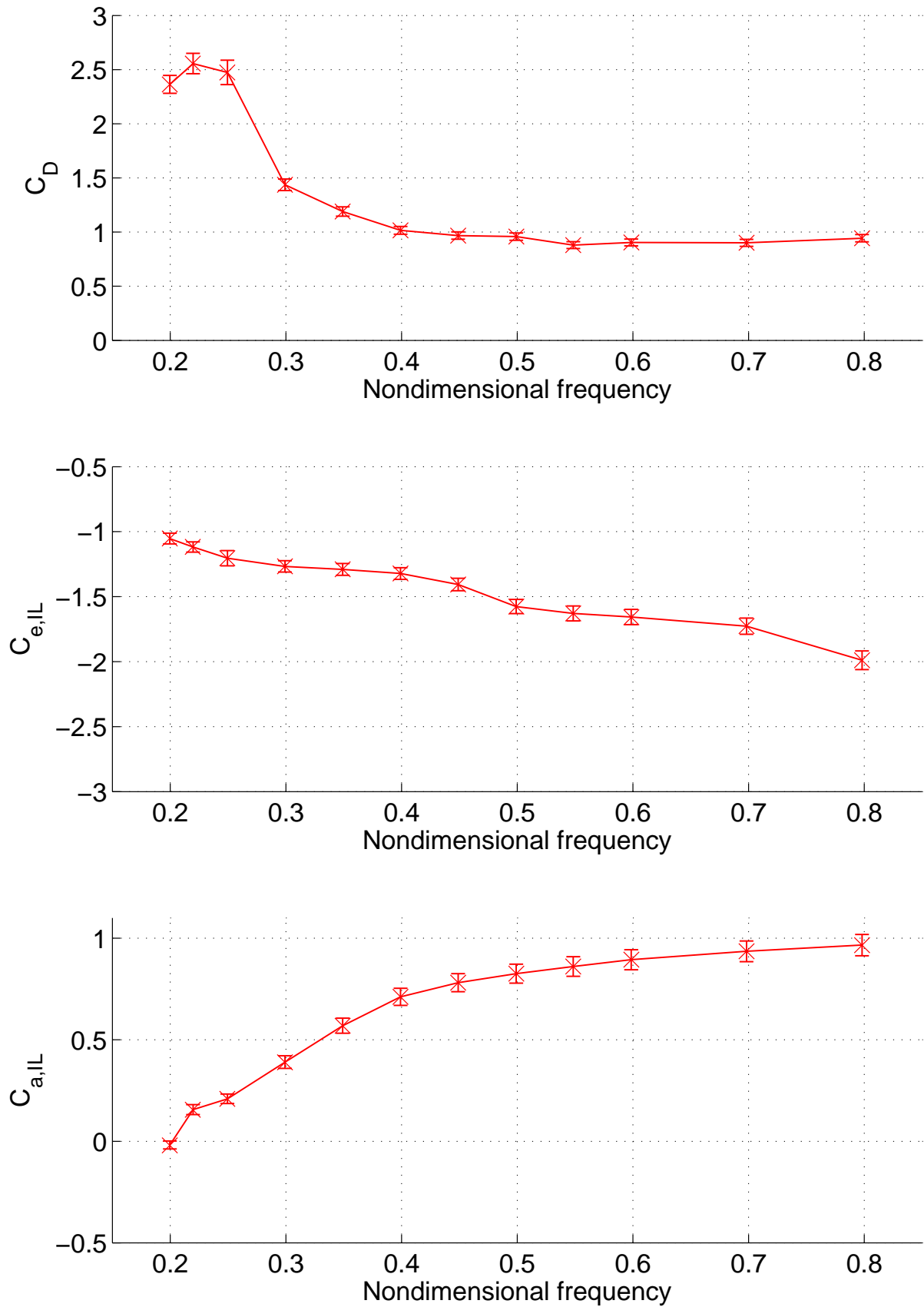
Figure C.1: Hydrodynamic coefficients for $(A/D)_{IL}$=0.5.
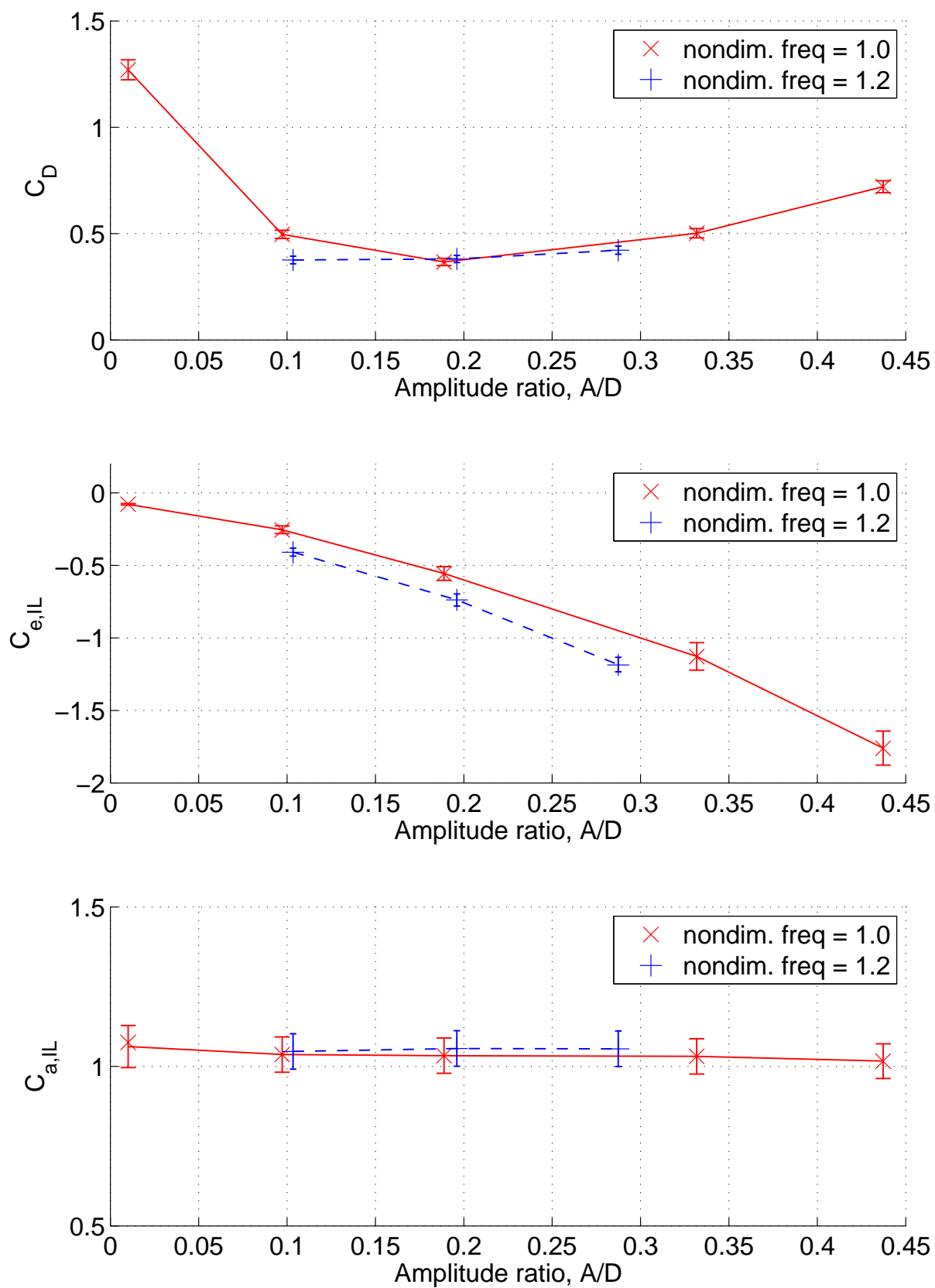
Figure C.2: Hydrodynamic coefficients for high frequency cases.

Appendix D

Pure IL PIV results

This appendix presents flow visualization results from four pure IL cases, see Figure D.2 through D.5. These results are from the same PIV project as the figures presented in section 8.7, but the results have not been published prior to the publication of this thesis. The PIV images are not processed by the author. Hence, the flow behind the cylinder will be based on the presented vorticity plots, but possible error sources from the process of generating these images will not be addressed.

The result sheets consist of 6 images showing the vorticity of the wake. These images represent 6 time steps over two oscillation cycles. At the bottom of each figure time series of CF and IL forces are shown together with IL motions. The 6 time instances corresponding to the vorticity plots are shown on the time series. Positive cylinder motion (IL direction) is defined as a downstream motion, i.e. to the right in the vorticity plots. Positive CF direction is up.

The four flow visualization cases are shown relative to the $C_{e,IL} = 0$ contour in Figure D.1. Detailed force coefficient results are given in Table D.1, and the coefficients are defined in chapter 4.

D.1 2nd instability region

The flow pattern within the second instability region, case A, is shown in Figure D.2. It is seen that the vortex shedding mode resembles the 2C mode, i.e. two co-rotating vorticies. Picture 1 shows one vortex that has just been shed from the top of the cylinder and a second that is about to be shed. In picture 2 also the second vortex is shed from the top of the cylinder and a vortex rotating in the opposite direction is formed underneath the cylinder. In picture 3 this vortex is shed and a second co-rotating vortex is formed. Picture 4 is from the same position in the oscillation cycle as picture 1, i.e. the cylinder is in the forward position upstream, and it is seen that vortex pattern is similar to that of picture 1. The important difference is however that the vortex pair in picture 1 is shed from the top of the cylinder while in picture 4 the vortex pair is shed from underneath. A vortex pair is alternatingly shed from the top and bottom of the cylinder every other IL oscillation cycle, which causes a strong CF force of frequency equal to half the IL frequency.

Figure D.3 shows the flow pattern of case B. Here the oscillation frequency is the same
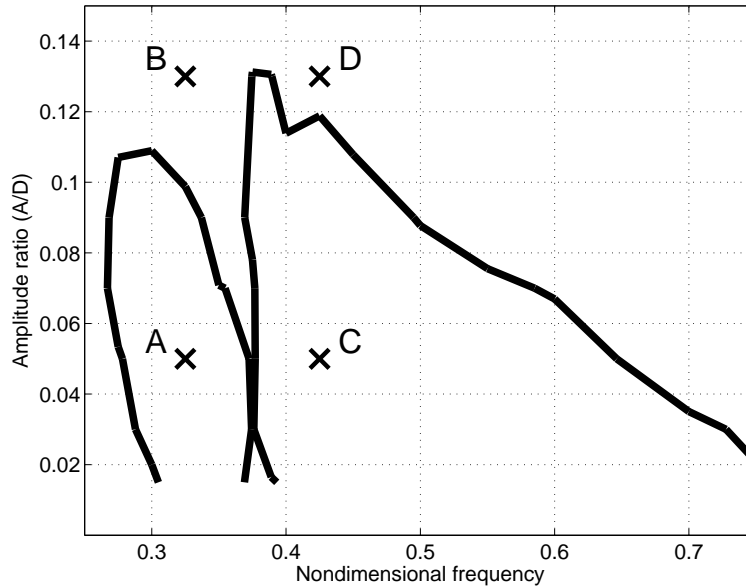
Figure D.1: Flow visualization cases shown relative to the IL instability regions.

as for case A, but the oscillation amplitude is higher and the case represents the damping region outside the 2nd instability region. Two co-rotating vortices (2C mode) seem to be shed, see picture 1, but they appear to merge downstream and form a single vortex (2S mode), see picture 2 to 4. The CF force is not as strong for this case as for the case within the excitation region, while the drag force is higher for case B.

From the flow visualization the 2nd instability region seems to be associated with the 2C and 2S vortex shedding modes. It is seen that the vortices are not shed as one well defined vortex, which looks to be the reason for the higher order force components in both IL and CF direction. Based on these two cases an increased oscillation amplitude seems to give a vortex shedding mode closer to the 2S mode, and it looks like this mode gives a higher drag force and a lower oscillating CF force than the 2C mode observed for the smaller oscillation amplitude.

D.2 1st instability region

Figure D.4 shows the flow pattern for case C within the 1st instability region. Picture 1 indicates a 2S vortex shedding mode while picture 3 indicates a symmetric vortex shedding mode. Thus, the vortex shedding within the first instability region must be seen as a combination of the symmetric and the 2S mode. This is in line with previously published results, see e.g. Sumer & Fredsøe [52].

Flow visualization for case D is shown in Figure D.5. It is seen that the symmetric shedding mode dominates, and picture 3 shows a symmetric vortex shedding mode that looks very similar to what is found in the literature. For the other pictures the shedding mode is not as well defined. This might be caused by the processing of the PIV pictures.

The flow visualization of the first instability region shows that within the excitation region the flow pattern is a combination of the 2S and the symmetric vortex shedding mode. The presence of the 2S mode causes a significant oscillating CF force and a drag coefficient exceeding that of a stationary cylinder in uniform flow. For increasing oscillation amplitude the 2S mode disappears which effectively reduces the oscillating CF force. It is also seen that symmetric mode reduces the drag force. It should be noted that the main oscillating force component of case C appears at a frequency different from 0.5 times the IL oscillation frequency, see Figure 6.17 (a).

Table D.1: Force coefficient results.

Coefficient	Case A	Case B	Case C	Case D
$\hat{f}_{IL}$	0.325	0.325	0.425	0.425
$\frac{A}{D}_{IL}$	0.05	0.13	0.05	0.13
C_D	1.64	2.02	1.43	0.92
$C_{e,IL}$	0.123	-0.163	0.121	-0.069
$C_{a,IL}$	0.450	0.440	0.590	0.820
$\rho_{xy,IL}$	0.979	0.985	0.963	0.998
$\rho_{xy,CF}$	0.999	0.781	0.827	0.465
$\frac{C_{t2,IL}}{C_{t,IL}}$	0.264	0.197	0.117	0.066
$\frac{C_{t3,IL}}{C_{t,IL}}$	0.352	0.098	0.375	0.104
$C_{rms,CF}$	1.801	0.901	0.989	0.132
$C_{t,CF}$	1.783	0.834	0.071	0.014
$C_{t3,CF}$	0.222	0.235	0.012	0.006
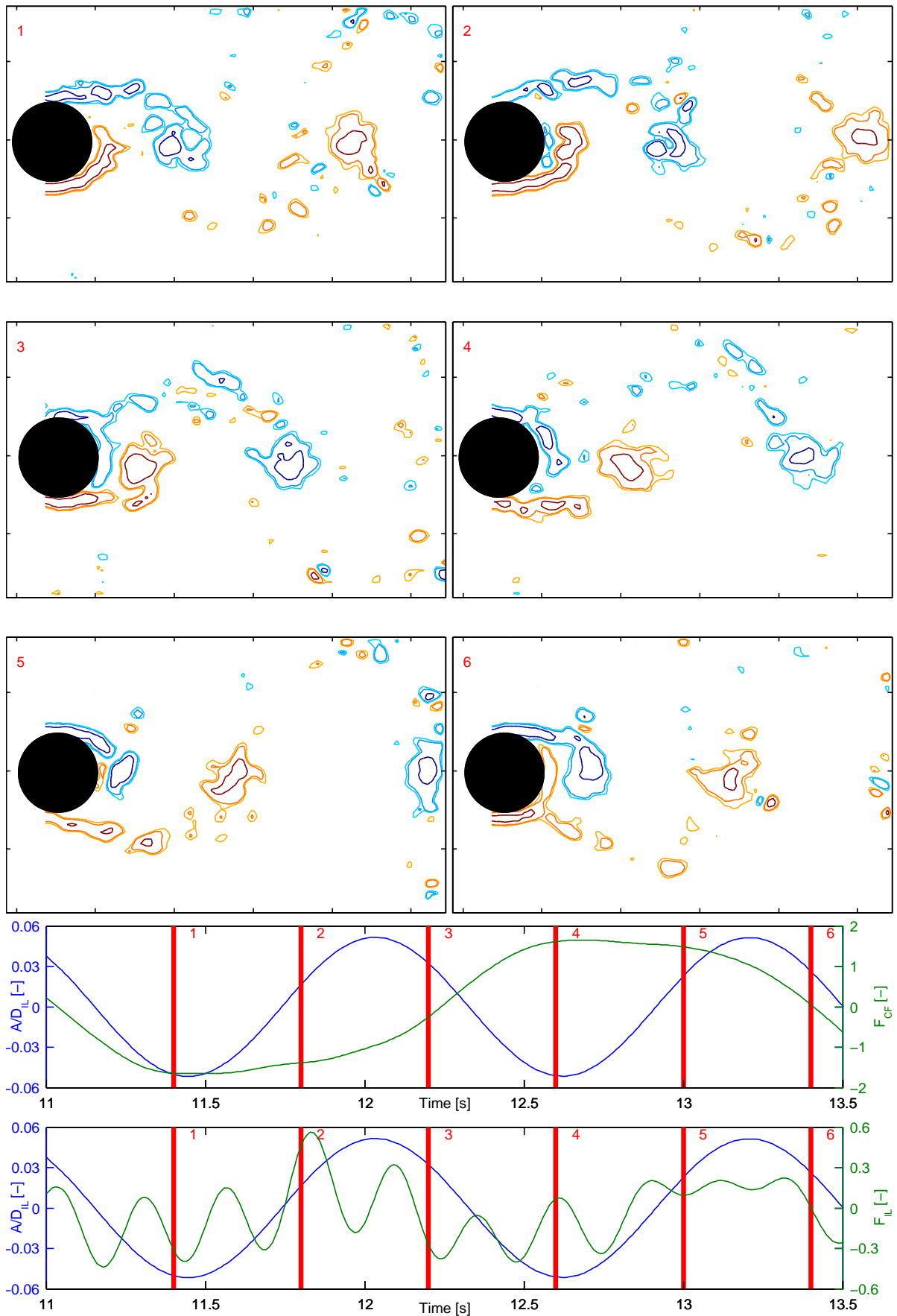
Figure D.2: Case A: 2nd instability region. $(A/D)_{IL}$=0.05 and $\hat{f}_{IL} = 0.325$.
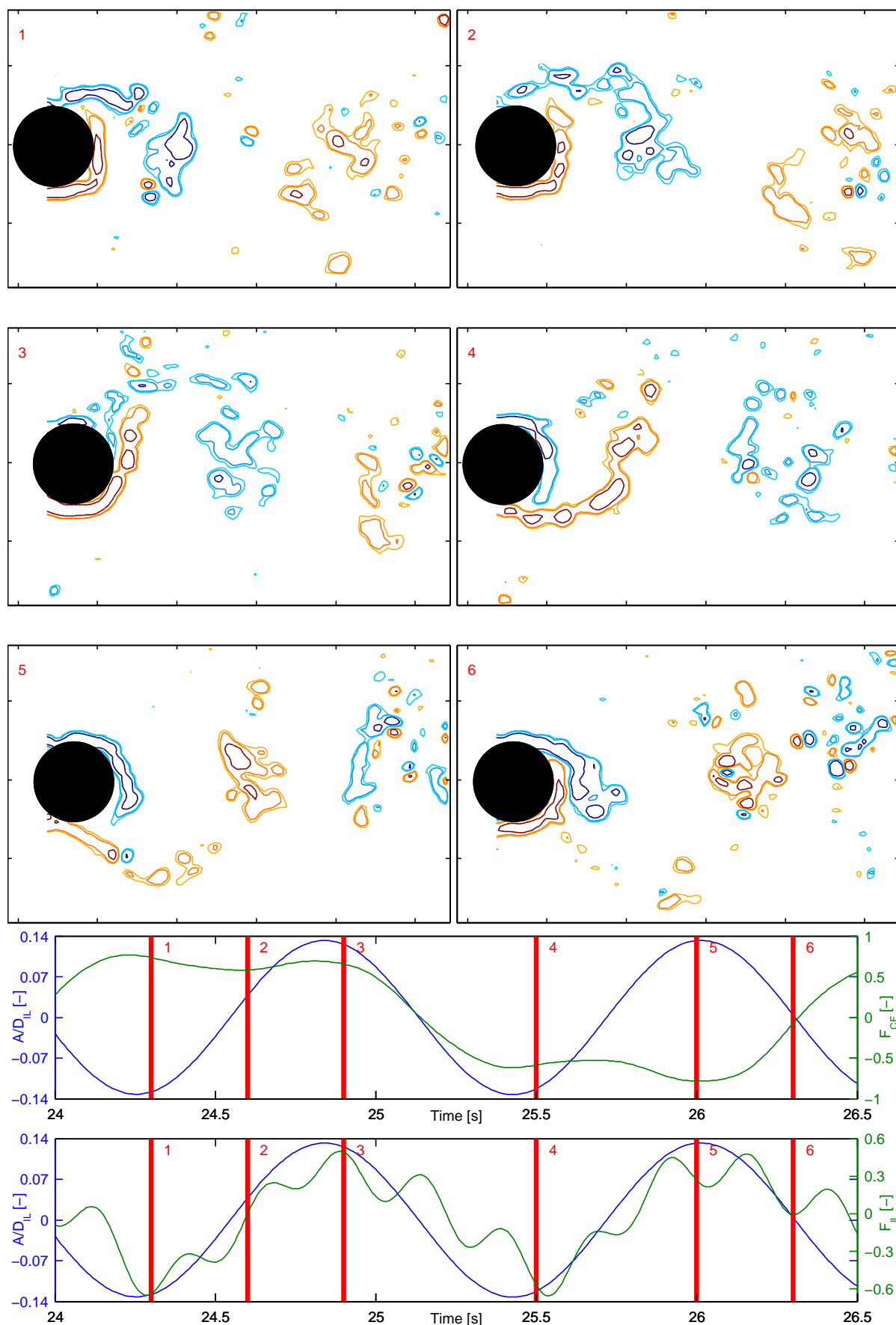
Figure D.3: Case B: 2nd instability region. $(A/D)_{IL}$=0.13 and $\hat{f}_{IL} = 0.325$.
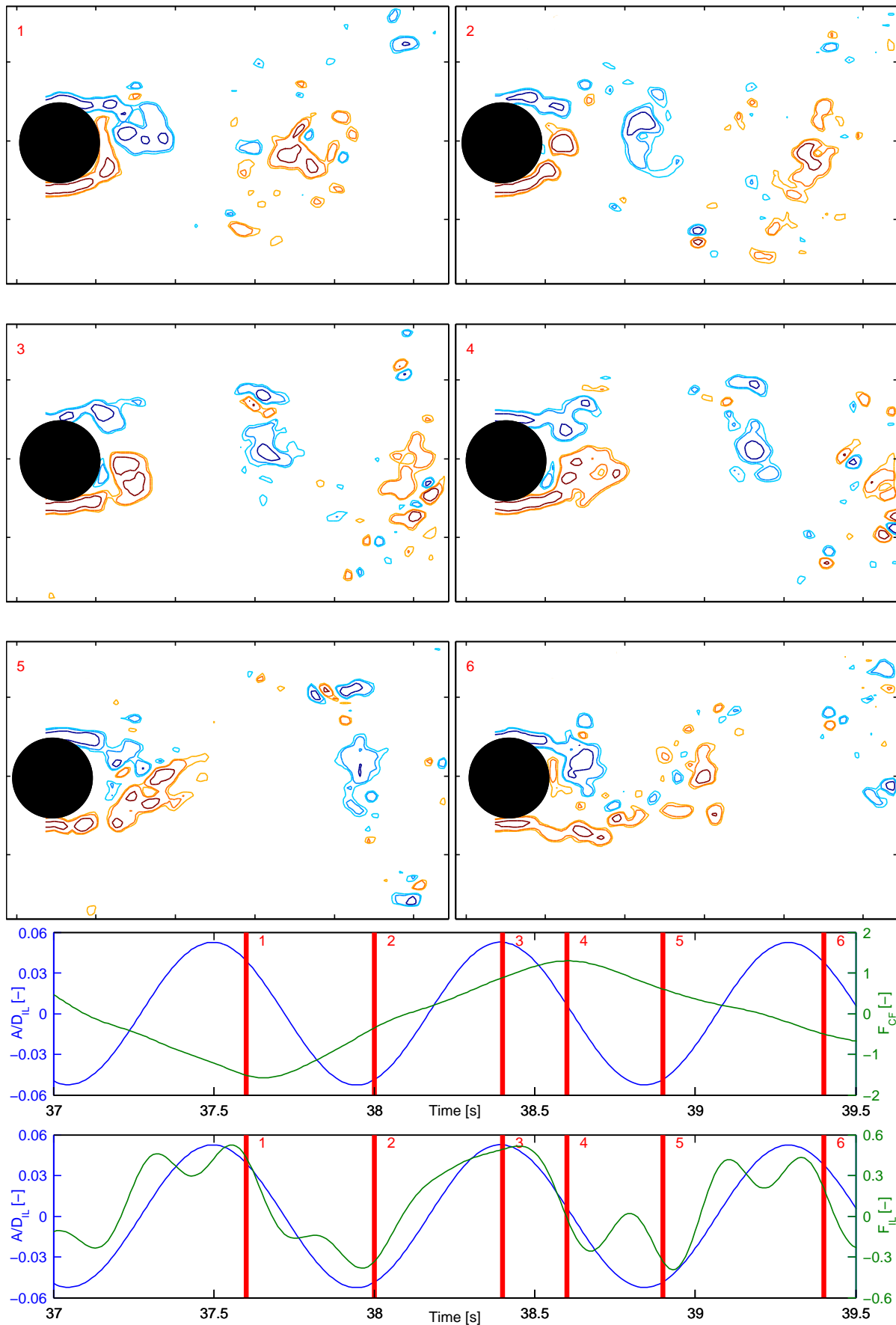
Figure D.4: Case C: 1st instability region. $(A/D)_{IL}$=0.05 and $\hat{f}_{IL} = 0.425$.
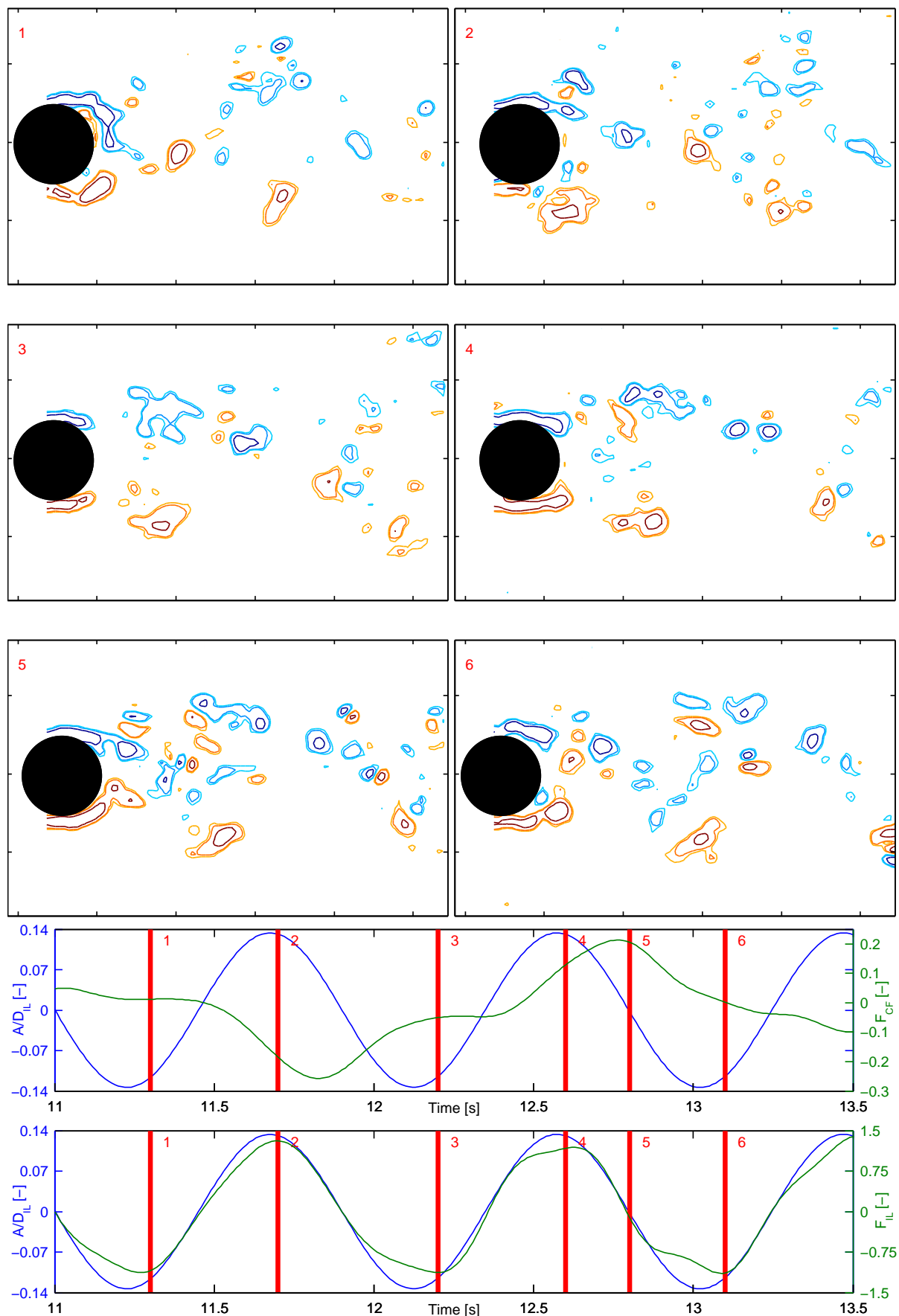
Figure D.5: Case D: 1st instability region. $(A/D)_{IL}$=0.13 and $\hat{f}_{IL} = 0.425$.

Appendix E

Results from CF experiments
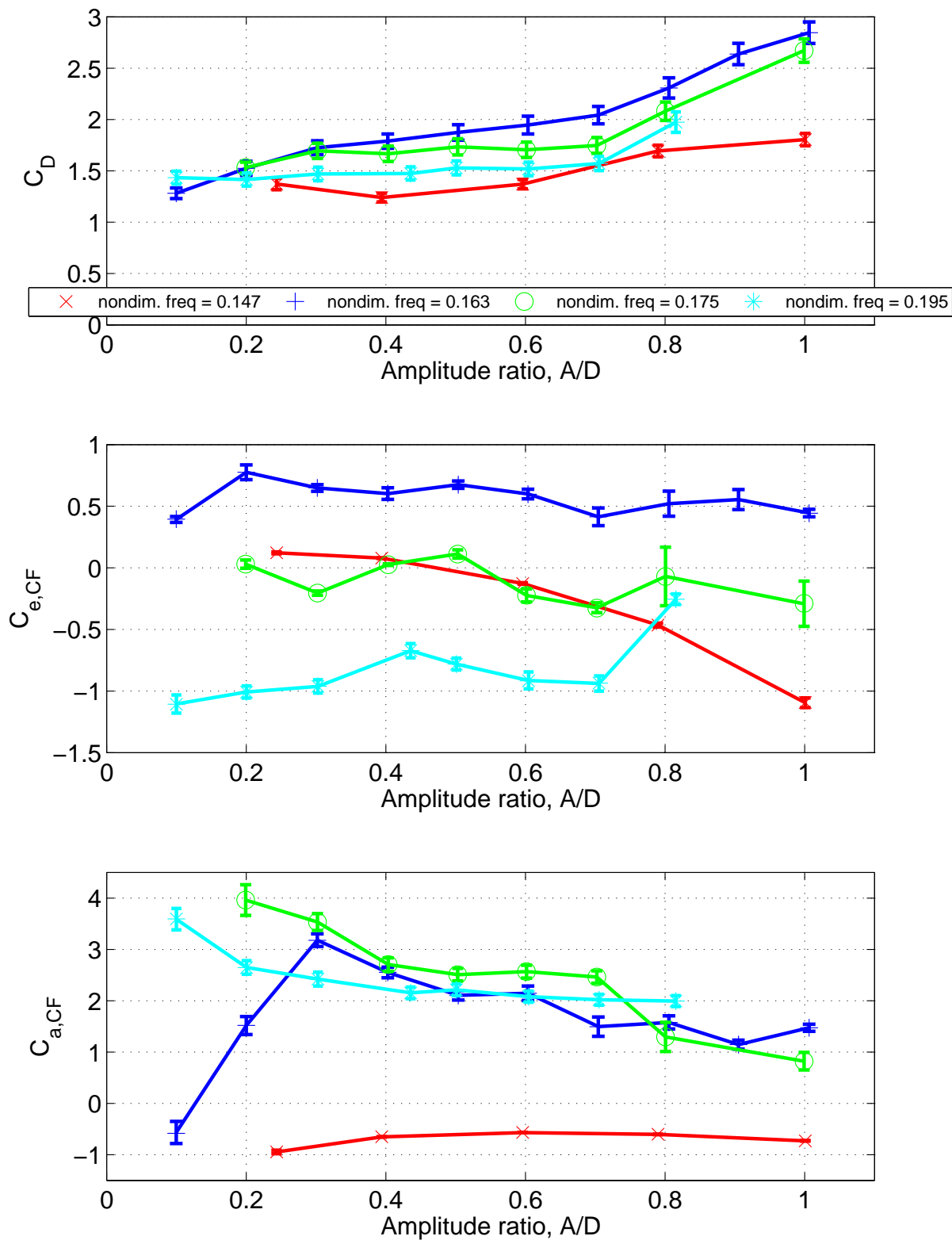
Figure E.1: Pure CF results.
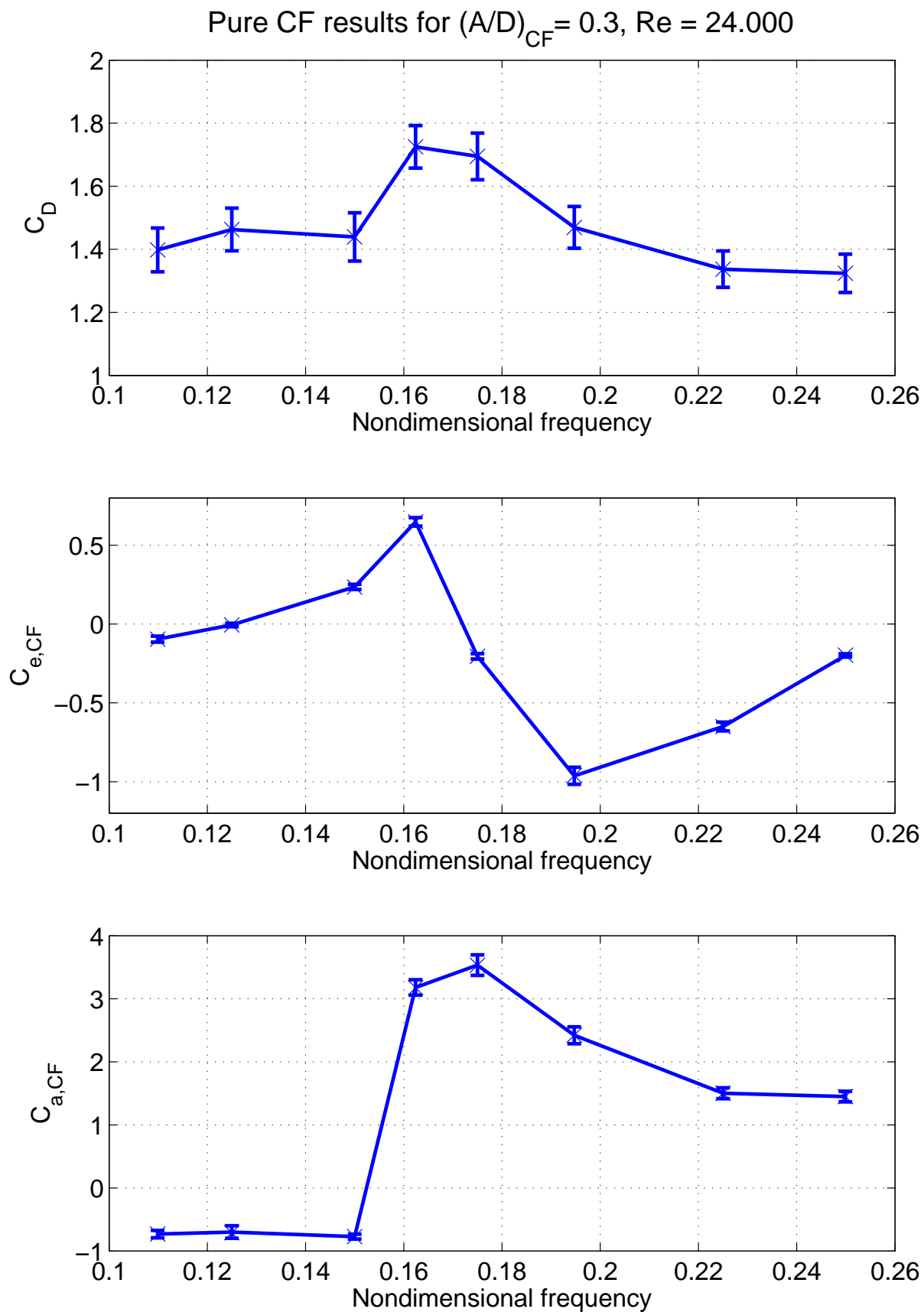
Figure E.2: Pure CF results for $(A/D)_{CF}$=0.3.
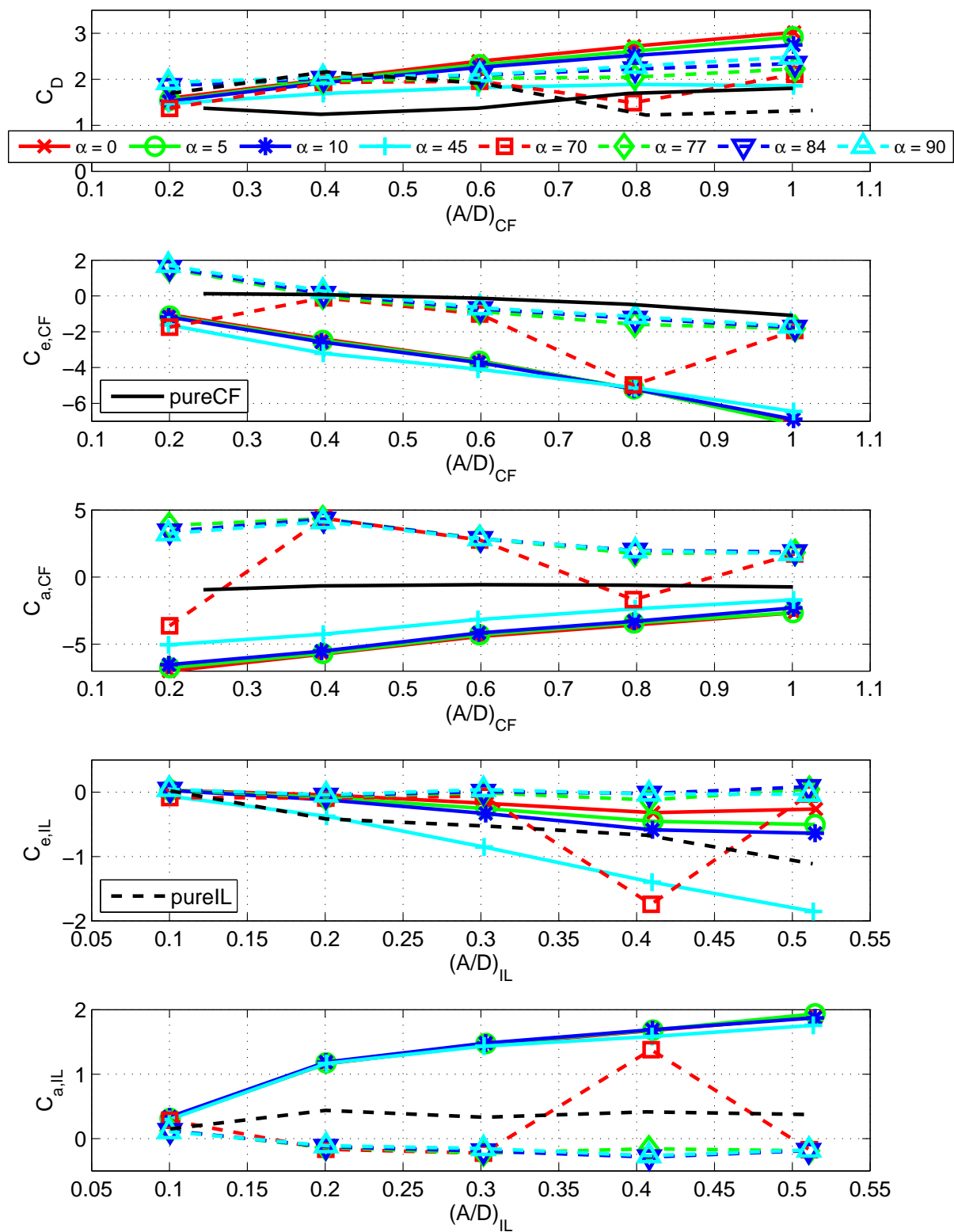
Figure E.3: Hydrodynamic coefficients for $\hat{f}_{CF}$=0.147.
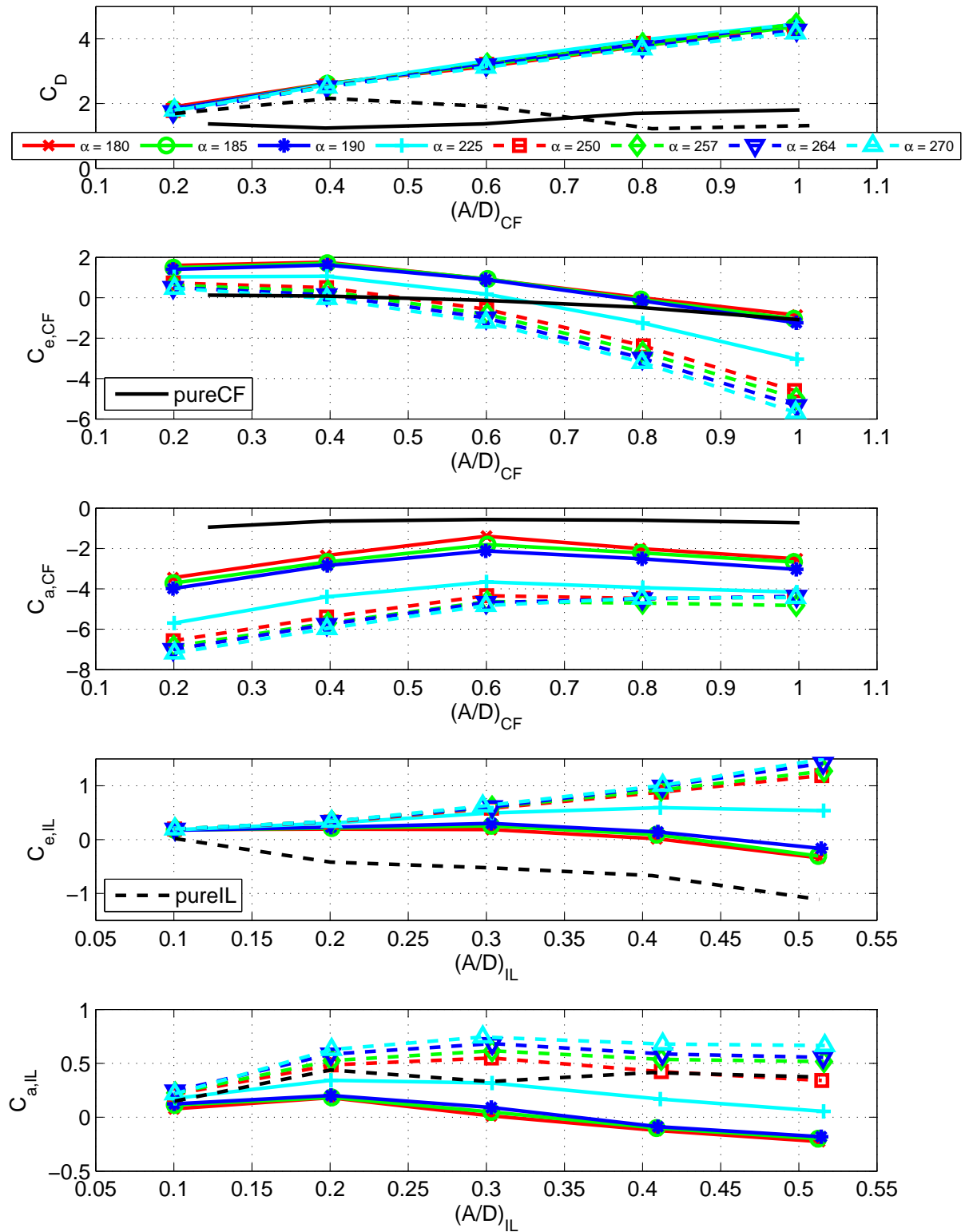
Figure E.4: Hydrodynamic coefficients for $\hat{f}_{CF}$=0.147.
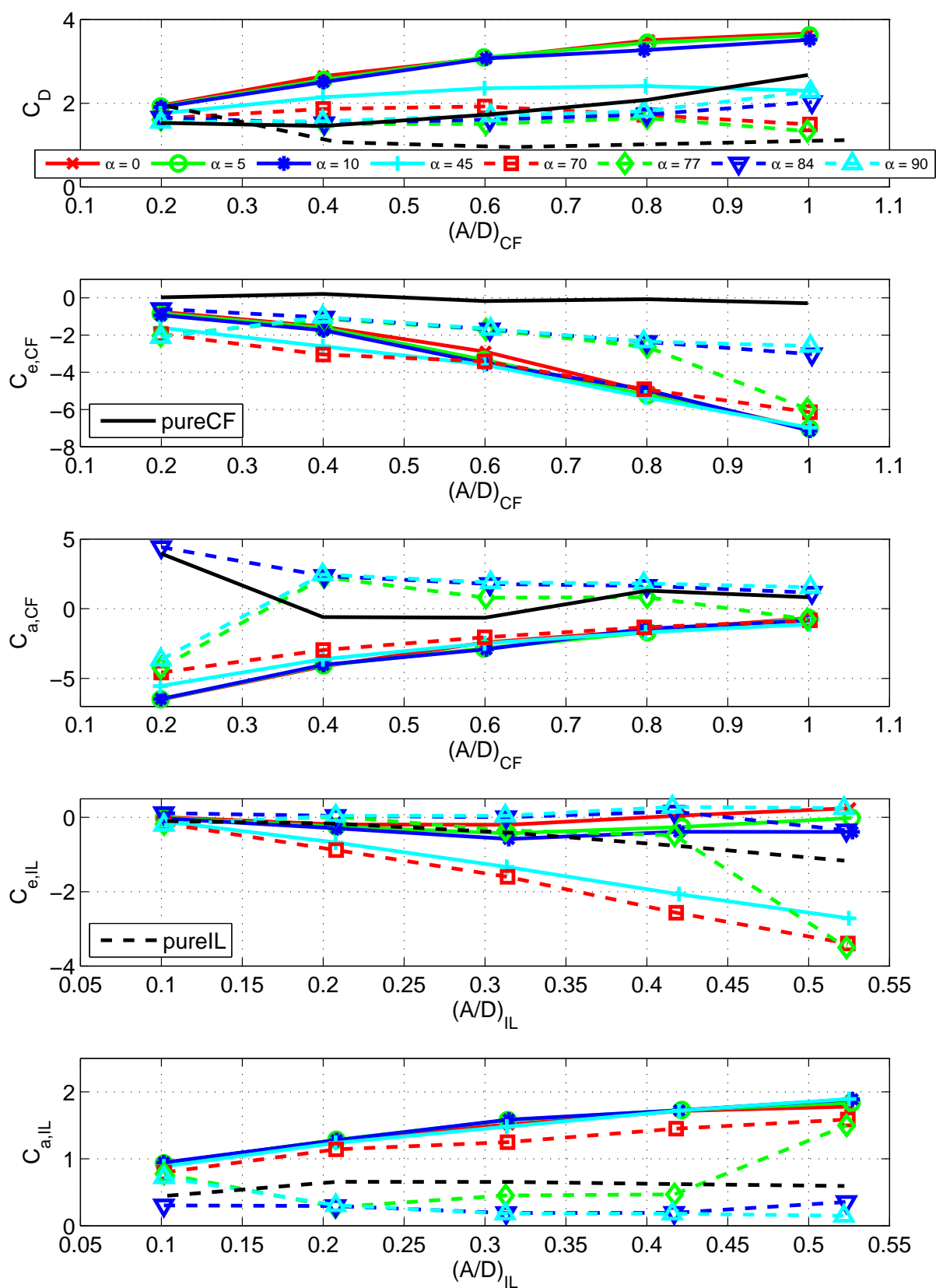
Figure E.5: Hydrodynamic coefficients for $\hat{f}_{CF}$=0.175.
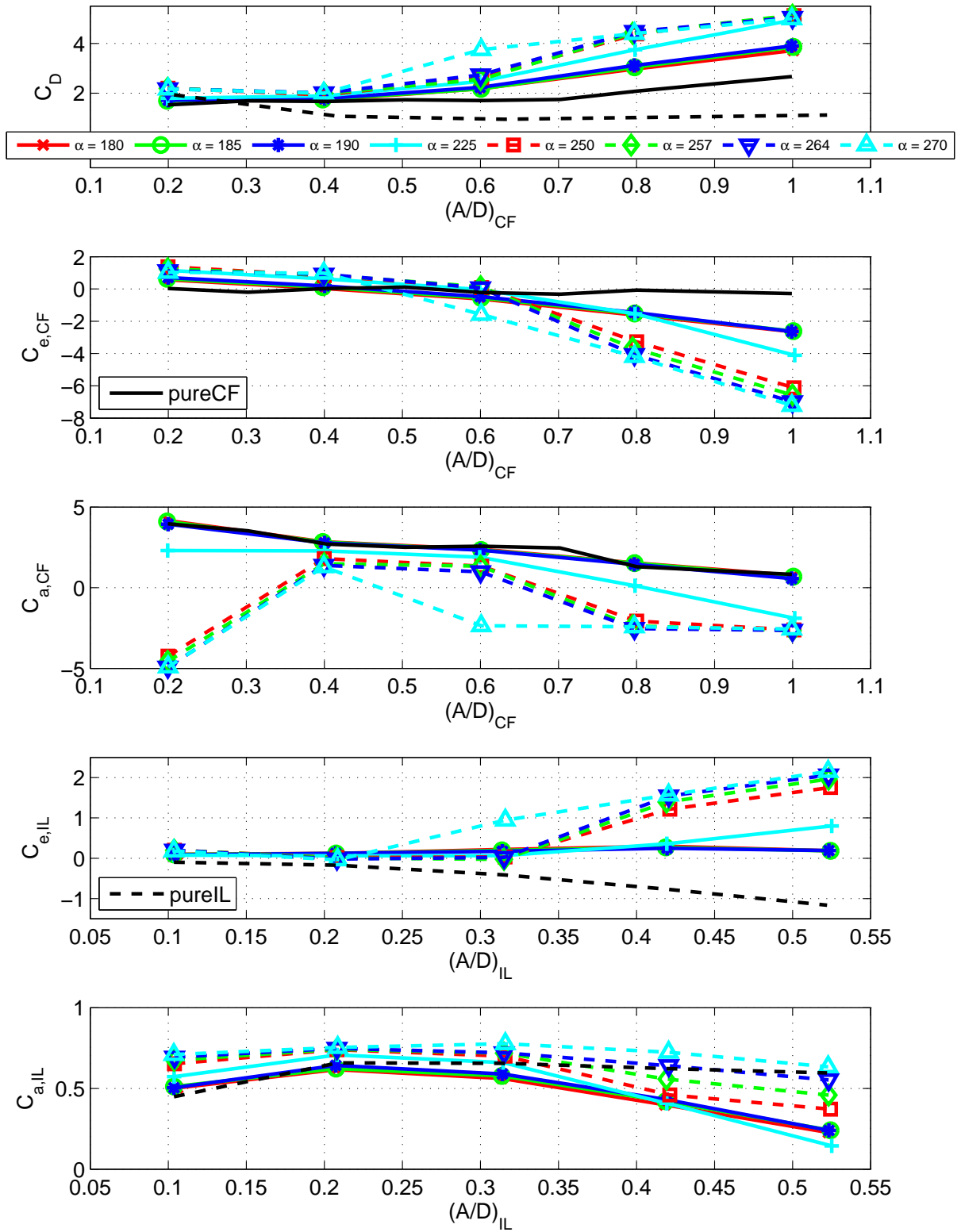
Figure E.6: Hydrodynamic coefficients for $\hat{f}_{CF}$=0.175.
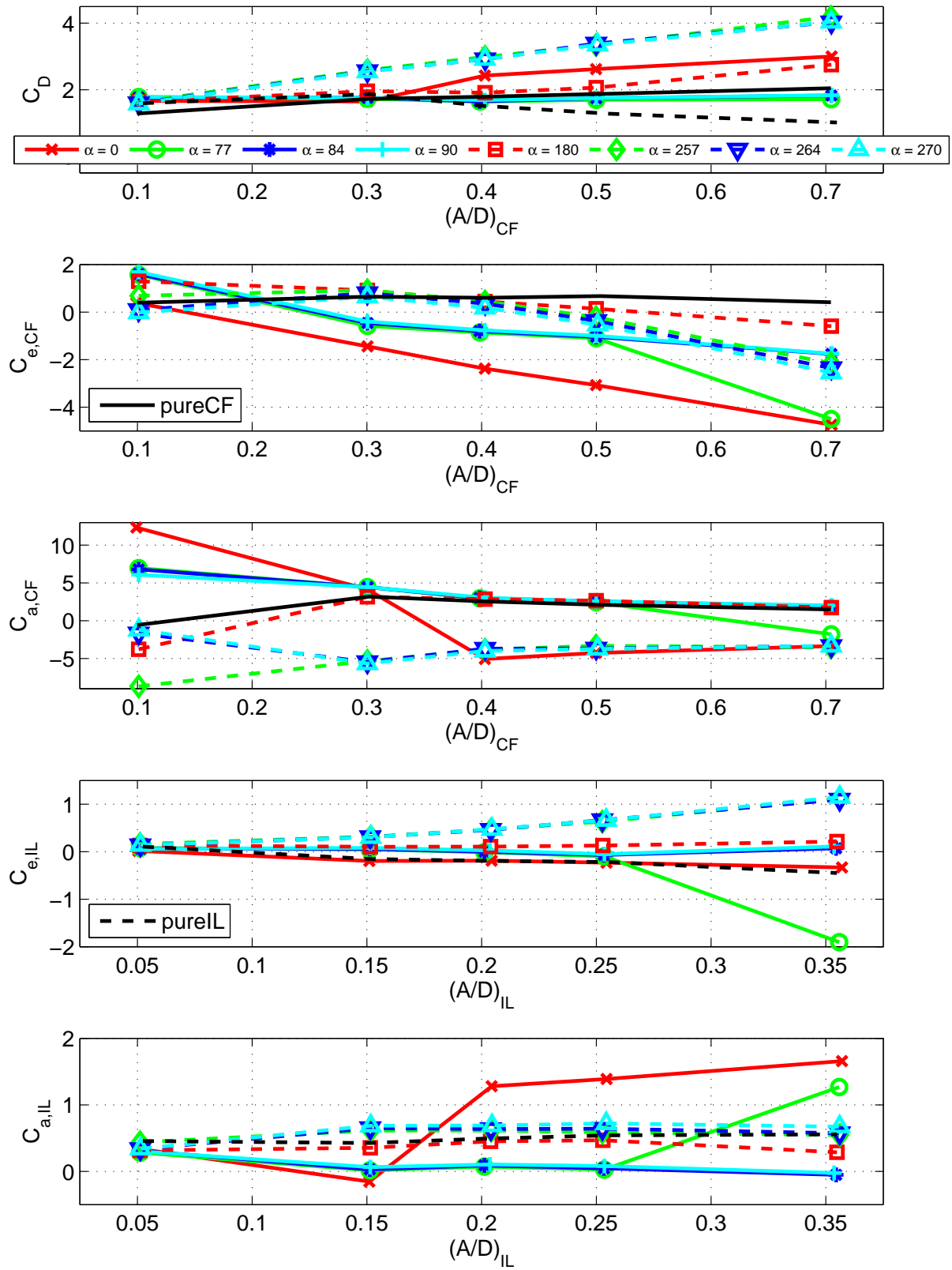
Figure E.7: Hydrodynamic coefficients for $\hat{f}_{CF}$=0.163.
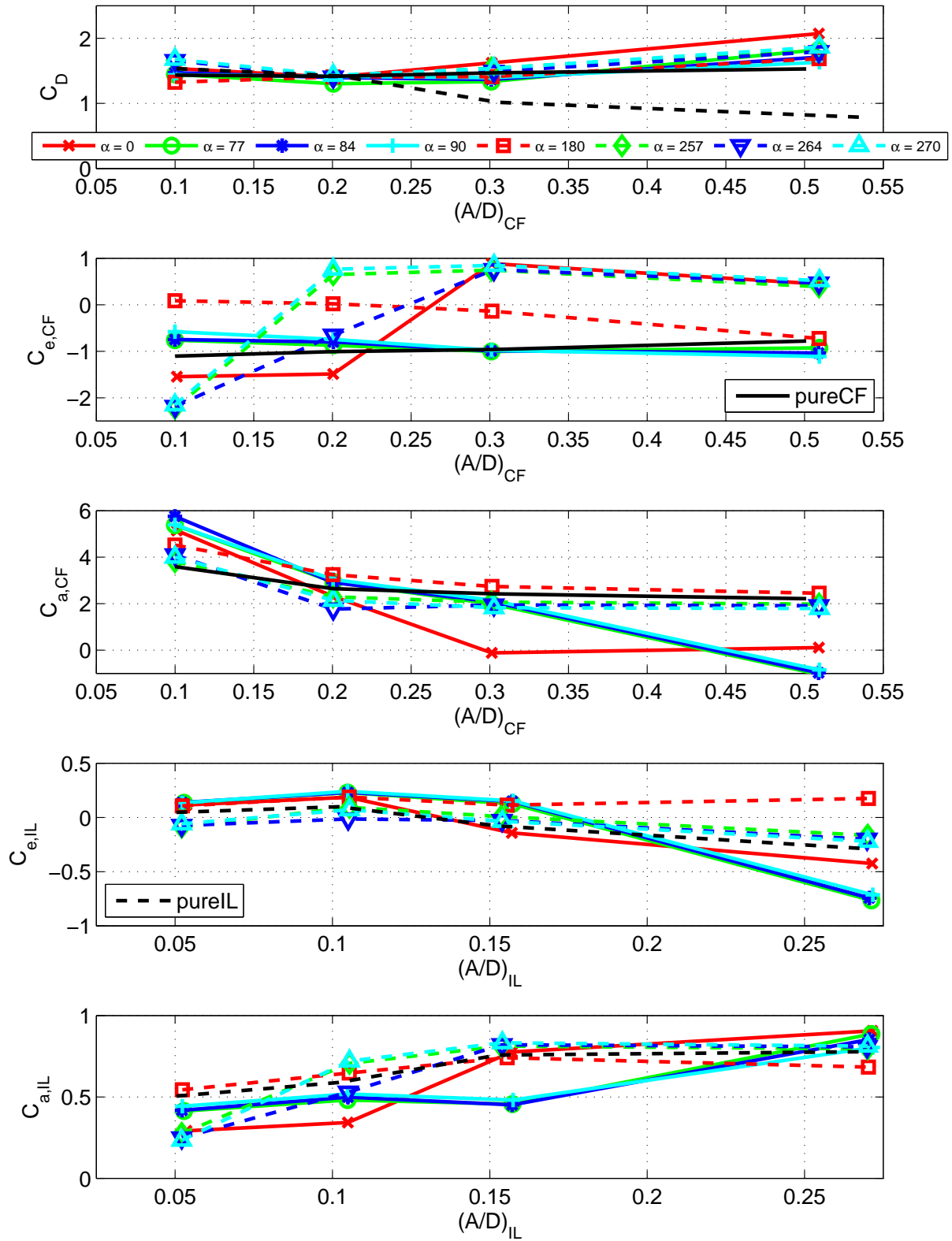
Figure E.8: Hydrodynamic coefficients for $\hat{f}_{CF}$=0.195.
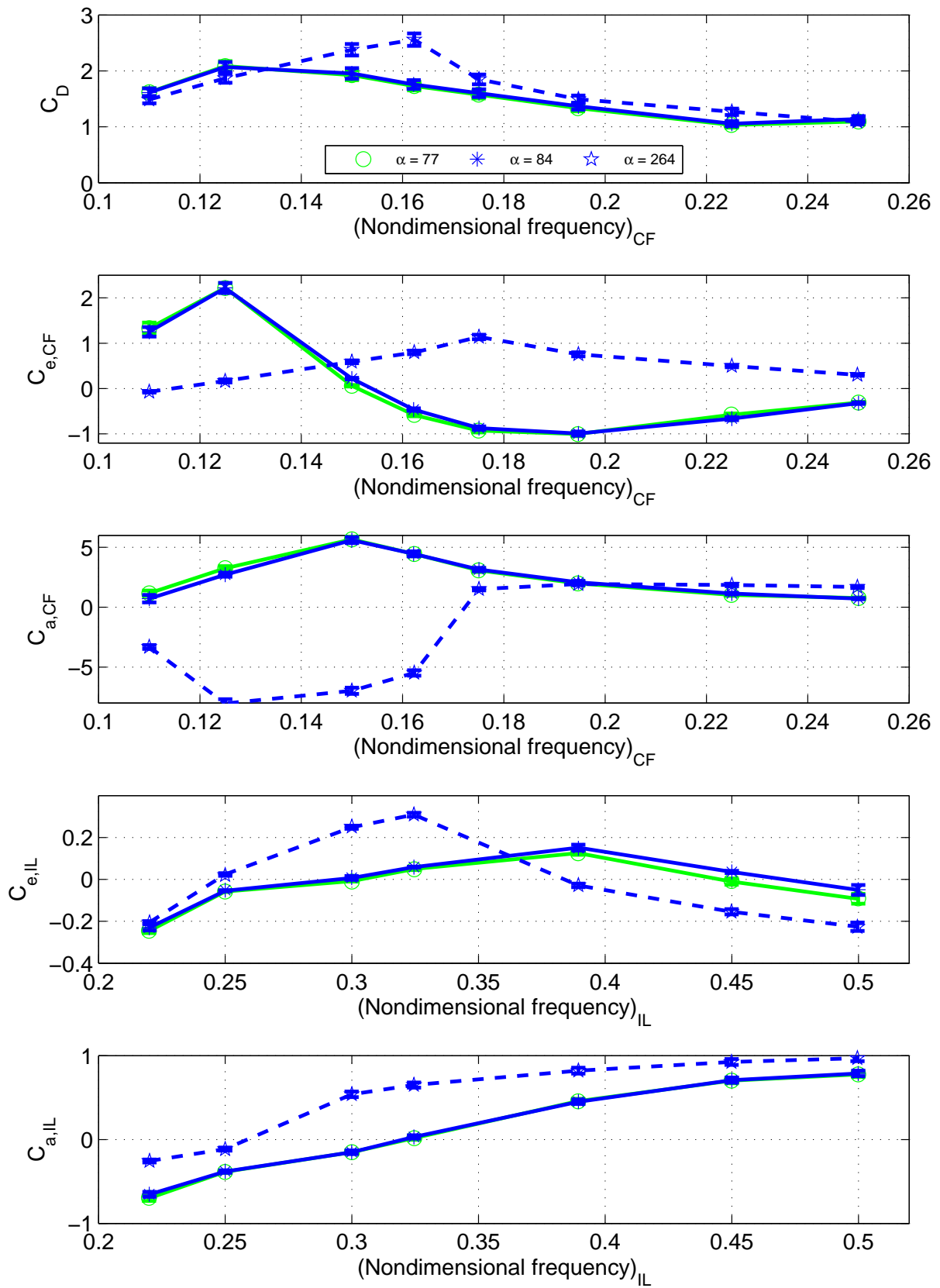
Figure E.9: Hydrodynamic coefficients for $(A/D)_{CF}$=0.3.
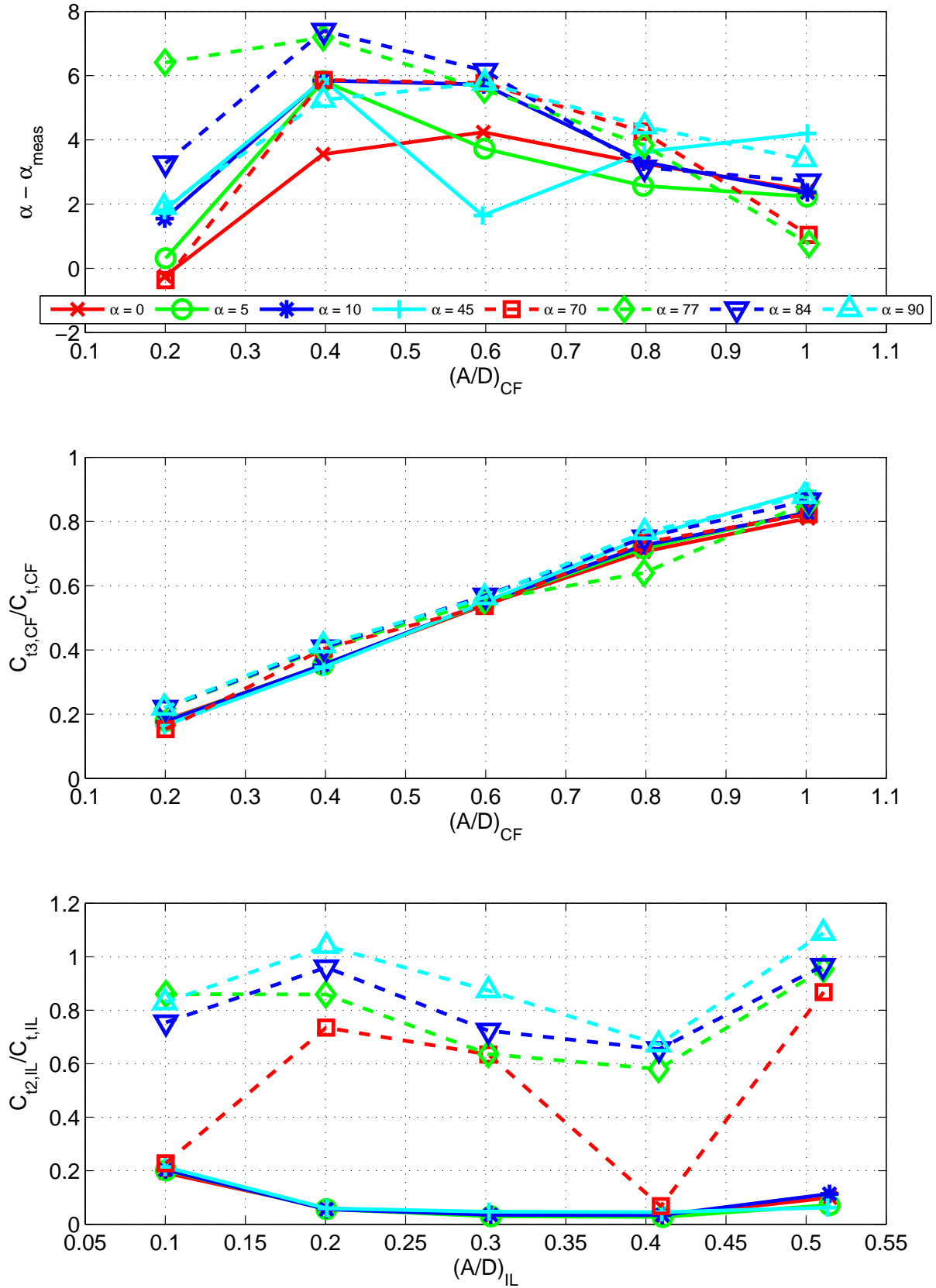
Figure E.10: Higher order harmonic forces for $\hat{f}_{CF}$=0.147 and α-values between 0 and 90. First plot shows the difference between the intended (reported) and measured α.
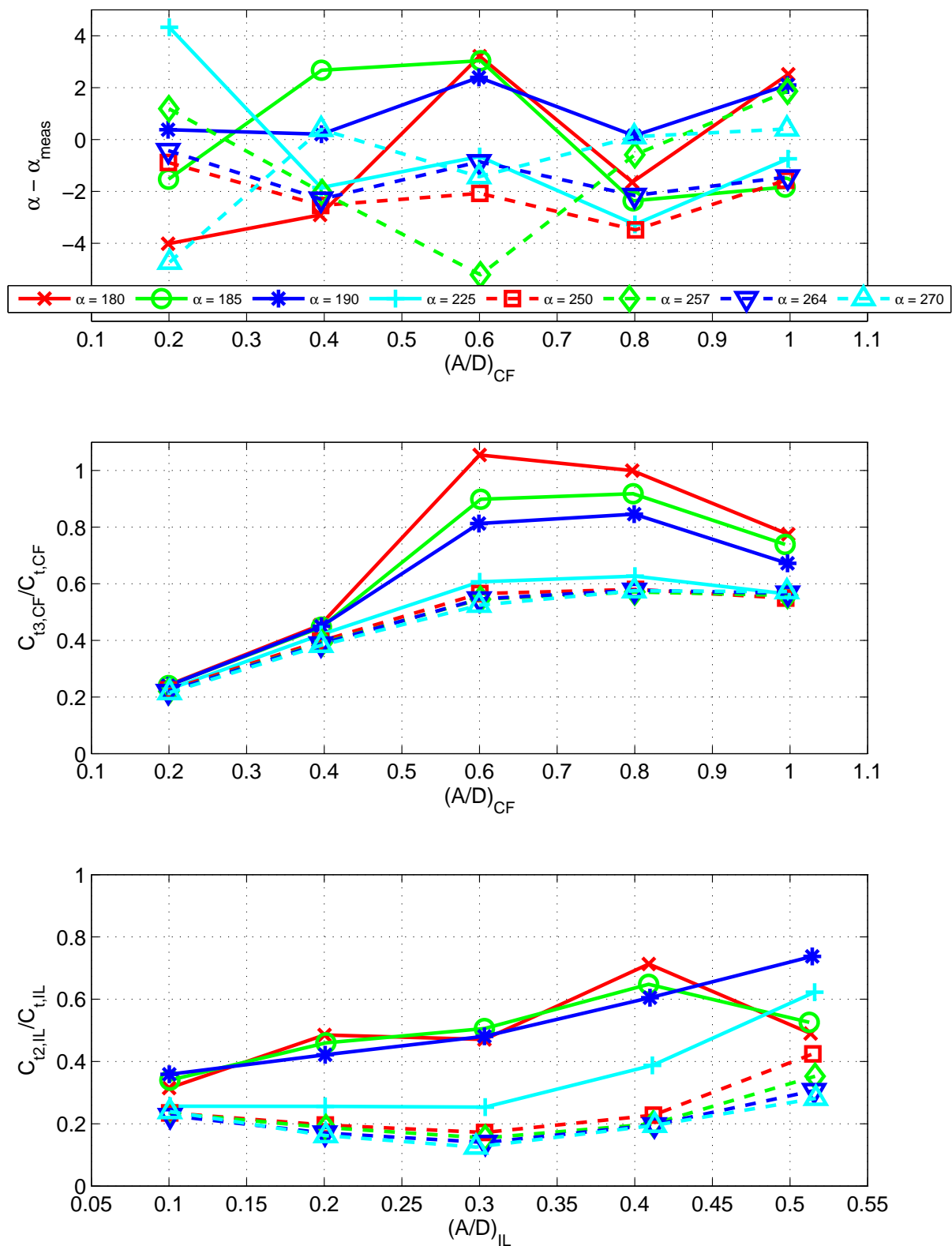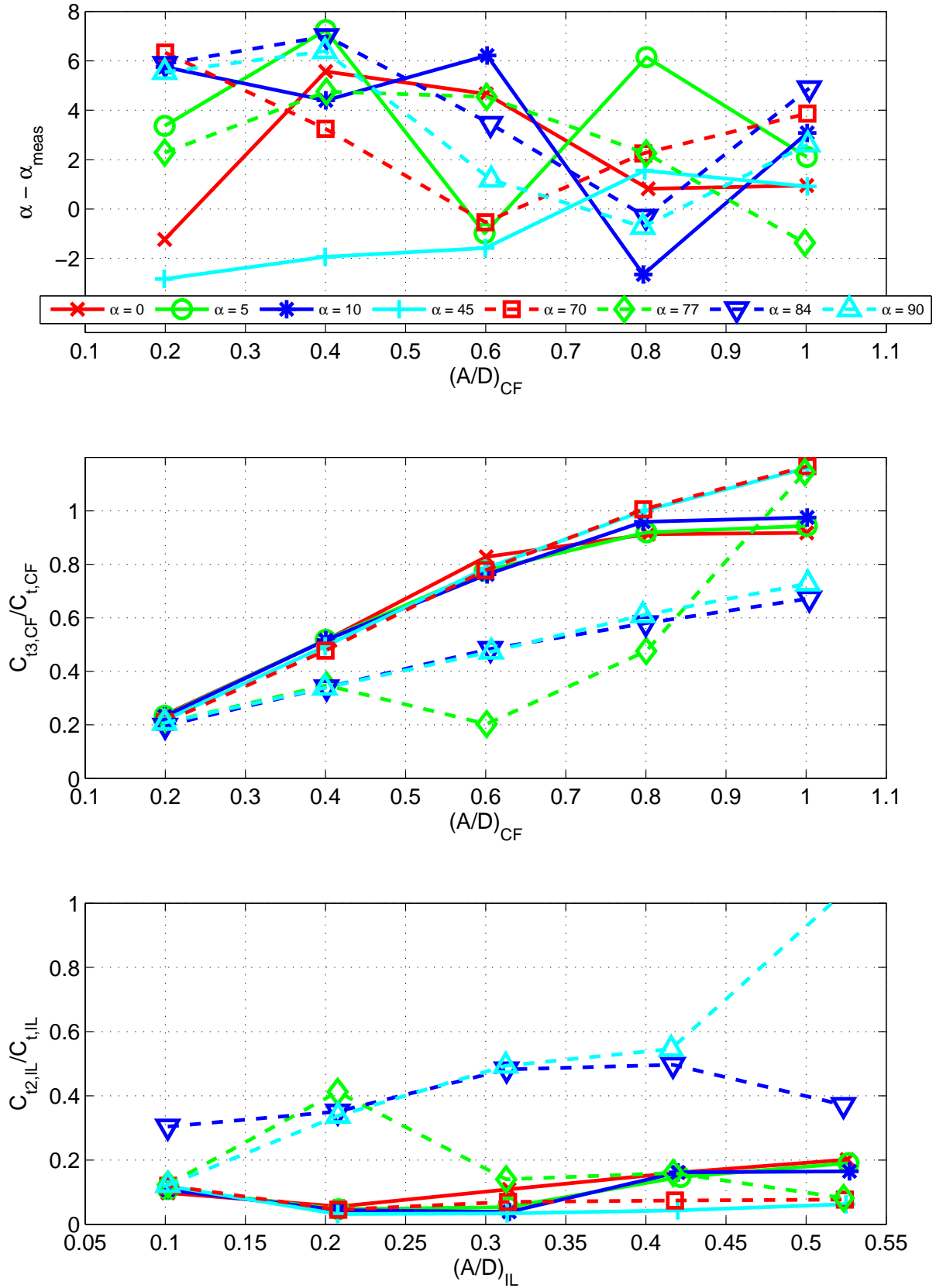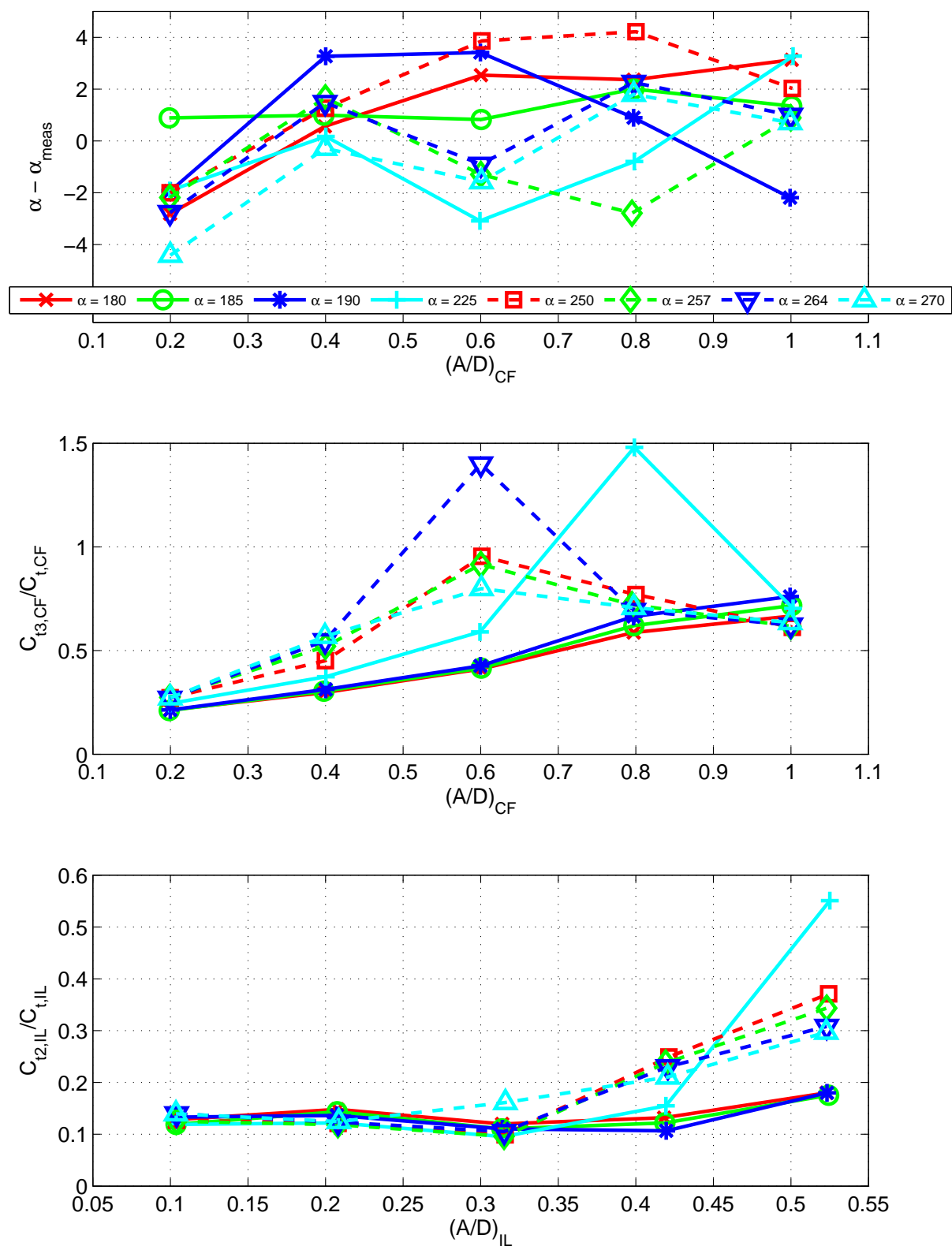
Figure E.11: Higher order harmonic forces for $\hat{f}_{CF}$=0.147 and α-values between 180 and 270. First plot shows the difference between the intended (reported) and measured α.

Figure E.12: Higher order harmonic forces for $\hat{f}_{CF}$=0.175 and α-values between 0 and 90. First plot shows the difference between the intended (reported) and measured α.

Figure E.13: Higher order harmonic forces for $\hat{f}_{CF}$=0.175 and α-values between 180 and 270. First plot shows the difference between the intended (reported) and measured α.
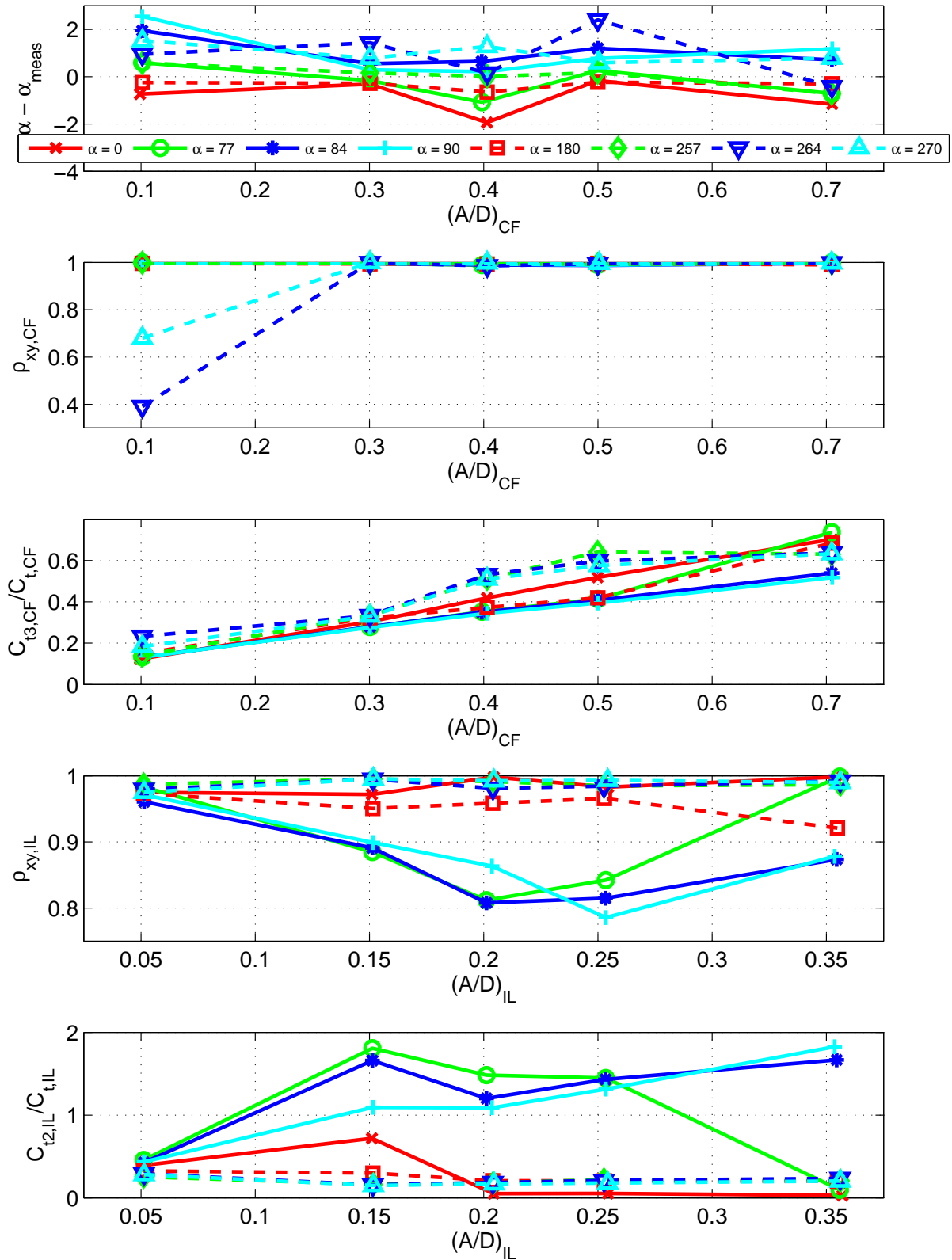
Figure E.14: Higher order harmonic forces for $\hat{f}_{CF}$=0.163. First plot shows the difference between the intended (reported) and measured α.
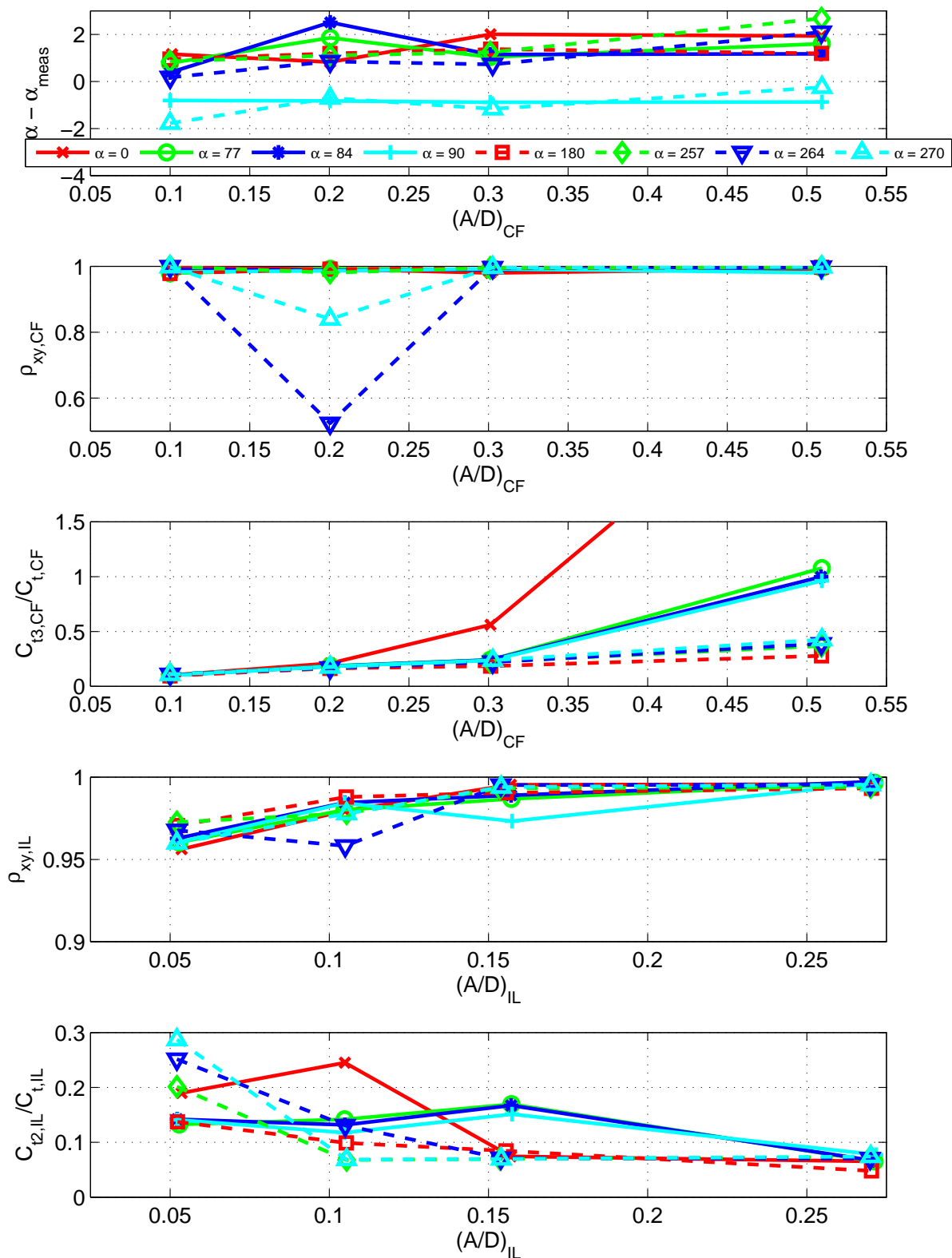
Figure E.15: Higher order harmonic forces for $\hat{f}_{CF}$=0.195. First plot shows the difference between the intended (reported) and measured α.